Diachronous Deformation, Metamorphism and Exhumation in the Northern Canadian Cordillera: Revealed from Pressure-Temperature-Time-Deformation Paths of Former Mid-Crustal Rocks

by

Reid Duncan Staples

M.Sc., Simon Fraser University, 2009
B.Sc., Simon Fraser University, 2007

Thesis Submitted in Partial Fulfillment of the
Requirements for the Degree of
Doctor of Philosophy

in the
Department of Earth Sciences
Faculty of Science

SIMON FRASER UNIVERSITY

Spring 2014

Approval

Name: **Reid Staples**

Degree: **Doctor of Philosophy (Earth Sciences)**

Title of Thesis: ***Diachronous deformation, metamorphism and exhumation in the northern Canadian Cordillera: revealed from pressure-temperature-time deformation paths of former mid-crustal rocks***

Examining Committee: **Chair:** Dr. Doug Stead
Professor, Department of Earth Sciences

Dr. Dan Gibson
Senior Supervisor
Associate Professor

Dr. Maurice Colpron
Supervisor
Adjunct Professor

Dr. Jim Ryan
Supervisor
Geological Survey of Canada

Dr. Rob Berman
Supervisor
Geological Survey of Canada

Dr. Lambertus Struik
Internal Examiner
Adjunct Professor
Department of Earth Sciences

Dr. Bill McClelland
External Examiner
Professor
Department of Geosciences
The Univeristy of Iowa

Date Defended/Approved: March 26, 2014

Partial Copyright Licence

Abstract

The lowest structural and stratigraphic levels of the Yukon-Tanana terrane and the structurally underlying parautochthonous North American margin rocks were metamorphosed at similar conditions (7.5 – 9 kbar; 600 – 680 °C) and share a common style of deformation, characterized by the transposition of lithologic contacts and primary compositional layering into a regional ductile foliation (S_T) with at least one generation of intrafolial isoclinal folds. Equilibrium assemblage modeling and *in situ* U-Th-Pb SHRIMP dating of monazite are used to place quantitative constraints on the conditions and timing of deformation, metamorphism and subsequent decompression. These data reveal that these fabrics, and the associated metamorphism, did not develop during a single tectono-metamorphic event. Rather, ductile deformation and high-grade metamorphism developed diachronously. Rocks deformed and metamorphosed in the Permo-Triassic and Early Jurassic were exhumed in the Early Jurassic, while rocks to the northeast in the Finlayson domain were buried, heated and ductiley deformed at mid-crustal levels (~25 km depth) from the Middle Jurassic to Early Cretaceous (c. 169 – 142 Ma). Metamorphism continued at an even deeper crustal level (~ 30 km depth, as recorded in the Australia Mountain domain), propagating downward into the parautochthonous North American crust in the Early Cretaceous (c. 146 – 118 Ma). Together, these data reveal a spatial and temporal pattern of structurally downward younging deformation and metamorphism that corresponds with the foreland-directed growth of a critically tapered orogenic wedge. In this model, rocks in front of the wedge are episodically underthrust downward into a distributed, high-grade transposition shear zone at 25 to 30 kilometres depth near the base of the overriding wedge. Rocks previously underthrust, buried and metamorphosed are progressively exhumed to higher structural levels within the wedge, as the upper crust enters a state of extension in order to maintain a critically tapered wedge. Rocks that occupied the mid-crustal shear zone in the Middle Jurassic and Early Cretaceous (Finlayson and Australia Mountain domains) were exhumed in the mid-Cretaceous along southeast-directed (orogen-parallel) extensional faults, from beneath a supracrustal 'lid' that had previously been metamorphosed and ductiley deformed at amphibolite facies in the Permo-Triassic and Early Jurassic.

Keywords: Northern Canadian Cordillera; Yukon-Tanana terrane; SHRIMP; *in situ* monazite geochronology; *P-T-t* path

Acknowledgements

I am very grateful to my supervisor Dan Gibson for his mentorship, allowing me to work freely and independently, and for always having an open door to discuss working ideas and provide critical insight. My co-supervisors Maurice Colpron and Jim Ryan are thanked for proposing this thesis project as part of the Edges project, funded by the GEM (Geo-Mapping for Energy and Minerals) Program of Natural Resources Canada. Maurice Colpron and Jim Ryan were excellent mentors, and provided crucial insight and a wealth of knowledge of the regional geology and tectonics of the Cordillera orogen. Rob Berman is thanked for being on my supervisory committee and providing critical insight and guidance on everything P-T-t-D path related. I am grateful to all of my supervisors Dan Gibson, Maurice Colpron, Jim Ryan and Rob Berman for their detailed critical reviewing of the thesis and manuscripts. Don Murphy is thanked for assisting and guiding me in the Finlayson Lake district, for sharing his wealth of knowledge of the Yukon-Tanana terrane and the Cordilleran orogen, and providing critical insight and review to portions of this thesis and a published manuscript.

Nicole Rayner, Bill Davis, Tom Pestaj and Rob Berman are thanked for their assistance and guidance with in situ SHRIMP monazite analyses at the Geological Survey of Canada in Ottawa. Pat Hunt is thanked for locating and mapping monazite in thin section and providing high-quality BSE images. Mike Williams and Mike Jercinovic at UMASS are thanked for providing high-quality chemical X-ray maps of monazite. Mati Raudsepp and Edith Czech and thanked for their asistance with eletron microprobe analyses at UBC. Doug Tinkham is thanked and acknowledged for providing the thermodynamic data set tcds55 formatted for use with Theriak-Domino. Janet Gabites is thanked for providing the $^{40}Ar/^{39}Ar$ analyses. John Mayer, Sarah Shoniker and Sydney vanLoon are thanked for their assistance in the field. Bill McClelland is thanked for his insightful comments and constructive criticism as the external examiner. I am very grateful and thankful to Bert Struik, not only for providing insightful comments as the internal examiner, but also for giving me this opportunity by recommending me to the EDGES project leaders.

In addition to GEM funding, I would like to acknowledge other funding for this project provided by research grants from the Natural Science and Engineering Research Coouncil (NSERC) to Maurice Colpron and Dan Gibson, as well as financial and logistical support from the Yukon Geological Survey, and scholarships and awards from NSERC and the Northern Studies Training Program.

I would also like to thank my family, especially my mother, for all of their love and support. Finally, I would like to thank and extend my love and appreciation to Melissa Jackson for her support, love and encouragement.

Method of Presentation

This thesis is presented as three self-contained papers (Chapters 2, 3, and 4), each contributing to a common goal of unraveling the tectonometamorphic history of the hinterland of the northern Canadian Cordilleran orogen. This format is intended to facilitate the publication of this research; however, it introduces some unavoidable redundancies. Chapters 1 and 5 are introductory and conclusion chapters, respectively, which outline the aim of the study and how each of the three self-contained papers (chapters 2, 3, and 4) fit together into the single coherent theme mentioned above. I was the primary author for all manuscripts (Chapters 2, 3 and 4). These three manuscripts/chapters are coauthored by my co-supervisors Dan Gibson and Maurice Colpron, as well as my committee members Jim Ryan and Rob Berman. Don Murphy provided field assistance, guidance of regional geology and contributed comments to an early version of chapter 3, warranting co-authorship of this paper. Chapter 2 has been published in the Journal of Metamorphic Geology in September 2013. Chapter 3 has been accepted with minor revisions to the journal Geological Society of America Bulletin.

Table of Contents

List of Tables

List of Figures

Chapter 1.

Introduction

1.1. Presentation of the Problem

The metamorphic hinterland of the northern Canadian Cordilleran orogen in Yukon largely consists of the allochthonous Yukon-Tanana terrane and structurally underlying parautochthonous North American margin rocks (Fig. 1.1). These rocks have experienced a protracted and transitory history of sedimentation, continental arc magmatism, rifting, intraoceanic arc magmatism (only Yukon-Tanana terrane), arc-continent collision and subsequent crustal shortening (Nelson et al., 2006). This complex history is recorded, in part, by multiple phases of deformation and metamorphism in the lowest structural levels of the Yukon-Tanana terrane and the structurally underlying parauthochthonous North American margin rocks. Much of these lowest exposed structural levels have been metamorphosed to amphibolite facies and share a common style of deformation characterized by the transposition of lithologic contacts and primary compositional layering into a regional ductile foliation (S_T) with at least one generation of intrafolial isoclinal folds (Foster et al., 1994; Hansen and Dusel-Bacon, 1998; Dusel-Bacon et al., 1995, 2002, 2006; Gordey and Ryan, 2005; Berman et al., 2007).

The majority of published quantitative P-T data from the hinterland of the northern Cordillera comes from scattered eclogite occurrences both within and along the boundaries of Yukon-Tanana terrane (Fig. 1.2; Creaser et al., 1997; Erdmer et al., 1998). The poorly resolved geological and structural context of these eclogites with respect to the regional greenschist to amphibolite facies metamorphism within Yukon-Tanana terrane suggests they may not be representative of the terrane as a whole. There are a few additional metamorphic studies within Yukon-Tanana terrane (Hansen, 1992; Johnston, 1993; Dusel-Bacon et al., 1995; de Keijzer, 2000; and the structurally underlying parautochthonous rocks (Dusel-Bacon et al., 1995). However, given the

transitory and diachronous nature of deformation and metamorphism, and polytectonic history of orogenic belts, the absence of prograde metamorphic dates linked to these P-T estimates prevents any significant understanding of the orogen's history. Prior to the study of Berman et al. (2007), which provided in situ SHRIMP U-Pb ages linked to changing P-T conditions, estimates for the timing of metamorphism came primarily from metamorphic cooling ages (e.g. Hansen et al., 1991; Dusel-Bacon et al., 2002). However, as Berman et al. (2007) revealed, Yukon-Tanana terrane has experienced several moderate pressure (~9 kbar) amphibolite facies metamorphic events; therefore, K-Ar and $^{40}Ar/^{39}Ar$ ages will only provide the time of cooling following the youngest metamoarphic event.

Two different, yet overlapping, timing constraints for the development of the transposition foliation within the northern Yukon-Tanana terrane in west-central Yukon have been proposed (c. 260-240 Ma; Berman et al., 2007; and 260-253 Ma; Beranek and Mortensen, 2011). However, deformation and metamorphism is commonly diachronous both across and along strike within orogens (e.g. Collins and Vernon, 1992; Hatcher et al., 2002; Berman et al., 2010); therefore, it is uncertain to what extent the timing of this deformation and metamorphism can, or should be correlated throughout the terrane. In fact, the style, orientation and sequence of deformation, and the amphibolite facies metamorphism accompanying it, is a common feature of many orogenic belts worldwide (Turner and Weiss, 1963; Hobbs et al., 1976; Williams and Jiang, 2005). It is therefore possible that the nearly identical transposition foliation and amphibolite facies metamorphism observed throughout Yukon-Tanana terrane and the structurally underlying parautochthonous North American margin rocks may have formed during very different times in different places (both spatially and structurally) and in different geodynamic settings.

Hints of this diachronous tectono-metamorphism have been revealed from the in situ U-Pb monazite dating of Berman et al. (2007), who not only documented a Permo-Triassic deformational and metamorphic event, but also a 9 kbar Early Jurassic metamorphic overprint, and a separate Early Cretaceous metamorphic domain around Mount Burnham in the eastern Stewart River area. In fact, prior to the work of Berman et al. (2007) most of the ductile deformation and amphoibolite-facie metamorphism throughout Yukon-Tanana terrane had been attributed to the Jurassic based on

evidence for Early Jurassic contraction and imbrication (Hansen and Dusel-Bacon, 1998; Murphy et al., 2006) and widespread K-Ar and $^{40}Ar/^{39}Ar$ cooling ages (Hansen et al., 1991; Johnston et al., 1996; Dusel-Bacon et al., 2002).

Thus, the problem being addressed here deals with resolving the temporal and spatial evolution of deformational and metamorphic events throughout Yukon-Tanana terrane and the structurally underlying parautochthonous North American margin rocks. In particular, to what extent do we assign the main transposition event and associated amphibolite facies metamorphism to the initiation of subduction and subsequent arc magmatism in the Devonian and Mississippian, versus Permo-Triassic accretion, or later Jura-Cretaceous crustal shortening? Are the numerous phases of deformation observable across the terrane and at different structural levels coeval or diachronous, and were they created by the same tectonic processes? Also, if deformation and metamorphism was diachronous throughout this portion of the orogen, by what means did different domains escape earlier or later deformation and metamorphic events in adjacent or structurally underlying or overlying portions of the orogen? The answers to these questions will not only improve our understanding of the tectonic evolution of this portion of the northern Canadian Cordillera, but may also provide insight into the orogenic processes responsible for mountains building events throughout the world.

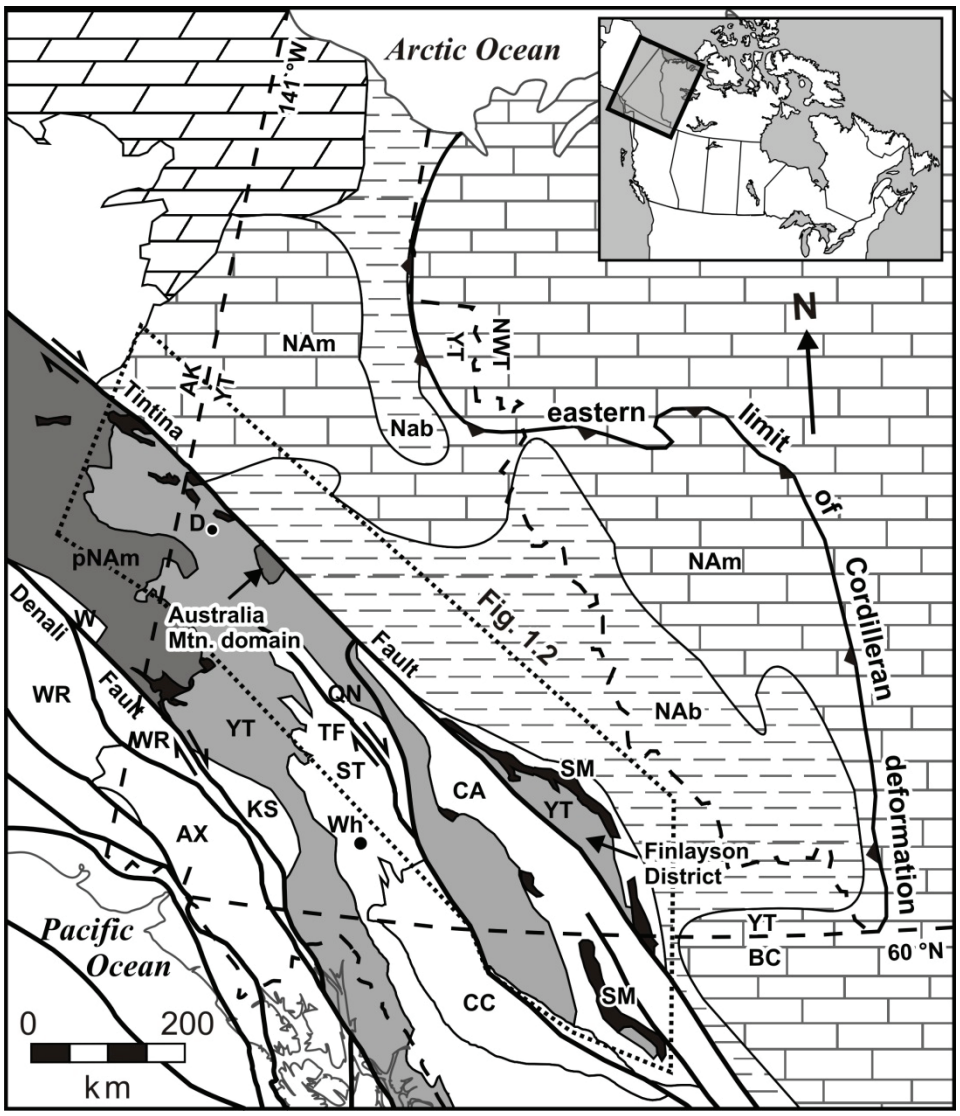

Figure 1.1. **Simplified terrane map of the northern Canadian Cordillera (modified from Colpron et al., 2006). Abbreviations: D – Dawson; Wh – Whitehorse; TF – Teslin fault. Lithotectonic terrane abbreviations: AX – Alexander; CA – Cassiar; CC – Cache Creek; KS – Kluane Schist; NAb – North American basinal strata; NAm – North American platformal strata; pNAm – parautochthonous North American continental margin; SM – Slide Mountain; ST – Stikinia; YT Yukon-Tanana; W – Windy; WR – Wrangellia.**

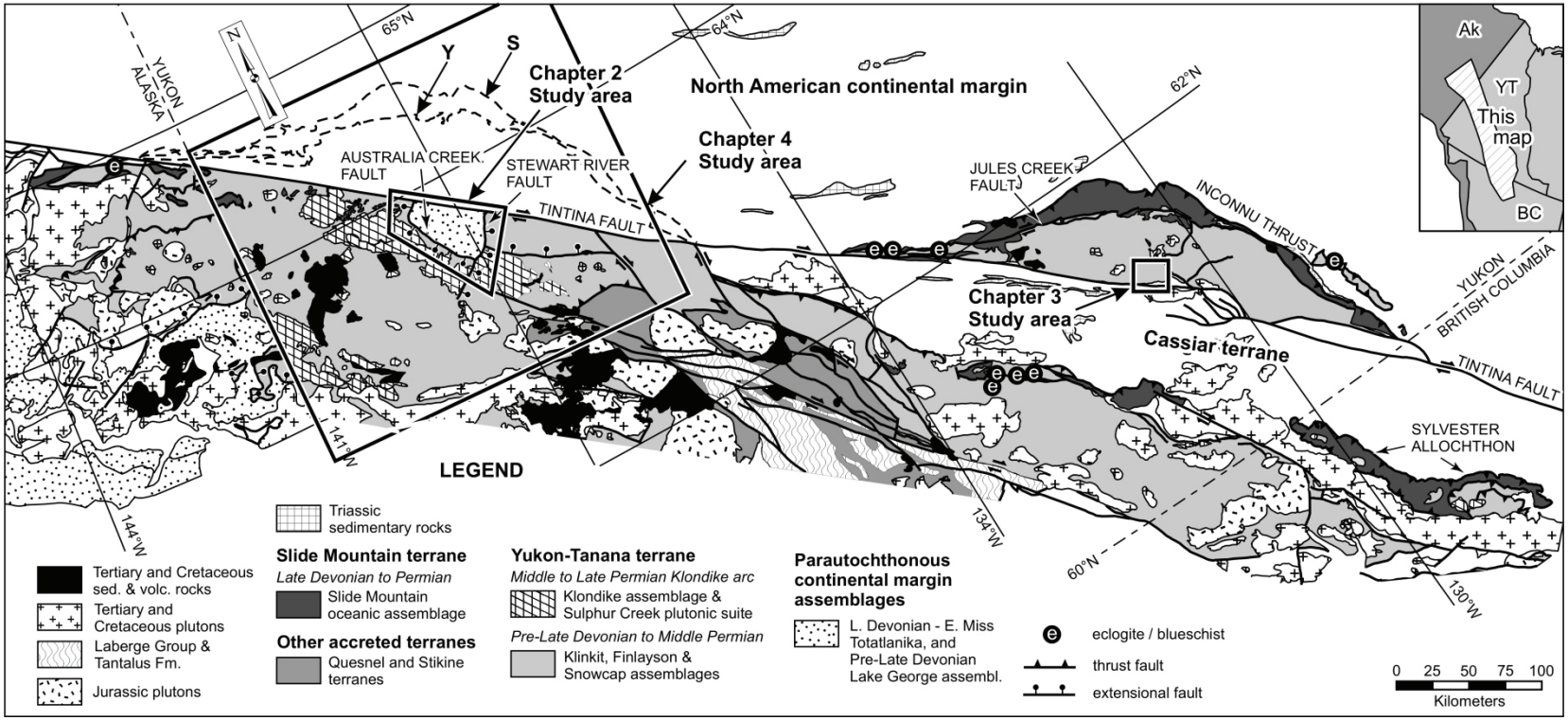
YUKON
ALASKA
65°N
64°N
62°N
60°N
144°W
141°W
134°W
130°W
Y
S
Chapter 2
Study area
North American continental margin
Chapter 4
Study area
AUSTRALIA CREEK
FAULT
STEWART RIVER
FAULT
TINTINA FAULT
JULES CREEK
FAULT
INCONNU THRUST
Chapter 3
Study area
Cassiar terrane
YUKON
BRITISH COLUMBIA
TINTINA FAULT
SYLVESTER
ALLOCHTHON
Ak
YT
This
map
BC
LEGEND
Triassic
sedimentary rocks
Tertiary and Cretaceous
sed. & volc. rocks
Tertiary and
Cretaceous plutons
Laberge Group &
Tantalus Fm.
Jurassic plutons
Slide Mountain terrane
Late Devonian to Permian
Slide Mountain
oceanic assemblage
Other accreted terranes
Quesnel and Stikine
terranes
Yukon-Tanana terrane
Middle to Late Permian Klondike arc
Klondike assemblage &
Sulphur Creek plutonic suite
Pre-Late Devonian to Middle Permian
Klinkit, Finlayson &
Snowcap assemblages
Parautochthonous
continental margin
assemblages
L. Devonian - E. Miss
Totatlanika, and
Pre-Late Devonian
Lake George assembl.
eclogite / blueschist
thrust fault
extensional fault
0 25 50 75 100
Kilometers

Figure 1.2. Tectonic assemblage map of the Yukon-Tanana terrane and adjacent terranes of the northern Cordillera in east-central Alaska, central Yukon, and northern British Columbia. The locations of the study areas of chapters 2, 3, and 4 are outlined by thick black squares. Dashed outlines labelled S and Y show the original position of the offset of the Slide Mountain and Yukon-Tanana terranes within the Finlayson Lake district, respectively, prior to displacement along the Tintina fault (Gabrielse et al., 2006). Figure modified from Colpron et al. (2006).

1.2. Methodological Approach

Williams (1985) illustrated the difficulty of correlating deformational and metamorphic events throughout an orogen on the basis of structural overprinting, style, pattern of orientation, and relationship of fabrics to metamorphic minerals and assemblages. However, understanding how deformation and metamorphism vary temporally throughout the orogen is critical to our understanding of the tectonic processes operating in orogenic belts. Therefore, my research is focused on placing quantitative pressure-temperature-time-deformation constraints on the regional tectono-metamorphism.

The advent of in situ U-Pb monazite geochronology allows monazite to be dated in its petrological context with respect to metamorphic assemblages and fabric elements, thereby providing a greater level of confidence in establishing not only the age of metamorphism and the associated P–T conditions (Foster et al., 2002, 2004; Gibson et al., 2004), but also the timing of deformation fabrics (Williams and Jercinovic, 2002; Berman et al., 2005, 2012). Additionally, when coupled with analysis of garnet zoning patterns, phase diagram modeling, and an understanding of the partitioning of REE's between accessory phase chronometers (e.g., monazite) and the major phases used to establish the P-T history (Pyle and Spear, 1999; Foster et al., 2002), in situ U-Pb monazite dating can establish the timing of points along specific P–T paths (Berman et al., 2007, 2010, 2012; Caddick et al., 2007; Gaidies et al., 2008). Applications of this method have also identified domains of contrasting P–T–t histories in areas previously considered to be part of a single tectono-metamorphic unit (Berman et al., 2007; Horváth et al., 2010).

Berman et al. (2007) have successfully applied this method to amphibolite facies rocks in the Stewart River region of Yukon-Tanana terrane and have delineated five metamorphic and three deformational events spanning from Devonian to Cretaceous time. This study expands the application of this method to the northeast across Yukon-Tanana terrane and the structurally underlying parautochthonous North American margin rocks to further constrain the timing, nature and regional extent of Cretaceous metamorphism and decompression in west-central Yukon (see Chapter 2 study area outline in Fig. 1.2). This work also reveals a previously unrecognized Middle Jurassic to earliest Cretaceous mid-crustal tectono-metamorphic event in the eastern portion of the Yukon-Tanana terrane (Finlayson Lake district, southeast Yukon; see Chapter 3 study area outline in Fig 1.2).

Based on these newly acquired data, together with previously published structural, thermobarometric, in situ U-Pb SHRIMP and K-Ar and $^{40}Ar/^{39}Ar$ data, it is concluded that the transposition fabrics and the associated amphibolite facies metamorphism that is nearly ubiquitous throughout the northern Yukon-Tanana terrane, and the underlying parautochthoous North American rocks, did not develop during a single tectono-metamorphic event. Rather, deformation and metamorphism developed diachronously across the northern portion of Yukon-Tanana terrane and underlying parautochthonous North American margin rocks in west-central Yukon. Chapter 4 summarizes the regional data, and presents a model wherein this diachronous pattern of deformation and metamorphism is reconciled by the foreland-directed growth of a critically tapered orogenic wedge. This model is inspired by a similar model originally proposed by Platt (1986) and later adapted by Brown (2004) to explain a similar, and partly coeval, diachronous pattern of structurally downward younging ductile deformation in the southeastern Canadian Cordillera.

1.3. Pre-accretionary Geology of the Yukon-Tanana Terrane and structurally Underlying Parautochthonous North American Margin

The Yukon-Tanana terrane consists of a metasedimentary basement (Snowcap assemblage) of pre-Late Devonian age, overlain by Late Devonian to Permian

subduction generated arcs (Colpron et al., 2006; Piercey and Colpron, 2009). The Snowcap assemblage contains lithological, geochemical and isotopic compositions, and detrital zircon signatures, which suggest that it represents a rifted portion of the northwestern Laurentian continental margin (Piercey and Colpron, 2009; Colpron and Nelson, 2009). Strongly foliated calc-alkaline granitoids of Late Devonian to Mississippian age intrude the Snowcap assemblage, and is overlain by three unconformity bounded Upper Devonian to Permian volcanic arc sequences (Finlayson, Klinkit, and Klondike assemblages; Fig. 1.2; Mortensen, 1992; Ruks et al., 2006; Colpron *et al*., 2006a). Coeval back-arc assemblages of the adjacent Slide Mountain terrane in the eastern portion of Yukon-Tanana terrane (Dawson and Finlayson map sheets), suggest a west-facing Devonian-Mississippian arc (Nelson et al., 2006). In contrast to voluminous magmatism in the Yukon-Tanana terrane that continued into the Permian (Colpron et al., 2006a; Nelson et al., 2006), there is an absence of contemporaneous igneous rocks younger than c. 350 Ma within the parautochthonous continental margin, suggesting that Yukon-Tanana had rifted and migrated away to the west by Early Mississippian time (Nelson et al., 2006). A Late Devonian to Permian basinal assemblage of oceanic chert, carbonaceous clastic sediments and MORB mafic volcanic rocks of the Slide Mountain terrane, which presently intervenes structurally between Yukon-Tanana terrane and the North American continental margin, reflects the evolution of a back-arc marginal ocean contemporaneous with the arc history of Yukon-Tanana terrane (Mortensen, 1992; Nelson et al., 2006; Colpron et al., 2007).

Sedimentation, magmatism and syngenetic VHMS deposits indicate an intra-arc and back-arc extensional tectonic environment for the Yukon-Tanana terrane throughout Devonian-Mississippian time (Piercey et al., 2006; Murphy et al., 2006; Nelson et al., 2006). Devonian and Mississippian unconformities and post-kinematic Devonian and Mississippian intrusions (Gabrielse et al., 1993; Colpron et al., 2006a,b; Murphy et al., 2006) indicate this period was punctuated by brief episodes of cryptic compressional deformation, uplift and erosion. Accompanying metamorphism within the Stewart River area at this time is recorded by the presence of metamorphic titanite dated at ~365 – 350 Ma (Berman et al., 2007). To the southeast, in the Glenlyon map area, Colpron *et al*. (2006b) noted that rocks of the Snowcap assemblage appear to have experienced a more complex deformational and metamorphic history than the overlying Upper

Devonian to Carboniferous strata, which despite containing a pervasive transposition foliation, locally preserve primary textures. In contrast, the Snowcap assemblage is more penetratively foliated and lineated, and the dominant regional foliation within the Snowcap assemblage is axial planar to rootless, tight to isoclinal folds that deform at least one earlier schistosity (Colpron et al., 2006b).

Intruded into and overlying both the pre-Late Devonian metasedimentary rocks of the Snowcap assemblage, and the overlying Devonian and Mississippian rocks in the region, are comagmatic, dominantly felsic, calc-alkaline metavolcanic and metaplutonic rocks of the middle to late Permian Klondike assemblage and Sulphur Creek suite (c. 265-253; Mortensen, 1990; Piercey *et al*., 2006; Ruks *et al*., 2006; Beranek and Mortensen, 2011; Fig. 1.2). The Klondike assemblage, and a discontinuous belt of early to middle Permian (c. 273-260 Ma) blueschist and eclogite to the northeast locally found along the eastern side of the Yukon-Tanana terrane (Fig. 1.2; Creaser et al., 1997; Erdmer et al., 1998), are interpreted to record a Permian northeast-facing magmatic arc and accretionary wedge, respectively (Mortensen, 1992; Nelson et al., 2006).

The development of a regional transposition foliation and associated amphibolite facies metamorphism (~9 kbar and 600 °C; Berman et al., 2007) in the north-central portion of Yukon-Tanana terrane in west-central Yukon is constrained to the late Permian to Middle Triassic (c. 260-253 Ma, Beranek and Mortensen, 2011; and c. 260-239 Ma, Berman et al., 2007), coeval with arc magmatism. By the Early to Middle Triassic (251 – 235 Ma), siliciclastic strata that contain detrital zircon sourced from the Paleozoic arc assemblages of Yukon-Tanana terrane were deposited on the ancestral North American continental margin (Beranek et al., 2010; Beranek and Mortensen, 2011). This depositional relationship implies that the Slide Mountain ocean had closed by the Early Triassic and the Yukon-Tanana terrane had been accreted and uplifted, and shedding detritus that was incorporated into adjacent Laurentian strata. Beranek and Mortensen (2011) suggest that the Late Permian tectono-metamorphism is therefore the result of the accretion of the Yukon-Tanana terrane onto the western Laurentian margin.

1.4. Tectonic Setting of the Northern Cordilleran Orogen

The North American Cordilleran orogen formed as a result of the successive accretion of allochthonous terranes to the western Laurentian margin (Coney et al., 1980). The core of the northern Cordilleran orogen in British Columbia, Yukon and Alaska, consists of an interrelated set of magmatic arcs (Quesnel and Stikine terranes), continental fragments (Yukon-Tanana terrane) and an ocean basin (Slide Mountain terrane), collectively referred to as the peri-Laurentian terranes that were accreted between late Paleozoic and Mesozoic time (Fig. 1.1; Colpron et al., 2007). These rocks enclose the Cache Creek terrane – an accretionary complex consisting in part of carbonate bodies that cap seamounts or oceanic plateaus and which contain exotic Tethyan fauna that suggest portions of the Cache Creek terrane lay far to the west of the North American continent during the Permian to Middle Triassic (Orchard et al., 2001; Nelson et al., 2013). Crustal fragments and magmatic arcs of the Insular terranes (Peninsular, Alexander and Wrangellia terranes) were subsequently accreted to the outboard margin of the Yukon-Tanana and Stikine terranes (Fig. 1.1). In the southern Canadian Cordillera, the accretion of the peri-Laurentian and Insular terranes, and the subsequent crustal thickening resulted in two major metamorphic belts separated by a zone of low-grade, weakly deformed rocks of the Quesnel, Cache Creek, and Stikine terranes (Monger et al., 1982). By contrast, in the northern Cordillera in west-central Yukon and east-central Alaska, amphibolite facies metamorphism is laterally continuous across the Yukon-Tanana terrane west of North American margin sedimentary rocks to the Denali fault. The absence of an intervening zone of low grade rocks between two separate metamorphic welts as observed in the southern Cordillera, may at present be best explained by a position within the northern hinge of a south-facing orocline (Fig. 1.3). Mihalynuk et al (1994) suggest that the Yukon-Tanana terrane formed a northern join between the Quesnel and Stikine arc terranes, and was located in the northern axis of an oroclinal enclosure that entrapped the more exotic Cache Creek terrane as the peri-Laurentian terranes were accreted to the western Laurentian margin. The subsequent collision of the Insular terranes against the accreted peri-Laurentian terranes resulted in complex overprinting and reworking of earlier deformation and metamorphism within the evolving northern Cordilleran hinterland. The thesis is focused on the tectono-metamorphic history of the north-central and northeastern portions of Yukon-Tanana

terrane and the structurally underlying parautochthonous continental margin rocks (see chapter 4 study area outline in Fig. 1.2), which preserve both the early accretionary history with western Laurentia, as well as events coeval with the subsequent accretion of the Insular terranes.

1.5. References

Beranek, L.P., Mortensen, J K., Orchard, M.J., and Ullrich, T., 2010, Provenance of North American Triassic strata from west-central and southeastern Yukon: Correlations with coeval strata in the Western Canada Sedimentary Basin and Canadian Arctic Islands: Canadian Journal of Earth Sciences, v. 47, 53–73.

Beranek, L.P., and Mortensen, J.K., 2011, The timing and provenance record of the Late Permian Klondike orogeny in northwestern Canada and arc-continent collision along western North America: Tectonics, v. 30, TC5017, doi:10.1029/2010TC002849.

Berman, R., Sanborn-Barrie, M., Stern, R., and Carson, C., 2005, Tectonometamorphism at c. 2.35 and 1.85 Ga in the Rae domain, western Churchill Province, Nunavut, Canada: insights from structural, metamorphic and in situ geochronological analysis of the southwestern Committee Bay belt: Canadian Mineralogist, v. 43, p. 409–442.

Berman, R.G., Ryan, J.J., Gordey, S.P., and Villeneuve, M., 2007, Permian to Cretaceous polymetamorphic evolution of the Stewart River region, Yukon-Tanana terrane, Yukon, Canada: P-T evolution linked with in-situ SHRIMP monazite geochronology: Journal of Metamorphic Geology, v. 25, p. 803–827.

Berman, R.G., Sandeman, H.A.I., and Camacho, A., 2010, Diachronous deformation and metamorphism in the Committee Bay belt, Rae Province, Nunavut: insights from 40Ar/39Ar cooling ages and thermal modeling: Journal of Metamorphic Geology, v. 28, p.439–457.

Berman, R.G., Rayner, N., Sanborn-Barrie, M., and Whalen, J., 2012, The tectonometamorphic evolution of Southampton Island, Nunavut: Insight from petrologic modeling and in situ SHRIMP geochronology of multiple episodes of monazite growth: Precambrian Research v. 232, p. 140–166.

Brown, R.L., 2004, Thrust belt accretion and hinterland underplating of orogenic wedges: an example from the Canadian Cordillera, *in* McClay, K.R. ed., Thrust Tectonics and Hydrocarbon Systems, American Association of Petroleum Geologists, Memoir 82, p. 51–64.

Caddick, M.J., Bickle, M.J., Harris, N.B.W., Holland, T.J.B., Horstwood, M.S.A., and Ahmad, T., 2007, Burial and exhumation history of a Lesser Himalayan schist: recording the formation of an inverted metamorphic sequence in NW India: Earth and Planetary Science Letters, v. 264, p. 375–390.

Collins, W., and Vernon, R., 1992, Palaeozoic arc growth, deformation and migration across the Lachlan fold belt, southeastern Australia: Tectonophysics, v. 214, p. 381–400.

Coney, P.J., Jones, D.L., and Monger, J.W.H., 1980, Cordilleran suspect terranes: Nature, v. 288, p. 329–333.

Colpron, M., and Nelson, J.L., 2009, A Palaeozoic northwest passage: incursion of Caledonian, Baltican and Siberian terranes into eastern Panthalassa, and the early evolution of the North American Cordillera, *in* Cawood, P.A., and Kröner, A., eds., Earth Accretionary Systems in Space and Time: The Geological Society of London Special Publications, v. 318, p. 273–307.

Colpron, M., Nelson, J.L., and Murphy, D.C., 2006a, A tectonostratigraphic framework for the pericratonic terranes of the northern Canadian Cordillera, *in* Colpron, M., and Nelson, J. L., eds., Paleozoic Evolution and Metallogeny of Pericratonic Terranes at the Ancient Pacific Margin of North America, Canadian and Alaskan Cordillera: Geological Association of Canada Special Paper 45, p. 1–23.

Colpron, M., Mortensen, J.K., Gehrels, G.E. and Villeneuve, M., 2006b, Basement complex, Carboniferous magmatism and Paleozoic deformation in Yukon-Tanana terrane of central Yukon: Field, geochemical and geochronological constraints from Glenlyon map area, *in* Colpron, M., and Nelson, J. L., eds., Paleozoic Evolution and Metallogeny of Pericratonic Terranes at the Ancient Pacific Margin of North America, Canadian and Alaskan Cordillera: Geological Association of Canada Special Paper 45, p. 131-151.

Colpron, M., Nelson, J.L., and Murphy, D.C., 2007, Northern Cordilleran terranes and their interactions through time: GSA Today, v. 17, p. 4–10.

Creaser, R.A., Heaman, L.M., and Erdmer, P., 1997, Timing of high-pressure metamorphism in the Yukon–Tanana terrane, Canadian Cordillera: Constraints from U–Pb zircon dating of eclogite from the Teslin tectonic zone: Canadian Journal of Earth Sciences, v. 34, p. 709–715.

De Keijzer, M., 2000, Tectonic evolution of the Tesline zone and the western Cassiar terrane, northern Canadian Cordillera [PhD thesis]: Fredericton, University of New Brunswick.

Dusel-Bacon, C., Hansen, V.L., and Scala, J.A., 1995, High-pressure amphibolite facies dynamic metamorphism and the Mesozoic tectonic evolution of an ancient continental margin, east-central Alaska: Journal of Metamorphic Geology, v. 13, p. 9–24.

Dusel-Bacon, C., Lanphere, M.A., Sharp, W.D., Layer, P.W., and Hansen, V.L., 2002, Mesozoic thermal history and timing of structural events for the Yukon-Tanana Upland, east-central Alaska: $^{40}Ar/^{39}Ar$ data from metamorphic and plutonic rocks: Canadian Journal of Earth Sciences, v. 39, p. 1013–1051.

Dusel-Bacon, C., Hopkins, M.J., Mortensen, J.K., Dashevsky, S.S., Bressler, J.R. & Day, W.C., 2006, Paleozoic tectonic and metallogenic evolution of the pericratonic rocks of eastcentral Alaska and adjacent Yukon, *in* Colpron, M., and Nelson, J.L., eds., Paleozoic Evolution and Metallogeny of Pericratonic Terranes at the Ancient Pacific Margin of North America, Canadian and Alaskan Cordillera: Geological Association of Canada Special Paper 45, p. 75–105.

Erdmer, P., Ghent, E. D., Archibald, D. A., and Stout, M. Z., 1998, Paleozoic and Mesozoic high-pressure metamorphism at the margin of ancestral North America in central Yukon: Geological Society of America Bulletin, v. 110, p. 615–629.

Foster, G., Gibson, H.D., Parrish, R.R., Horstwood, M., Fraser, J., and Tindle, A., 2002, Textural, chemical and isotopic insights into the nature and behaviour of metamorphic monazite: Chemical Geology, v. 191, p. 183–207.

Foster, G., Parrish, R.R., Horstwood, M.S.A., Chenery, S., Pyle, J., and Gibson, H.D., 2004, The generation of prograde P–T–t points and paths; a textural, compositional, and chronological study of metamorphic monazite: Earth Planetary Science Letters, v. 228, p. 125–142.

Foster, H.L., Keith, T.E.C., and Menzie, W.D., 1994, Geology of the Yukon-Tanana area of east-central Alaska, *in* Plafker, G. and Berg, H.C., eds., The Geology of Alaska: Geological Society of America, The Geology of North America, v. G-1, p. 205-240.

Gabrielse, H., Mortensen, J.K., Parrish, R.R., Harms, T.A., Nelson, J.L., and van der Heyden, P., 1993, Late Paleozoic plutons in the Sylvester allochthon, northern British Columbia, *in* Radiogenic Age and Isotopic Studies, Report 7: Geological Survey of Canada Paper 93-1, p. 107–118.

Gabrielse, H., Murphy, D.C., and Mortensen, J.K., 2006, Cretaceous and Cenozoic dextral orogen-parallel displacements, magmatism and paleogeography, north-central Canadian Cordillera, *in* Haggart, J.W., Monger, J.W.H., and Enkin, R.J., eds., Paleogeography of the North American Cordillera: Evidence For and Against Large-Scale Displacements: Geological Association of Canada Special Paper 46, p. 255–276.

Gaidies, F. Krenn, E, de Capitani, C., and Abart, R., 2008, Coupling forward modelling of garnet growth with monazite geochronology: an application to the Rappold Complex (Austroalpine crystalline basement): Journal of Metamorphic Geology, v. 26, p. 775–793.

Gibson, H. D., Carr, S. D., Brown, R. L., and Hamilton, M. A., 2004, Correlations between chemical and age domains in monazite, and metamorphic reactions involving major politic phases: an integration of ID-TIMS and SHRIMP geochronology with Y–Th–U X-ray mapping: Chemical Geology, v. 211, p. 237–260.

Gordey, S. P., and Ryan, J. J., 2005, Geology, Stewart River area (115N, 115-O and part of 115J), Yukon Territory: Geological Survey of Canada Open File 4970, scale 1:250 000, 1 sheet.

Hansem V.L., 1992. P-T evolution of the Teslin suture zone and Cassiar tectonites, Yukon, Canada: evidence for A- and B-type subduction. Journal of Metamorphic Geology, 239, 239–263.

Hansen, V.L., and Dusel-Bacon, C., 1998, Structural and Kinematic evolution of the Yukon-Tanana upland tectonites, east-central Alaska: a record of late Paleozoic to Mesozoic crustal assembly: Geological Society of America Bulletin, v. 110, p. 211–230.

Hansen, V.L., Heizler, M.T., and Harrison, T.M., 1991, Mesozoic thermal evolution of the Yukon-Tanana composite terrane; new evidence from $^{40}Ar/^{39}Ar$ data: Tectonics, v. 10, p. 51-76.

Hatcher, R.D., Martinez Catalan, J.R., Arenas, R., and Diaz Garcia, F., 2002, Alleghanian (Appalachian) Orogeny, a product of zipper tectonics; rotational transpressive continentcontinent collision and closing of ancient oceans along irregular margins. Geological Society of America Special Paper, v. 364, p. 199–208.

Hobbs, B.E., Means, W.D, and Williams, P.F., 1976., An outline of structural geology. John Wiley and Sons, New York.

Horváth, P., Balen, D., Finger, F., Tomljenović, B., and Krenn, E., 2010, Contrasting P–T–t paths from the basement of the Tisia Unit (Slavonian Mts., NE Croatia): Application of quantitative phase diagrams and monazite age dating: Lithos, v. 117, p. 269–282.

Johnston, S.T., 1993. Geologic evolution of the Nisling assemblage and Stikine terrane in the Aishihik Lake area, southwest Yukon. [PhD thesis]: Edmonton, University of Alberta.

Johnston, S. T., Mortensen, J. K., and Erdmer, P., 1996, Igneous and metaigneous age constraints for the Aishihik metamorphic suite, southwest Yukon: Canadian Journal of Earth Sciences, v. 33, p. 1543–1555.

Mihalynuk, M.G., Nelson, J.L., and Diakow, L.J., 1994, Cache Creek terrane: oroclinal paradox within the Canadian Cordillera: Tectonics, v. 13, p. 575-5–595.

Mortensen, J.K., 1990, Geology and U-Pb geochronology of the Klondike District, west-central Yukon Territory: Canadian Journal of Earth Sciences, v. 27, p. 903–914.

Mortensen, J. K., 1992, Pre-mid-Mesozoic tectonic evolution of the Yukon-Tanana terrane, Yukon and Alaska: Tectonics, v. 11, p. 836–853.

Monger, J.W.H., and Price, R.A., 2002, The Canadian Cordillera: Geology and tectonic evolution: Canadian Society of Exploration Geophysicists Recorder, February 2002, p. 17–36.

Monger, J.W.H., Price, R.A., and Tempelman-Kluit, D.J., 1982, Tectonic accretion and the origin of the two major metamorphic and tectonic welts in the Canadian Cordillera: Geology, v. 10, p. 70–75.

Murphy, D.C., Mortensen, J.K., Piercey, S.J., Orchard, M.J., and Gehrels, G.E., 2006, Mid-Paleozoic to early Mesozoic tectonostratigraphic evolution of Yukon-Tanana and Slide Moutnain terranes and affiliated overlap assemblages, Finlayson Lake massive sulphide district, southeastern Yukon, *in* Colpron, M., and Nelson, J.L., eds., Paleozoic Evolution and Metallogeny of Pericratonic Terranes at the Ancient Pacific Margin of North America, Canadian and Alaskan Cordillera: Geological Association of Canada Special Paper 45, p. 75–105.

Nelson, J.L., Colpron, M., Piercey, S.J., Dusel-Bacon, C., Murphy, D.C., and Roots, C.F., 2006, Paleozoic tectonic and metallogenic evolution of the pericratonic terranes in Yukon, northern British Columbia and eastern Alaska., *in* Colpron, M., and Nelson, J.L., eds., Paleozoic Evolution and Metallogeny of Pericratonic Terranes at the Ancient Pacific Margin of North America, Canadian and Alaskan Cordillera: Geological Association of Canada Special Paper 45, p. 323–360.

Piercey, S.J., and Colpron, M., 2009, Composition and provenance of the Snowcap assemblage, basement to the Yukon-Tanana terrane, northern Cordillera: Implications for Cordilleran crustal growth: Geosphere, v. 5, p. 439–464.

Piercey, S.J., Nelson, J.L., Colpron, M., Dusel-Bacon, C., Roots, C.F. and Simard, R.L., 2006, Paleozoic magmatism and crustal recycling along the ancient Pacific margin of North America, northern Cordillera, *in* Colpron, M., and Nelson, J.L., eds., Paleozoic Evolution and Metallogeny of Pericratonic Terranes at the Ancient Pacific Margin of North America, Canadian and Alaskan Cordillera: Geological Association of Canada Special Paper 45, p. 281–322.

Platt, J.P., 1986, Dynamics of orogenic wedges and the uplift of high-pressure metamorphic rocks: Geological Society of America Bulletin, v. 97, p. 1037–1053.

Pyle, J.M., and Spear, F.S, 1999, Yttrium zoning in garnet: coupling of major and accessory phases during metamorphic reactions: Geological Materials Research, v. 1, p. 1–49.

Ruks, T.W., Piercey, S.J., Ryan, J.J., Villeneuve, M.E., and Creaser, R.A., 2006, Mid- to Late Paleozoic K-feldspar augen granitoids of the Yukon-Tanana terrane, Yukon: Implications for crustal growth and tectonic evolution of the northern Cordillera: Geological Society of America Bulletin, v. 118, p. 1212–1231.

Turner, F.J., and Weiss, L.E., 1963, Structural analysis of metamorphic tectonites. McGraw-Hill, New York.

Williams, M.L., and Jercinovic, M.J., 2002, Microprobe monazite geochronology: putting absolute time into microstructural analysis: Journal of Structural Geology, v. 24, p. 1013–1028.

Williams, P.F., 1985, Multiply deformed terrains-problems of correlation: Journal of Structural Geology, v. 7, p. 269–280.

Williams, P.F., and Jiang, D., 2005, An investigation of lower crustal deformation: Evidence for channel flow and its implications for tectonics and structural studies: Journal of Structural Geology, v. 27, p. 1486–1504.

Chapter 2.

A window into the Early to mid-Cretaceous infrastructure of the Yukon-Tanana terrane recorded in multi-stage garnet of west-central Yukon, Canada

2.1. Abstract

Amphibolite facies metasedimentary schists within the Yukon-Tanana terrane in the northern Canadian Cordillera reveal a two-stage, polymetamorphic garnet growth history. *In situ* U-Th-Pb SHRIMP dating of monazite provide timing constraints for the late stages of garnet growth, deformation and subsequent decompression. Distinct textural and chemical growth zoning domains, separated by a large chemical discontinuity, reveal two stages of garnet growth characterized in part by: (i) a syn-kinematic, inclusion-rich stage-1 garnet core, and (ii) an inclusion-poor, stage-2 garnet rim that crystallized with syn- to post-kinematic staurolite and kyanite. Phase equilibria modelling of garnet molar and compositional isopleths suggest stage-1 garnet growth initiated at ~ 600 °C, 8 kbar along a clockwise *P-T* path. Growth of the compositionally distinct, grossular-rich, pyrope-poor inner portion of the stage-2 overgrowth is interpreted to have initiated at higher P and/or lower T than the stage-1 core along a separate *P-T* loop, culminating at peak *P-T* conditions of ~ 650 – 680 °C and 9 kbar. Stage-2 metamorphism and the waning development of a composite transposition foliation (S_T) is dated at *c.* 118 Ma from monazite aligned parallel to S_T, and inclusions in syn- to post-S_T staurolite and kyanite. Slightly younger ages (*c.* 112 Ma) are obtained from Y-rich monazite that occurs within resorbed areas of both stage-1 and stage-2 garnet, together with retrograde staurolite and plagioclase. The younger ages obtained from these texturally and chemically distinct grains are interpreted, with the aid of phase equilibria calculations, to date the growth of monazite from the breakdown of garnet during

decompression at *c.* 112 Ma. Evidence for continued near-isothermal decompression is provided by the presence of retrograde sillimanite, and cordierite after staurolite, which indicates decompression below ~4-5 kbar prior to cooling below ~550 °C. As most other parts of the Yukon-Tanana terrane were exhumed to upper crustal levels in the Early Jurassic, these data suggest this domain represents a tectonic window revealing a much younger, high-grade tectono-metamorphic core (infrastructure) within the northern Cordilleran orogen. This window may be akin to extensional core complexes identified in east-central Alaska and in the southeastern Canadian Cordillera.

2.2. Introduction

The geodynamic evolution of orogenic belts is dictated to a large extent by the rheology of the lithosphere, which in turn is controlled, in part, through a dynamic interplay between metamorphism and deformation. Our understanding of the evolution of orogenic belts is therefore significantly aided by establishing the *P-T* conditions and style of deformation and metamorphism operating at various times and locations throughout an orogen. However, the diachronous and transitory nature of deformation and metamorphism across an orogen prohibits the correlation of metamorphic and deformational events solely on the basis of similarities in metamorphic mineral assemblage and structural style (Williams, 1985). This issue is compounded in the cores of orogenic belts, which may experience multiple episodes of deformation and metamorphism under nearly identical conditions.

The advent of *in situ* U-Pb monazite geochronology allows us to date monazite in its petrologic context with respect to metamorphic assemblages and fabric elements, thereby providing a greater level of confidence in establishing not only the age of metamorphism and the associated *P-T* conditions (Foster *et al*., 2002, 2004; Gibson *et al*., 2004), but also the timing of deformation fabrics (Williams & Jercinovic, 2002; Berman *et al*., 2005, 2012). Additionally, when coupled with analysis of garnet zoning patterns and phase diagram modeling, *in situ* U-Pb monazite dating can establish the timing of points along specific *P-T* paths (Berman *et al*., 2007a, 2010, 2012; Caddick *et al*., 2007; Gaidies *et al*., 2008). Applications of this method have also identified domains

of contrasting *P-T*-t histories in areas previously considered to be part of a single tectono-metamorphic unit (Berman *et al*., 2007a; Horvath *et al*., 2010).

We apply similar techniques to amphibolite facies rocks of the Yukon-Tanana terrane, which occupies much of the metamorphic core of the orogen in the northern Canadian Cordillera and easternmost Alaska (Figs 2.1 & 2.2). Typical of the core zone of many orogenic belts, the Yukon-Tanana terrane rocks are poly-deformed and metamorphosed, with metamorphic and deformational events recorded in the Devono-Mississippian, Permo-Triassic, Jurassic and Cretaceous (See Berman *et al*., 2007a for a review). Further complicating matters, mapping and *P-T-t-D* data (Berman *et al*., 2007a) reveal that the style, pattern and grade of metamorphism and deformation was nearly identical in each of the Permo-Triassic, Jurassic and Cretaceous tectono-metamorphic events.

Difficulty in identifying distinct tectono-metamorphic domains within the Yukon-Tanana terrane, and deciphering discrete deformational and metamorphic events within an individual domain, are overcome herein by a detailed analysis of textural relationships and monazite and garnet chemistry. The timing of deformation and a segment of an individual *P-T* path are determined by *in situ* Sensitive High Resolution Ion Microprobe (SHRIMP) monazite geochronology, with monazite growth texturally and chemically linked to deformation fabrics as well as metamorphic porphyroblasts and their modelled *P-T* stability conditions. These data, together with the data of Berman *et al*. (2007a), elucidate a high-pressure Cretaceous tectono-metamorphic domain (Australia Mountain domain) that is distinct from an adjacent domain affected by Permo-Triassic and Early Jurassic events, and exhumed to upper crustal levels in the Early Jurassic. In this study, we better constrain the timing, nature and regional extent of Cretaceous metamorphism and decompression in west-central Yukon, and elucidate the structural-thermal architecture of the northern Cordilleran orogen in the Cretaceous.

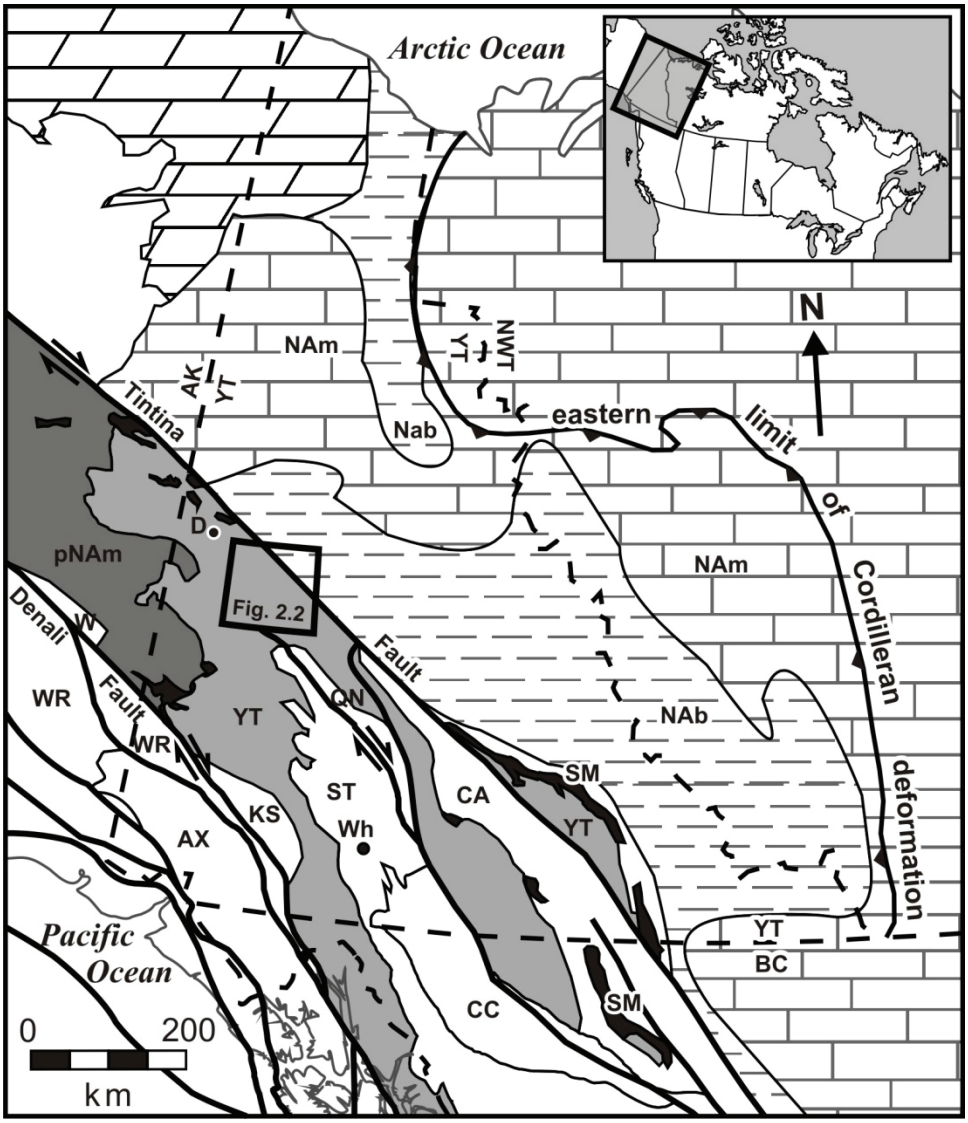

Figure 2.1. **Simplified terrane map of the northern Canadian Cordillera showing location of Figure 2.2, and the study area, within the northern portion of Yukon-Tanana terrane (modified from Colpron et al., 2006). Abbreviations: D – Dawson; Wh – Whitehorse. Lithotectonic terrane abbreviations: AX – Alexander; CA – Cassiar; CC – Cache Creek; KS – Kluane Schist; NAb – North American basinal strata; NAm – North American platformal strata; pNAm – parautochthonous North American continental margin; SM – Slide Mountain; ST – Stikinia; YT Yukon-Tanana; W – Windy; WR – Wrangellia.**

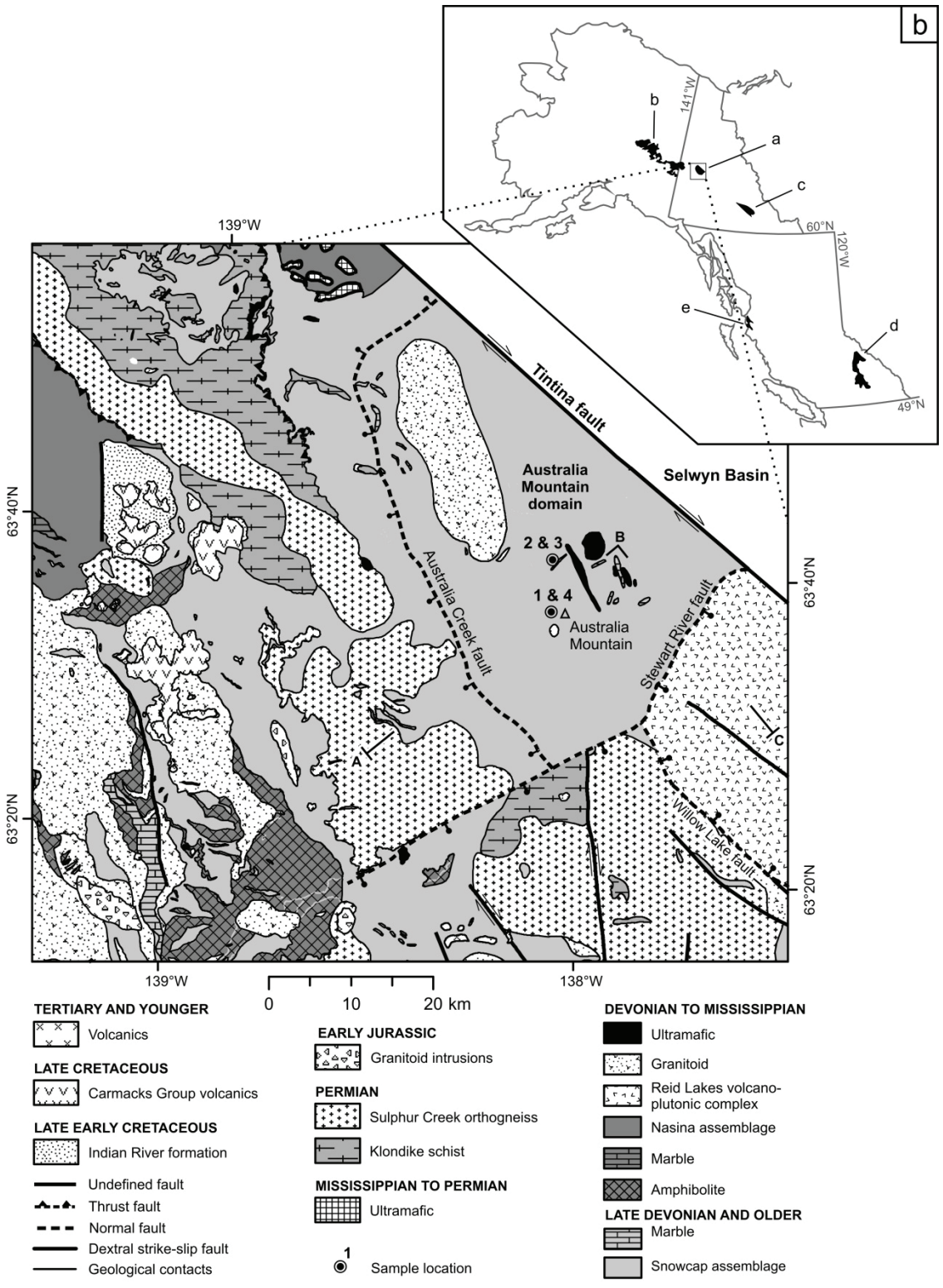
b
141°W
b
a
c
60°N
120°W
e
d
49°N
139°W
Tintina fault
Selwyn Basin
Australia Mountain domain
2 & 3
B
1 & 4
Australia Mountain
Australia Creek fault
Stewart River fault
A
C
Willow Lake fault
63°40'N
63°20'N
139°W
138°W
0
10
20 km
TERTIARY AND YOUNGER
Volcanics
LATE CRETACEOUS
Carmacks Group volcanics
LATE EARLY CRETACEOUS
Indian River formation
Undefined fault
Thrust fault
Normal fault
Dextral strike-slip fault
Geological contacts
EARLY JURASSIC
Granitoid intrusions
PERMIAN
Sulphur Creek orthogneiss
Klondike schist
MISSISSIPPIAN TO PERMIAN
Ultramafic
1
Sample location
DEVONIAN TO MISSISSIPPIAN
Ultramafic
Granitoid
Reid Lakes volcano-plutonic complex
Nasina assemblage
Marble
Amphibolite
LATE DEVONIAN AND OLDER
Marble
Snowcap assemblage

Figure 2.2. **(a) Simplified geology for portions of Stewart River and McQuesten map areas showing the distribution of sample locations and the approximate boundary of the Early to mid-Cretaceous Australia Mountain metamorphic domain bounded by the Australia Creek, Stewart River and Tintina faults. Modified from Gordey & Ryan, 2005; Ryan et al., 2010. (b) Map showing the distribution of rocks at mid- to lower crustal levels in the Early to mid-Cretaceous in the BC, Yukon and Alaskan Cordillera. Location abbreviations and references: a – this study and Berman et al. (2007a); b – east-central Alaska (Dusel-Bacon et al., 2002; Pavlis et al., 1993); c – Finlayson region (Murphy, 2004); d – Shushwap complex (Parrish, 1995; Crowley et al., 2000; Gibson et al., 2008); e – Prince Rupert area (Wolf et al., 2010).**

2.3. Geologic Background

2.3.1. Northern Cordilleran Orogen

The Yukon-Tanana terrane, together with Stikinia, Quesnellia and the oceanic Slide Mountain terrane, represent late Palaeozoic to Mesozoic arc and back-arc systems that lay outboard of the previously thinned, western ancestral North American margin (Colpron *et al*., 2007). The timing and nature of accretion of the above terranes have been well documented in both the northern and the southern Canadian Cordillera (e.g. Monger *et al*., 1982; Nelson *et al*., 2006; Colpron *et al*., 2007; Beranek & Mortensen, 2011). In the Mesozoic, the orogen grew as a consequence of protracted compression and crustal thickening during arc-continent collisions (e.g., Berman *et al*., 2007a; Gibson *et al*., 2008) as the North American craton moved westward, converging with its offshore subduction zone (Monger & Price, 2002). In the southern Canadian Cordillera, a significant body of geochronologic data from the metamorphic core of the orogen has revealed that despite similarities in regional metamorphic grade and deformation patterns, both were strongly diachronous, younging systematically with increasing structural depth (Parrish, 1995). Rocks presently in the upper exposed structural levels were buried, heated and exhumed in the Jurassic (Murphy *et al*., 1995; Colpron *et al*., 1996; Gibson *et al*., 2005), while structurally deeper rocks were progressively buried and heated from at least Cretaceous to earliest Eocene (Carr, 1991; Parrish, 1995; Gibson *et al*., 1999, 2005; Crowley & Parrish, 1999; Crowley *et al*., 2000). The deepest structural levels within the core of the orogen, which includes autochthonous and

parautochthonous North American crust, were largely exhumed by extensional shear zones in the early Eocene (Parrish *et al*., 1988; Brown *et al*., 2012), marking a shift to a transtensional tectonic setting.

The deformational and metamorphic history of the Yukon-Tanana terrane within the northern Cordillera differs from the southeastern Canadian Cordillera in that the main phase of metamorphism (amphibolite facies) and deformation appears to have occurred earlier, in the Late Permian to Early Triassic (Berman *et al*., 2007a; Beranek & Mortensen, 2011). There was an ~8 kbar metamorphic overprint in the Early Jurassic before much of the metamorphic core of the northern Cordilleran orogen was rapidly exhumed in the Early to Middle Jurassic (Hansen *et al*., 1991; Stevens *et al*., 1993; Johnston *et al*., 1996; Berman *et al*., 2007a).

In east-central Alaska, the allochthonous Yukon-Tanana terrane is structurally underlain by a large area of metamorphic rocks interpreted by Dusel-Bacon *et al*. (1995, 2002) to be part of the parautochthonous western continental margin of ancestral North America. In the pre-latest Triassic (>212 Ma), the uppermost structural levels of the allochthonous Yukon-Tanana terrane were affected by northeast-directed shear at 8-12 kbar (Dusel-Bacon *et al*., 1995). By Early Jurassic (>188 Ma), both the lower structural levels of the allochthonous Yukon-Tanana terrane and the underlying parautochthonous rocks were deformed and metamorphosed at amphibolite facies conditions (7-12 kbar) during northwest-directed contraction and imbrication (Dusel-Bacon *et al*., 1995). Early Jurassic $^{40}Ar/^{39}Ar$ cooling ages are interpreted by Hansen & Dusel-Bacon (1998), and Dusel-Bacon *et al*. (2002) to date the time of cooling of the upper plate following the aforementioned northwest-directed contraction that emplaced the allochthonous rocks of Yukon-Tanana terrane onto the parautochthonous continental margin. The lower plate was subsequently exhumed by southeast-directed crustal extension as recorded in *c.* 135-110 Ma $^{40}Ar/^{39}Ar$ cooling ages in parautochtonous continental margin rocks (Pavlis *et al*., 1993; Hansen & Dusel-Bacon, 1998; Dusel-Bacon *et al*., 2002). Exhumation of ductiley deformed amphibolite facies rocks in the Early to mid-Cretaceous is also recorded < 200 kilometres to the east of the Cretaceous domain of east-central Alaska, in the Australia Mountain area of west-central Yukon. Although the timing of deformation and metamorphism appears to be older in the northern Cordillera, this diachroneity of

tectonism, which may be a function of structural level and position within the orogenic wedge, suggests similarity with what is recorded in the southern Canadian Cordillera.

2.3.2. Australia Mountain Area

The Yukon-Tanana terrane has been dissected and offset ~430 km by the Tintina fault, an Eocene dextral strike-slip fault (Gabrielse *et al*., 2006). The study area is located at Australia Mountain (Figs 2.1 & 2.2), immediately southwest of the Tintina fault, and is underlain by highly deformed psammite, semi-pelite and quartzite with lesser amounts of pelite, mafic volcanic and ultramafic rocks that have been metamorphosed to amphibolite facies. These rocks are widely accepted to be part of Yukon-Tanana terrane (eg. Mortensen, 1990; Gordey & Ryan, 2005; Ruks *et al*., 2006; Berman *et al*., 2007), and we treat them as such here. However, as is elaborated in the discussion section, our data allows that the rocks could equally represent parautochthonous North American continental margin rocks that are structurally juxtaposed with Yukon-Tanana terrane similar to what is described by Dusel-Bacon *et al*. (2002; 2006) in east-central Alaska. West and south of the Australia Mountain area are polydeformed and transposed amphibolite facies Palaeozoic rocks of the Yukon-Tanana terrane, which are intruded by weakly to undeformed plutons of Triassic, Jurassic, Cretaceous and Eocene age (Gordey & Ryan, 2005). These are overlain by Cretaceous and Paleocene volcanic and sedimentary rocks, and rare Quaternary basalt (Gordey & Ryan, 2005).

The main episode of deformation to the west and south of Australia Mountain, and generally considered representative for the Yukon-Tanana terrane in general, produced a regional transposition foliation that is interpreted by Berman *et al*. (2007a) and Beranek & Mortensen (2011) to be bracketed between *c.* 260 and 253 Ma. This constraint is based upon the ages obtained from the strongly foliated Sulphur Creek orthogneiss (*c.* 260 Ma), as well as the undeformed Jim Creek pluton (253 Ma), which cuts across the transposition foliation in the Devono-Mississippian Nasina assemblage (Beranek & Mortensen, 2011). A *c.* 239 Ma monazite included within garnet was interpreted by Berman *et al*. (2007a) to constrain the latter stages of a Late Permian to Middle Triassic tectono-metamorphic event that was initiated at low pressure and culminated with the growth of garnet at approximately 9 kbar and 600 °C. A subsequent episode of metamorphism is recorded in *c.* 195 – 187 Ma monazite inclusions within

garnet and kyanite porphyroblasts, which are interpreted by Berman *et al*. (2007a) to date an Early Jurassic metamorphic event with peak conditions of ~ 8 kbar and 600 °C. Unlike the Permo-Triassic event, this Early Jurassic metamorphism was not accompanied by significant fabric development, rather Berman *et al.* (2007a) suggest the strain was partitioned heterogeneously into regional high-strain zones. West of Australia Mountain, amphibolite facies rocks of the Snowcap assemblage and structurally lower level Permian rocks at greenschist facies are interpreted by Mackenzie & Craw (2012) to be thrust imbricated along localised ductile and brittle Jurassic shear zones that were active at greenschist facies conditions.

The amphibolite facies rocks west and south of the Australia Mountain area yield Early to Middle Jurassic K-Ar cooling ages (Hunt & Roddick, 1992), interpreted to record widespread exhumation and cooling below ~ 300 °C. In contrast, strongly deformed, amphibolite facies rocks at Australia Mountain are juxtaposed to the southeast against essentially undeformed and unmetamorphosed rocks of the Mississippian Reid Lakes volcano-plutonic complex (Colpron & Ryan, 2010). The preservation of Mississippian $^{40}Ar/^{39}Ar$ cooling ages throughout the Reid Lakes complex (Knight *et al*., 2013) indicates it was not significantly buried or heated during the Permian and Jurassic tectonometamorphic events. This is also consistent with the lack of observed deformation and metamorphism within the complex. The boundary between the Australia Mountain domain and these adjacent distinct domains are inferred as normal faults, herein named the Australia Creek and Stewart River faults (Fig. 2.2).

At Australia Mountain, the rocks are characterized by a strong, penetrative foliation that is parallel to the axial planes of tight to isoclinal folds. Primary compositional layering in metasedimentary rocks and a pre-existing foliation can be traced around the closures of these tight to isoclinal folds indicating that the folds are at least F_2 structures. The presence of rootless intrafolial isoclinal folds suggests this foliation is likely a composite transposition foliation in the sense of Williams (1983) and Tobisch & Paterson (1988). Following Williams & Compagnoni (1983), we have notated this composite transposition foliation as S_T. S_T has in turn been deformed by at least two later episodes of folding, herein denoted F_{T+1} and F_{T+2}. F_{T+1} folds are sub-horizontal to gently plunging, steeply to moderately inclined, tight asymmetric chevron folds with more open parasitic crenulations. The F_{T+1} folds lack an axial planar foliation, and show no signs of

development of a crenulation cleavage. The latest phase of folding, F_{T+2}, consists of sub-horizontal, upright gentle to open folds. The metamorphic grade, style, orientation and pattern of successive phases of deformation within this Cretaceous domain are strikingly similar to those found in the surrounding Permo-Triassic and Jurassic metamorphic domain (Ryan *et al*., 2003). Through the application of high-resolution *in situ* U-Pb monazite dating, linked to the *P-T* history and deformation fabrics, we herein shed light on the unique Early to mid-Cretaceous metamorphic, deformational and exhumation history for this portion of the Yukon-Tanana terrane.

2.4. Petrological Methods

2.4.1. Thermobarometry

Mineral compositions were quantitatively analyzed using a fully automated CAMECA SX-50 instrument, operating in wavelength-dispersion mode with the following operating conditions: excitation voltage, 15 kV; beam current, 20 nA (10 nA for micas); peak count time, 20 s (40 s for F, Cl); background count-time, 10 s (20 s for F, Cl); spot diameter, 5 μm. Quantitative data were obtained for garnet, biotite, plagioclase and muscovite (Table 2.1). Temperatures and pressures were calculated using the winTWQ program (version 2.32; Berman, 2007), which uses internally consistent thermodynamic data for end-members and mixing properties to calculate the average *P-T* values from the intersections among the following independent set of equilibria (mineral abbreviations after Kretz, 1983):

$$Alm + Phl = Pyp + Ann \quad (1)$$

$$Grs + 2Ky + Qtz = 3An \quad (2)$$

$$3East + 2Grs + Pyp + 6Qtz = 3Phl + 6An \quad (3)$$

$$Alm + Grs + Ms = 3An + Ann \quad (4)$$

The winTWQ software incorporates solution solid solution models for garnet and biotite (Berman, 2007), as well as for plagioclase (Fuhrman and Lindsley, 1988) and muscovite (Chatterjee & Froese, 1975). For samples 1 and 2 with sodic-rich plagioclase,

the aluminum-avoidance plagioclase model of Aranovich (1991) was used. This model yields lower pressures that are generally more consistent with independent estimates (Aranovich, 1991). Absolute errors of thermobarometric data are considered to be approximately ± 50 °C and 1 kbar (Berman, 1991), with appreciably smaller errors associated with relative differences between samples.

Table 2.1. Microprobe analyses used in P-T calculations.

	Sample 1 (09RS190A1)			Sample 2 (09RS172B1)				Sample 3 (09RS171A1)				
Mineral	Grt-2	Pl	Bt	Grt-1	Grt-2	Pl	Bt	Grt-1	Grt-2	Pl	Bt	Ms
Position	rim			core	rim			core	rim			
wt% oxides												
SiO_2	37.13	63.13	37.32	36.74	36.52	61.61	35.50	37.03	36.90	61.22	35.30	44.76
TiO_2	0.00	n.d	1.56	0.06	0.03	n.d.	1.84	0.07	0.00	n.d.	2.26	0.37
Al_2O_3	21.94	22.59	17.94	21.20	21.46	24.08	18.61	21.43	21.68	24.90	20.14	35.82
FeO*	32.79	0.35	17.40	35.72	34.46	0.10	20.53	33.31	30.75	0.18	21.21	1.17
MgO	4.93	0.00	12.50	2.53	3.20	0.00	9.35	1.23	2.63	0.00	7.72	0.48
MnO	0.55	0.02	0.05	1.02	0.50	0.02	0.03	2.08	4.35	0.00	0.25	0.00
CaO	2.18	3.68	0.00	2.28	3.59	5.36	0.00	5.53	3.93	6.09	0.00	0.04
Na_2O	0.00	9.21	0.45	0.02	0.01	8.42	0.27	0.00	0.03	7.84	0.30	0.87
K_2O	n.d.	0.11	8.61	n.d.	n.d.	0.09	8.99	n.d.	n.d.	0.19	9.02	9.83
Total	99.53	99.09	96.32	99.58	99.81	99.67	95.70	100.72	100.28	100.42	96.57	93.69
cations												
Oxygen	12	8	11	12	12	8	11	12	12	8	11	11
Si	2.96	2.82	2.78	2.98	2.94	2.74	2.72	2.97	2.96	2.72	2.68	3.03
Ti	0.00	n.d.	0.09	0.00	0.00	n.d.	0.11	0.00	0.00	n.d.	0.13	0.02
Al	2.06	1.19	1.57	2.03	2.04	1.26	1.68	2.03	2.05	1.30	1.80	2.86
Fe*	2.18	0.01	1.08	2.42	2.32	0.00	1.31	2.24	2.06	0.01	1.34	0.07
Mn	0.04	0.00	0.00	0.07	0.03	0.00	0.00	0.14	0.30	0.00	0.02	0.00
Mg	0.59	0.00	1.39	0.31	0.38	0.00	1.07	0.15	0.31	0.00	0.87	0.05
Ca	0.19	0.18	0.00	0.20	0.31	0.26	0.00	0.48	0.34	0.29	0.00	0.00
Na	0.00	0.80	0.06	0.00	0.00	0.73	0.04	0	0.00	0.67	0.04	0.11
K	n.d.	0.01	0.82	n.d.	n.d.	0.01	0.88	n.d.	n.d.	0.01	0.87	0.85
Fe/(Fe + Mg)	0.79		0.44	0.89	0.86		0.55	0.94	0.87		0.61	
X_{Alm}	0.73			0.81	0.76			0.75	0.69			
X_{Pyp}	0.20			0.10	0.13			0.05	0.10			
X_{Grs}	0.06			0.07	0.10			0.16	0.11			
X_{Sps}	0.01			0.02	0.01			0.05	0.10			
X_{An}		0.26				0.26				0.30		

* All Fe assumed to be Fe^{2+}

2.4.2. Phase Diagram Calculations

Isochemical phase diagram sections were calculated in the system MnO-Na_2O–CaO–K_2O–FeO–MgO–Al_2O_3–SiO_2–H_2O–TiO_2-Fe_2O_3 with the program Domino (de Capitani & Brown, 1987; de Capitani & Petrakakis, 2010; http://titan.minpet.unibas.ch/minpet/theriak/theruser.html, version 01.08.09), and the internally consistent thermodynamic dataset of Holland & Powell (1998); data set tcds55, created November 22, 2003. Activity-composition models were used for the following phases: muscovite, excluding the margarite component (Coggon & Holland, 2002), feldspar (Holland & Powell, 2003), garnet and biotite (White *et al*., 2007), ilmenite-hematite and magnetite-ulvospinel (White *et al*., 2000), chlorite, cordierite, chloritoid, staurolite and epidote (Holland & Powell, 1998). All other phases were treated as pure. Garnet, biotite, staurolite, chloritoid, chlorite and cordierite were extended to the Mn-bearing system as outlined in Tinkham *et al*. (2001). A pure H_2O fluid was considered in excess in all calculations. Additionally, excess SiO_2 was added for sample 1 calculations. Silicate melt was not included in the calculations. Bulk rock compositions (Table 2.2) were determined by whole rock XRF analysis from thin section offcuts. A nominal amount of Fe_2O_3 (0.01 mol% Fe_2O_3) was added to the system to be consistent with the garnet and biotite solution models of White *et al*. (2007), which incorporate Fe_2O_3. A small amount of Fe_2O_3 is consistent with Ilmenite as the only Fe-bearing oxide, suggesting these rocks are fairly reduced.

The effective bulk composition of a rock changes with P and T as material is progressively fractionated within the cores of mineral grains with slow intracrystalline diffusion rates (Stüwe, 1997). Evidence for such slow diffusivity, and a changing effective bulk composition, is seen in the preservation of zoned minerals, in particular garnet. Phase diagrams calculated from the bulk whole rock analysis are therefore only strictly correct at the *P-T* conditions during the initial stage of garnet growth. Phase diagrams and compositional isopleths calculated from the whole rock analysis were therefore used to estimate the prograde *P-T* path during the early stages of garnet growth. Isochemical phase diagrams more suitable for modelling peak and retrograde metamorphic conditions were constructed from an effective bulk composition calculated by subtracting the average composition of stage-1 garnet from the whole rock XRF analysis. Whole rock analyses and calculated effective bulk compositions used in the

construction of phase diagrams are listed in Tables 2.2 and 2.3, respectively. There is no evidence to suggest that that the bulk composition was further modified by open system behaviour. For instance, the absence of evidence for partial melt suggests the bulk composition was not modified by melt loss. Furthermore, the mineralogical, chemical and textural features suggest the rock was not affected by fluid alteration following regional metamorphism.

Some discrepancy in *P-T* estimates can be expected to arise from the different thermodynamic data utilized in the phase equilibria modeling and thermobarometric calculations. Nonetheless, the winTWQ program was utilized because its calibration of equilibrium (3), a useful barometer for the aluminosilicate- and muscovite-absent rocks, is based on experimental data directly constraining eastonite properties (Berman *et al*., 2007b).

Table 2.2. Representative bulk-rock geochemical analyses (wt%).

Sample	1	2	3
SiO_2	51.20	43.40	42.80
TiO_2	0.90	1.30	1.06
Al_2O_3	21.40	30.50	23.00
FeO*	10.15	11.25	16.90
MgO	3.01	3.23	2.38
MnO	0.12	0.10	0.92
CaO	2.37	1.37	4.00
Na_2O	5.72	2.44	2.20
K_2O	1.54	1.92	2.89
LOI	0.40	1.97	0.40
Total	96.81	97.48	96.55

Table 2.3. Normalized effective bulk composition for the growth of stage-2 garnet (wt%).

Sample	1	2	3
SiO_2	54.43	44.97	45.53
TiO_2	1.00	1.38	1.21
Al_2O_3	22.34	31.72	24.31
FeO*	8.37	10.50	15.40
MgO	2.83	3.29	2.51
MnO	0.03	0.07	0.89
CaO	2.48	1.35	3.90
Na_2O	6.36	2.59	2.51
K_2O	1.71	2.04	3.29
LOI	0.44	2.09	0.46
Total	100.00	100.00	100.00
*Grt-1 mode	7	3.4	9

*Modal amount of Grt-1 subracted in the calculation of the effective bulk composition.
Note. Compositions in Table 2.3 represent the effective bulk composition during growth of stage-2 garnet overgrowths (Grt-2) following the fractionation of components into the core of stage-1 garnet (Grt-1). The effective bulk compositions were calculated by subtracting the average composition of stage-1 garnet (Grt-1) from the whole rock XRF analysis, with the modal amount of Grt-1 estimated from image analysis of thin sections.

2.5. Petrography and Mineral Chemistry

Four samples from Australia Mountain were selected for thermobarometric and geochronologic analysis. Metamorphic mineral assemblages and coordinates of the sample localities are provided in Table 2.4. The investigated samples are garnet-bearing psammitic and pelitic schists characterized by garnet porphyroblasts that typically show two distinct domains: a resorbed, inclusion-rich darker colored core (Grt-1) and a lighter, inclusion-poor, euhedral overgrowth (Grt-2) (Fig. 2.3a,c-e). A penetrative foliation (S_T) is generally defined within psammitic schists by quartz ribbons, elongated plagioclase, and micaceous-rich layers. In some pelitic schists, staurolite and kyanite porphyroblasts are consistently aligned parallel to S_T, and exhibit kinked, bent and sweeping extinction indicative of syn-kinematic growth with respect to S_T (Fig. 2.3b,f). However, in other semipelitic schists staurolite and kyanite have a weak preferred orientation and may, or

may not, contain intracrystalline evidence for deformation. Many other staurolite and kyanite grains in this same rock are randomly oriented with homogenous extinction, showing no evidence of strain. Staurolite and kyanite growth in the Australia Mountain area is therefore interpreted as syn- to post-kinematic with respect to S_T.

Grt-1 occasionally contain a sigmoidal inclusion-trail (S_i) that in rare samples is continuous with the external transposition foliation (S_T) (Fig. 2.3a), suggestive of early growth under conditions of non-coaxial shearing. By contrast, Grt-2 has fewer primary inclusions, is typically subhedral to euhedral, and has well-developed crystal faces modified by late-stage resorption (Fig. 2.3c,d). Partial breakdown of Grt-2 rims to randomly oriented mats of biotite masks the relationship of the foliation to Grt-2. Where Grt-2 has not been resorbed it is characterized by straight, euhedral crystal faces that appear to truncate S_T (Fig. 2.3c,d), indicative of post-kinematic growth.

The boundary between Grt-1 and -2 is consistently marked by a large chemical discontinuity in all samples (Fig. 2.4). Grt-1 generally has low Fe/(Fe+Mg) and grossular contents that both decrease rimward in some samples. The inner portion of Grt-2 generally has markedly higher grossular, and lower almandine and pyrope than Grt-1. Fe/(Fe+Mg) and spessartine decrease toward the outer rim, characteristic of prograde growth zoning (Tracy *et al*., 1976; Spear *et al*., 1990; Florence & Spear, 1993). A slight kick-up in spessartine and Fe/(Fe+Mg) at the outer 100 μm of Grt-2 adjacent to both plagioclase and biotite is attributed to retrograde garnet resorption (Kohn & Spear, 2000). Biotite grains immediately adjacent to garnet have the highest Fe/(Fe+Mg) values. Otherwise, biotite grains > 300 μm from garnet are 0.05 to 0.07 lower in Fe/(Fe+Mg) and have very little compositional variation (< 0.02). Matrix plagioclase has a variable composition, with the lowest anorthite contents (X_{An}= 0.17-0.20) consistently within the cores of matrix grains of all samples, and the highest anorthite content (X_{An} = 0.25-0.34) within the rims of matrix grains immediately adjacent to strongly resorbed portions of garnet (X_{An} = 0.30).

Table 2.4. Summary of thermobarometric and geochronologic data.

Sample no.	Field no.	UTM (zone 7 NAD 83) Easting	Northing	Stage-2 Grt rim peak thermobarometry: Main assemblage	P[a] (kbar)	T (°C)	Eq.[b]	Age[c] (Ma)	Interpretation
1	09RS190A1	642809	7056955	St-Grt-Bt-Pl-Qtz[d]	8.8	650	1,3	120 ± 3	Prograde M2, syn- to post-S_T
					8	650	pd	112 ± 6	M2 decompression
2	09RS172B1	641621	7063232	Ky-St-Crd-Grt-Bt-Qtz-Pl	8.9	650	1,2,3	118 ± 2	Prograde M2, syn- to post-S_T
3	09RS171A1	641101	7063420	Ms-Bt-Grt-Pl-Qtz	9 - 10	680	1,3,4	–	Prograde M2, syn- to post-S_T
4	09RS188A2	642122	7057171	Sil-Grt-Crd-St-Ky-Bt-Pl-Qtz	–	–	–	117 ± 1	Prograde M2, syn- to post-S_T

[a]Estimated uncertainties are ± 1 kbar and 50 °C (Berman, 1991).
[b]Equilibria used to derive listed *P-T* values (pd = phase diagram constraints.
[c]All ages determined by *in situ* SHRIMP analysis of monazite.
[c]All ages represent weighted mean $^{206}Pb/^{238}U$ ages (2 sigma errors) of texturally and chemically similar monazite grains discussed in text.
[d]Minerals listed from least to most abundant.

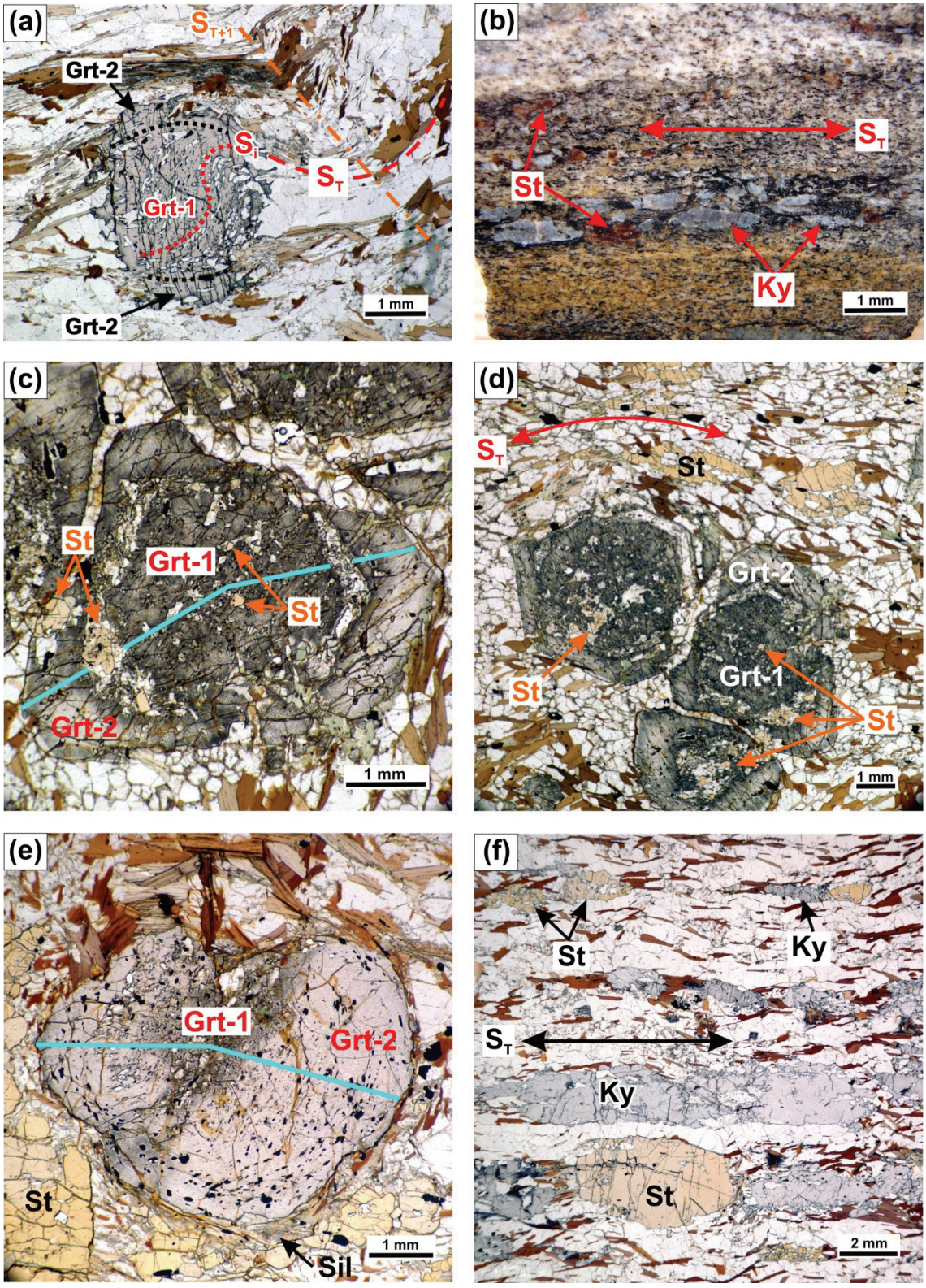
(a)
S_{T+1}
Grt-2
S_i
S_T
Grt-1
Grt-2
1 mm
(b)
S_T
St
Ky
1 mm
(c)
St
Grt-1
St
Grt-2
1 mm
(d)
S_T
St
Grt-2
St
Grt-1
St
1 mm
(e)
Grt-1
Grt-2
St
Sil
1 mm
(f)
St
Ky
S_T
Ky
St
2 mm

Figure 2.3. **Photomicrographs of samples 1, 2 and 4. (a) Garnet porphyroblast of sample 1 consisting of: (i) a syn-kinematic garnet core (Grt-1), which hosts a sigmoidal inclusion trail (Si) that is continuous with the external transposition foliation (S_T), and (ii) an inclusion-poor overgrowth (Grt-2) on the top and bottom of the porphyroblast. (b) Sample 4 hand sample with elongate syn-kinematic staurolite (St) and kyanite (Ky) porphyroblasts consistently aligned parallel to the transposition foliation (S_T). (c) Garnet porphyroblast from sample 1 consisting of an inclusion-rich core (Grt-1) surrounded by an annulus of euhedral staurolite and plagioclase, and an inclusion-poor garnet atoll (Grt-2). Both the garnet core and atoll from sample 1 are resorbed and replaced by staurolite and plagioclase. The microprobe traverse displayed in figure 2.4a is shown in blue. (d) Garnet core and atoll of sample 1 replaced by euhedral staurolite and plagioclase. Skeletal matrix staurolite aligned parallel to the transposition foliation (S_T) is deflected around the garnet porphyroblasts, and is interpreted as an earlier generation than that which replaced garnet. (e) Garnet porphyroblast from sample 2, which consists of an inclusion-rich garnet core (Grt-1), and, with the exception of ilmenite (black inclusion), a relatively inclusion-poor overgrowth (Grt-2). The blue line across garnet shows the location of the microprobe traverse displayed in Figure 2.4b. (f) Syn-kinematic porphyroblasts of staurolite and kyanite aligned parallel to S_T in sample 4. Fibrolitic sillimanite (Sil) occurs as small radiating fibers. Note: All mineral abbreviations used in figures are after Kretz (1983).**

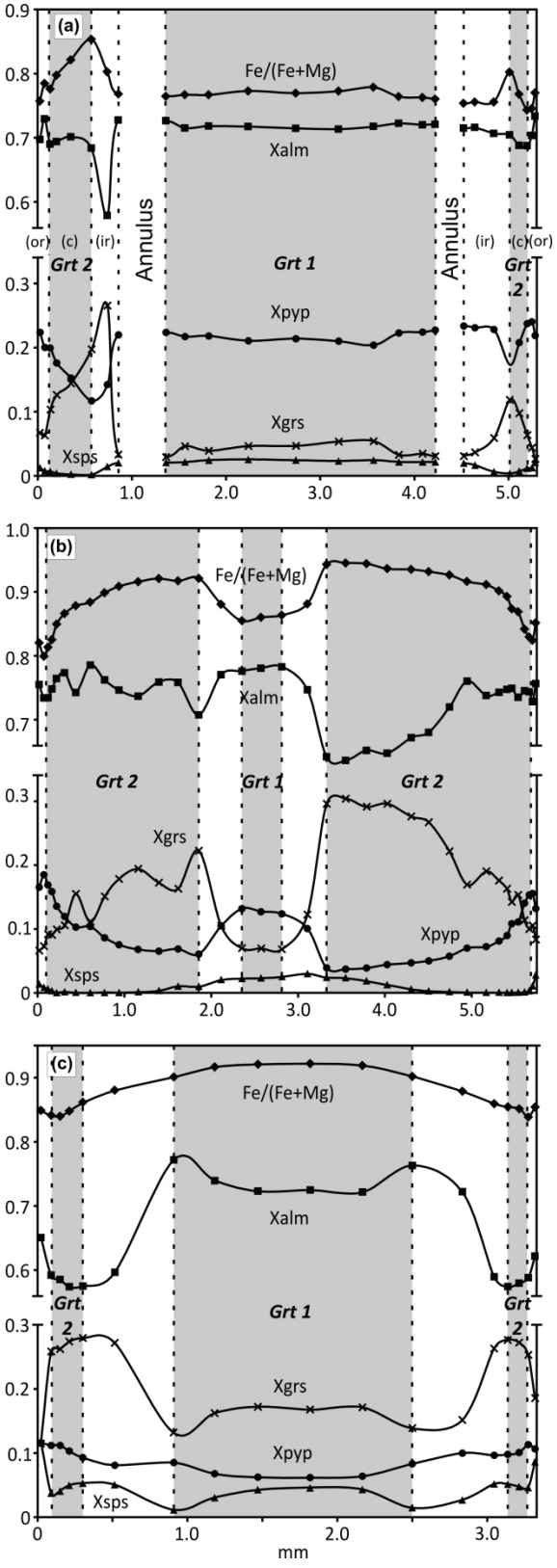
(a)
Fe/(Fe+Mg)
Xalm
Annulus
Annulus
(or)
(c)
(ir)
(ir)
(c)
(or)
Grt 2
Grt 1
Grt 2
Xpyp
Xgrs
Xsps
(b)
Fe/(Fe+Mg)
Xalm
Grt 2
Grt 1
Grt 2
Xgrs
Xpyp
Xsps
(c)
Fe/(Fe+Mg)
Xalm
Grt 2
Grt 1
Grt 2
Xgrs
Xpyp
Xsps
mm

Figure 2.4. Compositional profiles across garnet porphyroblasts. (a) Sample 1. Abbreviations for Grt-2: ir – inner rim; c – core; or – outer rim. Note the sharp compositional gradient between vertical dashed lines. (b) Sample 2. (c) Sample 3. Grey shading shows the boundaries of garnet 1 and garnet 2.

2.5.1. Sample 1

Sample 1 is an Ilm-St-Grt-Bt-Pl-Qtz-bearing psammitic schist. It shares the textural and chemical features described above, but shows additional complexities and a unique textural relationship with monazite that warrant more detailed description. Portions of Grt-1, the outer portion of Grt-2, as well as the interface between them have been partially replaced by plagioclase, fine-grained euhedral staurolite and Y-rich monazite (Fig. 2.3c,d), forming an island (Grt-1) and atoll (Grt-2) structure. Staurolite and monazite do not occur as inclusions in either Grt-1 or Grt-2. In addition to the garnet chemical zoning described above, it is noteworthy that garnet has the same composition at its interface with the replacement products, St-Pl-Mnz, at the Grt-1 rim, Grt-2 inner rim, and Grt-2 outer rim (Fig. 2.4). Skeletal staurolite also occurs within the matrix of sample 1 where it is aligned parallel to the relict foliation and is deflected around garnet (Fig. 2.3d). The pre- to syn-kinematic nature of this matrix staurolite, together with its resorbed/skeletal texture, suggests it is an earlier generation than the euhedral, retrograde staurolite that occurs within resorbed portions of garnet.

2.5.2. Sample 2

Sample 2 is a weakly foliated Ilm-Ky-St-Crd-Grt-Bt-Qtz-Pl-bearing semipelitic schist. Staurolite and kyanite have both a weak preferred orientation with undulatory extinction and are also randomly oriented with homogenous extinction. Staurolite, and less commonly kyanite, is rimmed by cordierite that contains numerous inclusions of fine-grained biotite. Garnet porphyroblasts are less than 8.0 mm in diameter and commonly have an atoll texture characterized by a subhedral garnet atoll (Grt-2) surrounding an interior of quartz, biotite, and plagioclase. Other garnet porphyroblasts are present which show no chemical indication of a multi-stage growth history. These porphyroblasts are interpreted as stage-2 garnet from their similarity in texture, composition and zoning pattern to stage-2 overgrowths.

2.5.3. Sample 3

Sample 3 is a garnet-rich Ilm-Ms-Bt-Grt-Pl-Qtz-bearing psammitic schist. A penetrative schistose foliation is defined at outcrop and hand sample scale by elongate feldspar grains, and aligned biotite and muscovite that are deflected around garnet porphyroblasts. At thin-section scale, micas are randomly oriented, possibly due to a late episode of static recrystallization that masks the foliation and its timing of development relative to garnet growth. However, the presence of quartz and plagioclase pressure shadows aligned parallel to the foliation on opposite sides of euhedral garnet porphyroblasts indicates that the latter stages of garnet growth were synchronous with deformation. Muscovite, which is present only in sample 3, has a slight phengitic content (Si pfu = 3.1 – 3.2), generally non-detectable Ca, and Na/(Na + K + Ca) values of 0.08 – 0.10.

2.5.4. Sample 4

Sample 4 is a Rt-Sil-Grt-Crd-St-Ky-Bt-Pl-Qtz-bearing metapelite. Garnet occurs as rare, small (< 1 mm), heavily resorbed grains both in the matrix and as inclusions within kyanite. Garnet that occurs both in the matrix and included in kyanite is partly replaced by biotite and plagioclase. Staurolite and kyanite contain kinked and sweeping extinction and are consistently aligned parallel to S_T, indicative of syn-kinematic growth with respect to S_T (Fig. 2.3b,f). Trains of elongated rutile grains are aligned parallel to, and help define, the S_T foliation. Cordierite appears texturally late, forming replacement rims around staurolite, and to a lesser extent around kyanite, and occurs throughout the matrix with numerous inclusions of biotite. A small amount of fibrolitic sillimanite is present in small patches of radiating fibers (Fig. 2.3f).

2.6. Paragenetic Interpretation of Textural and Chemical Relations in Garnet

Sample 3 is the only sample which records pronounced chemical zoning of the inclusion-rich garnet core, with rimward decreasing X_{Sps}, X_{Grs} and Fe/(Fe+Mg), and increasing X_{Alm} and X_{Pyp} characteristic of prograde growth zoning produced along a clockwise *P-T* path (Tracy *et al*., 1976; Spear *et al*., 1990; Florence & Spear, 1993).

However, the sharp compositional gradient/discontinuity between Grt-1 and Grt-2 (Fig. 2.4), with the latter characterized by an increase in Fe/(Fe+Mg) and a decrease in X_{Pyp}, does not conform to a *P-T* path of increasing temperature required for garnet growth (Figs 2.5 & 2.6). Rather, the sharp compositional gradient between Grt-1 and -2 is interpreted as a zone of incomplete diffusional re-equilibration that developed following growth of the chemically distinct garnet overgrowth (Grt-2). The arrangement of X_{Grs} isopleths for sample 2 (Fig. 2.5) suggests growth of the grossular-rich Grt-2 initiated at significantly higher pressure and/or lower temperature than Grt-1.

Within the core of Grt-2, the decreasing Fe/(Fe+Mg), X_{Sps} and X_{Grs} values away from the zone of diffusional re-equilibration toward the rim is interpreted as a growth zoning pattern similar to Grt-1, but one that developed during a subsequent metamorphic event. Enrichment of spessartine and Fe/(Fe+Mg) at the extreme Grt-2 rim, and Fe-enriched biotite immediately adjacent to resorbed portions of garnet, are features characteristic of retrograde diffusional re-equilibration during resorption of garnet (Kohn & Spear, 2000). Within sample 1, the replacement of Grt-1 and the outer portion of Grt-2, as well as the interface (annulus) between them, by the same assemblage (St-Plg-Mnz) suggests garnet was resorbed both from the inside and outside following growth of both Grt-1 and Grt-2. This is supported by the similarity in the composition of the complexly zoned garnet at its interface with the replacement products in the core, annulus, and outer atoll locations—a composition attributed above to garnet resorption during retrogression. The slightly higher Fe/(Fe+Mg) and grossular contents within the core of Grt-1 from sample 1 suggest incomplete diffusional re-equilibration across Grt-1 during retrogression.

More calcic plagioclase occurs adjacent to resorbed portions of garnet in all samples and at the rims of matrix grains, and thus, may likewise reflect the precipitation of new plagioclase upon garnet resorption during decompression (e.g., Spear *et al*., 1990). The alternative that this more calcic plagioclase is due to the progressive consumption of a Ca-bearing phase such as epidote is considered less likely as this mineral is not preserved as inclusions in garnet. The less calcic cores of matrix plagioclase and those at a distance from garnet likely record equilibrium compositions along the prograde path or an earlier metamorphic event. Thus, the most reliable *P-T* conditions derive from the composition of minerals associated with the calcic

plagioclase. Conventional barometric calculations will therefore yield a minimum estimate of near-peak *P-T* conditions.

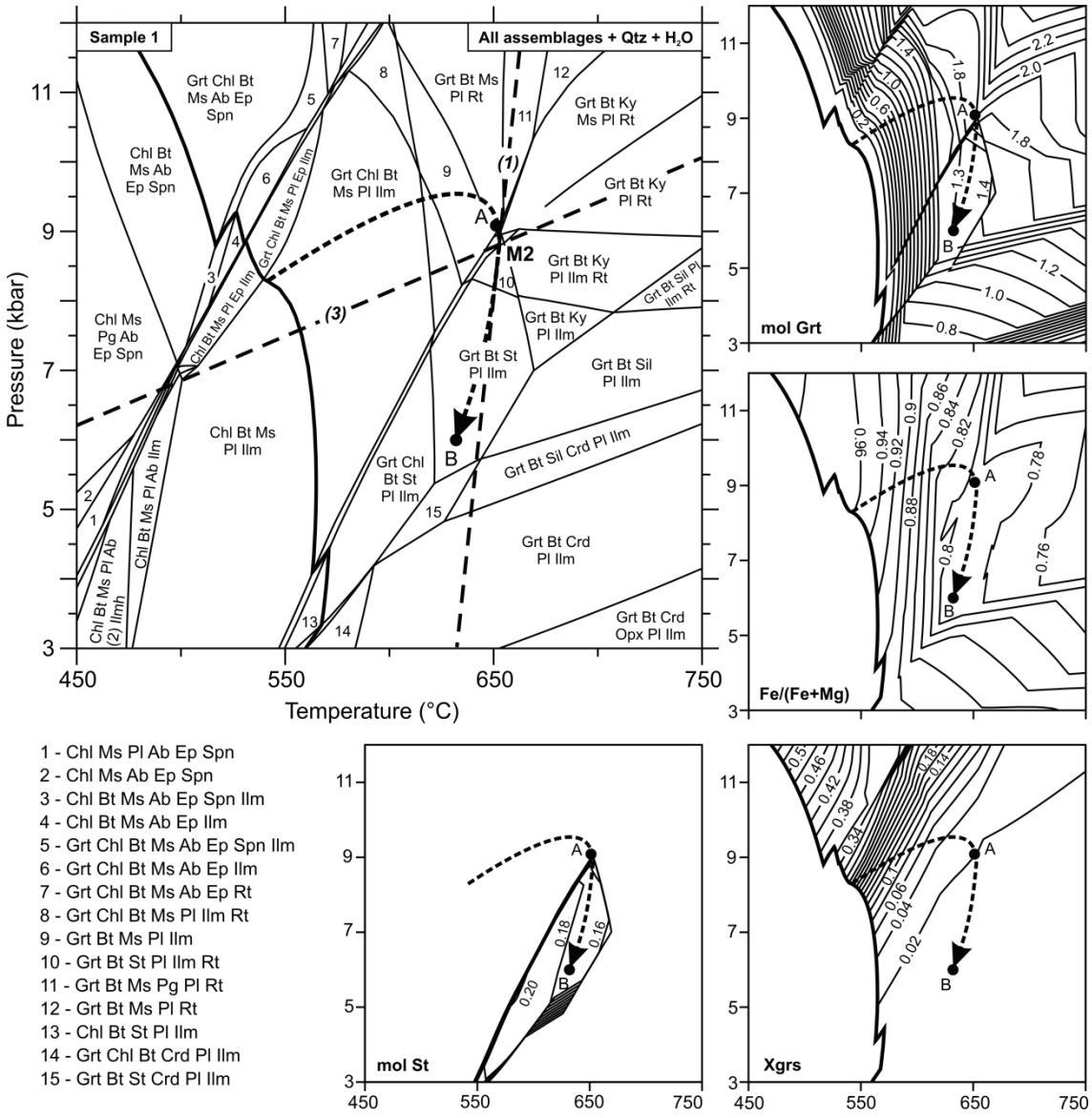

Figure 2.5. Isochemical phase diagram and molar isopleth sections calculated from the normalized effective bulk rock composition (Table 2.3) of sample 1 in the chemical system MnNCKFMASHTO. H2O and quartz calculated as in excess. Dashed lines display stage-2 garnet multi-equilibria thermobarometric estimates, with the stage-2 peak metamorphic estimate labeled M2, and each equilibria numbered as referenced in text. Our preferred stage-2 P-T path interpretation is shown by a dashed arrow (see text for discussion). The molar abundances of the main phases, shown in Figure 2.7, are calculated along the path from points A to B.

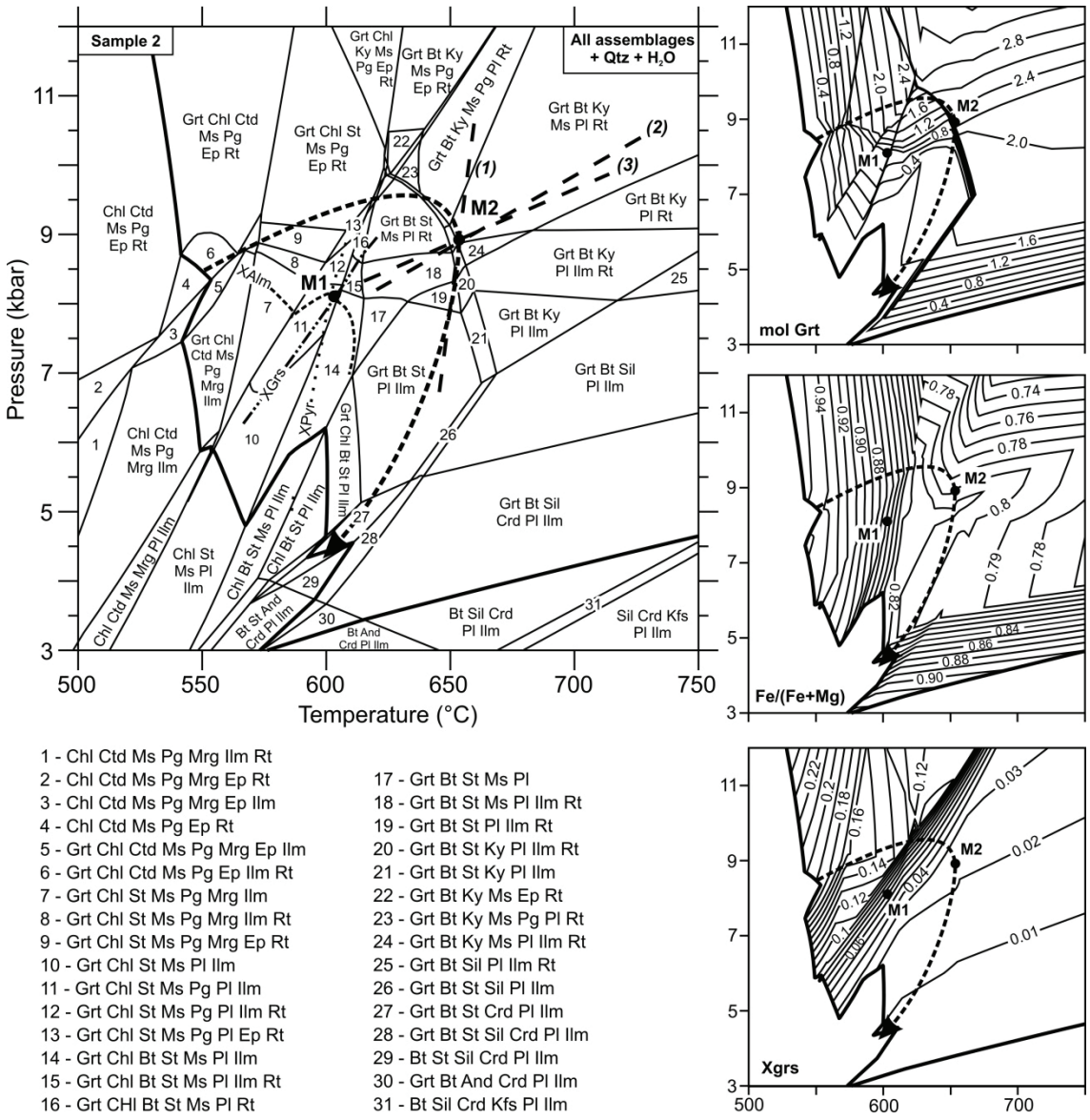

Figure 2.6. Isochemical phase diagram and molar isopleth sections calculated from the normalized effective bulk rock composition (Table 2.3) of sample 2 in the chemical system MnNCKFMASHTO. H2O calculated as in excess. P-T conditions of the incipient stages of stage-1 garnet growth (M1) are estimated from the intersection of XAlm (dashed), XPyr (dotted), and XGrs (dotted/dashed) isopleths corresponding to the Grt-1 core composition of sample 2. Dashed lines display stage-2 garnet multi-equilibria thermobarometric estimates, with the stage-2 peak metamorphic estimate labeled M2, and each equilibria numbered as referenced in text. The interpreted stage-2 P-T path is shown by a dashed arrow.

2.7. P-T-d History

2.7.1. Stage-1 P-T-d History

The earliest phase of deformation and metamorphism is recorded in the syn-kinematic, inclusion-rich core (Grt-1) of a two-stage garnet. A sigmoidal inclusion trail within the garnet core indicates non-coaxial shear, synchronous with the development of the dominant penetrative foliation (S_T). Due to the lack of suitable inclusions within the Grt-1core, the preserved growth zoning within samples 2 and 3 is the only indicator of the *P-T* evolution during the first stage of garnet growth. We used garnet isopleth thermobarometry (e.g. Vance & Mahar, 1998) to estimate the *P-T* conditions of this earliest garnet growth event. Isopleths of spessartine, almandine and pyrope corresponding to the Grt-1 core composition in sample 2 intersect tightly at approximately 600°C and 8 kbar (Fig. 2.6). Compositional isopleths corresponding to the center of Grt-1 in sample 3 do not intersect at a point, but define a narrow field from 565 to 585 °C and from 7.8 to 8.5 kbar. The near vertical slope of X_{Pyp} isopleths implies Grt-1 of samples 2 and 3 grew along a *P-T* path of increasing T. The outward decreasing grossular content within Grt-1 indicates these rocks followed a prograde *P-T* trajectory along a more shallow slope than X_{Grs} isopleths. Due to the absence of monazite inclusions within the garnet core, there is presently no upper age constraint on the timing of this metamorphic and deformational event. Grt-1 growth may be as old as Late Permian, similar to the metamorphic domain to the west, but we cannot rule out that it may be as young as Late Jurassic in age.

2.7.2. Stage-2 P-T-d History

Growth of euhedral to subhedral inclusion-poor garnet (Grt-2) during a discrete, later metamorphic event is supported by the following: (i) a large chemical gradient/ discontinuity at the boundary between the inclusion-rich core (Grt-1) and inclusion-poor overgrowth (Grt-2), and (ii) an increase in Fe/(Fe+Mg) and X_{Grs}, and a decrease in X_{Alm} and X_{Pyp} values from Grt-1 to Grt-2, which does not conform to a prograde path involving garnet growth (Fig. 2.6).

Multi-equilibria thermobarometric estimates are presented in Figs 2.5 & 2.6 and Table 2.4. In order to minimize the effects of retrograde diffusion, near thermal peak thermobarometric estimates of stage-2 garnet growth were calculated from minimum Fe/(Fe+Mg) values just inboard of the Mn- and Fe-enriched outer rim, together with the rims of plagioclase and the least Fe-enriched biotite. Thermobarometric estimates of stage-2 garnet growth for samples 1-3 range between 650 – 680 °C and 8 – 10 kbar. Garnet and plagioclase in samples 1 and 2 have low grossular and anorthite contents, which reduces the reliability of the geobarometric estimates (Ashworth & Evirgen, 1985; Todd, 1998). Part of the inaccuracy associated with low-anorthite contents may have been addressed here by using the plagioclase model of Aranovich (1991), which Aranovich found yields lower pressures for sodic plagioclase that are more consistent with independent estimates. Despite a potential inaccuracy associated with low grossular contents for Grt-2 of samples 1 and 2, the barometric estimates are consistent with the more reliable results of the more calcic mineral compositions in sample 3. Florence & Spear (1993) noted that diffusional modification of a sharp compositional gradient within garnet due to an intermittent period of garnet dissolution during staurolite growth along the prograde path will shift Fe/(Fe+Mg) at the garnet rim to a higher value, yielding a calculated temperature lower than the true thermal peak. Therefore, the slightly higher peak *P-T* estimates of 680°C and 9 – 10 kbar from sample 3, in which staurolite is absent, may be a closer estimate to near-peak stage-2 *P-T* conditions.

Conventional multi-equilibria thermobarometric estimates of peak stage-2 garnet growth are consistent with the presence of kyanite in sample 2. However, the *P-T* estimates of sample 2 lie on the upper thermal stability limit of staurolite (Fig. 2.6), yet well within overall uncertainties of thermobarometric and phase diagram calculations. Nevertheless, garnet-biotite thermometric estimates may overestimate peak temperatures if biotite was enriched in Fe during garnet resorption. Arguing against this caveat is the abrupt decrease of Fe/(Fe+Mg) in biotite > 300 μm from garnet (see above), with little Fe/(Fe+Mg) variation beyond this distance, suggesting that Fe-enrichment of biotite during garnet resorption was fairly restricted. Therefore, temperatures calculated from biotite with the lowest Fe/(Fe+Mg) composition are expected to yield a close approximation to peak temperatures. Alternatively, a small apparent discrepancy between thermobarometric estimates and equilibrium assemblage

modeling may reflect the metastable persistence of staurolite above its upper thermal stability limit (e.g., Waters & Lovegrove, 2002; Pattison & Tinkham, 2009; Pattison *et al*., 2011). The syn- to post-kinematic staurolite and kyanite in samples 2 and 4 is interpreted to have grown and equilibrated with Grt-2. This is based on the agreement between Grt-2 thermobarometry and the predicted stability fields of staurolite and kyanite, as well as the partially post-kinematic nature of staurolite, kyanite and Grt-2.

By contrast, the origin of prograde, matrix staurolite in sample 1 differs from the stage-2 paragenesis and its possible metastable existence in sample 2. Contrary to the near ubiquitous static recrystallization textures associated with stage-2 metamorphism, matrix staurolite of sample 1 has an anhedral and skeletal nature, and is aligned parallel to the foliation and is deflected around garnet (Fig. 2.3d), indicative of syn-kinematic growth. Though it remains unknown as to which garnet generation this staurolite is deflected around, the syn-kinematic stage-1 garnet core within other samples seems to be a more likely candidate. Based on these textures, it is interpreted that matrix staurolite within sample 1 is from an earlier metamorphic event, likely related to stage-1 garnet.

2.7.3. Stage-2 Retrograde P-T History

The P-T path is constrained for sample 1 by the production of staurolite from garnet and from the Ca-rich composition (X_{Grs} = 0.25) of the Grt-2 core. Although it is possible to produce staurolite with isobaric heating up to the peak temperature (M2, Fig. 2.5), this path is interpreted as unlikely since garnet resorption is negligible even near the metamorphic peak (Fig. 2.5). Preference is given to a clockwise, looping PT path in which staurolite growth and garnet resorption accompany the onset of decompression after peak P-T conditions. The retrograde segment of the path is constrained to be consistent with the absence of retrograde sillimanite in samples 1 (appearing above 620°C and 5.4 kbar) and 2, yet consistent with the presence of cordierite rims around staurolite in samples 2 and 4, and retrograde sillimanite in sample 4. These observations require decompression below 5 kbar prior to cooling below 600 °C (Fig. 2.6).

To highlight the consistency between observed mineral modes and reaction textures with that predicted for this steep to near isothermal decompression path within

the model system, molar mineral abundances were calculated for sample 1 (Fig. 2.7) and plotted based on the retrograde *P-T* path between points A and B in Figure 2.5. At 9 kbar and at near- peak conditions of metamorphism (point A in Fig. 2.5) muscovite and garnet are stable along with biotite and plagioclase. Early in the retrograde history, at 8.8 kbar, staurolite growth is predicted, together with plagioclase and biotite, at the expense of muscovite and garnet (Fig. 2.7). Upon decompressing through 8.6 kbar, muscovite is entirely consumed, consistent with its absence in the observed mineral assemblage, and below which staurolite remains stable. This modelling is consistent with the observed assemblage of staurolite, plagioclase and Y-rich monazite within resorbed portions of both stage-1 and -2 garnet of sample 1, and retrograde biotite recorded texturally as randomly oriented matrix grains and within the cores of atoll garnet. The presence of monazite within the resorbed garnet, and its otherwise complete absence as an included phase within both stage-1 and -2 garnet suggests that this monazite was an accessory product of these garnet and muscovite-consuming reactions. As discussed below, the consistently younger ages and distinctly high Y-content of monazite intimately associated with euhedral, inclusion-free staurolite within resorbed portions of both stage-1 and -2 garnet of sample 1, corroborates the interpretation that these staurolite grains grew at the expense of garnet following growth of the stage-2 garnet rims.

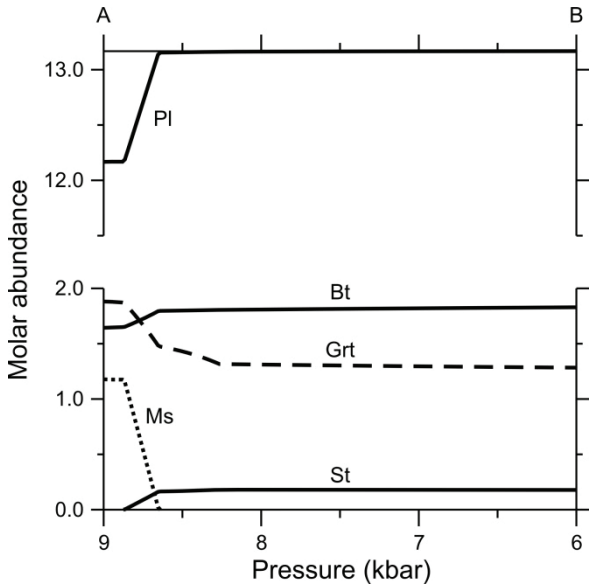

Figure 2.7. Diagram showing the evolution of the molar abundance in sample 1 of the main phases as calculated along the P-T path from point A to B in Figure 2.5.

2.8. Monazite Geochronology

2.8.1. Geochronologic Methods

Prior to U-Th-Pb analysis, the locations of all monazite grains in thin section were identified using an automated scanning routine on a Zeiss EVO 50 series scanning electron microscope (SEM) at the Geological Survey of Canada in Ottawa, operating at 20 kV accelerating voltage and 500 pA beam current. Back Scattered Electron (BSE) images of the *in situ* monazite grains were also obtained to provide insight into their petrological context and internal zoning, identify cracks and mineral inclusions, and to guide analytical spot placement. In order to better characterize chemical zonation and potential age domains within individual monazite grains, chemical X-ray maps of Y, U, Th and Ca in strategically selected monazite grains were produced using a Cameca SX50 electron microprobe at the University of Massachusetts operating at a high current (240-260 nA), with small step sizes (0.25-0.62 μm), and rastering of the electron beam. For each the Y maps, the approximate Y concentration in parts per million (ppm) for each pixel was calculated using the AgeMap program (Williams *et al*., 1999; modified by Goncalves *et al*., 2005) in order to estimate the approximate Y concentration for each SHRIMP spot (Table 2.5).

In situ U-Th-Pb analyses using the SHRIMP II at the Geological Survey of Canada in Ottawa were performed on monazite cored from polished thin sections and mounted in epoxy together with pre-polished monazite standards according to the methods of Rayner & Stern (2002). Targeted areas of monazite were analyzed using a mass-filtered O_2^- primary beam focused with a Kohler aperture to a spot measuring 9 x 12 μm. The methods employed follow the SHRIMP analytical protocols described in detail by Stern (1997), Stern & Sanborn (1998) and Stern & Berman (2000). Tera-Wasserburg and Concordia plots, data regression and weighted mean calculations were made using the program ISOPLOT 3.7 (Ludwig, 2008). Errors assigned to SHRIMP U–Th–Pb ages were determined using numerical propagation of all known sources of error as outlined by Stern (1997), Stern & Sanborn (1998), and Stern & Berman (2000). Uncertainties for individual analyses (ratios and ages) shown in Tables 2.5 and 2.6, and error ellipses shown in Fig. 2.8, are presented at the 1σ level, whereas weighted mean ages and 2σ uncertainties are provided in the text, Table 2.4 and Fig. 2.8.

Table 2.5. SHRIMP U-Th-Pb analytical data for monazite corrected using the ^{207}Pb-method.

Spot[a]	Texture[b]	Grain location	Y (ppm)[c]	Th/U	$^{204}Pb/^{206}Pb$	f(206)^{207} (%)[d]	Total $^{207}Pb/^{206}Pb$	Total $^{238}U/^{206}Pb$	Age (Ma)[e,f] $^{206}Pb/^{238}U$
Sample 1									
M131.1	Matrix || S_T	core	400	8.64	1.039E-03 ± 1.143E-04	1.67	0.0594 ± 0.0006	52.316 ± 0.628	120.4 ± 1.4
M102.1	Replac. Grt	core	1400	7.43	1.144E-03 ± 1.716E-04	1.64	0.0591 ± 0.0010	54.822 ± 0.877	115.0 ± 1.8
M102.2	Replac. Grt	rim	3400	6.39	2.215E-03 ± 1.329E-04	4.01	0.0780 ± 0.0026	56.004 ± 0.672	109.9 ± 1.4
M9.1	Replac. Grt	core	1700	2.82	4.817E-04 ± 6.263E-05	1.15	0.0552 ± 0.0005	56.010 ± 0.672	113.1 ± 1.4
Sample 2									
M55.1	St	core	5800	5.35	6.104E-04 ± 6.714E-05	0.98	0.0539 ± 0.0004	53.241 ± 0.639	119.1 ± 1.5
M55.2	St	rim	5200	6.44	8.427E-04 ± 9.269E-05	1.52	0.0582 ± 0.0006	54.034 ± 0.540	116.8 ± 1.2
M156.1	St	rim	8500	7.50	9.815E-04 ± 1.080E-04	1.68	0.0595 ± 0.0011	54.207 ± 0.759	116.2 ± 1.6
M157.1	St	N/A	8500	9.19	1.112E-03 ± 1.223E-04	1.45	0.0576 ± 0.0009	53.001 ± 0.742	119.1 ± 1.7
M157.2	St	N/A	6500	4.18	4.238E-04 ± 5.085E-05	9.33	0.0535 ± 0.0004	53.004 ± 0.583	119.7 ± 1.3
M118.1	Matrix ⊥ S_T	core	2300	4.53	4.112E-04 ± 6.169E-05	0.77	0.0522 ± 0.0006	53.624 ± 0.590	118.5 ± 1.3
M118.2	Matrix ⊥ S_T	rim	5500	6.71	7.765E-04 ± 9.317E-05	1.43	0.0574 ± 0.0006	55.046 ± 0.661	114.7 ± 1.4
Sample 4									
M144.1	Ky || S_T	rim	11000	6.45	9.508E-04 ± 9.508E-05	1.50	0.0580 ± 0.0005	53.439 ± 0.748	118.1 ± 1.6
M123.1	Matrix || S_T	core	14000	2.83	3.323E-04 ± 3.988E-05	0.79	0.0523 ± 0.0004	52.814 ± 0.634	120.4 ± 1.4
M107.1	Crd || S_T	rim	10000	7.71	8.232E-04 ± 9.055E-05	1.10	0.0548 ± 0.0010	54.144 ± 0.653	117.0 ± 1.4
M246.1	Crd || S_T	core	15000	4.63	2.726E-04 ± 6.271E-05	0.76	0.0521 ± 0.0004	55.165 ± 0.591	115.3 ± 1.2
M246.2	Crd || S_T	rim	10000	5.84	5.949E-04 ± 9.518E-05	1.42	0.0574 ± 0.0005	55.265 ± 0.653	114.3 ± 1.3
M511.1	Matrix	core	13500	5.73	4.610E-04 ± 7.376E-05	1.06	0.0545 ± 0.0004	53.780 ± 0.743	117.9 ± 1.6
M511.2	Matrix	rim	3700	8.69	8.827E-04 ± 8.827E-05	1.27	0.0562 ± 0.0005	54.366 ± 0.577	116.3 ± 1.2
M511.3	Matrix	core	13500	5.21	4.710E-04 ± 5.181E-05	0.83	0.0527 ± 0.0004	53.599 ± 0.595	118.5 ± 1.3
M516.1	Matrix	rim	6800	7.50	6.238E-04 ± 9.357E-05	1.05	0.0544 ± 0.0011	54.233 ± 0.875	116.9 ± 1.9
M516.2	Matrix	core	17300	5.17	3.895E-04 ± 5.842E-05	0.77	0.0522 ± 0.0007	53.687 ± 0.842	118.4 ± 1.8
M516.3	Matrix	rim	6800	9.71	8.472E-04 ± 7.625E-05	1.30	0.0564 ± 0.0005	54.064 ± 0.617	117.0 ± 1.3

[a]Spot: M157.2 = 2nd spot on monazite grain #157.
[b]Texture: location of monazite as inclusion in St, Ky, Crd, or as a matrix grain (|| = elongate monazite grain parallel to foliation).
[c]Y: approximate Y concentration calculated from Y X-ray maps using the AgeMap program as modified by Goncalves *et al.* (2005).
[d]f(206)^{207} refers to the fraction of total ^{206}Pb that is common Pb, calculated using the ^{207}Pb-method.
[e]Ages have been corrected for common Pb using the ^{207}Pb-method.
[f]Uncertainties reported at 1σ (absolute) and are calculated by numerical propagation of all known sources of error (Stern & Berman, 2000).

Table 2.6. SHRIMP U-Th-Pb analytical data for monazite corrected using the ^{204}Pb-method.

Spot[a]	Texture[b]	f(206)^{204} (%)[c]	^{208*}Pb/^{206*}Pb[d]	^{206*}Pb/^{238}U	^{207*}Pb/^{235}U	Corr. coeff.	^{207*}Pb/^{206*}Pb	Age (Ma)[e,f,g] ^{207}Pb/^{235}U	^{208}Pb/^{232}Th	^{206}Pb/^{238}U
Sample 1										
M131.1	Matrix || S_T	1.92	3.0201 ± 0.0124	0.01875 ± 0.00022	0.1137 ± 0.0005	0.284	0.0440 ± 0.0018	109.4 ± 4.9	132.1 ± 1.7	119.7 ± 1.4
M102.1	Resorbed Grt	2.12	2.3840 ± 0.0150	0.01785 ± 0.00029	0.1037 ± 0.0069	0.241	0.0421 ± 0.0027	100.1 ± 7.0	115.5 ± 1.8	114.1 ± 1.8
M102.2	Resorbed Grt	4.11	2.1681 ± 0.0154	0.01712 ± 0.00021	0.1068 ± 0.0080	0.163	0.0452 ± 0.0033	103.0 ± 8.1	117.1 ± 1.2	109.4 ± 1.3
M9.1	Resorbed Grt	0.89	0.8948 ± 0.0135	0.01769 ± 0.00021	0.1174 ± 0.0029	0.491	0.0481 ± 0.0011	112.7 ± 3.0	113.2 ± 1.9	113.1 ± 1.4
Sample 2										
M55.1	St	1.13	1.6870 ± 0.0114	0.01857 ± 0.00023	0.1148 ± 0.0031	0.457	0.0448 ± 0.0011	110.4 ± 3.1	118.1 ± 1.2	118.6 ± 1.4
M55.2	St	1.56	2.0704 ± 0.0092	0.01822 ± 0.00019	0.1148 ± 0.0040	0.303	0.0457 ± 0.0015	110.4 ± 4.0	118.1 ± 1.3	116.4 ± 1.2
M156.1	St	1.82	2.4887 ± 0.0034	0.01811 ± 0.00025	0.1123 ± 0.0053	0.292	0.0450 ± 0.0020	108.0 ± 5.4	121.1 ± 1.4	115.7 ± 1.6
M157.1	St	2.06	2.9256 ± 0.0209	0.01848 ± 0.00026	0.1046 ± 0.0055	0.271	0.0411 ± 0.0021	101.0 ± 5.6	118.6 ± 1.9	118.0 ± 1.7
M157.2	St	0.78	1.3654 ± 0.0053	0.01872 ± 0.00020	0.1219 ± 0.0026	0.498	0.0472 ± 0.0009	116.8 ± 2.6	123.1 ± 1.3	119.6 ± 1.3
M118.1	Matrix ⊮ S_T	0.76	1.4638 ± 0.0096	0.01851 ± 0.00020	0.1177 ± 0.0031	0.406	0.0461 ± 0.0011	113.0 ± 3.1	120.6 ± 1.3	118.2 ± 1.3
M118.2	Matrix ⊮ S_T	1.44	2.1416 ± 0.0156	0.01791 ± 0.00022	0.1134 ± 0.0040	0.350	0.0459 ± 0.0015	109.1 ± 4.1	115.2 ± 1.3	114.4 ± 1.4
Sample 4										
M144.1	Ky || S_T	1.76	2.1321 ± 0.0156	0.01839 ± 0.00026	0.1115 ± 0.0041	0.374	0.0440 ± 0.0015	107.3 ± 4.2	122.5 ± 1.3	117.5 ± 1.6
M123.1	Matrix || S_T	0.62	0.9061 ± 0.0094	0.01882 ± 0.00023	0.1230 ± 0.0023	0.627	0.0474 ± 0.0007	117.8 ± 2.4	121.6 ± 1.2	120.2 ± 1.4
M107.1	Crd || S_T	1.53	2.5176 ± 0.0098	0.01819 ± 0.00022	0.1068 ± 0.0043	0.301	0.0426 ± 0.0016	103.0 ± 4.4	119.6 ± 1.2	116.2 ± 1.4
M246.1	Crd || S_T	0.51	1.4985 ± 0.0061	0.01804 ± 0.00019	0.1195 ± 0.0028	0.454	0.0481 ± 0.0010	114.6 ± 2.9	117.6 ± 1.4	115.2 ± 1.2
M246.2	Crd || S_T	1.10	1.9012 ± 0.0085	0.01790 ± 0.00021	0.1200 ± 0.0041	0.354	0.0486 ± 0.0015	115.1 ± 4.1	117.4 ± 1.4	114.3 ± 1.4
M511.1	Matrix	0.85	1.8792 ± 0.0071	0.01844 ± 0.00026	0.1212 ± 0.0035	0.487	0.0477 ± 0.0012	116.2 ± 3.5	121.9 ± 1.4	117.8 ± 1.6
M511.2	Matrix	1.64	2.8322 ± 0.0155	0.01809 ± 0.00019	0.1076 ± 0.0037	0.315	0.0431 ± 0.0014	103.7 ± 3.7	118.8 ± 1.4	115.6 ±1.2
M511.3	Matrix	0.87	1.6847 ± 0.0056	0.01849 ± 0.00021	0.1166 ± 0.0025	0.523	0.0457 ± 0.0008	112.0 ± 2.5	120.5 ± 1.2	118.1 ± 1.3
M516.1	Matrix	1.16	2.4401 ± 0.0182	0.01823 ± 0.00030	0.1136 ± 0.0048	0.384	0.0452 ± 0.0018	109.3 ± 4.9	119.5 ± 1.5	116.4 ± 1.9
M516.2	Matrix	0.72	1.6676 ± 0.0107	0.01849 ± 0.00029	0.1183 ± 0.0033	0.557	0.0464 ± 0.0011	113.5 ± 3.4	120.1 ± 1.5	118.1 ± 1.8
M516.3	Matrix	1.57	3.1407 ± 0.0110	0.01821 ± 0.00021	0.1101 ± 0.0035	0.365	0.0439 ± 0.0013	106.1 ± 3.5	118.6 ± 1.2	116.3 ± 1.8

[a]Spot: M157.2 = 2nd spot on monazite grain #157.

[b]Texture: location of monazite as inclusion in St, Ky, Crd, or as a matrix grain (|| = elongate monazite grain parallel to foliation).

[c]f(206)^{207} refers to the fraction of total ^{206}Pb that is common Pb, calculated using the ^{204}Pb-method.

[d] *Radiogenic Pb (corrected for common Pb using the ^{204}Pb-method).

[e]Ages have been corrected for common Pb using the ^{204}Pb-method.

[f] ^{207}Pb/^{235}U age is poorly constrained due to the low abundance of ^{207}Pb in young monazite.

[g]Uncertainties reported at 1σ (absolute) and are calculated by numerical propagation of all known sources of error (Stern & Berman, 2000).

2.8.2. Geochronologic Results

A plot of the monazite SHRIMP data for sample 4 on a conventional (Wetherill) U-Pb concordia diagram reveals a reverse discordance exhibited by some monazite analyses (Fig. 2.8d). Excess ^{206}Pb due to incorporation of ^{230}Th into monazite at the time of crystallization will lead to an overestimation of $^{206}Pb/^{238}U$ ages and reverse discordance paralleling the $^{206}Pb/^{238}U$ axis on conventional U-Pb concordia diagrams (Schärer, 1984). Our data show a subtle trend of increasing reverse discordance with increasing $^{208}Pb/^{206}Pb$ (the radiogenic proxy of Th/U), which indicates that to some minor degree the reverse discordance may be the result of excess ^{206}Pb due to ^{230}Th disequilibrium. Unfortunately the $^{208}Pb/^{232}Th$ chronometer, which is ideal for monazite since it is not known to be affected by isotopic disequilibrium (i.e., unsupported ^{206}Pb), cannot be used in this study because one of the three monazite standards routinely yielded a high Th-Pb age possibly due to an indeterminate matrix effect. This creates an unquantifiable uncertainty in the Th-Pb ages for the monazite. However, this problem seems to have affected only 1/3 of the standards, so it is likely some, or possibly all, of the monazite unknowns were similarly unaffected. Consequently, given that the $^{206}Pb/^{238}U$ ages are consistently younger than $^{208}Pb/^{232}Th$ ages (Table 2.6) would suggest these grains do not contain significant excess ^{206}Pb. Additionally, when applying the excess ^{206}Pb correction of Schärer (1984) it at most produces an excess in age of 1.2 – 1.9 Ma, which is no greater than analytical error, even for monazite that grew from a metamorphic fluid with extremely low Th/U (0.3 - 0.7) and had a large amount of Th fractionation. Thus, despite any minor excess of ^{206}Pb, we are confident the $^{206}Pb/^{238}U$ ages will provide reasonably accurate constraints within the resolution required for this study to differentiate the metamorphic and deformation events.

We can infer a further reduction in the significance of the contribution of excess ^{206}Pb to reverse discordance based on analyses from sample 4. These analyses do not plot in a vertical trend above concordia, as would be expected if the reverse discordance was due to excess ^{206}Pb. Rather, the analyses trend to the left of concordia parallel to the $^{207}Pb/^{235}U$ axis (Fig. 2.8d). This trend is interpreted to be largely the result of an overcorrected $^{207}Pb/^{235}U$ ratio using the ^{204}Pb method. The errors arising from low ^{204}Pb counts, background interference and a 204 isobar, can overcorrect for common Pb, which most adversely affects young samples with relatively low concentrations of ^{207}Pb.

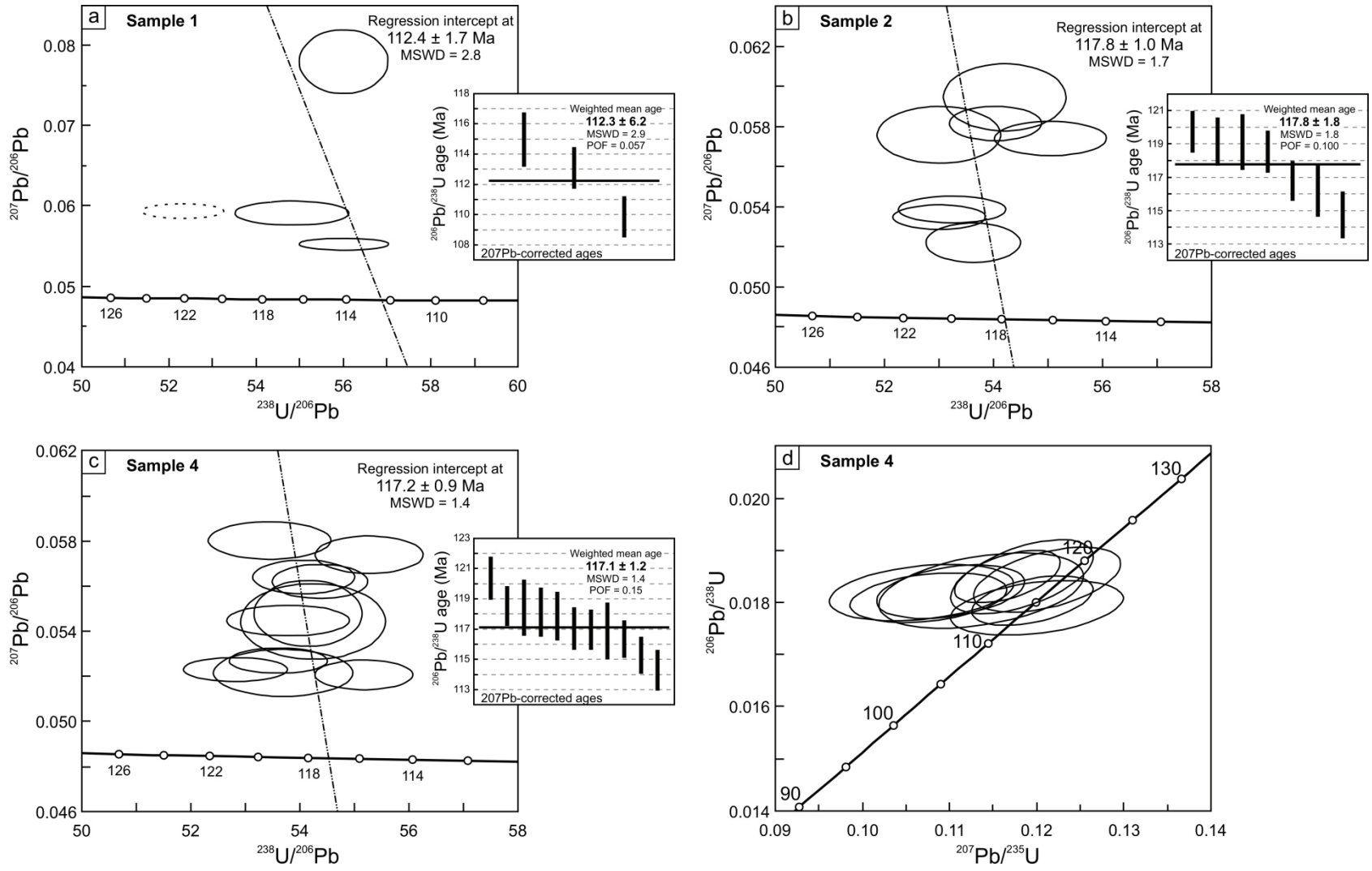
a
Sample 1
Regression intercept at
112.4 ± 1.7 Ma
MSWD = 2.8
Weighted mean age
112.3 ± 6.2
MSWD = 2.9
POF = 0.057
207Pb-corrected ages
b
Sample 2
Regression intercept at
117.8 ± 1.0 Ma
MSWD = 1.7
Weighted mean age
117.8 ± 1.8
MSWD = 1.8
POF = 0.100
207Pb-corrected ages
c
Sample 4
Regression intercept at
117.2 ± 0.9 Ma
MSWD = 1.4
Weighted mean age
117.1 ± 1.2
MSWD = 1.4
POF = 0.15
207Pb-corrected ages
d
Sample 4
207Pb/206Pb
238U/206Pb
206Pb/238U age (Ma)
206Pb/235U age (Ma)
206Pb/238U
207Pb/235U

Figure 2.8. U-Pb isotopic plots for samples 1, 2 and 4. (a-c) Tera–Wasserburg plots for samples 1, 2 and 4 showing isotopic data uncorrected for common Pb. Regression is fitted through a Late Cretaceous common Pb isotopic composition (Stacey & Kramers, 1975). Dashed ellipse excluded from the regression (see text for discussion). Error ellipses represent 1σ level of uncertainty. Inset shows distribution of (207Pb-corrected) 206Pb/238U ages, with error bars at 1σ. Bold horizontal line is reference mean age. (d) Concordia plot for monazite from sample 4. Note the horizontal trend parallel to the 207Pb/235U axis in the discordant data.

For the sake of thoroughness, the analyses were corrected for common Pb based on the ^{207}Pb (Table 2.5) and ^{204}Pb (Table 2.6) methods following the procedure of Stern & Berman (2000) and Ireland & Gibson (1998). The two correction methods yield ages indistinguishable within error. However, all things considered, the ^{206}Pb/^{238}U chronometer corrected using the ^{207}Pb method is thought to provide the most meaningful ages for this study; accordingly, all ages quoted and displayed on Tera-Wasserburg concordia diagrams (Fig. 2.8a-c) are based on the ^{206}Pb/^{238}U chronometer.

Sample 1

Analyses of monazite within sample 1 were obtained on a single matrix grain, as well as two monazite crystals that occur together with plagioclase and euhedral staurolite within replacement textures inside garnet (Fig. 2.9a,b). Elongated matrix monazite are consistently aligned parallel to S_T. The matrix grain, monazite 131 (Fig. 2.9c), is acicular, measuring < 35 μm in shortest dimension and up to 165 μm in the longest dimension, and is approximately parallel to the foliation (S_T). Monazite 131 has a broad, uniform low Y (<700 ppm) core surrounded by a thin (<5 μm) Y-depleted zone, and a thin (<5 μm) Y-rich rim. A single spot analysis of the low-Y core of this matrix monazite yields an age of 120.4 ± 1.4 Ma. Grain 102 (Fig. 2.9a) is a subhedral, 20 x 45 μm grain that occurs with plagioclase and euhedral staurolite within a resorption ring between Grt-1 and -2. Grain 102 has a uniform, moderate-Y (700-1500 ppm) core and high-Y (2000-3400 ppm) rim, with a sharp boundary between the two zones. Spot analyses of the moderate-Y core and high-Y rim yield ages of 115.0 ± 1.8 Ma and 109.9 ± 1.4 Ma, respectively. Grain 9 (Fig. 2.9b) is a subhedral, 30 x 50 μm grain that occurs together with plagioclase and euhedral staurolite within a resorbed hole inside Grt-1. Monazite 9 has a fairly uniform moderate-Y concentration (1000-2000 ppm), and a very

thin (<5 μm) high-Y (3500-4000 ppm) rim. A single analysis from the center of grain 9 yields a $^{206}Pb/^{238}U$ age of 113.1 ± 1.4 Ma.

Sample 2

Analyses of monazite within sample 2 were obtained on three inclusions within two different staurolite porphyroblasts (Fig. 2.9d,e), and a single matrix grain. Two of the monazite inclusions within staurolite are anhedral to subhedral grains that are ~30 x 100 μm. The third inclusion within staurolite is very elongated, ~160 μm in the longest dimension oriented roughly parallel to a weakly defined and statically overprinted external foliation (S_T). Only one of the three inclusions within staurolite is intersected by a very fine micro-crack (Fig. 2.9e). X-ray mapping revealed three distinct compositional domains within monazite included in staurolite and in the matrix: (i) moderate-Y, high-Th core; (ii) an intermediate low-Y, low-Th zone; and (iii) high-Y, moderate-Th rim. Despite the different textural positions and discrete chemical domains, both the core and outer high-Y rim yield a restricted range of ages between 119.7 ± 1.3 Ma and 114.7 ± 1.4 Ma (see Table 2.5) that are interpreted to form a single population with a weighted mean age of 117.8 ± 1.7 (MSWD = 1.8) (Fig. 2.8b).

Sample 4

Analyses of monazite from sample 4 were obtained on one inclusion in kyanite, two inclusions in cordierite and two matrix grains. Monazite inclusions within cordierite and syn-kinematic kyanite are elongate, euhedral to subhedral grains, > 30 μm in the shortest dimension and up to 200 μm in the longest dimension. Elongate monazite inclusions within kyanite and cordierite, as well as matrix grains, are aligned parallel to S_T, which is defined by the rutile trains and aligned kyanite and staurolite (Fig. 2.9f). All monazite grains, regardless of textural location, show similar concentrations and compositional zoning patterns characterized by a Y-rich (12000-18000 ppm) core surrounded by a uniform zone relatively depleted in Y (6000-10000 ppm) (Fig. 2.9g-j). This Y zoning is mimicked by Th. In spite of the observed textural and chemical differences described here, all eleven analyses of these five monazite grains form a single population with a weighted mean $^{206}Pb/^{238}U$ age of 117.1 ± 1.2 Ma (MSWD = 1.4) (Fig. 2.8c).

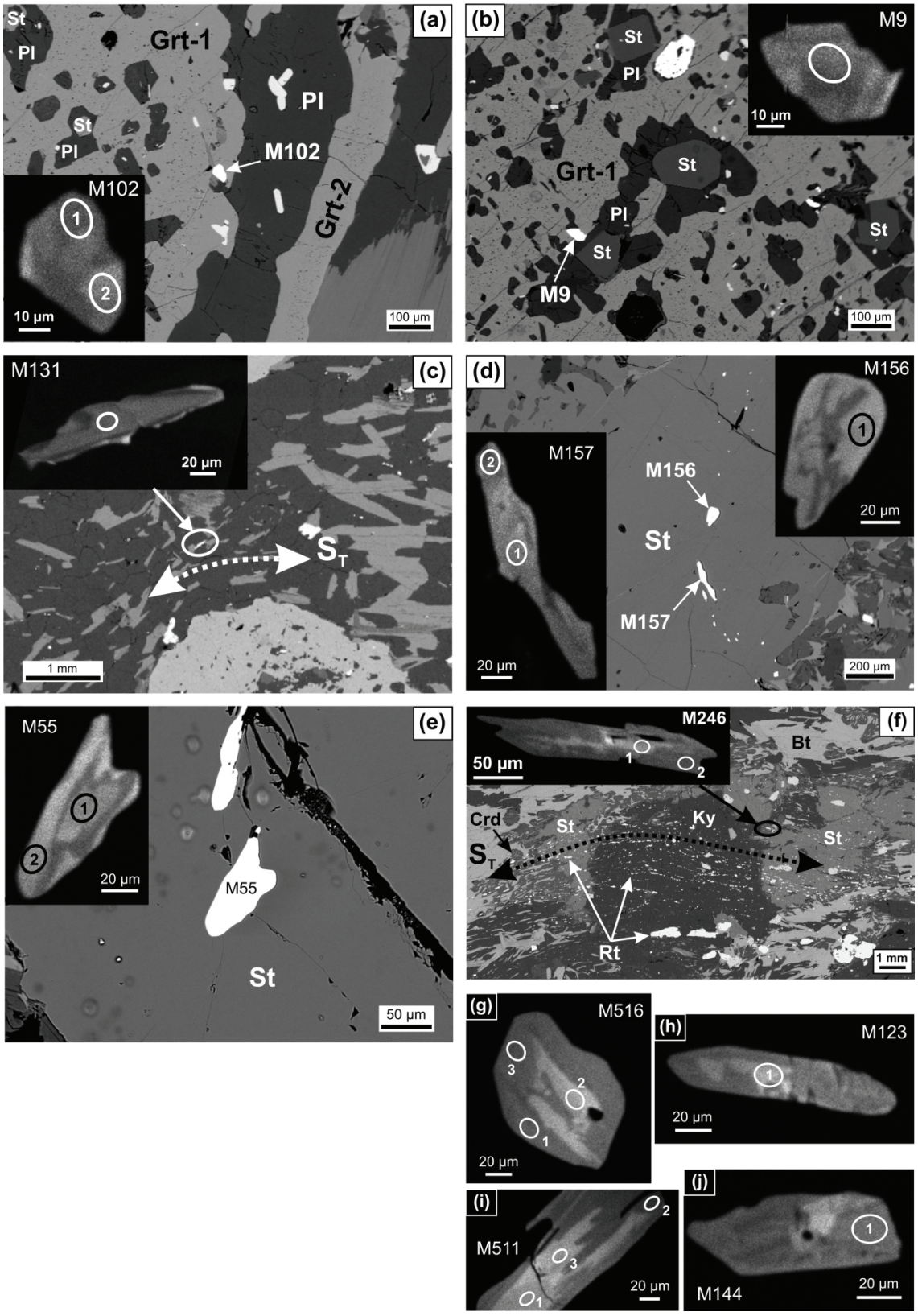
(a)
St
Pl
Grt-1
Pl
St
Pl
M102
Grt-2
M102
1
2
10 µm
100 µm
(b)
M9
St
Pl
10 µm
Grt-1
St
Pl
St
St
M9
100 µm
M131
20 µm
(c)
S$_T$
1 mm
(d)
M156
M157
1
20 µm
2
M157
M156
St
1
M157
20 µm
200 µm
M55
1
2
20 µm
(e)
M55
St
50 µm
M246
50 µm
1
2
(f)
Bt
Crd
St
Ky
St
S$_T$
Rt
1 mm
(g)
M516
3
2
1
20 µm
(h)
M123
1
20 µm
(i)
2
M511
3
1
20 µm
(j)
1
M144
20 µm

Figure 2.9. SEM backscattered images of monazite and the surrounding area in samples 1, 2 and 4. Ellipses on inset Yttrium (Y) X-ray maps of monazite show the location of SHRIMP analysis spots. Lighter shades of grey on Y maps indicate relatively higher concentration. (a) M102 and (b) M9, both associated with staurolite and plagioclase within heavily resorbed garnet porphyroblasts in sample 1. (c) Elongate matrix monazite M131 aligned near parallel to the transposition foliation (ST). (d) M156 and M157, and (e) M55, within staurolite from sample 2. (f) Elongate monazite, M246, aligned parallel to the relict transposition foliation (ST) in sample 4, which is defined by rutile trains within the matrix, and as inclusion trains within porphyroblasts of kyanite, staurolite and cordierite. (g-j) Y maps of monazite grains from sample 4.

Contrary to samples 1 and 2, there is no high-Y rim observed on monazites from sample 4. This is interpreted to be due to the relatively small amount of garnet observed in sample 4. In this garnet poor sample there would not be a significant amount of Y tied up in garnet, nor excess Y released upon garnet breakdown.

2.8.3. Interpretation of Geochronologic Data – Constraining a Cretaceous P-T path

It is unlikely that the monazite ages have been reset by diffusive Pb loss. Based on experimentally determined diffusion parameters, Cherniak *et al*. (2004) and Gardés *et al*. (2006) have determined that monazite would have to be exposed to temperatures greater than 800 °C for a geologically unrealistic length of time for there to be any appreciable Pb loss, and predict closure temperatures comparable to zircon (i.e. 900 °C). These conclusions are consistent with numerous observations of sharp boundaries between domains of contrasting Pb concentrations, and the preservation of significantly older ages through younger granulite facies metamorphic events (e.g. DeWolf *et al*., 1993; Spear & Parrish, 1996; Braun *et al*., 1998; Cocherie *et al*., 1998; Crowley & Ghent, 1999; Zhu & O'Nions, 1999). Given the peak temperature estimates for these samples (~ 650-680 °C), we interpret that these grains have not been reset due to Pb loss by thermally-activated volume diffusion.

More plausibly, several studies (Seydoux-Guillaume *et al*., 2002; Harlov & Hetherington, 2010; Hetherington *et al*., 2010; Harlov *et al*., 2011; Williams *et al*., 2011) have shown that monazite ages may be reset by fluid-assisted coupled dissolution-

reprecipitation, which may operate at temperatures well below the closure temperature of monazite. Unlike the matrix grains, monazite inclusions in staurolite are shielded from an intergranular fluid, and should therefore retain their primary metamorphic age. However, if monazite inclusions in staurolite are intersected by a microcrack within the third dimension, this could provide a pathway for fluid assisted dissolution, reprecipitation and Pb loss. Williams *et al*. (2011) examined the resetting of monazite ages during fluid-related coupled dissolution-reprecipitation, and observed that altered rims yield a scattering of reset ages, whereas the age of unaltered monazite cores were largely unaffected. Contrary to the results of Williams *et al*. (2011), the ages obtained from distinct core-rim compositional domains of monazite inclusions in staurolite from this study (Fig. 2.9e) agree within error (Table 2.5), leaving no indication that these grains have been affected by fluid-assisted coupled dissolution-reprecipitation. Ages from these grains are therefore interpreted as primary metamorphic ages. Furthermore, because monazite both in the matrix and included in staurolite yield a single age population, we interpret matrix monazite to also preserve their primary metamorphic age.

Timing of Stage-2 Metamorphism and Deformation

Nineteen $^{206}Pb/^{238}U$ analyses from all 11 monazite grains (excluding the Y-rich monazite within resorbed Grt-2 of sample 1) yield a single age population at 117.5 ± 0.9 Ma (MSWD = 1.7). The incorporation of *c.* 118 Ma monazite within syn- to post-kinematic, stage-2 porphyroblasts of staurolite and kyanite indicates this population of monazite grew prior to, or synchronous with, these near-peak stage-2 porphyroblasts. As discussed below, slightly younger ages (*c.* 112 Ma) from distinct, Y-rich monazite within resorbed portions of both stage-1 and -2 garnet of sample 1, are interpreted to have formed as garnet broke down during the onset of decompression following the peak of stage-2 metamorphism. The absence of monazite included in stage-1 garnet, and the limited time between prograde metamorphism (*c.* 118 Ma) and stage-2 decompression (*c.* 112 Ma) suggest it is unlikely the *c.* 118 Ma monazite population grew during stage-1 metamorphism. Instead the *c.* 118 Ma monazite population is interpreted to date stage-2 prograde metamorphism. Furthermore, the common alignment of monazite parallel to S_T in the matrix (Fig. 2.9c,f), and its inclusion in syn- to post-S_T porphyroblasts of staurolite and kyanite, suggests monazite grew during the waning phase of protracted development of S_T during prograde stage-2 metamorphism.

The partially syn-kinematic nature of both Grt-1 and stage-2 staurolite and kyanite porphyroblasts with respect to S_T, suggests S_T is a composite D_1/D_2 transposition foliation in the sense of Williams (1983) and Tobisch & Paterson (1988). The presence of intrafolial isoclinal folds suggests this composite transposition foliation developed by isoclinal folding and rigid body rotation of the older D_1 foliation into parallelism with the new D_2 foliation, such that the elements defining the new foliation (S_T) are inherited from the old foliation (*cf.* Williams, 1983).

Approximately 1.2 km to the east of sample 2, slightly older Early Cretaceous dates were obtained by Berman *et al*. (2007a), who calculated an average $^{206}Pb/^{238}U$ age of 146 ± 3 Ma from 3 different monazite grains (sample 4 of Berman *et al*., 2007a). Berman *et al*. interpreted these grains as primary inclusions within post-kinematic staurolite porphyroblasts that grew during a high-P (~ 9 kbar) metamorphic event. The *c*. 117.5 ± 0.9 Ma age determined in this study records the time at which these samples passed through the monazite growth reaction, which is a function of pressure, temperature and the bulk composition. Given the considerable chemical variability between sample 4 of Berman *et al*. (2007a) (Ca/Na = 0.14) and that of samples 2 (Ca/Na = 0.56) and 4 (Ca/Na = 0.99) of this study, there is no reason to expect that the monazite-producing reactions were the same between the two studies. Nor should we expect that the reactions were operating under the same pressure temperature conditions, and hence time. For example, Fitzsimons *et al*. (2005) demonstrate that variations in the evolving metamorphic mineral assemblages, between samples of contrasting composition in AFM space, resulted in the growth and preservation of monazite from different metamorphic reactions and under considerably different *P-T* conditions (e.g. greenschist vs. amphibolite facies). Janots *et al*. (2008) also found that monazite stability is sensitive to bulk composition. In their study of the stability and phase relations between allanite and monazite, Janots *et al*. (2008) offered the following generalized prograde reaction:

Allanite + apatite + Al-Fe-Mg phases1 = monazite + anorthite + Al-Fe-Mg phases2

Janots *et al*. (2008) suggested that metapelites with a high Ca/Na ratio, and subsequently high anorthite activity in plagioclase, would shift the above equilibrium to the right, stabilizing allanite to higher temperature. Given the considerably higher Ca/Na

and X_{An} contents from samples of the present study versus that of sample 4 of Berman *et al*. (2007a), it follows from Janots *et al*. (2008) that the monazite-after-allanite equilibrium would occur at higher temperatures in rocks of this study. Consequently, monazite in our study should yield younger ages for rocks following a clockwise *P-T* path, precisely as observed. We therefore interpret that prograde metamorphism may have occurred between 146 and 118 Ma in this region. Such protracted metamorphism, ~28 m.y., does not seem unreasonable considering recent work which document a 25 m.y. duration of eclogite facies conditions (Mattison *et al*., 2006), and prograde garnet growth sustained over a 25 to 40 m.y. interval (Skora *et al*., 2009; Cheng *et al*., 2011).

Timing of Stage-2 Retrogression and Exhumation

Monazite grains M9 and M102 in sample 1 occur within resorbed portions of garnet associated with post-kinematic staurolite, and yield a weighted mean age of 112.3 ± 6.2 Ma (MSWD = 2.9) (Fig. 2.8a). This age is nominally younger than the 120.4 ± 1.4 Ma matrix monazite, but the difference is considered significant given their distinctly higher yttrium content (~ 1000-10000 ppm Y) compared to the older matrix monazite (<500 ppm). Bea & Montero (1999) and Pyle & Spear (1999) have determined that garnet and xenotime are the only significant reservoirs of yttrium in metapelitic rocks, and that the growth of garnet is accompanied by the consumption of xenotime. Given the large volume of garnet in these rocks, it follows that the majority of yttrium resides within garnet. Therefore, we interpret that the high-Y, younger monazite formed during the release of yttrium accompanying breakdown of garnet (e.g. Pyle & Spear, 1999; Foster *et al*., 2002), which is interpreted to have occurred during decompression from the stage-2 metamorphic peak (~ 650-680 °C and 9 kbar) into the staurolite stability field. This conclusion is supported by the occurrence of 114.3 ± 1.3 Ma monazite within cordierite, which is constrained by phase relationships to have crystallized below ~ 5 kbar (Fig. 2.6) after *c.* 114 Ma. It is also consistent with results from 7-12 km northwest of sample 1, where 115-107 Ma relatively Y-rich monazite in two rocks formed during garnet resorption and re-equilibration at pressures less than 6 kbar (Berman *et al*., 2007a). Finally, we note that these younger ages directly linked to decompression from peak stage-2 metamorphism further support our interpretation that the older ages (*c.* 118 Ma) for monazite inclusions within staurolite and kyanite date the prograde history of the ~ 9 kbar stage-2 metamorphic event.

2.9. Tectonic Implications

Previous work in the Yukon-Tanana terrane of easternmost Alaska and west-central Yukon suggest the terrane was strongly transposed and metamorphosed to amphibolite facies in the Permo-Triassic (Dusel-Bacon *et al*., 1995, 2002; Berman *et al*., 2007a; Beranek & Mortensen, 2011), followed by a metamorphic overprint in the Early Jurassic before being exhumed to upper crustal levels in the Early to Middle Jurassic (Dusel-Bacon *et al*., 1995, 2002; Hansen & Dusel-Bacon, 1998; Berman *et al*., 2007a). However, the results of this study, together with the work of Berman *et al*. (2007a), indicate a more protracted and heterogeneous tectono-thermal history for the Yukon-Tanana terrane. In particular, rocks in this part of west-central Yukon appear to be stratigraphically correlative with, and share a similar structural style, deformation sequence, and metamorphic grade as the surrounding Permian to Early Jurassic metamorphic domain. However, the Australia Mountain domain records a transposition event associated with burial and metamorphism to 8 –10 kbar and 650 – 680 °C in the Early to mid-Cretaceous (*c.* 146-118 Ma), which is not recorded in the surrounding Permian to Early Jurassic metamorphic domain. These observations require that the Australia Mountain domain occupied a deeper crustal level in the Early to mid-Cretaceous than the surrounding Permian to Early Jurassic metamorphic domain, and therefore provides a window into the Early to mid-Cretaceous infrastructure of the orogen in west-central Yukon. We apply the term 'infrastructure' in a similar sense to that suggested by De Sitter & Zwart (1960) and Culshaw *et al*. (2006) when describing mid- to lower-crustal levels in an orogen characterized by high-grade, shallowly dipping, ductiley deformed and transposed rocks. Conversely, the overlying 'superstructure' would be characterized by upright, brittle structures and low-metamorphic grade. For us, this rheological contrast between upper and lower crustal levels is time specific, in our case, the Early to mid-Cretaceous. We make this distinction because, as explained above, rocks formerly situated in the lower crust, the infrastructure, were progressively exhumed in the Jurassic and were incorporated into the superstructure above the Early to mid-Cretaceous infrastructure.

Our study indicates a pattern of structurally downward younging deformation and metamorphism in the Yukon-Tanana terrane, similar to what has been described in the

southeastern Cordillera (Carr, 1991; Parrish, 1995, Crowley *et al*., 2000; Gibson *et al.,* 2005). There, rocks buried, heated and exhumed in the Jurassic (Archibald *et al*., 1983; Brown *et al*., 1992; Colpron *et al*., 1996; Gibson *et al*., 2005), are now juxtaposed against structurally deeper rocks that were progressively buried and heated from Cretaceous to earliest Eocene (Brown & Carr, 1990; Carr, 1991; Parrish, 1995; Gibson *et al*., 1999, 2005; Crowley & Parrish, 1999; Crowley *et al*., 2000). Parrish (1995), Brown (2004), and Gibson *et al.* (2008) have all attributed this downward younging tectonism in the southeastern Canadian Cordillera to the progressive incorporation and burial of material as the burgeoning orogen propagated northeastward toward the foreland.

Monazite from this study dated at *c.* 112 Ma record the terminus of metamorphism and onset of near isothermal decompression and exhumation of deep seated metamorphic rocks of the Australia Mountain domain. Exhumation of this domain in the mid-Cretaceous is substantiated by the presence of metamorphic detritus (quartz with undulatory extinction, and lesser amounts of muscovite, feldspar, and foliated lithic fragments) in the mid-Cretaceous (Albian) Indian River Formation (Lowey & Hills, 1988), approximately 35 km to the west. An isothermal decompression path alone may not be sufficient to distinguish between normal faulting and erosion as the dominant mechanism of exhumation (Ring *et al.,* 1999). However, the abrupt juxtaposition of the Cretaceous metamorphic domain at Australia Mountain against rocks with Early to Middle Jurassic cooling ages (Hunt & Roddick, 1992) strongly suggests the Australia Mountain domain is bound on its west side by a mid-Cretaceous normal fault, herein named the Australia Creek fault (Figs 2.2 & 2.10). Likewise, the juxtaposition of the Australia Mountain domain to the southeast against largely undeformed and unmetamorphosed rocks of the Mississippian Reid Lakes complex is interpreted to have been accommodated along a normal fault, herein named the Stewart River fault (Figs 2.2 & 2.10). Both of these faults are interpreted to have accommodated a significant amount of extensional exhumation in the mid-Cretaceous. Unfortunately, poor exposure in the area of the proposed faults has prevented the identification of corroborating deformation fabrics. Rather, the position of the fault is constrained by the jump in thermochronometric ages, the presence of a distinct discontinuity in aeromagnetic data for this region (Hayward *et al*., 2012), and differences in lithologies (Permian Klondike schist present on west side of fault, abundant pre-late Devonian marble unit east of the fault).

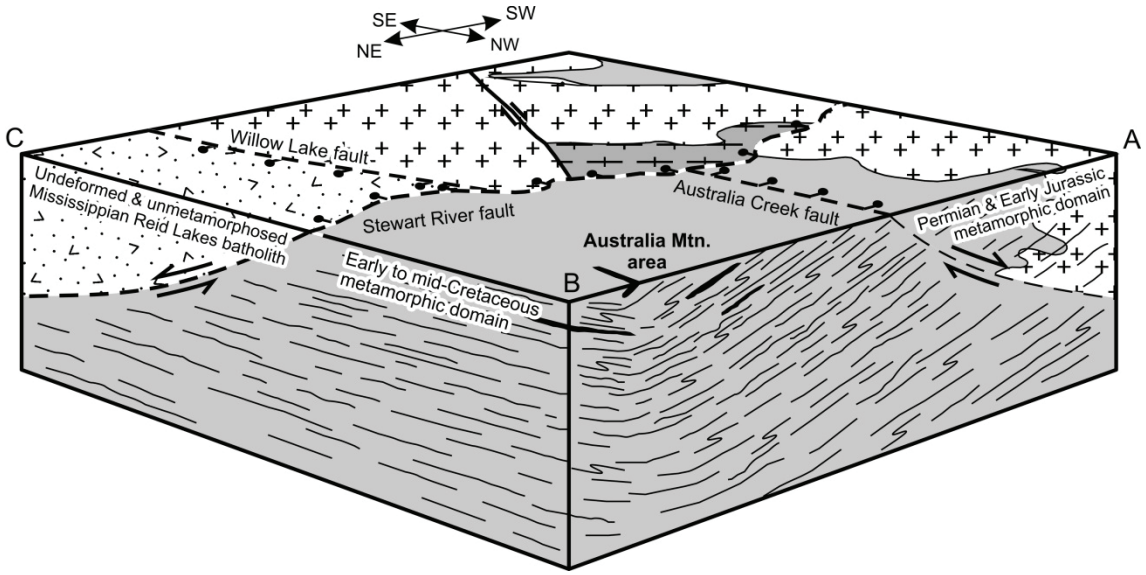

Figure 2.10. Schematic block diagram depicting the Cretaceous metamorphic domain (core complex?) at Australia Mountain, juxtaposed against the Mississipian Reid Lake plutonic complex and the Permian and Early Jurassic metamorphic domain by the Stewart River and Australia Creek faults. View is to the south. Location of cross-section lines indicated on Figure 2.2. Fill patterns are in legend of Figure 2.2.

Some 100 km to the west of Australia Mountain, rocks in east-central Alaska also record a shift to extensional tectonics in the mid-Cretaceous. The majority of metamorphic rocks in east-central Alaska are parautochthonous North American continental margin rocks with top-down-to-the-southeast shear fabrics and mid-Cretaceous cooling ages (Pavlis *et al.,* 1993; Hansen & Dusel-Bacon, 1998; Dusel-Bacon *et al.,* 2002). These amphibolite facies rocks with mid-Cretaceous $^{40}Ar/^{39}Ar$ and K-Ar cooling ages are juxtaposed across mylonitic shear zones against greenschist to amphibolite facies allochthonous rocks of Yukon-Tanana terrane with Early Jurassic cooling ages. Hansen & Dusel-Bacon (1998) and Dusel-Bacon *et al*. (2002) interpret the top-down-to-the-southeast mylonitic shear zones to have formed during exhumation of the parautochthonous rocks from beneath the structurally overlying allochthonous Yukon-Tanana terrane.

The Cretaceous metamorphic domain in the Australia Mountain area likewise represents a window through a Cretaceous superstructure, with a Palaeozoic to Jurassic metamorphic and deformational history, revealing a much younger amphibolite facies

Cretaceous infrastructure. Late Devonian (*c.* 363 Ma, Mortensen, 1990) and Early Mississippian (*c.* 348 Ma, Ruks *et al*., 2006) U-Pb ages from the Mount Burnham orthogneiss within the Australia Mountain domain are consistent with igneous activity known in both parautochthonous North American margin rocks and allochthonous Yukon-Tanana terrane in east-central Alaska as described by Dusel-Bacon *et al*. (2006). However, if the Australia Mountain domain is of parautochthonous North American continental margin affinity, then the Australia Creek fault represents a major terrane bounding extensional fault analogous to coeval mid-Cretaceous extensional faults described by Hansen & Dusel-Bacon (1998) and Dusel-Bacon *et al*. (2002) in east-central Alaska. Exhumation of structurally deep parautochthonous continental rocks from beneath the structurally overlying Yukon-Tanana terrane is highly conceivable considering that 25-30 km of crustal section (equivalent to the 9 kbar stage-2 peak metamorphic estimate) was removed in the middle Cretaceous following an earlier episode of exhumation of the Yukon-Tanana terrane in the Early Jurassic.

The Cretaceous domains at Australia Mountain and in east-central Alaska may be akin to the extensional core complexes identified throughout the North American Cordillera (Coney, 1980; Armstrong, 1982; Coney & Harms, 1984; Parrish, 1988; Struik, 1993), both in style and geological process. However, Cretaceous extensional exhumation in the northern Cordillera is distinctly older than the Eocene extension recorded in core complexes in the southern Canadian Cordillera and northwestern U.S. (Parrish, 1988), and the Oligocene-Miocene extension in southwestern U.S. (Coney, 1980).

2.10. Conclusions

Garnet growth zoning patterns within compositionally distinct inclusion-rich core and inclusion-poor rim domains, separated by an abrupt chemical discontinuity, are interpreted with the aid of modelled compositional and molar isopleths to record a two-stage garnet growth history, each reflective of a distinct metamorphic event. The early stages of growth of the inclusion-rich, stage-1 core (Grt-1) is interpreted to have initiated at conditions of approximately 600 °C, 8 kbar along a clockwise *P-T* path synchronous with the development of the external composite transposition foliation (S_T). Due to an

absence of monazite inclusions within stage-1 garnet cores, this event remains undated. Growth of the relatively grossular-rich, pyrope-poor stage-2 overgrowth (Grt-2) is interpreted to have initiated at higher P, and/or lower T, than Grt-1, culminating at near-thermal peak *P-T* conditions of approximately 650-680 °C and 9 kbar. These peak thermobarometric estimates calculated from the composition of the rim of post-kinematic stage-2 garnet overgrowths (Grt-2) are consistent with the presence of syn- to post-kinematic kyanite, and require only minimal reaction overstepping (< 20 °C) to explain the presence of syn- to post-kinematic staurolite. *In situ* U-Th-Pb SHRIMP dating of elongate monazite aligned with S_T in the matrix, and monazite included in syn- to post-kinematic, stage-2 porphyroblasts of staurolite and kyanite yield a single age population *c*. 117.5 ± 0.9 Ma. This age is interpreted to date the waning development of a reworked composite transposition foliation during stage-2 prograde metamorphism. These data, together with the data from Berman *et al*. (2007a), record a *c.* 146-118 Ma, 9 kbar amphibolite facies metamorphic and deformational event in the Australia Mountain area of west-central Yukon. However, contrary to the interpretation of Berman *et al*. (2007a), the younger mid-Cretaceous monazite ages (*c.* 112 Ma, this study; 114-107 Ma, Berman *et al*., 2007a) are not interpreted to date a distinct low-P contact metamorphic event. Rather, the presence of consistently young, Y-rich monazite, intimately associated with retrograde staurolite and plagioclase within resorbed portions of garnet, is interpreted to date the timing of garnet breakdown during decompression from the peak of metamorphism following the stage-2 garnet growth event. The results presented above indicate that in contrast to the majority of the Yukon-Tanana terrane, which was deformed and metamorphosed in the Permo-Triassic and exhumed to upper crustal levels in the Jurassic, the Australia Mountain domain occupied a deep crustal level (~ 25–30 km) in the Early to mid-Cretaceous. This area therefore represents a tectonic window into Early to -mid Cretaceous infrastructure of the Yukon-Tanana terrane, potentially comparable to parautochthonous North American continental margin rocks beneath the Yukon-Tanana terrane in east-central Alaska, and may be akin to, but older than, extensional core complexes identified throughout the North American Cordillera.

2.11. References

Aranovich, L. Ya., 1991. Mineral Equilibria of Multicomponent Solid Solutions. Nauka Press, Moscow.

Archibald, D. A., Glover, J. K., Price, R. A., Farrar, E. & Carmichael, D. M., 1983. Geochronology and tectonic implications of magmatism and metamorphism, southern Kootenay Arc and neighbouring regions, southeastern British Columbia. Part I: Jurassic to mid-Cretaceous. Canadian Journal of Earth Sciences, **20,** 1891–1913.

Armstrong, R.L., 1982. Cordilleran metamorphic core complexes—From Arizona to southern Canada. Annual Review of Earth and Planetary Science Letters, **10,** 129–154.

Asworth, J.R. & Evirgen, M.M., 1985. Plagioclase relations in pelites, central Menderes Massif, Turkey. II. Perturbation of garnet-plagioclase geobarometers. Journal of Metamorphic Geology, **3,** 219–229.

Bea, F. & Montero, P., 1999. Behavior of accessory phases and redistribution of Zr, REE, Y, Th, and U during metamorphism and partial melting of metapelites in the lower crust: an example from the Kinzigite Formation of Ivrea–Verbano, NW Italy. Geochimica et Cosmochimica Acta, **63,** 1113– 1153.

Beranek, L.P. & Mortensen, J.K., 2011. The timing and provenance record of the Late Permian Klondike orogeny in northwestern Canada and arc-continent collision along western North America. Tectonics, **30**: TC5017, doi:10.1029/2010TC002849.

Berman, R. G., 1991. Thermobarometry using multi-equilibrium calculations: a new technique, with petrological applications. Canadian Mineralogist, **29,** 833–855.

Berman, R.G. 2007. winTWQ (version 2.3): A Microsoft Windows-compatible software package for performing internally-consistent thermobarometric calculations. Geological Survey of Canada Open File, 5462.

Berman, R., Sanborn-Barrie, M., Stern, R. & Carson, C., 2005. Tectonometamorphism at c. 2.35 and 1.85 Ga in the Rae domain, western Churchill Province, Nunavut, Canada: insights from structural, metamorphic and in situ geochronological analysis of the southwestern Committee Bay belt. Canadian Mineralogist, **43,** 409–442.

Berman, R.G., Ryan, J.J., Gordey, S.P. & Villeneuve, M., 2007a. Permian to Cretaceous polymetamorphic evolution of the Stewart River region, Yukon-Tanana terrane, Yukon, Canada: P-T evolution linked with in-situ SHRIMP monazite geochronology. Journal of Metamorphic Geology, **25,** 803–827.

Berman, R.G., Aranovich, L.Ya, Rancourt, D.G. & Mercier, P.H.J., 2007b. Reversed phase equilibrium constraints on the stability of Mg-Fe-Al biotite. American Mineralogist, **92,** 139–150.

Berman, R.G., Sanborn-Barrie, M., Rayner, N., Carson, C., Sandeman, H.A., & Skulski, T., 2010. Petrological and in situ SHRIMP geochronological constraints on the tectonometamorphic evolution of the Committee Bay belt, Rae Province, Nunavut. Precambrian Research, **181,** 1–20.

Berman, R.G., Rayner, N., Sanborn-Barrie, M. and Whalen, J., 2012. The tectonometamorphic evolution of Southampton Island, Nunavut: insight from petrologic modeling and in situ SHRIMP geochronology of multiple episodes of monazite growth. Precambrian Research (in press).

Braun, I., Montel, J.M. & Nicollet, C., 1998. Electron microprobe dating of monazites from high-grade gneisses and pegmatites of the Kerala Khondalite Belt, southern India. Chemical Geology, **146,** 65–85.

Brown, R.L., 2004. Thrust-belt accretion and hinterland underplating of orogenic wedges: An example from the Canadian Cordillera. In: Thrust Tectonics and Hydrocarbon Systems (Ed. McClay, K.R.) American Association of Petroleum Geologists (AAPG) Memoir 82, p. 51–64.

Brown, R.L. & Carr, S.D., 1990. Lithospheric thickening and orogenic collapse within the Canadian Cordillera. Proceedings of the Pacific Rim 90 Congress, Australian Institute of Mining and Metallogeny, **2,** 1–10.

Brown, R. L., McNicoll, V. J., Parrish, R. R. & Scammell, R. J., 1992. Middle Jurassic plutonism in the Kootenay Terrane, northern Selkirk Mountains, British Columbia. In: Radiogenic age and isotopic studies: Report 5: Geological Survey of Canada, Paper 91-2, pp. 135–141.

Brown, S.R., Gibson, H.D., Andrews, G.D.M., Thorkelson, D.J., Marshall, D.D., Vervoort, J.D. & Rayner, N., 2012. New constraints on Eocene extension within the Canadian Cordillera and identification of Phanerozoic protoliths for footwall gneisses of the Okanagan Valley shear zone. Lithosphere, **4,** 354–377.

Caddick, M.J., Bickle, M.J., Harris, N.B.W., Holland, T.J.B., Horstwood, M.S.A. & Ahmad, T., 2007. Burial and exhumation history of a Lesser Himalayan schist: recording the formation of an inverted metamorphic sequence in NW India. Earth and Planetary Science Letters, **264,** 375–390.

de Capitani, C. & Brown, T.H., 1987. The computation of chemical equilibrium in complex systems containing non-ideal solutions. Geochimica et Cosmochimica Acta, **51,** 2639–2652.

de Capitani, C. & Petrakakis, K., 2010. The computation of equilibrium assemblage diagrams with Theriak/Domino software. American Mineralogist, **95,** 1006–1016.

Carr, S.D., 1991. Three crustal zones in the Thor-Odin-Pinnacles area, southern Omineca belt, British Columbia. Canadian Journal of Earth Sciences, **28,** 2003–2023.

Chatterjee, N. D. & Froese, E., 1975. A thermodynamic study of the pseudobinary join muscovite-paragonite in the system $KAlSi_3O_8$–$NaAlSi_3O_8$-Al_2O_3-SiO_2-H_2O. American Mineralogist, **60,** 985–993.

Cheng, H., Vervoort, J.D., Li, X, Zhang, C., Li, Q. & Zheng, S., 2011. The growth interval of garnet in the UHP eclogites from the Dabie orogen, China. American Mineralogist, **96,** 1300–1307.

Cherniak, D.J., Watson, E.B., Grove, M. & Harrison, T.M., 2004. Pb diffusion in monazite: a combined RBS/SIMS study. Geochimica et Cosmochimica Acta, **68,** 829–840.

Cocherie, A., Legendre, O., Peucat, J.J. & Kouamelan, A.N., 1998. Geochronology of polygenetic monazites constrained by in situ electron-microprobe Th–U total lead determination—implications for lead behavior in monazite. Geochimica et Cosmochimica Acta, **62,** 2475–2497.

Coggon, R. & Holland, T.J.B., 2002. Mixing properties of phengitic micas and revised garnet-phengite thermobarometers. Journal of Metamorphic Geology, **20,** 683–696.

Colpron, M. & Ryan, J.J., 2010. Bedrock geology of southwest McQuesten (NTS 115P) and part of northern Carmacks (NTS 115I) map area. In: Yukon Exploration and Geology 2009 (eds MacFarlane, K.E., Weston, L.H. & Blackburn, L.R.), pp. 159–184. Yukon Geological Survey.

Colpron, M., Price, R.A., Archibald, D.A., & Carmichael, D.M., 1996. Middle Jurassic exhumation along the western flank of the Selkirk fan structure: Thermobarometric and thermochronometric constraints from the Illecillewaet synclinorium, southeastern British Columbia. Geological Society of America Bulletin, **108,** 1372–1392.

Colpron, M., Nelson, J.L. & Murphy, D.C., 2006. A tectonostratigraphic framework for the pericratonic terranes of the northern Canadian Cordillera. In: Paleozoic Evolution and Metallogeny of Pericratonic Terranes at the Ancient Pacific Margin of North America, Canadian and Alaskan Cordillera, Special Paper 45 (eds Colpron, M. & Nelson, J. L.), pp. 1–23. Geological Association of Canada.

Colpron, M., Nelson, J.L. & Murphy, D.C., 2007. Northern Cordilleran terranes and their interactions through time. GSA Today, **17,** 4–10.

Coney, P.J., 1980. Cordilleran core complexes; an overview. In: Cordilleran metamorphic core complexes, Memoir 153 (eds Crittenden, M.D., Coney, P.J. & Davis, G.H.), pp. 7–34. Geological Society of America, Boulder Colorodo.

Coney, P.J., & Harms, T.A. 1984. Cordilleran metamorphic core complexes: Cenozoic extensional relics of Mesozoic compression. Geology, **12**, 550–554.

Crowley, J.L. & Ghent, E.D., 1999. An electron microprobe study of the U-Th-Pb systematics of metamorphosed monazite: the role of Pb diffusion versus overgrowth and recrystallization. Chemical Geology, **157,** 285–302.

Crowley, J.L. & Parrish, R.R., 1999. U–Pb isotopic constraints on diachronous metamorphism in the northern Monashee complex, southern Canadian Cordillera. Journal of Metamorphic Geology, **17,** 483–502.

Crowley, J.L., Ghent, E.D., Carr, S.D., Simony, P.S. & Hamilton, M.A., 2000. Multiple thermotectonic events in a continuous metamorphic sequence, Mica Creek area, southeastern Canadian Cordillera. Geological Materials Research, **2,** 1–45.

Culshaw, N.G., Beaumont, C. & Jamieson, R.A., 2006. The orogenic superstructure-infrastructure concept: Revisited, quantified, and revived. Geology, **34,** 733–736.

De Sitter, L.U. & Zwart, H.J., 1960. Tectonic development in supra- and infra-structures of a mountain chain. 21st International Geological Congress, Copenhagen, **18,** 249–256.

DeWolf, C.P., Belshaw, N. & O'Nions, R.K., 1993. A metamorphic history from micron-scale $^{207}Pb/^{206}Pb$ chronometry of Archean monazite. Earth and Planetary Science Letters, **120,** 207–220.

Dusel-Bacon, C., Hansen, V.L., and Scala, J.A., 1995. High-pressure amphibolite facies dynamic metamorphism and the Mesozoic tectonic evolution of an ancient continental margin, east-central Alaska. Journal of Metamorphic Geology, **13,** 9–24.

Dusel-Bacon, C., Lanphere, M.A., Sharp, W.D., Layer, P.W. & Hansen, V.L., 2002. Mesozoic thermal history and timing of structural events for the Yukon-Tanana Upland, east-central Alaska: $^{40}Ar/^{39}Ar$ data from metamorphic and plutonic rocks. Canadian Journal of Earth Sciences, **39,** 1013–1051.

Dusel-Bacon, C., Hopkins, M.J., Mortensen, J.K., Dashevsky, S.S., Bressler, J.R. & Day, W.C., 2006. Paleozoic tectonic and metallogenic evolution of the pericratonic rocks of east-central Alaska and adjacent Yukon. In: Paleozoic Evolution and Metallogeny of Pericratonic Terranes at the Ancient Pacific Margin of North America, Canadian and Alaskan Cordillera, Special Paper 45 (eds Colpron, M. & Nelson, J.L.), pp. 1–23. Geological Association of Canada, St. John's, Newfoundland.

Fitzsimons, I.C.W., Kinny, P.D., Wetherley, S. & Hollingsworth, D.A., 2005. Bulk chemical control on metamorphic monazite growth in pelitic schists and implications for U–Pb age data. Journal of Metamorphic Geology, **23,** 261–277.

Florence, F.P. & Spear, F.S., 1993. Influences of reaction history and chemical diffusion on P-T calculations for staurolite schists from the Littleton Formation, northwestern New Hampshire. American Mineralogist, **78,** 345–359.

Foster, G., Gibson, H.D., Parrish, R.R., Horstwood, M., Fraser, J. & Tindle, A., 2002. Textural, chemical and isotopic insights into the nature and behaviour of metamorphic monazite. Chemical Geology, **191,** 183–207.

Foster, G., Parrish, R.R., Horstwood, M.S.A., Chenery, S., Pyle, J., & Gibson, H.D. 2004. The generation of prograde P–T–t points and paths; a textural, compositional, and chronological study of metamorphic monazite. Earth Planetary Science Letters, **228,** 125–142.

Fuhrman, M. L. & Lindsley, D. H., 1988. Ternary-feldspar modeling and thermometry. American Mineralogist, **73,** 201–216.

Gabrielse, H., Murphy, D.C. & Mortensen, J.K., 2006. Cretaceous and Cenozoic dextral orogen-parallel displacements, magmatism and paleogeography, north-central Canadian Cordillera. In: Paleogeography of the North American Cordillera: Evidence For and Against Large-Scale Displacements, Special Paper 46 (eds Haggart, J.W., Monger, J.W.H. & Enkin, R.J.), pp. 255-276. Geological Association of Canada.

Gaidies, F. Krenn, E, de Capitani, C. & Abart, R., 2008. Coupling forward modelling of garnet growth with monazite geochronology: an application to the Rappold Complex (Austroalpine crystalline basement). Journal of Metamorphic Geology, **26,** 775–793.

Gardés, E., Jaoul, O., Montel, J.-M., Seydoux-Guillaume, A.-M. & Wirth, R., 2006. Pb diffusion in monazite: An experimental study of $Pb^{2+}+Th^{4+} \Leftrightarrow 2Nd^{3+}$ interdiffusion. Geochimica et Cosmochimica Acta, **70,** 2325–2336.

Gibson, H.D., Brown, R.L., & Parrish, R.R., 1999. Deformation-induced inverted metamorphic field gradients: an example from the southeastern Canadian Cordillera. Journal of Structural Geology, **21,** 751–767.

Gibson, H. D., Carr, S. D., Brown, R. L. & Hamilton, M. A., 2004. Correlations between chemical and age domains in monazite, and metamorphic reactions involving major politic phases: an integration of ID-TIMS and SHRIMP geochronology with Y–Th–U X-ray mapping. Chemical Geology, **211,** 237–260.

Gibson, H.D., Brown, R.L., & Carr, S.D., 2005. U-Th- Pb geochronologic constraints on the structural evolution of the Selkirk fan, northern Selkirk Mountains, southern Canadian Cordillera. Journal of Structural Geology, **27,** 1899–1924.

Gibson, H.D., Brown, R.L. & Carr, S.D., 2008. Tectonic evolution of the Selkirk fan, southeastern Canadian Cordillera: A composite Middle Jurassic–Cretaceous orogenic structure. Tectonics, **27,** TC6007, doi:10.1029/2007TC002160.

Goncalves, P., Williams, M.L. & Jercinovic, M.J., 2005. Electron-microprobe age mapping of monazite. American Mineralogist, **90,** 578–585.

Gordey, S. P. & Ryan, J. J., 2005. Geology, Stewart River area (115N, 115-O and part of 115J), Yukon Territory. Geological Survey of Canada, Open File 4970 (1 sheet, 1:250 000 scale).

Hansen, V.L., Heizler, M.T. & Harrison, T.M., 1991. Mesozoic thermal evolution of the Yukon-Tanana composite terrane; new evidence from $^{40}Ar/^{39}Ar$ data. Tectonics, **10,** 51–76.

Hansen, V.L. & Dusel-Bacon, C. 1998. Structural and Kinematic evolution of the Yukon-Tanana upland tectonites, east-central Alaska: a record of late Paleozoic to Mesozoic crustal assembly. Geological Society of America Bulletin, **110,** 211–230.

Harlov, D.E. & Hetherington, C.J., 2010. Partial high-grade alteration of monazite using alkali-bearing fluids: experiment and nature. American Mineralogist, **95,** 1105–1108.

Harlov, D.E., Wirth, R. & Hetherington, C.J., 2011. Fluid-mediated partial alteration in monazite: the role of coupled dissolution–reprecipitation in element redistribution and mass transfer. Contributions to Mineralogy and Petrology, **162,** 329–348.

Hayward, N., Miles, W. & Oneschuk, D. 2012. Geophysical Series, detailed geophysical compilation project, Yukon Plateau, Yukon, NTS 115-I, J, K, N, O, P and 116A and B. Geological Survey of Canada, Open File 7279 (2 sheets, 1:350 000 Scale).

Hetherington, C.J., Harlov, D.E. & Budzyń, B., 2010. Experimental metasomatism of monazite and xenotime: mineral stability, REE mobility and fluid composition. Mineralogy and Petrology, **99,** 165–184.

Holland, T. J. B. & Powell, R., 1998. An internally consistent thermodynamic data set for phases of petrological interest. Journal of Metamorphic Geology, **16,** 309–343.

Holland, T. & Powell, R., 2003. Activity-composition relations for phases in petrological calculations; an asymmetric multicomponent formulation. Contributions to Mineralogy and Petrology, **145,** 492–501.

Horváth, P., Balen, D., Finger, F., Tomljenović, B. & Krenn, E., 2010. Contrasting P–T–t paths from the basement of the Tisia Unit (Slavonian Mts., NE Croatia): Application of quantitative phase diagrams and monazite age dating. Lithos, **117,** 269–282.

Hunt, P.A., & Roddick, J.C., 1992. A compilation of K–Ar and 40Ar–39Ar ages: report 22. In: Radiogenic age and isotopic studies: Report 6. Geological Survey of Canada, Paper 92-2, pp. 179–226.

Ireland, T.R. & Gibson, G.M., 1998. SHRIMP monazite and zircon geochronology of high-grade metamorphism in New Zealand. Journal of Metamorphic Geology, **16,** 149–167.

Janots, E., Engi, M., Berger, A., Allaz, J., Schwarz, J.O. & Spandler, C., 2008. Prograde metamorphic sequence of REE minerals in pelitic rocks of the Central Alps, implications for allanite–monazite–xenotime phase relations from 250 to 610 °C. Journal of Metamorphic Geology, **26,** 509–526.

Johnston, S.T., Mortensen, J.K. & Erdmer, P., 1996. Igneous and metaigneous age constraints for the Aishihik metamorphic suite, southwest Yukon. Canadian Journal of Earth Sciences, **33,** 1543–1555.

Knight, E., Schneider, D.A. & Ryan, J.J., in press. Thermochronology of the Yukon-Tanana terrane, west-central Yukon: evidence for Jurassic extension and exhumation in the northern Canadian Cordillera. Journal of Geology.

Kohn, M.J. & Spear, F., 2000. Retrograde net transfer reaction insurance for pressure-temperature estimates. Geology, **28,** 1127–1130.

Kretz, R., 1983. Symbols for rock-forming minerals. American Mineralogist, **68,** 277–279.

Lowey, G.W. & Hills, L.V., 1988. Lithofacies, petrography, and environments of deposition, Tantalus Formation (Lower Cretaceous), Indian River area, west-central Yukon. Bulletin of Canadian Petroleum Geology, **36,** 296–310.

Ludwig, K.R., 2008. Manual for Isoplot 3.7: A Geochronological Toolkit for Microsoft Excel. Special Publication No. 4. rev. August 26, 2008, Berkeley Geochronology Center, pp. 77.

Mackenzie, D. & Craw, D., 2012. Contrasting structural settings of mafic and ultramafic rocks in the Yukon-Tanana terrane. In: Yukon Exploration and Geology 2011 (eds MacFarlane, K.E. & Sack, P.J.), pp. 115 – 127. Yukon Geological Survey.

Mattison, C.G., Wooden, J.L., Liou, J.G., Bird, D.K. & Wu, C.L., 2006. Age and duration of eclogite-facies metamorphism, north Qaidam HP/UHP terrane, western China. American Journal of Science, **306,** 683–711.

Monger, J.W.H. & Price, R.A., 2002. The Canadian Cordillera: Geology and tectonic evolution. Canadian Society of Exploration Geophysicists Recorder, **27,** 17–36.

Monger, J.W.H., Price, R.A. & Tempelman-Kluit, D.J., 1982. Tectonic accretion and the origin of the two major metamorphic and plutonic welts in the Canadian Cordillera. Geology, **10,** 70–75.

Mortensen, J.K., 1990. Geology and U-Pb geochronology of the Klondike District, west-central Yukon Territory. Canadian Journal of Earth Sciences, **27,** 903–914.

Murphy, D.C., van der Heyden, P., Parrish, R.R., Klepacki, D.W., McMillan, W., Struik, L.C. & Gabites, J., 1995. New geochronological constraints on Jurassic deformation of the western edge of North America, southeastern Canadian Cordillera. In: Jurassic Magmatism and Tectonics of the North American Cordillera, Special Paper 299 (eds Miller, D.M. & Busby, C.), pp. 159–171. Geological Society of America.

Murphy, D.C., 2004. Devonian-Mississippian metavolcanic stratigraphy, massive sulphide potential and structural re-interpretation of Yukon-Tanana Terrane south of the Finlayson Lake massive district, southeastern Yukon (105G/1, 105H/3,4,5). In: Yukon Exploration and Geology 2003 (eds Emond, D.S. & Lewis, L.L.), pp. 157–175. Yukon Geological Survey.

Nelson, J.L., Colpron, M., Piercey, S.J., Dusel-Bacon, C., Murphy, D.C. & Roots, C.F., 2006. Paleozoic tectonic and metallogenic evolution of the pericratonic terranes in Yukon, northern British Columbia and eastern Alaska. In: Paleozoic Evolution and Metallogeny of Pericratonic Terranes at the Ancient Pacific Margin of North America, Canadian and Alaskan Cordillera, Special Paper 45 (eds Colpron, M. & Nelson, J.L.), pp. 323–360. Geological Association of Canada.

Parrish, R.R., 1995. Thermal evolution of the southeastern Canadian Cordillera. Canadian Journal of Earth Sciences, **32,** 1618–1642.

Parrish, R.R., Carr, S.D. & Parkinson, D.L., 1988. Eocene extensional tectonics and geochronology of the southern Omineca belt, British Columbia and Washington. Tectonics, **7,** 181-212.

Pattison, D.R.M. & Tinkham, D.T., 2009. Interplay between equilibrium and kinetics in prograde metamorphism of pelites: an example from the Nelson aureole, British Columbia. Journal of Metamorphic Geology, **27,** 249–279.

Pattison, D.R.M., de Capitani, C. & Gaidies, F., 2011. Petrological consequences of variations in metamorphic reaction history. Journal of Metamorphic Geology, **29,** 953–977.

Pavlis, T.L., Sisson, V.B., Foster, H.L., Nockleberg, W.J., & Plafker, G., 1993. Mid-Cretaceous extensional tectonics of the Yukon–Tanana terrane, Trans-Alaskan Crustal Transect (TACT), east-central Alaska. Tectonics, **12,** 103–122.

Pyle, J.M. & Spear, F.S, 1999. Yttrium zoning in garnet: coupling of major and accessory phases during metamorphic reactions. Geological Materials Research, **1,** 1–49.

Rayner, N. & Stern, R. A., 2002. Improved Sample Preparation Method for SHRIMP Analysis of Delicate Mineral Grains Exposed in Thin Sections. Geological Survey of Canada, Current Research 2002-F10, 1–3.

Ring, U., Brandon, M.T., Willet, S.D. & Lister, G.S., 1999. Exhumation processes. In: Exhumation Processes: Normal Faulting, Ductile Flow, and Erosion (eds Ring, U., Brandon, M.T., Lister, G.S. & Willet, S.D.), pp. 1–27. Geological Society of London, Special Publications.

Ruks, T.W., Piercey, S.J., Ryan, J.J., Villeneuve, M.E. & Creaser, R.A., 2006. Mid- to Late Paleozoic K-feldspar augen granitoids of the Yukon-Tanana terrane, Yukon: Implications for crustal growth and tectonic evolution of the northern Cordillera. Geological Society of America Bulletin, **118,** 1212–1231.

Ryan, J.J., Gordey, S.P., Glombick, P., Piercey, S.J. & Villeneuve, M.E., 2003. Update on bedrock geological mapping of the Yukon-Tanana terrane, southern Stewart River map area, Yukon Territory. Geological Survey of Canada, Current Research 2003-A9. 7 p.

Ryan, J.J., Colpron, M. & Hayward, N., 2010. Geology, southwestern McQuesten and parts of northern Carmacks, Yukon; Geological Survey of Canada, Canadian Geoscience Map 7, (preliminary version), scale 1:125 000.

Schärer, U., 1984. The effect of initial 230Th disequilibrium on young U–Pb ages: the Makalu case, Himalaya. Earth and Planetary Science Letters, **67,** 191– 204.

Seydoux-Guillaume, A.M., Paquette, J.L., Wiedenbeck, M., Montel, J-M. & Heinrich, W., 2002. Experimental resetting of the U–Th–Pb systems in monazite. Chemical Geology, **191,** 165–181.

Skora, S., Lapen, T.J., Baumgartner, L.P., Johnson, C.M., Hellebrand, E. & Mahlen, M.J., 2009. The duration of prograde garnet crystallization in the UHP eclogites at Lago di Cignana, Italy. Earth and Planetary Science Letters, **287,** 402–411.

Spear, F.S. & Parrish, R.R., 1996. Petrology and cooling rates of the Valhalla complex, British Columbia, Canada. Journal of Petrology, **37,** 733–765.

Spear, F.S., Kohn, M.J., Florence, F.P. & Menard, T., 1990. A model for garnet and plagioclase growth in pelitic schists: implications for thermobarometry and P-T path determinations. Journal of Metamorphic Geology, **8,** 683–696.

Stacey, J.S. & Kramers, J.D., 1975. Approximation of terrestrial lead isotope evolution by a two-stage model. Earth and Planetary Science Letters, **26,** 207–221.

Stern, R. A., 1997. The GSC sensitive high resolution ion microphobe (SHRIMP): analytical techniques of zircon U-Th-Pb age determinations and performance evaluation. Radiogenic Age and Isotopic Studies: Report 10. Geological Survey of Canada, Current Research 1997-F, 1–31.

Stern, R. A. & Berman, R. G., 2000. Monazite U-Pb and Th-Pb geochronology by ion microprobe, with an application to in situ dating of an Archean metasedimentary rock. Chemical Geology, **172,** 113–130.

Stern, R.A. & Sanborn, N., 1998. Monazite U–Pb and Th–Pb geochronology by high-resolution secondary ion mass spectrometry. Radiogenic Age and Isotopic Studies: Report 11. Geological Survey of Canada, Current Research 1998-F. 1–18.

Stevens, R.A., Mortensen, J.K., & Hunt, P.A., 1993. U–Pb and $^{40}Ar/^{39}Ar$ geochronology of plutonic rocks from the Teslin suture zone, Yukon Territory. In: Radiogenic and isotope studies, Report 7. Geological Survey of Canada, Paper 93-2, pp. 83–90.

Struik, L.C. 1993. Intersecting intracontinental Tertiary transform fault systems in the North American Cordillera. Canadian Journal of Earth Sciences, **30,** 1262–1274.

Stüwe, K., 1997. Effective bulk composition changes due to cooling: a model predicting complexities in retrograde reaction textures. Contributions to Mineralogy and Petrology, **129,** 43–52.

Tinkham, D.K., Zuluaga, C.A. & Stowell, H.H., 2001. Metapelite phase equilibria modeling in MnNCKFMASH: the effect of variable Al_2O_3 and MgO/(MgO+FeO) on mineral stability. Geological Materials Research, **3,** 1–42.

Tobisch O.T. & Paterson, S.C., 1988. Analysis and interpretation of composite foliations in an area of progressive deformation. Journal of Structural Geology, **10,** 745–754.

Todd, C., 1998. Limits on the precision of geobarometry at low grossular and anorthite content. American Mineralogist, **83,** 1161–1167.

Tracy, R.J, Robinson, P. & Thompson, A.B., 1976. Garnet composition and zoning in the determination of temperature and pressure of metamorphism, central Massachusetts. American Mineralogist, **61,** 762–775.

Vance, D. & Mahar, E., 1998. Pressure–temperature paths from P–T pseudosections and zoned garnets; potential, limitations and examples from the Zanskar Himalaya, NW India. Contributions to Mineralogy and Petrology, **132,** 225–245.

Waters, D.J. & Lovegrove, D.P., 2002. Assessing the extent of disequilibrium and overstepping of prograde metamorphic reactions in metapelites from the Bushveld Complex aureole, South Africa. Journal of Metamorphic Geology, **20,** 135–149.

Wolf, D.E., Andronicos, C.L., Vervoort, J.D., Mansfield, M.R. & Chardon, D., 2010. Application of Lu-Hf garnet dating to unravel the relationships between deformation, metamorphism and plutonism: An example from the Prince Rupert area, British Columbia. Tectonophisics, **485,** 62–77.

White, R. W., Powell, R., Holland, T. J. B. & Worley, B. A., 2000. The effect of TiO_2 and Fe_2O_3 on metapelitic assemblages at greenschist and amphibolite facies conditions: mineral equilibria calculations in the system K_2O–FeO–MgO–Al_2O_3–SiO_2–H_2O–TiO_2–Fe_2O_3. Journal of Metamorphic Geology, **18,** 497–511.

White, R.W., Powell, R. & Holland, T.J.B., 2007. Progress relating to calculations of partial melting equilibria for metapelites. Journal of Metamorphic Geology, **25,** 511–527.

Williams, M.L. & Jercinovic, M.J., 2002. Microprobe monazite geochronology: putting absolute time into microstructural analysis. Journal of Structural Geology, **24,** 1013–1028.

Williams, M.L., Jercinovic, M.J. & Terry, M.P., 1999. Age mapping and dating of monazite on the electron microprobe: Deconvoluting multistage tectonic histories. Geology, **27,** 1023–1026.

Williams, M.L., Jercinovic, M.J., Harlov, D.E., Budzyń, B. & Hetherington, C.J., 2011. Resetting monazite ages during fluid-related alteration. Chemical Geology, **283,** 218–225.

Williams, P.F., 1983. Large scale transposition by folding in Northern Norway. Geologische Rundschau, **72,** 589–604.

Williams, P.F. 1985. Multiply deformed terrains-problems of correlation. Journal of Structural

Geology, **7,** 269–280.

Williams, P.F. & Compagnoni, R., 1983. Deformation and metamorphism in the Bard area of the Sesia Lanzo zone, Western Alps, during subduction and uplift. Journal of Metamorphic Geology, **1,** 117-140.

Zhu, X.K. & O'Nions, R.K., 1999. Zonation of monazite in metamorphic rocks and its implications for high temperature thermochronology: a case study from the Lewisian terrain. Earth and Planetary Science Letters, **171,** 209–220.

Chapter 3.

Middle Jurassic to earliest Cretaceous mid-crustal tectono-metamorphism in the northern Canadian Cordillera: Recording foreland-directed migration of an orogenic front

3.1. Abstract

In situ SHRIMP monazite geochronology and garnet isopleth thermobarometry reveal a previously unrecognized Middle Jurassic to earliest Cretaceous mid-crustal tectono-metamorphic event in the eastern portion of the Yukon-Tanana terrane (Finlayson Lake district, southeast Yukon) in the northern Canadian Cordillera. Intersection of garnet end-member compositional isopleths applied to single-stage, growth-zoned garnet record progressive garnet growth from 550 °C and 6.1-6.6 kbar to 600 °C and 7.5 kbar. Monazite textures, chemical zoning and in situ U-Pb ages record a single protracted episode of monazite growth from c. 169 to 142 Ma coeval with the development of transposition fabrics and the late stages of garnet growth. This event post-dates widespread Early Jurassic exhumation of Yukon-Tanana terrane rocks west of the Tintina fault in west-central Yukon, which were previously ductiley deformed and metamorphosed in the Permo-Triassic. The lack of evidence for Permo-Triassic ductile deformation and high-grade metamorphism within the Finlayson Lake district, and its position east of the Permian arc-center and west of Permian blueschists and eclogites suggests this eastern portion of the terrane occupied the cool forearc at this time. These data indicate younger, more protracted mid-crustal orogenesis in the northern Cordillera than was previously recognized, with deformation and metamorphism migrating toward the foreland and downwards in the Middle Jurassic to Early Cretaceous, in part contemporaneous with and analogous to that in the southeastern Canadian Cordillera.

3.2. Introduction

The Yukon-Tanana terrane is characterized by intense deformation and metamorphism that has been interpreted to be a consequence of the accretion of the allochthonous peri-Laurentian terranes (Fig. 3.1; Yukon-Tanana, Quesnel and Stikine terranes) to the western margin of ancestral North America (Monger et al., 1982; Colpron et al., 2007; Colpron and Nelson, 2009; Beranek and Mortensen, 2011). Previous work suggests that deformation and metamorphism associated with terrane accretion and subsequent crustal thickening was diachronous from north to south within the Canadian Cordillera (e.g., Parrish, 1995; Gibson et al., 2008; Berman et al., 2007). Geochronologic investigations in the north-central portion of Yukon-Tanana terrane in Yukon indicate that the main episode of ductile deformation and amphibolite facies metamorphism occurred in the Permo-Triassic (Berman et al., 2007; Beranek and Mortensen, 2011). K/Ar and $^{40}Ar/^{39}Ar$ data from a large portion of greenschist- and amphibolite facies rocks of the Yukon-Tanana terrane in the Yukon and Alaskan Cordillera (referred to herein as 'northern Cordillera') yield Early to Middle Jurassic cooling ages (Hansen et al., 1991; Hunt and Roddick, 1992; Stevens et al., 1993; Johnston et al., 1996; Gordey et al., 1998; Dusel-Bacon et al., 2002; Knight et al., 2013) that are interpreted to record widespread regional uplift and exhumation (Johnston et al., 1996; Berman et al., 2007; Beranek and Mortensen, 2011). The timing of such events contrasts with those documented in the southeastern Canadian Cordillera where deformation and metamorphism related to accretion of the peri-Laurentian terranes (Quesnel and Stikine terranes) and westward underthrusting of the North American plate apparently occurred in the Early Jurassic through early Paleogene (Evenchick et al., 2007, and references therein).

Furthermore, geochronologic data from the metamorphic hinterland of the orogen in the southern Canadian Cordillera has revealed that despite similarities in metamorphic grade and deformation patterns, deformation and metamorphism was diachronous with depth and across strike. Rocks presently in the upper structural levels were buried, heated and exhumed in the Jurassic (Murphy et al., 1995; Parrish, 1995; Colpron et al., 1996; Crowley et al., 2000; Gibson et al., 2005, 2008), while structurally deeper rocks continued to be buried and heated from Cretaceous to earliest Eocene (Carr, 1991;

Parrish, 1995; Gibson et al., 1999, 2005, 2008; Crowley and Parrish, 1999; Crowley et al., 2000). Additionally, numerous authors have suggested that the deformation migrated from the metamorphic and plutonic hinterland to the foreland thrust and fold belt to the northeast in the Mesozoic and Tertiary, and that there was a dynamic link between these two structural domains (e.g., Price, 1981; Brown et al., 1992; Johnson and Brown, 1996; Simony and Carr, 2011).

Herein, we present results of an integrated metamorphic and microstructural study coupled with in situ Sensitive High Resolution Ion Microprobe (SHRIMP) analysis of monazite within amphibolite facies rocks from the Finlayson Lake district (southeast Yukon) in the eastern portion of Yukon-Tanana terrane in the northern Cordillera. This study provides an example of a successful application of garnet isopleth thermobarometry that incorporates the effects of a changing bulk composition caused by the fractionation of components during garnet growth, to determine P-T conditions at successive increments along the prograde P-T path. The combined data reveal that deformation and metamorphism were diachronous within the Yukon-Tanana terrane, with younger events recorded at progressively deeper structural levels in a manner analogous to, and partly coincident with, the southeastern Canadian Cordillera.

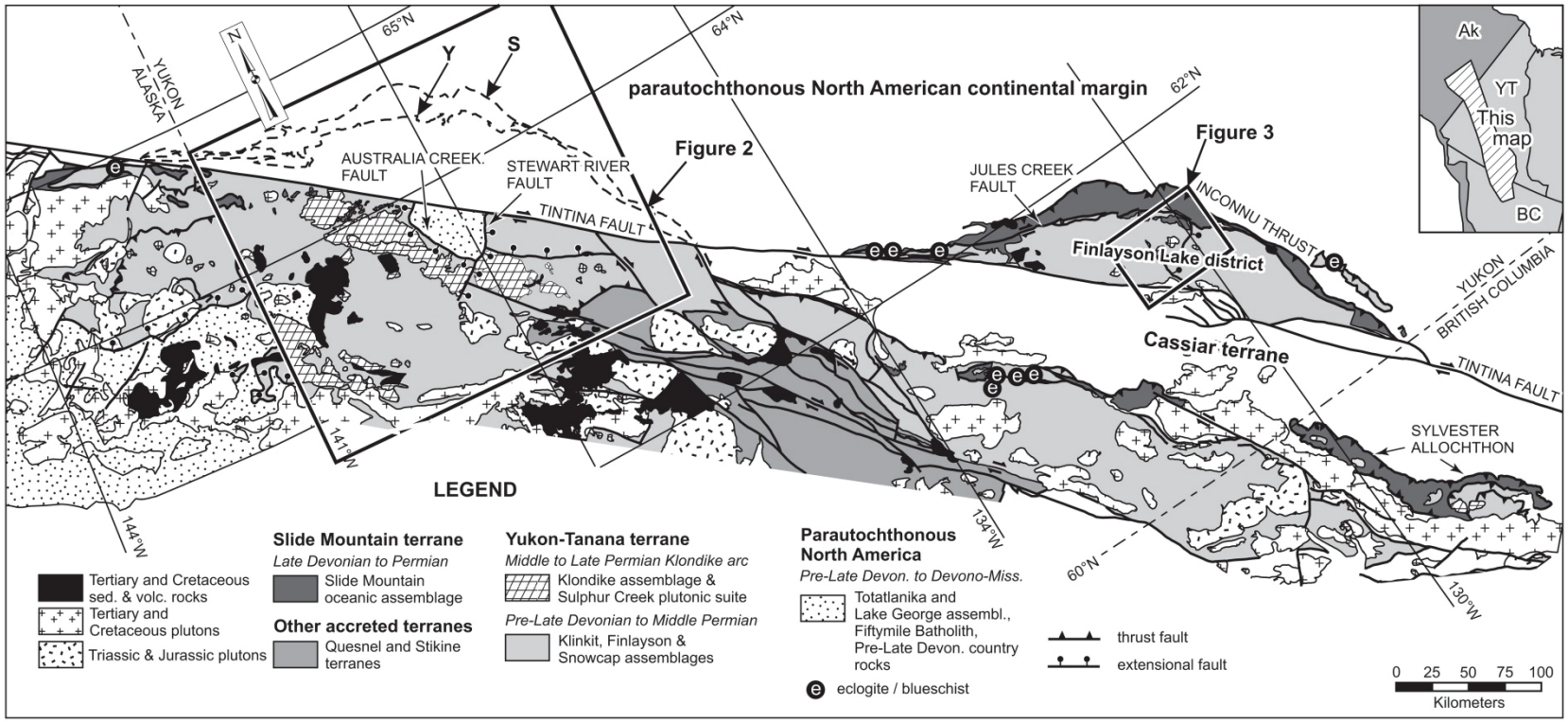
YUKON
ALASKA
65°N
64°N
62°N
60°N
144°W
141°W
134°W
130°W
Y
S
parautochthonous North American continental margin
Figure 2
Figure 3
AUSTRALIA CREEK FAULT
STEWART RIVER FAULT
TINTINA FAULT
JULES CREEK FAULT
INCONNU THRUST
Finlayson Lake district
YUKON
BRITISH COLUMBIA
Cassiar terrane
TINTINA FAULT
SYLVESTER ALLOCHTHON
Ak
YT
This map
BC
LEGEND
Tertiary and Cretaceous sed. & volc. rocks
Tertiary and Cretaceous plutons
Triassic & Jurassic plutons
Slide Mountain terrane
Late Devonian to Permian
Slide Mountain oceanic assemblage
Other accreted terranes
Quesnel and Stikine terranes
Yukon-Tanana terrane
Middle to Late Permian Klondike arc
Klondike assemblage & Sulphur Creek plutonic suite
Pre-Late Devonian to Middle Permian
Klinkit, Finlayson & Snowcap assemblages
Parautochthonous North America
Pre-Late Devon. to Devono-Miss.
Totatlanika and Lake George assembl., Fiftymile Batholith, Pre-Late Devon. country rocks
eclogite / blueschist
thrust fault
extensional fault
0 25 50 75 100
Kilometers

Figure 3.1. Tectonic assemblage map of the Yukon-Tanana terrane and adjacent terranes of the northern Cordillera in east-central Alaska, central Yukon, and northern British Columbia. The locations of Figures 3.2 and 3.3 areas outlined by thick black squares. Dashed outlines labelled S and Y show the original position of the eastern offset block of the Slide Mountain and Yukon-Tanana terranes (Finlayson Lake district), respectively, relative to the main body of the terrane (but not the North American continental margin), prior to offset along the Tintina fault (Gabrielse et al., 2006). Figure modified from Colpron et al. (2006).

3.3. Geologic Setting

The Yukon-Tanana and Slide Mountain terranes occupy the innermost position of the accreted terranes in the northern Cordillera. The Yukon-Tanana terrane consists of a pre-Late Devonian metasedimentary basement (Snowcap assemblage) with lithological, geochemical and isotopic compositions that suggest it represents a rifted portion of the western Laurentian continental margin (Piercey and Colpron, 2009; Colpron and Nelson, 2009). The Snowcap assemblage is overlain by three unconformity-bound Upper Devonian to Permian volcanic arc sequences (Finlayson, Klinkit, Klondike assemblages) that are coeval with oceanic chert, argillite and mafic volcanic rocks of the Slide Mountain terrane (Colpron et al., 2006). The Yukon-Tanana and Slide Mountain terranes are thought to have originated as an arc and back-arc pair, respectively, during the Late Devonian to Permian opening of the Slide Mountain ocean (Nelson et al., 2006). Closure of the Slide Mountain ocean and the initial accretion of Yukon-Tanana to the western Laurentian margin is interpreted by Beranek and Mortensen (2011) to have occurred in the Late Permian.

In southeast Yukon, portions of the Yukon-Tanana and Slide Mountain terranes have been offset 490 kilometers to the southeast, relative to the main body to the west, through a combined 430 kilometres of dextral strike-slip displacement along the Tintina fault in the Paleogene, and 60 kilometres of extension in the Cretaceous (Gabrielse et al., 2006). Figure 3.1 shows the restored position of this offset block of the Yukon-Tanana terrane (Finlayson Lake district) relative to its counterpart to the west. In the Finlayson Lake district, the Yukon-Tanana and Slide Mountain terranes are separated from marginal rocks of ancestral North America to the northeast by the Inconnu thrust, a

major Jurassic-Cretaceous contractional fault that carried the Slide Mountain and Yukon-Tanana terranes on top of the North American continental margin sequence (Murphy et al., 2006).

In their pre-Paleogene configuration, rocks of the Finlayson Lake district lie immediately northeast of a tectonic window that exposes an Early to mid-Cretaceous high-grade metamorphic infrastructural domain of the Yukon-Tanana terrane southwest of the Tintina fault (Staples et al., 2013; Fig. 3.2). West of the Cretaceous domain, across the Australia Creek fault (Staples et al., 2013), Yukon-Tanana terrane rocks were transposed and metamorphosed in the Late Permian to Early Triassic and in the Early Jurassic (Berman et al., 2007; Beranek and Mortensen, 2011; Fig. 3.2) before they were exhumed to upper crustal levels in the Early to Middle Jurassic (Johnston et al., 1996; Dusel-Bacon et al., 2002; Berman et al., 2007). Southeast of the Cretaceous domain, across the Stewart River normal fault are sub-greenschist facies, weakly to undeformed Devonian and Mississippian volcanic and plutonic rocks that record Paleozoic and Mesozoic $^{40}Ar/^{39}Ar$ cooling ages (Knight et al., 2013). Both the Permo-Jurassic metamorphic domain to the west and the Devono-Mississippian rocks to the southeast were presumably the suprastructural 'lid' from beneath which the Cretaceous metamorphic domain (essentially a core complex) was exhumed along the Australia Creek and Stewart River faults, respectively, in the mid-Cretaceous (Staples et al., 2013).

Similar high-grade, ductiley deformed rocks in east-central Alaska are interpreted as parautochthonous North American continental margin rocks (Lake George assemblage in Fig. 3.1) exhumed from beneath the Yukon-Tanana terrane along mylonitic extensional faults in the mid-Cretaceous (Hansen, 1990; Hansen and Dusel-Bacon, 1998; Dusel-Bacon et al., 1995; 2002; 2006). A parautochthonous North American origin for these rocks in east-central Alaska is based on Archean and Proterozoic U-Pb zircon inheritance and detrital ages, stratigraphic similarity with rocks in the Selwyn Basin, their structural position, and a lack of late Paleozoic arc assemblages characteristic of the Yukon-Tanana terrane (Dusel-Bacon et al., 2006; Nelson et al., 2006; Dusel-Bacon and Williams, 2009). Similar characteristics, including the exhumation of moderate to high-pressure amphibolite facies rocks from beneath the Yukon-Tanana terrane along mid-Cretaceous extensional shear zones, suggests the

Australia Mountain domain in west-central Yukon may also be parautochthonous North American margin (Staples et al., 2013).

Permo-Triassic metamorphism in the central portion of the Yukon-Tanana terrane was spatially and temporally associated with a belt of Permian arc magmatism (Klondike assemblage) (Mortensen, 1990; Gordey and Ryan, 2005; Berman et al., 2007). Permian magmatic rocks and a discontinuous belt of coeval blueschist and eclogite to the northeast crop out along the eastern side of the Yukon-Tanana terrane (Fig. 3.1; Creaser et al., 1997; Erdmer et al., 1998) and are interpreted to record a Permian northeast-facing magmatic arc and accretionary wedge, respectively (Mortensen, 1992; Nelson et al., 2006). By the Early to Middle Triassic (251 – 235 Ma), siliciclastic strata that contain detrital zircon inferred to have been sourced in the Paleozoic arc assemblages of Yukon-Tanana terrane were deposited on the western Laurentian continental margin (Beranek and Mortensen, 2011). This depositional relationship implies that the Slide Mountain ocean had closed by the Early Triassic and the Yukon-Tanana terrane had been uplifted and accreted to the western Laurentian margin, forming a downward slope onto Laurentian strata. Beranek and Mortensen (2011) suggest that the Late Permian tectono-metamorphism within Yukon-Tanana terrane is therefore the result of the accretion of the Yukon-Tanana terrane onto the western Laurentian margin.

The study area lies in the structurally lowest of three thrust sheets which imbricate Yukon-Tanana terrane in the Finlayson Lake district. This lowest sheet, the Big Campbell thrust sheet, is bound below by the Big Campbell thrust and above by the Money Creek thrust (Fig. 3.2; Murphy et al., 2006). The Big Campbell thrust is a post-metamorphic thrust juxtaposing amphibolite grade rocks of Yukon-Tanana terrane over Upper Triassic shale and spatially associated ultramafic rocks correlated with Slide Mountain terrane (Fig. 3.2). The Big Campbell thrust has been inferred to be related to the post-Late Triassic, pre-mid-Cretaceous Inconnu thrust in a duplex structure (Murphy et al., 2006). The Big Campbell thrust sheet is exposed in the footwall of the North River fault, a regional-scale mid-Cretaceous normal fault that cuts across the thrust sheets of Yukon-Tanana terrane in the Finlayson Lake district in a northeast-southwest trend (Figs. 3.3 and 3.4; Murphy, 2004). The Money Creek thrust sheet, and the structurally higher Cleaver Lake thrust sheet, are preserved to the southeast in the hanging-wall of

the North River fault. Rocks in the footwall of the North River fault yield mid-Cretaceous K-Ar cooling ages (Hunt and Roddick, 1992; Murphy et al., 2001), are intruded by mid-Cretaceous granite plutons (Murphy et al., 2001), and have been ductiley deformed at amphibolite facies, prior to the emplacement of the granites. The mid-Cretaceous granites are massive and discordant with respect to deformation in their wall rocks, except in their roof areas near the North River fault where a weak foliation is locally developed. Low grade rocks in the hanging-wall to the southeast comprise the upper thrust sheets of Yukon-Tanana terrane; these lack Cretaceous granites and record Mississippian K-Ar cooling ages (Hunt and Roddick, 1987; Murphy, 2004). The North River fault is inferred to have been the northern extension of the mid-Cretaceous Stewart River fault (Staples et al., 2013) in western McQuesten and eastern Stewart River map areas prior to Paleogene offset on the Tintina fault (Fig. 3.2).

The metapelitic samples examined in this study lie in the footwall of the North River fault (Fig. 3), in the oldest exposed rock unit in the Finlayson Lake district, the pre-Upper Devonian North River formation. This formation consists of quartzose psammite, non-carbonaceous metapelite, marble, calcareous schist and felsic metavolcanic members at or near its top (Murphy et al., 2006). The samples were collected from a horizon dominated by calcareous and pelitic schist immediately northeast of the Tintina fault (Fig. 3.3). The North River formation is considered part of the Snowcap assemblage (Colpron et al., 2006). In the Finlayson Lake district, this unit has been intruded and overlain by Late Devonian to Early Mississippian arc and back-arc facies igneous rocks (Murphy et al., 2006). Metamorphic grade and stratigraphic and structural depth broadly increases within the footwall of the North River fault from chlorite-bearing assemblages in the northeast to garnet-staurolite bearing assemblages in the southwest, reflecting increased normal throw along the fault to the southwest. Samples were collected within the lowest exposed structural levels within the footwall, which have been ductiley deformed during, or after, amphibolite facies metamorphism, as evidenced by wrapping of the penetrative foliation around garnet and staurolite porphyroblasts. Parallelism of compositional layering and lithologic contacts with a pervasive shallowly-dipping foliation that contains rare intrafolial isoclinal folds suggests these rocks experienced at least one generation of high-strain transposition.

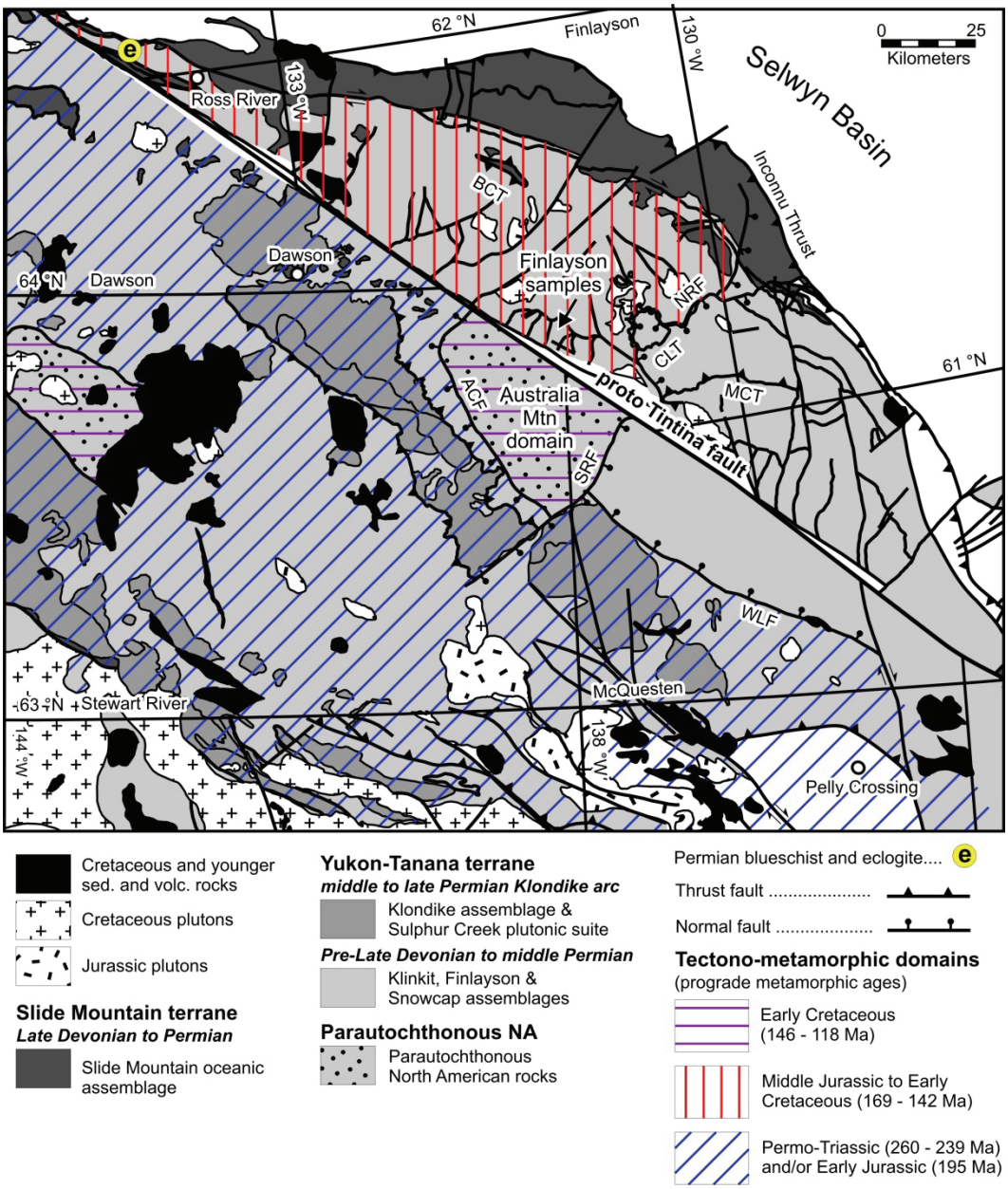

Figure 3.2. **Simplified tectonic assemblage map of the northern Yukon-Tanana terrane, with the main body of Yukon-Tanana terrane on the southwest side of the Tintina fault restored to its pre-Paleogene position adjacent to the segment of Yukon-Tanana terrane in the Finlayson Lake district. This map shows the inferred distribution of the Permo-Triassic/Early Jurassic, Middle Jurassic – Early Cretaceous, and Early Cretaceous tectono-metamorphic domains prior to Paleogene offset along the Tintina fault. ACF = Australia Creek fault; SRF = Stewart River fault; NRF = North River fault; WLF = Willow Lake fault; MCT = Money Creek thrust. Names of the 1:250 000 quadrangles are labeled in one of the corners of each map sheet.**

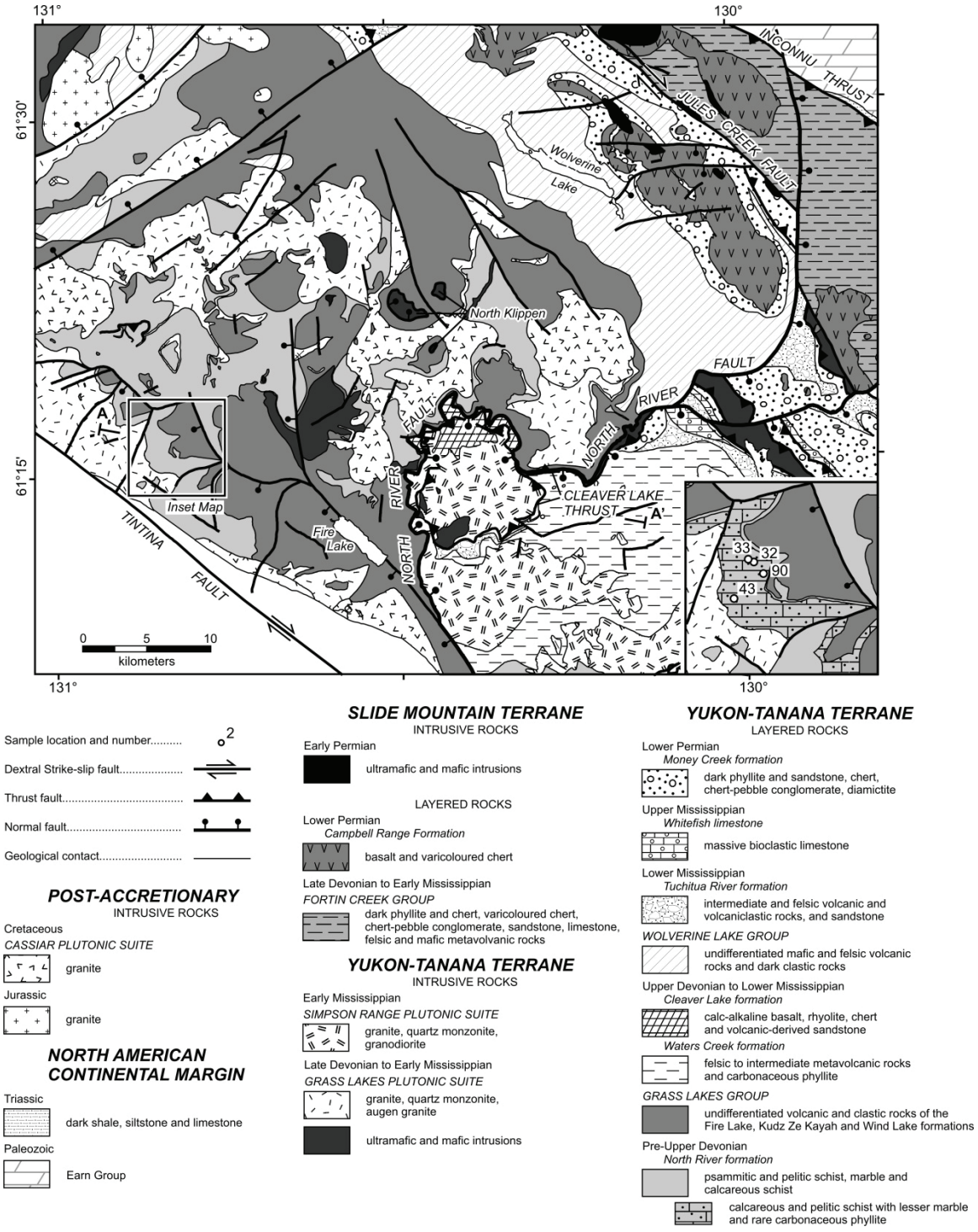

Figure 3.3. Geological map of a portion of the Finlayson Lake district showing the position of the sample locations within the footwall of the mid-Cretaceous North River fault, and immediately east of the Tintina fault. Labels A and A' locate the end points of line of section for the cross-section in Fig. 3.4. Map modified from Murphy et al. (2006).

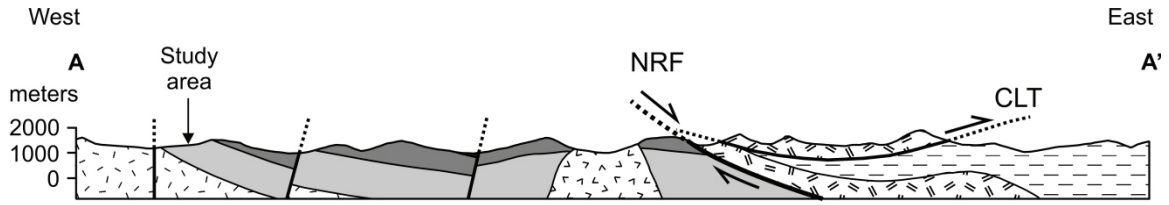

Figure 3.4. Cross-section from points A to A' on Figure 3, roughly perpendicular to the strike of the North River fault. This section shows that rocks of this study area are located in the footwall of the North River fault. This fault exposes ductiley deformed, amphibolite facies rocks with mid-Cretaceous K/Ar cooling ages within the footwall, against low-grade rocks with Mississippian K/Ar cooling ages in the hanging-wall to the southeast. Fault abbreviations: NRF, North River fault; CLT, Cleaver Lake thrust.

Resolving the paleogeographic setting of the Yukon-Tanana terrane in the Late Jurassic – Early Cretaceous when metamorphism and deformation documented in this study occurred, particularly with respect to what lay outboard (to the west) of the Intermontane terranes, is critical to understanding the overall dynamic of the northern Cordilleran orogen at that time. In British Columbia and southeast Alaska, the Insular terranes (Peninsular–Alexander–Wrangellia) lie west of the Yukon-Tanana terrane, with the Alexander terrane lying structurally beneath rocks correlated with the Yukon-Tanana and Stikine terranes (Gehrels, 2001, 2002; Saleeby, 2000). Evidence for the initial accretion of the Alexander terrane to western Yukon-Tanana terrane in British Columbia and southeastern Alaska in the Middle to Late Jurassic include: (i) the presence of detrital zircons derived from both the Alexander and Yukon-Tanana terranes in Upper Jurassic – Lower Cretaceous strata of the Gravina belt (Kapp and Gehrels, 1998), (ii) depositional overlap of Middle Jurassic (c. 175 Ma) volcanic rocks and Upper Jurassic – Lower Cretaceous strata of the Gravina belt on both the Alexander and Yukon-Tanana terranes (Gehrels, 2001), (iii) the presence of Late Jurassic (c. 162-140 Ma) dikes that cross cut a low-angle ductile tectonic boundary between Yukon-Tanana terrane and the structurally underlying Alexander terrane in southeastern Alaska (Saleeby, 2000), and (iv) an Early to Middle Jurassic shear zone within and along the eastern margin of the Alexander terrane further north in southeastern Alaska (McClelland and Gehrels, 1990).

In contrast, to the north, in mainland Alaska, earliest estimates of Insular terranes accretion are Late Jurassic, based on the cessation of magmatism, uplift and exhumation of the Talkeetna arc (Peninsular terrane) and deposition of conglomerates in the Late Jurassic (Clift et al., 2005; Trop and Ridgway, 2007). However, Hults et al. (2013) interpret the presence of two Jura-Cretaceous flysh belts separated by a Late Cretaceous deformation zone, each basin receiving detritus solely from Wrangellia (to the south) or the previously accreted Yukon-Tanana and Farewell terranes (to the north), to indicate that Wrangellia did not accrete to Yukon-Tanana terrane until the Late Cretaceous. These studies from different parts of the Insular-Intermontane terrane boundary imply that accretion of the Insular terranes outboard of Yukon-Tanana terrane was diachronous, with oblique collision initiating in the south and younging to the northwest.

After restoring approximately 430 kilometres of dextral offset along the Tintina fault in the Paleogene, and 60 kilometres of extension in the Cretaceous (Gabrielse et al., 2006), as well as approximately 300-400 km of dextral displacement along the Denali fault (Eisbacher, 1976; Lowey, 1998, and references therein), the Finlayson Lake district of Yukon-Tanana restores east of Wrangellia in mainland Alaska. However, Nelson et al. (2013) suggest that in mid-Cretaceous (c. 120–90 Ma) a crustal block comprising the Intermontane terranes (including the Yukon-Tanana terrane) was bound by a set of roughly coeval sinistral and dextral strike-slip faults systems and was extruded to the northwest. Total motion on the dextral system is estimated at about 250 km (Nelson et al., 2013), with as much as 400-800 km of sinistral displacement estimated along the western fault system (Monger et al., 1994; Nelson et al., 2013). Further restoration along these fault systems places the Finlayson Lake district to the east of the Insular terranes of coastal British Columbia and southeast Alaska, where their accretion to the Yukon-Tanana terrane occurred in Middle to Late Jurassic (McClelland et al., 1992; van der Hayden, 1992, Saleeby, 2000; Gehrels, 2001; Trop and Ridgway, 2007).

3.4. Petrological Analytical Methods

3.4.1. Microprobe and Conventional Garnet-Biotite Thermometry

Mineral compositions were quantitatively analyzed using a fully automated CAMECA SX-50 instrument, operating in wavelength-dispersion mode with the following operating conditions: excitation voltage, 15 kV; beam current, 20 nA (10 nA for micas); peak count time, 20 s (40 s for F, Cl); background count-time, 10 s (20 s for F, Cl); spot diameter, 5 μm. Quantitative data were obtained for garnet and biotite (Table 3.1). Garnet end-member compositions were calculated using a Fe^{3+} content estimated from charge balance and stoichiometry (e.g., Droop, 1987). Temperatures were calculated using the winTWQ program (version 2.32; Berman, 2007), which uses internally consistent thermodynamic data for end-members and mixing properties to calculate an independent set of equilibria. The following garnet-biotite thermometer was used: (mineral abbreviations after Kretz, 1983).

$$Alm + Phl = Pyr + Ann \quad (1)$$

The winTWQ software incorporates solid solution models for garnet and biotite (Berman, 2007). Absolute errors of thermometric data are considered to be approximately ± 50 °C (Berman, 1991), with appreciably smaller errors associated with relative differences between samples. Pressures based on garnet-plagiolcase equilibria were not calculated because of the low anorthite content (X_{An}, = < 10%), which reduces the reliability of the geobarometric estimates (Ashworth and Evirgen, 1985; Todd, 1998).

Table 3.1. Microprobe analyses used in P-T calculations.

	Mineral composition							
	Sample 11RS033				Sample 11RS043			
	Grt core	Grt near-rim	Grt rim	Bt	Grt core	Grt near-rim	Grt rim	Bt
Oxides (wt%)								
SiO_2	36.23	36.91	36.93	36.33	36.60	36.37	36.84	35.23
TiO_2	0.13	0.08	0.02	2.25	0.05	0.07	0.05	1.90
Al_2O_3	21.17	21.38	21.23	19.16	20.99	21.37	21.24	19.21
FeO[a]	31.80	36.22	36.62	20.16	32.25	36.72	36.59	20.75
MgO	0.97	2.02	2.78	8.95	0.92	2.43	3.08	9.15
MnO	3.98	0.13	0.16	0.00	4.26	0.10	0.10	0.06
CaO	4.80	3.54	2.17	0.01	4.32	2.64	1.99	0.09
Na_2O	0.12	0.02	0.03	0.32	0.12	0.04	0.04	0.26
K_2O	N.D.[b]	N.D.	N.D.	8.52	N.D.	N.D.	N.D.	7.04
Total	99.20	100.32	99.95	96.38	99.52	99.74	99.92	94.26
Cations								
Oxygen	12	12	12		12	12	12	
Si	2.96	2.97	2.98	2.74	2.99	2.94	2.97	2.71
Ti	0.01	0.01	0.00	0.13	0.00	0.00	0.00	0.11
Al	2.04	2.03	2.02	1.70	2.02	2.04	2.02	1.74
[c]Fe^{3+}	0.02	0.02	0.02	0.00	0.00	0.07	0.04	0.00
Fe^{2+}	2.16	2.42	2.45	1.27	2.20	2.42	2.42	1.33
Mn	0.28	0.01	0.01	0.00	0.30	0.01	0.01	0.00
Mg	0.12	0.24	0.33	1.01	0.11	0.29	0.37	1.05
Ca	0.42	0.31	0.19	0.00	0.38	0.23	0.17	0.01
Na	N.D.	N.D.	N.D.	0.05	N.D.	N.D.	N.D.	0.04
K	N.D.	N.D.	N.D.	0.82	N.D.	N.D.	N.D.	0.69
Fe/(Fe + Mg)	0.95	0.91	0.88	0.56	0.95	0.89	0.87	0.56
X_{Alm}[d]	0.726	0.813	0.821	N.A.[e]	0.737	0.821	0.815	N.A.
X_{Pyr}	0.040	0.082	0.112	N.A.	0.038	0.100	0.125	N.A.
X_{Grs}	0.140	0.101	0.062	N.A.	0.126	0.075	0.057	N.A.
X_{Sps}	0.093	0.003	0.004	N.A.	0.099	0.002	0.002	N.A.

[a] All Fe assumed to be Fe^{2+}.
[b] N.D. = Not Determined.
[c] Fe^{3+} calculated by stoichiometric constraints.
[d] $X_{Alm} = Fe^{2+}/(Fe^{2+} + Mg + Ca + Mn)$.
[e] N.A. = Not Applicable.

3.4.2. Isochemical Phase Diagram Calculations

Isochemical phase diagrams (Equilibrium assemblage diagrams) and mineral-composition isopleths were calculated in the system MnNCKFMASTO (MnO-Na_2O–CaO–K_2O–FeO–MgO–Al_2O_3–SiO_2–H_2O–TiO_2-Fe_2O_3) using the Gibbs free-energy minimization software Theriak-Domino (de Capitani and Brown, 1987; de Capitani and Petrakakis, 2010). This program utilizes the internally consistent thermodynamic dataset of Holland and Powell (1998); data set tcds55, created November 22, 2003, with the following solution models: muscovite, excluding the margarite component (Coggon and Holland, 2002), feldspar (Holland and Powell, 2003), garnet and biotite (White et al., 2007), ilmenite-hematite and magnetite-ulvospinel (White et al., 2000), chlorite, cordierite, chloritoid, staurolite and epidote (Holland and Powell, 1998). Garnet, biotite, staurolite, chloritoid, chlorite and cordierite were extended to the Mn-bearing system as outlined in Tinkham et al. (2001). All other phases were treated as pure. A pure H_2O fluid was considered in excess in all calculations. Bulk rock compositions (Table 3.2) were determined by whole rock XRF analysis from thin section offcuts. Ilmenite is the only Fe-bearing oxide, suggesting these rocks are fairly reduced. Therefore, a nominal amount of Fe_2O_3 (0.01 mol% Fe_2O_3) was added to the model system to be consistent with the garnet and biotite solution models of White et al. (2007), which incorporate Fe_2O_3.

Table 3.2. Normalized effective bulk compositions corresponding to different stages of garnet growth.

	Sample 11RS033			Sample 11RS043		
	Grt Core (point1)	Grt Near-rim (point 2)	Grt rim (point 3)	Grt Core (point1)	Grt Near-rim (point 2)	Grt rim (point 3)
Oxides (wt%)						
SiO2	61.80	62.60	62.87	57.19	58.87	59.01
TiO2	0.99	1.02	1.03	1.30	1.41	1.42
Al2O3	19.52	19.47	19.45	21.58	21.61	21.62
FeO	6.90	6.02	5.69	8.70	6.52	6.33
MgO	2.19	2.23	2.23	2.40	2.49	2.49
MnO	0.07	0.02	0.01	0.10	0.01	0.01
CaO	0.58	0.45	0.42	0.59	0.29	0.27
Na2O	1.18	1.22	1.23	1.34	1.45	1.46
K2O	3.53	3.65	3.69	3.23	3.49	3.51
H2O	3.23	3.34	3.37	3.56	3.85	3.87
Total	100.00	100.00	100.00	100.00	100.00	100.00
Cations (mol%)						
Si	49.99	50.28	50.42	45.51	46.05	46.10
Ti	0.60	0.62	0.62	0.78	0.83	0.83
Al	18.61	18.43	18.38	20.24	19.92	19.91
* Fe^{3+}	0.02	0.02	0.02	0.02	0.02	0.02
Fe^{2+}	4.67	4.04	3.82	5.79	4.27	4.14
Mn	0.05	0.01	0.01	0.07	0.01	0.01
Mg	2.64	2.67	2.67	2.85	2.90	2.90
Ca	0.50	0.39	0.36	0.50	0.24	0.23
Na	1.85	1.90	1.91	2.07	2.20	2.21
K	3.64	3.74	3.77	3.28	3.48	3.50
H	17.43	17.90	18.03	18.90	20.09	20.17
Total	100.00	100.00	100.00	100.00	100.00	100.00

* A nominal amount of Fe^{3+} was added to the system to be consistent with the use of solution models which incorporate Fe^{3+}.

3.5. Petrography and Mineral Chemistry

Four monazite-bearing samples (Fig. 3.3 inset map) that are lithologically and texturally similar were selected for in situ U-Pb monazite SHRIMP geochronology. Two of these samples (33 and 43) were selected for quantitative metamorphic (*P-T*) analysis. All investigated samples are quartz- and muscovite-rich, garnet-bearing schist that are intercalated with calcareous metapelite and meta-psammite of the 'calcareous unit' of the North River formation described by Murphy (1998) and Murphy et al. (2006). The samples contain an assemblage of Grt + St + Bt + Ms + Pl + Qtz + Ilm (after Rt). Muscovite and quartz comprise the bulk of the mineral mode (70%). Garnet constitutes approximately 15% of the mode. Biotite (5 - 10%) is much less abundant than muscovite, and staurolite and plagioclase constitute a very minor component (< 5% individually). Fine-grained tourmaline, monazite and zircon are common accessory phases.

A penetrative transposition foliation (S_T) is defined by the preferred alignment of muscovite, biotite and ribbons of quartz. This foliation wraps tightly around garnet and staurolite porphyroblasts indicating deformation outlasted growth of these porphyroblasts (Fig. 3.5A–D). Garnet ranges from 2 to 4 mm in diameter and is typically rounded and subhedral to euhedral. Garnet is symmetrically chemically zoned from core to rim (Fig. 3.6), characterized by a decrease in spessartine and Fe/(Fe + Mg), and an increase in almandine and pyrope components from core to rim, typical of prograde growth zoning (Hollister, 1966; Spear et al., 1990). All components in sample 43, as well as the spessartine component in sample 33, have a flat profile across the garnet core, suggesting rapid early growth over a short P-T interval. Zoning of the grossular component shows slightly more variation in the two samples, either decreasing from core to rim, or characterized by a slight rise outward from the core before decreasing toward the rim. The absence of discontinuities or sharp inflections in the chemical zoning profiles is most consistent with growth during a single metamorphic event. In some analyzed garnet, there is a slight rise in the Mn content at the garnet rim adjacent to quartz, suggestive of a small amount of garnet resorption during retrogression (Kohn and Spear, 2000). Despite the absence of increasing Fe/(Fe+Mg) values at the garnet rim that is characteristic of retrograde diffusional re-equilibration (Spear, 1991), the

possibility remains that the garnet rim Fe/(Fe+Mg) content may have increased by some unknown amount during cooling. A higher than peak Fe/(Fe+Mg) composition at the garnet rim may be further compounded if garnet experienced an intermittent period of garnet dissolution at the staurolite isograd, yielding an even larger underestimate of the thermal peak temperature (e.g., Florence and Spear, 1993). Chlorite occurs adjacent to garnet rims, and is interpreted to be retrograde. In a manner similar to the production of staurolite, the resorption of the garnet rim to form retrograde chlorite may remove the chemical composition reflective of peak metamorphism, resulting in an underestimate of peak metamorphism.

In samples 33 and 43, biotite within 0.4 mm of garnet has retrogressed to chlorite. Matrix biotite further than 0.4 mm from garnet has an unsystematic, slight compositional variation (Fe/(Fe+Mg) = 0.56 – 0.57). Because biotite comprises a small volume of the rock in comparison to garnet, even a small mass flux out of the rim of this Fe-rich garnet during resorption may increase the Fe/(Fe + Mg) content of biotite. Therefore, near thermal peak temperatures were calculated using garnet-biotite Fe-Mg exchange thermometry (Figs. 3.7 and 3.8) with the composition of the least Fe-enriched biotite.

Staurolite occurs as rare 0.5 mm subhedral porphyroblasts with their long axis aligned roughly parallel to S_T. Inclusions trails (S_i) within staurolite porphyroblasts appear to curve into S_T (Fig. 3.5D) suggesting staurolite growth was syn-kinematic with respect to S_T. The transposition foliation is deflected around staurolite porphyroblasts (Fig. 3.5C and 3.5D) indicating this deformation outlasted staurolite growth. Subhedral to euhedral ilmenite and ilmenite-after-rutile laths occur both as randomly oriented inclusions in garnet and as matrix phases consistently oriented parallel to the foliation.

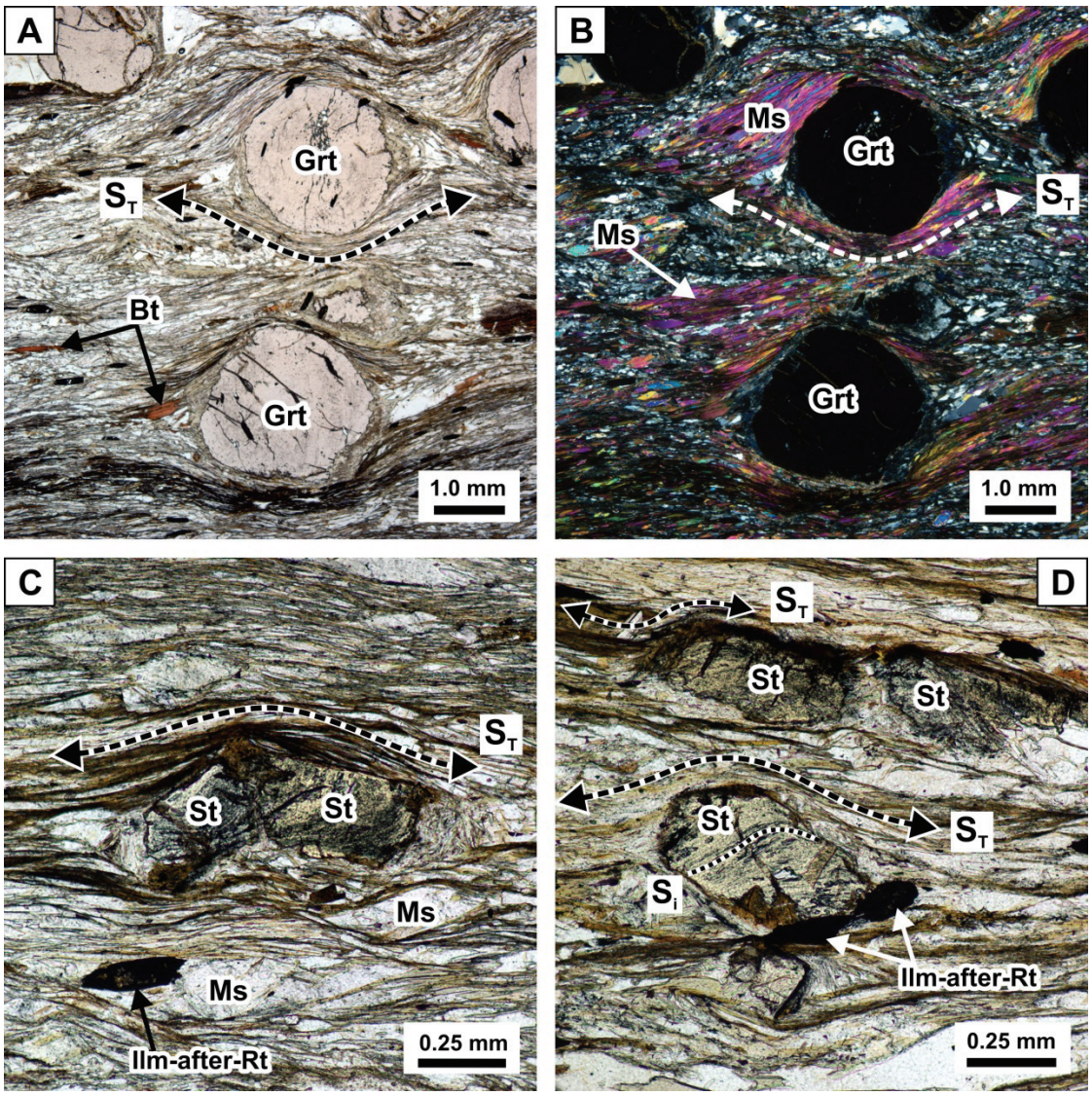

Figure 3.5. **Photomicrographs showing the deflection and tight wrapping of the transposition foliation around pre- to syn-kinematic porphyroblasts of garnet and staurolite in sample 33. Inclusions trails within staurolite porphyroblasts appear to curve into ST, suggesting staurolite growth was syn-kinematic with respect to ST. Note: All mineral abbreviations used in figures are after Kretz (1983).**

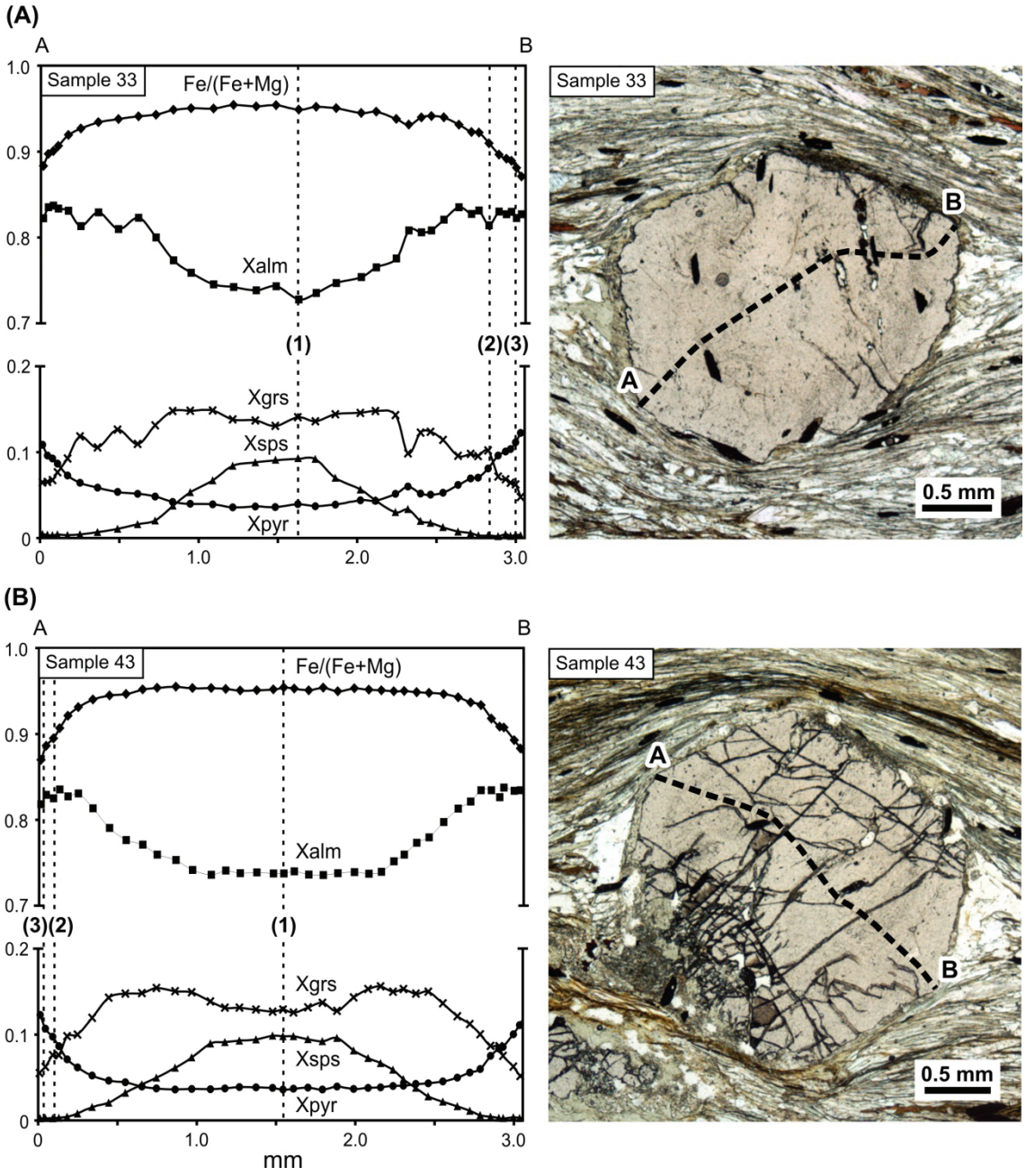

Figure 3.6. **Compositional profiles across garnet porphyroblasts of samples 33 (A), and 43 (B), with photomicrographs showing the location of the microprobe traverse across garnet. P-T estimates for points (1), (2) and (3) in garnet shown for samples 33 and 43, are given in Figures 3.6 and 3.7, respectively.**

3.6. P-T Phase Diagram Sections and Derived P-T paths

3.6.1. Garnet Isopleth Thermobarometry

P-T conditions at successive increments along the prograde P-T path were determined from the intersection of garnet end-member compositional isopleths for core, near-rim, and rim compositions. This thermobarometric method requires that the evolving surface of the growing garnet is continuously in equilibrium with all matrix phases at a scale large enough to be representative of the bulk composition of the rock. However, due to chemical inhomogeneities and sluggish intergranular element diffusivities, the length scale for equilibration may potentially be too short to satisfy the assumption of equilibrium at this scale (Chernoff and Carlson, 1997; Spear and Daniel, 2001; Hirsch et al., 2003). Most work that has found evidence for disequilibrium has done so by the identification of complex, patchy chemical zoning patterns that exhibit variations in the concentration of a single component that is anomalous, or discordant, with respect to the other end-member components (e.g., Chernoff and Carlson, 1997; Spear and Daniel, 2001; Hirsch et al., 2003). However, Mn profiles within garnet samples used in this study approach a bell shape profile (Figs. 3.6A and 3.6B), and all end-member components vary sympathetically or antithetically in a symmetric manner with respect to one another and the garnet crystal faces. This pattern suggests these elements were controlled by similar factors in the matrix, suggestive of a state of equilibrium.

Application of this technique to reconstruct a prograde P-T path from successive garnet growth increments is dependent on the evolving effective bulk composition within the equilibrium volume that is available to the reacting phases. The presence of zoned garnet porphyroblasts, which reflects the slow intragranular diffusion rates at the temperatures experienced by these rocks, indicates that chemical components within the core of garnet have been progressively isolated, or fractionated, and no longer constitute part of the effective bulk composition that is available for reaction with the matrix (Stüwe, 1997; Vance and Mahar, 1998). Several methods have been proposed to calculate effective bulk compositions affected by the fractionation of components during garnet growth (Marmo et al., 2002; Evans, 2004; Tinkham and Ghent, 2005; Zeh, 2006). For this study, we used the method described by Evans (2004) and applied by Gaidies et al.

(2006), which uses a Rayleigh fractionation model (Hollister, 1966) to quantitatively link the modal proportion of garnet with its Mn content to generate composition – modal proportion curves for garnet. The effective bulk composition at any increment of garnet growth may then be obtained by integrating these curves between the most primitive core analysis and the increment of garnet growth that is of interest, and then subtracting these values from the bulk composition of the rock. The effective bulk composition calculated for different garnet compositions along a core-rim traverse were then utilized to estimate successive P-T points along the prograde P-T path using the intersection of garnet compositional isopleths. This technique, which relies solely on the garnet composition and the correlative effective bulk composition, provides a novel solution for determining P-T conditions in rocks such as these for which plagioclase is either absent, or low in anorthite content, thus significantly limiting the availability of conventional barometers. Garnet compositions and the corresponding effective bulk rock composition used for each isopleth thermobarometric estimate are provided in Tables 3.1 and 3.2, respectively.

For garnet core compositions, the X_{Sps} isopleths plot at the point of intersection with the other end-members (Figs. 3.7A and 3.8A); however, the X_{Sps} isopleths increasingly diverge from this point of intersection for successive rimward compositions (not shown on Figs. 3.7B, 3.7C, 3.8B, and 3.8C). This increasing discrepancy of the X_{Sps} isopleth toward higher temperature and pressure with increasing distance from the garnet core is interpreted to reflect an error in the estimated extent of fractionation within garnet due to analyses of garnet that were not sectioned through the true center of the garnet. Because the spessartine component has the lowest concentration and is partitioned within garnet more strongly than the other end-members, an error in the extent of garnet fractionation will have the largest impact on the calculated Mn content. For this reason, the isopleths of X_{Alm}, X_{Pyr}, and X_{Grs} were used for intersections outside the garnet core.

3.6.2. Derived P-T Path for Sample 33

The isochemical P-T phase diagram section calculated for the unfractionated bulk composition of sample 33 (Fig. 3.7A; Table 3.2) was used to determine the pressure-temperature conditions during the incipient stages of garnet growth. Due to a

lack of suitable inclusions within the garnet cores of this sample, the intersection of the compositional isopleths for the garnet core is the only indicator of the P-T conditions during the earliest stage of growth. Because Mn is strongly fractionated within garnet during growth (Hollister, 1966), the earliest stage of garnet growth in the samples of this study is assumed to be the point within the core of the garnet porphyroblast characterized by the highest X_{Sps} content (point 1, Fig. 3.6A). The $X_{Pyr,}$ X_{Grs}, and X_{Sps} isopleths (dashed lines) from this point intersect in the Grt + Chl + Bt + Ms + Pl + Ilm + Qtz + H_2O stability field at approximately 550 °C and 6.6 kbars (Figs. 3.7A and 3.7C).

Isopleth calculations for two additional points (points 2 and 3, Fig. 3.6A) take into account the effects of chemical fractionation during garnet growth. At point 2, the isopleths intersect at approximately 580 °C and 7.4 kbars (Fig. 3.7C). The equilibrium assemblage is predicted to have remained unchanged during growth from point 1 to 2 (phase diagram calculated from the bulk composition of point 2 is not shown). The topology and equilibrium mineral assemblages at the P-T conditions predicted along the prograde path (Fig. 3.7B) are similar to Figure 7A, with the most notable exception being the significantly decreased stability field for garnet. Previous work has shown that Mn stabilizes garnet to substantially lower temperatures and pressures (Symmes and Ferry, 1992; Mahar et al., 1997; Tinkham et al., 2001). Therefore, the removal of Mn from the effective bulk composition as a result of being strongly fractionated into crystallizing garnet has the effect of progressively raising the lower garnet stability limit to higher temperatures and pressures. The staurolite stability field is slightly narrower at low pressures for this fractionated composition, but is expanded upward by approximately 0.2 – 0.3 kbar. For the composition at the garnet rim (point 3, Fig. 3.6A), the isopleths intersect within the Grt + Chl + Bt + St + Ms + Pl + Ilm (+Qtz + H_2O) stability field at approximately 595 °C and 7.3 kbars (Figs. 3.7B and 3.7C). This intersection is in good agreement with garnet-biotite thermometry (dotted line, Fig. 3.7B), and is consistent with the peak assemblage of Grt + Bt + St + Ms + Pl + Qtz + Ilm.

Rutile, which is present in sample 33 within the cores of ilmenite grains, is predicted to be stable at pressures above 8 kbar (Fig. 3.7B) at temperatures over 550 °C, and low pressures at temperatures below 500 °C (neither stability field shown in Fig. 3.7A). The presence of rutile with rims of ilmenite included in garnet and the estimate of peak P-T conditions below 8 kbar indicates a low temperature, low-pressure origin for

rutile. The compositions at points 1, 2 and 3 within garnet (Fig. 3.6A) therefore record progressive garnet growth along a clockwise P-T path initiated at 550 °C and 6.6 kbars and culminating at peak conditions at approximately 595 °C and 7.3 kbars (Fig. 3.7C).

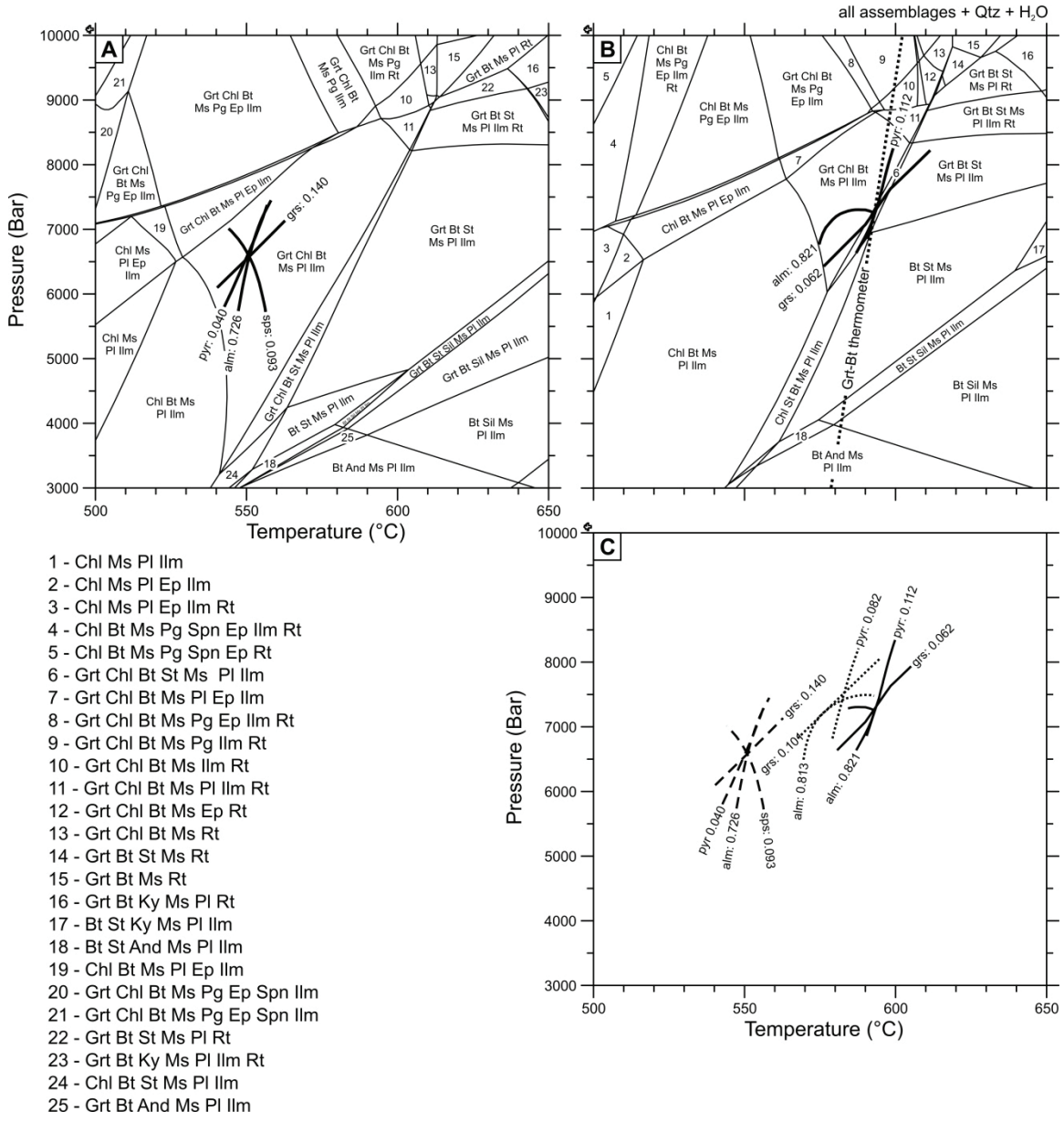

Figure 3.7. **Isochemical phase diagram sections and compositional isopleths calculated for different stages of garnet growth in sample 33. (A) Calculated from the unfractionated bulk rock composition that corresponds to the incipient stage of garnet growth (garnet core, point 1). (B) Calculated for the fractionated effective bulk rock composition that corresponds to the late stage of garnet growth (garnet rim, point 3). (C) Garnet compositional isopleths corresponding to the garnet core (point 1), near-rim (point 2) and rim (point 3) compositions, calculated from the corresponding appropriate effective bulk compositions. The equilibrium mineral assemblages listed numerically from 1 to 25 correspond to the analogous number within stability fields too small to be directly labeled in (A) and (B).**

3.6.3. Derived P-T Path for Sample 43

The isochemical phase diagram section and isopleth thermobarometry representative of the incipient stages of garnet growth (point 1, Fig. 3.6B) in sample 43 were calculated from the unfractionated bulk-rock composition of this sample (Table 3.2). Garnet compositional isopleths intersect in the Grt + Chl + Bt + Ms + Pl + Ilm (+Qtz + H2O) stability field at approximately 545 °C and 6.1 kbars (Fig. 3.8A), in good agreement with the P-T estimate for the earliest increment of garnet growth in sample 33. However, for both samples 33 and 43, the isopleth intersection for the earliest increment of garnet growth lies approximately 15-20 °C above the garnet-in line calculated for the accompanying phase diagram. This discrepancy may simply reflect the uncertainty of the thermobarometric calculations. There are several other possible explanations for this observation. During the earliest stages of garnet growth, when garnet was very small, the length scale of diffusion may have been short enough to re-equilibrate the initial core composition to the continually changing equilibrium composition imposed on the rim. For a rock following a clockwise P-T path, this modification would move the garnet core isopleth intersection toward higher temperatures than experienced during initial garnet growth. Measurement of the garnet composition from an un-centered garnet section would have a similar effect. Additionally, the placement of the garnet core isopleth intersection above the low-temperature stability limit of garnet may be due to some amount of reaction overstepping caused by a kinetic impediment to garnet nucleation such as limited volume diffusion of Mn. Assuming a larger amount of Fe_2O_3 in the model chemical system acted to shift the garnet-in line to higher temperature. However, the core isopleth intersection likewise shifted to higher temperatures, ruling out the uncertain Fe_2O_3 content as the source of discreprency between the garnet-in line and the intersection of the core isopleths.

The compositions at points 2 and 3 (Fig. 3.6B) are representative of intermediate and final stages of garnet growth, respectively; therefore, the isopleth calculations of these points take into account the effects of chemical fractionation during garnet growth. The isopleths for point 2 intersect at approximately 590 °C and 7.5 kbars (Fig. 3.8C) where biotite is added to the assemblage (phase diagram calculated from the bulk composition of point 2 is not shown). Near peak conditions of approximately 600 °C and 7.5 kbar result from the calculated isopleths corresponding to the composition of point

(3), although almandine and pyrope isopleths very narrowly (~ 2 degrees) miss intersecting. These conditions lie the upper thermal stability limit of chlorite within the assemblage Grt + Chl + Bt + St + Ms + Pl + Ilm (+Qtz + H_2O), approximately 15 °C lower than the garnet-biotite thermometer results. Similar to sample 33, the presence of rutile inclusions within garnet supports a low P-T origin for rutile prior to the incipient stages of garnet growth at 550 °C and 6.7 kbars.

The Rayleigh fractionation model used here to estimate the effective bulk composition at successive increments of garnet growth assumes a constant garnet-matrix coefficient (K_d) for Mn following the incipient stages of garnet growth. Because the equilibrium assemblage does not change until the latest increments of garnet growth, it follows that K_d is not affected by changes in phase relations. By contrast, the equilibrium constant between garnet and chlorite (the other most significant Mn-bearing phase) would be expected to vary, and thus change K_d, to some unknown extent with increasing temperature during garnet growth. However, the tight isopleth intersections from core to rim, and agreement in P-T estimates between samples 33 and 43, suggest that any potential variation in K_d had a negligible effect, and the technique appears to yield a reasonable estimate of the physical conditions during progressive stages of garnet growth.

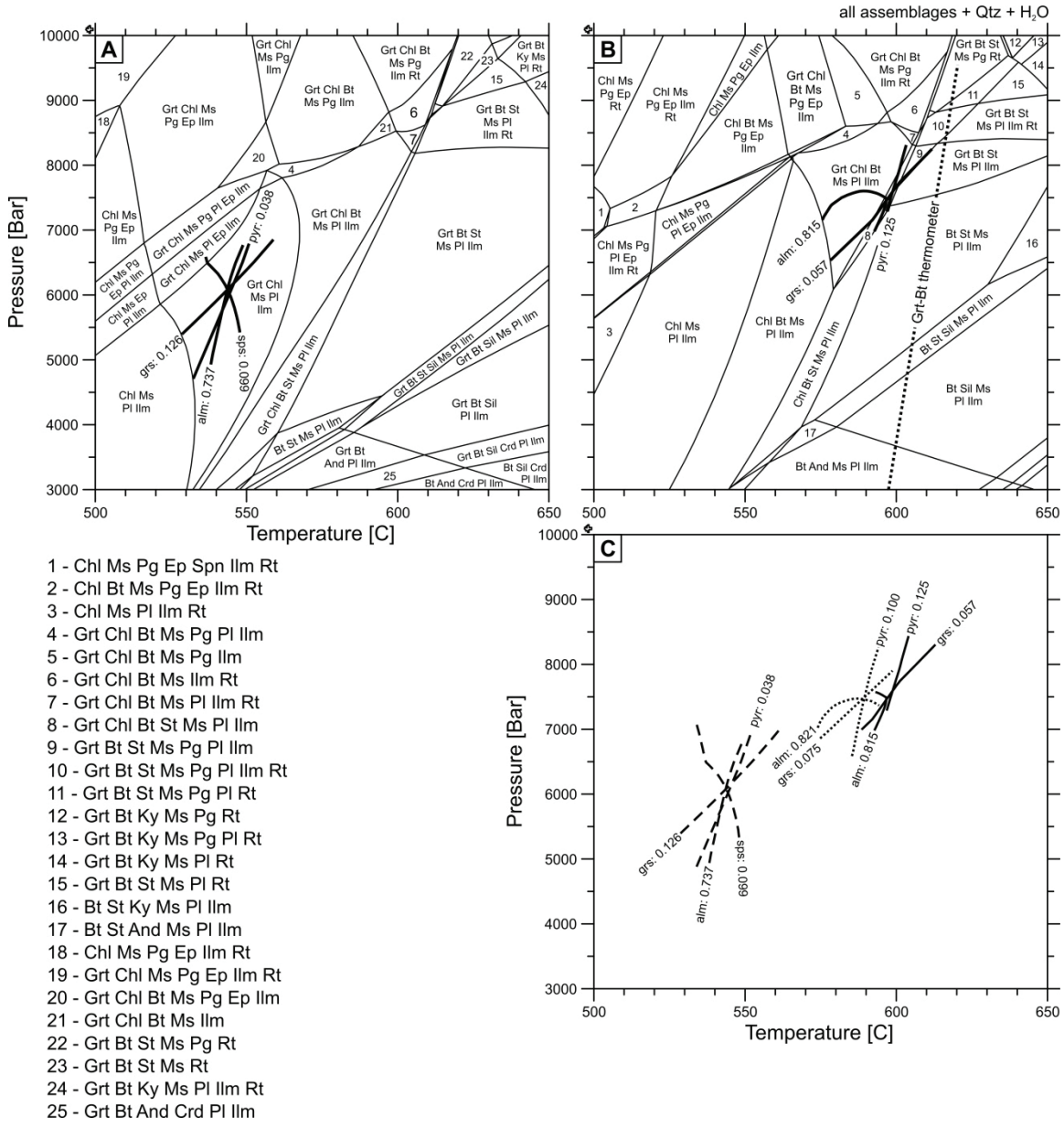

1 - Chl Ms Pg Ep Spn Ilm Rt
2 - Chl Bt Ms Pg Ep Ilm Rt
3 - Chl Ms Pl Ilm Rt
4 - Grt Chl Bt Ms Pg Pl Ilm
5 - Grt Chl Bt Ms Pg Ilm
6 - Grt Chl Bt Ms Ilm Rt
7 - Grt Chl Bt Ms Pl Ilm Rt
8 - Grt Chl Bt St Ms Pl Ilm
9 - Grt Bt St Ms Pg Pl Ilm
10 - Grt Bt St Ms Pg Pl Ilm Rt
11 - Grt Bt St Ms Pg Pl Rt
12 - Grt Bt Ky Ms Pg Rt
13 - Grt Bt Ky Ms Pg Pl Rt
14 - Grt Bt Ky Ms Pl Rt
15 - Grt Bt St Ms Pl Rt
16 - Bt St Ky Ms Pl Ilm
17 - Bt St And Ms Pl Ilm
18 - Chl Ms Pg Ep Ilm Rt
19 - Grt Chl Ms Pg Ep Ilm Rt
20 - Grt Chl Bt Ms Pg Ep Ilm
21 - Grt Chl Bt Ms Ilm
22 - Grt Bt St Ms Pg Rt
23 - Grt Bt St Ms Rt
24 - Grt Bt Ky Ms Pl Ilm Rt
25 - Grt Bt And Crd Pl Ilm

Figure 3.8. Isochemical phase diagram sections and compositional isopleths calculated for different stages of garnet growth in sample 43. (A) Calculated from the unfractionated bulk rock composition that corresponds to the incipient stage of garnet growth (garnet core, point 1). (B) Calculated for the fractionated effective bulk rock composition that corresponds to the late stage of garnet growth (garnet rim, point 3). (C) Garnet compositional isopleths corresponding to the garnet core (point 1), near-rim (point 2) and rim (point 3) compositions, calculated from the corresponding appropriate effective bulk compositions. The equilibrium mineral assemblages listed numerically from 1 to 25 correspond to the analogous number within stability fields too small to be directly labeled in (A) and (B).

3.7. Monazite Geochronology

3.7.1. Methods

Prior to U-Th-Pb analysis, petrographic and back scattered electron (BSE) images of the in situ monazite grains were obtained to provide insight into their petrological context and internal zoning, identify cracks and mineral inclusions, and guide analytical spot placement (Figs 3.9 and 3.10). In order to better characterize chemical zonation and potential age domains within individual monazite grains, chemical X-ray maps of Y, U, Th and Ca in strategically selected monazite grains were produced using a Cameca SX50 electron microprobe at the University of Massachusetts operating at a high current (240-260 nA), with small step sizes (0.25-0.62 μm) and rastering of the electron beam.

In situ U-Th-Pb analyses using the SHRIMP II at the Geological Survey of Canada in Ottawa were performed on monazite cored from polished thin sections and mounted in epoxy together with pre-polished monazite standards according to the methods of Rayner and Stern (2002). Targeted areas of monazite were analyzed using a mass-filtered O_2^- primary beam focused with a Kohler aperture to a spot measuring 9 x 12 μm. The methods employed follow the SHRIMP analytical protocols described in detail by Stern (1997), Stern and Sanborn (1998) and Stern and Berman (2000). Tera-Wasserburg and concordia plots, data regression and weighted mean calculations were made using the program ISOPLOT (Ludwig, 2008). Errors assigned to SHRIMP U–Th–Pb ages were determined using numerical propagation of all known sources of error as outlined by Stern (1997), Stern and Sanborn (1998), and Stern and Berman (2000). Uncertainties for individual analyses (ratios, ages and error ellipses) shown in Figures 3.10, 3.11 and 3.12, Tables 3.3 and 3.4, and in the text are presented at the 1σ level.

The analyses were corrected for common Pb based on the ^{204}Pb (Table 3.4) and ^{207}Pb (Table 3.3) methods following the procedures of Stern and Berman (2000) and Ireland and Gibson (1998), respectively. The two correction methods yield ages indistinguishable within error. However, considering the potential for overcorrection using the ^{204}Pb method due to errors arising from low ^{204}Pb counts, background interference and a 204 isobar (different ionic species having the same nominal mass), the ^{206}Pb/^{238}U

chronometer corrected using the ^{207}Pb method is thought to provide the most meaningful ages for this study. Accordingly, all ages quoted and displayed on the Tera-Wasserburg concordia diagram (Fig. 3.12) are based on the $^{206}Pb/^{238}U$ chronometer corrected using the ^{207}Pb method.

Although the $^{208}Pb/^{232}Th$ chronometer is considered ideal for monazite since it is not known to be affected by isotopic disequilibrium, namely unsupported ^{206}Pb (due to an excess intermediate isotope (^{230}Th) in the ^{238}U-^{206}Pb chain; Schärer, 1984), we chose not to use it because one of the three monazite standards routinely yielded a high Th-Pb age. The problem may arise from an indeterminate matrix effect, which creates an unquantifiable uncertainty in the Th-Pb ages for the monazite. Fortunately, the $^{206}Pb/^{238}U$ ages do not appear to be affected by significant excess ^{206}Pb because they are consistently younger than $^{208}Pb/^{232}Th$. Additionally, the majority of the analyses are concordant within error. If the monazite were affected by excess ^{206}Pb due to ^{230}Th disequilibrium, they would plot reversely discordant parallel to the $^{206}Pb/^{238}U$ axis. The few analyses that are reversely discordant do not plot in a vertical trend above concordia, and show no trend of increasing reverse discordance with increasing $^{208}Pb/^{206}Pb$ (the radiogenic proxy of Th/U), as would be expected if the reverse discordance was due to ^{230}Th disequilibrium. Furthermore, the excess ^{206}Pb correction of Schärer (1984) reveals that even monazite that grew from a metamorphic fluid with extremely low Th/U (0.2 - 0.8), and hence a large amount of Th fractionation (f = 16-30), should produce an excess in age no greater than 1.6 – 3.0 Ma, which is less than analytical error. Thus, despite any minor excess of ^{206}Pb, we are confident the $^{206}Pb/^{238}U$ ages provide reasonably accurate constraints within the resolution required for this study to differentiate the metamorphic and deformation events.

3.7.2. Results and Interpretation

Monazite in the four analyzed samples are all typically elongate matrix grains with an average aspect ratio of 2.5:1, and measuring between 70 and 350 μm in their longest dimension. With the exception of monazite M27 and M35, the other nine analyzed monazite grains occur within, and are aligned parallel to, the dominant penetrative transposition foliation (S_T) (Fig. 3.9; Table 3.3), which is characteristic of

nearly all observed monazite grains. Only one grain is partly enclosed within the rim of a garnet porphyroblast in sample 043.

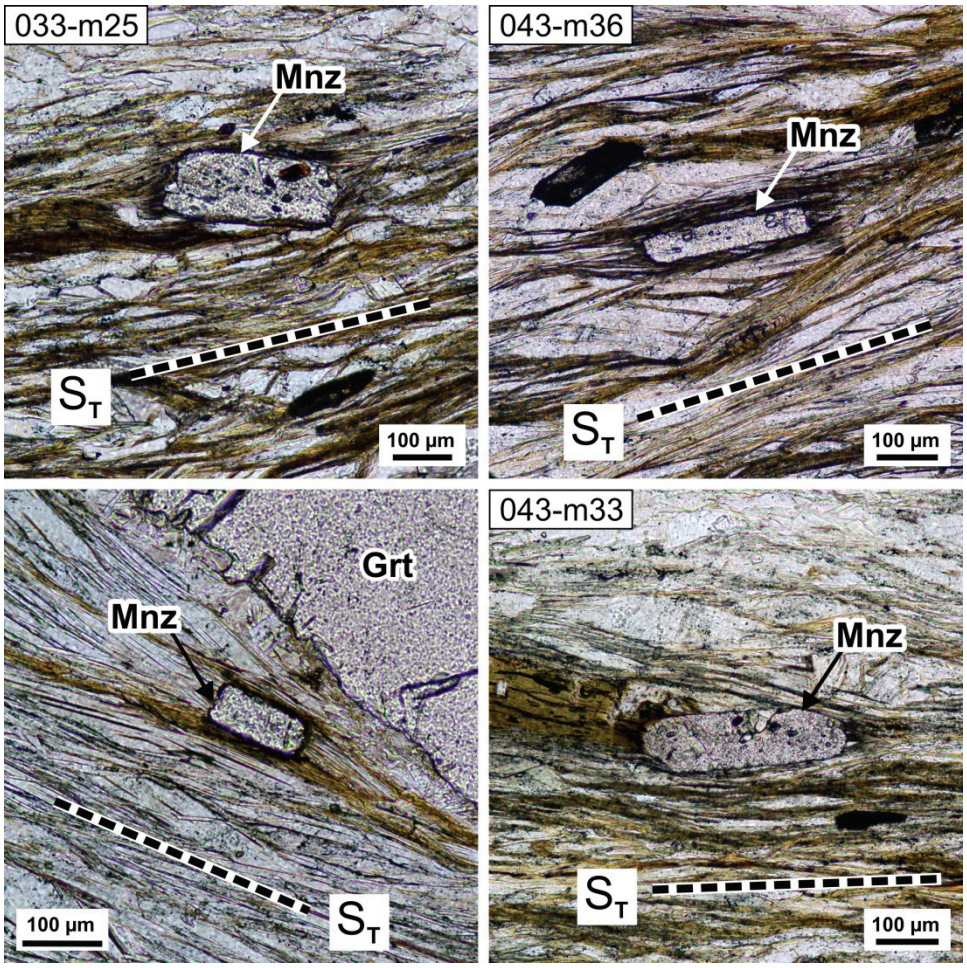

Figure 3.9. Representative photomicrographs of samples 33 and 43 showing the alignment of monazite parallel to the transposition foliation (ST), deflection of ST around monazite, and the presence of strain-caps and -shadows around monazite. These textures suggest that monazite grew prior to and/or during the development of ST. Note, monazite 043-M30 was not analyzed for U-Th-Pb geochronology.

Most monazite grains consistently display a radially symmetric zoning pattern that parallels the crystal faces, and is characterized by a Th-rich core that decreases continuously toward a low-Th rim (Fig. 3.10). This Th zoning is interpreted to reflect Rayleigh fractionation during a single episode of monazite growth (e.g., Kohn and Malloy, 2004; Pyle et al., 2005; Spear et al., 2008). Ca also decreases toward the rim, mimicking very closely the Th zoning pattern (Fig. 3.10). This similarity between Ca and

Th zoning likely reflects a brabantite substitution in which Ca^{2+} charge balances Th^{4+} in the substitution for $2REE^{3+}$.

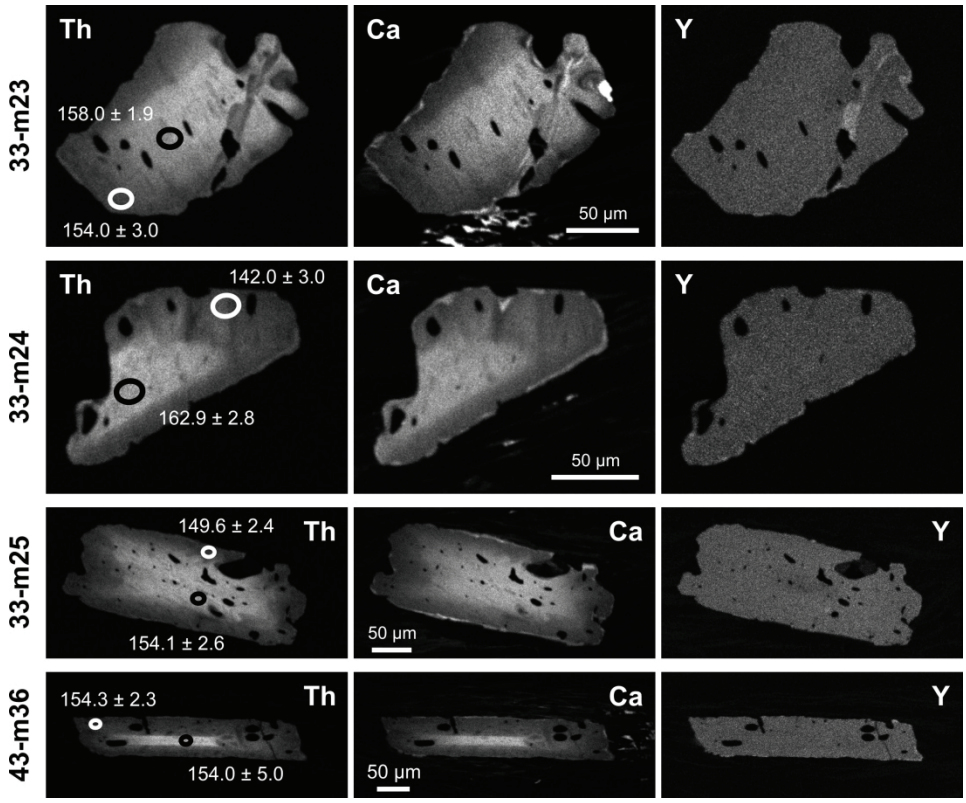

Figure 3.10. Yttrium (Y), thorium (Th), and calcium (Ca) X-ray maps of monazite representative of grains in all samples. The low, homogenous Y zoning and monotonic outward decrease in Th is interpreted to record a single episode of monazite growth while garnet was a stable phase. Ellipses on Th maps of monazite show the location and ages of SHRIMP analysis spots.

Analyses of both core and rim of all monazite grains from all four samples yield ages that range between c. 169 and 142 Ma (Fig. 3.11, Table 3.3), with individual samples also yielding a large spread in ages (up to 20 Myr). Ages from the high-Th core either agree within error, or are consistently older than the low-Th rim within any individual grain (Table 3.3). However, the high-Th core of one grain is sometimes younger than the low-Th rim of another grain, within any individual sample. This pattern is interpreted to be due to slow intergranular transport of Th, creating a localized equilibration volume that is smaller than the distance between monazite grains within a single thin-section.

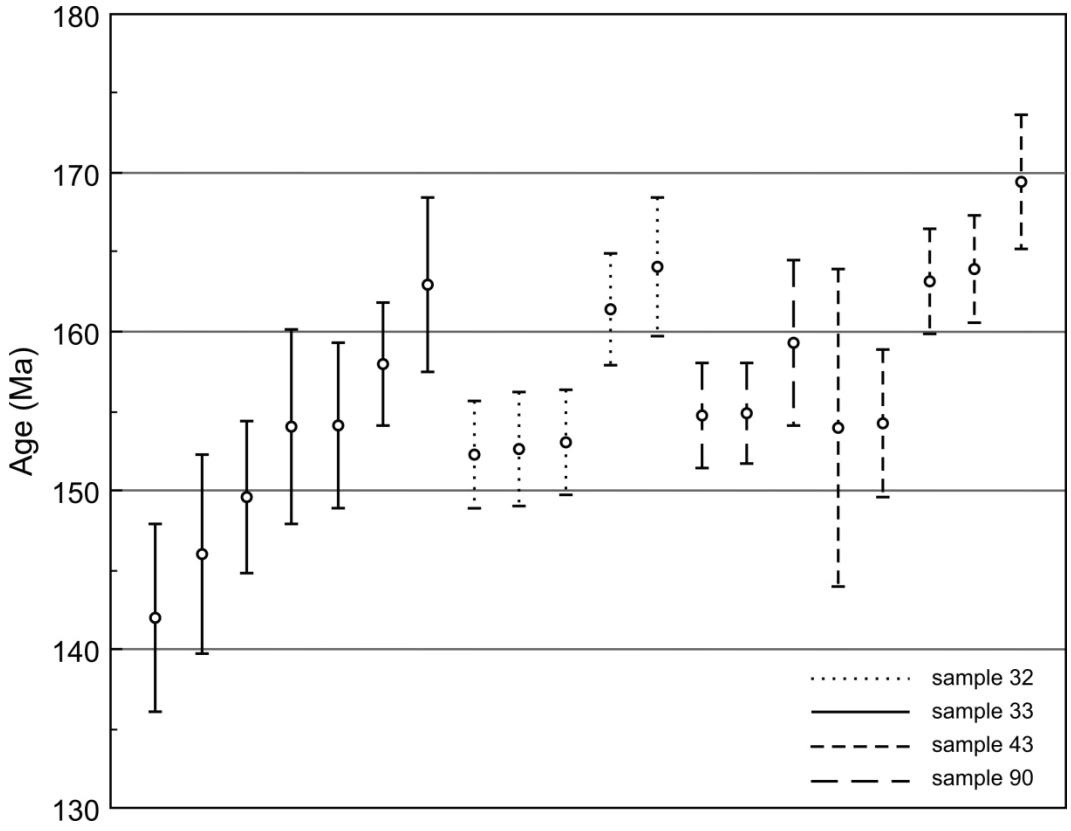

Figure 3.11. Distribution of (207Pb-corrected) $^{206}Pb/^{238}U$ ages between c. 142 and 169 Ma, with error bars at 2σ. Samples 32, 33, 43, and 90 are shown by different dotted, dashed and solid lines. Note samples with numerous analyses yield a wide range, overlapping with the range provided by all samples.

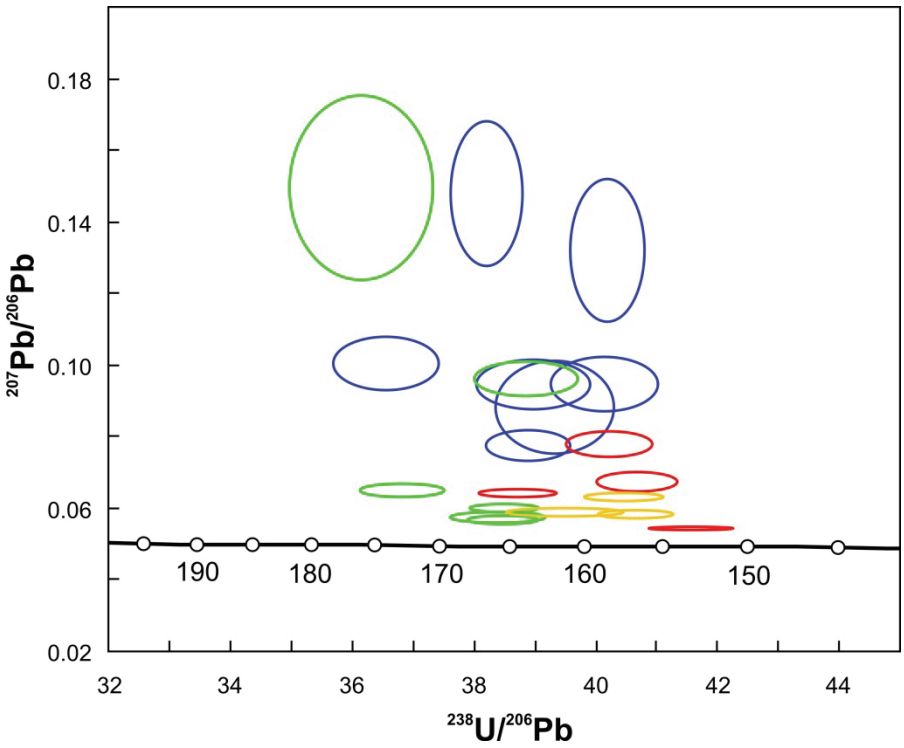

Figure 3.12. Tera-Wasserburg plot of samples 32 (red), 33 (blue), 43 (green) and 90 (yellow) showing isotopic data uncorrected for common Pb. Error ellipses represent 1σ level of uncertainty, with the ellipses of each sample shown in a different color.

The Y content is low and homogenous throughout every monazite grain imaged in this study (Fig. 3.10). Garnet and xenotime are significant reservoirs of Y in metapelitic rocks, and the prograde growth of garnet is accompanied by the consumption of xenotime (Bea and Montero, 1999; Pyle and Spear, 1999). Given the abundance of garnet porphyroblasts in these rocks, it follows that monazite grown after significant garnet crystallization should be depleted in Y, precisely as observed. The near absence of monazite inclusions in garnet further suggests that monazite grew during the late stages of garnet growth, and hence near the thermal peak of metamorphism.

The consistent alignment of monazite parallel to S_T and the deflection of S_T with strain-caps and -shadows around monazite (Fig. 3.9) suggest that monazite grew pre- to syn-development of S_T. The Th-rich core, thought to reflect Rayleigh-type fractionation of Th during early stages of monazite growth, further constrains the timing as the zoning consistently parallels the crystallographic long axis. These observations suggest that the

early stages of monazite growth occurred within the flattening plane of S_T deformation, and were therefore syn-kinematic. Syn-kinematic growth of monazite coeval with the late stages of garnet growth is consistent with the observation that S_T wraps tightly around garnet (Figs. 3.5A and 3.5B), indicating deformation was also ongoing during the latest stage of garnet growth.

The nearly continuous array of monazite ages in this study (Fig. 3.11), as well as the homogenous Y zoning and outwardly decreasing Th zoning characteristic of Rayleigh fractionation suggests a single, protracted episode of monazite growth in at least this part of the Finlayson Lake district. This interpretation is consistent with thermodynamic modeling of monazite growth in a low-Ca metapelite by Spear and Pyle (2010). They suggest that monazite can grow continuously in the subsolidus region for most reasonable metamorphic P-T paths, representing a significant portion of the metamorphic episode. In our study, the low-Y monazite and their near absence as inclusions within garnet suggest that monazite growth occurred between an initial period of garnet growth at ~ 550 °C and 6 kbar and the peak of metamorphism at ~ 600 °C and 7.5 kbar. The weighted mean of all analyses is 157 ± 2.8 Ma, and nearly half (45%) of the U-Pb monazite analyses yield ages that cluster between c. 155 and 152 Ma. This cluster may reflect a period of rapidly changing P-T conditions. Alternatively, this concentration of ages may simply be due to a small sample size, and may disappear with a larger number of analyses. The K/Ar cooling ages on Hbl, Bt and Ms from rocks at this same structural level indicate cooling through ~ 300-500 °C did not occur until the Early to middle Cretaceous (c. 140-103 Ma; Hunt and Roddick, 1992).

Table 3.3. SHRIMP U-Th-Pb analytical data for monazite corrected using the ^{207}Pb-method.

Spot[a]	Texture[b]	Grain location	Th[c]	Th/U	$^{204}Pb/^{206}Pb$	[d]f(206)^{207} (%)	$^{207}Pb/^{206}Pb$	Total $^{238}U/^{206}Pb$	Age (Ma)[e] $^{206}Pb/^{238}U$
Sample 32									
M20.1	∥ to S_T	core	high	10.0	1.189E-03 ± 1.533E-04	2.25	0.0640 ± 0.0008	38.710 ± 0.427	161.4 ± 1.8
M20.2	∥ to S_T	rim	low	8.8	1.242E-03 ± 2.262E-04	2.66	0.0673 ± 0.0017	40.684 ± 0.437	153.0 ± 1.7
M21.1	∥ to S_T	N.A.	hom	2.4	4.578E-04 ± 3.656E-05	1.04	0.0544 ± 0.0003	41.566 ± 0.461	152.3 ± 1.7
M21.2	∥ to S_T	N.A.	hom	7.4	2.515E-03 ± 4.803E-04	3.99	0.0780 ± 0.0023	40.230 ± 0.467	152.6 ± 1.8
Sample 33									
M23.3	∥ to S_T	rim	low	8.7	2.634E-03 ± 3.315E-04	5.27	0.0882 ± 0.0087	39.320 ± 0.640	154.0 ± 3.0
M23.4	∥ to S_T	core	high	14.9	1.841E-03 ± 2.302E-04	3.92	0.0774 ± 0.0028	38.877 ± 0.459	158.0 ± 1.9
M24.3	∥ to S_T	core	high	15.3	4.657E-03 ± 6.102E-04	6.80	0.1004 ± 0.0050	36.559 ± 0.574	162.9 ± 2.8
M24.4	∥ to S_T	rim	low	5.5	6.598E-03 ± 1.413E-03	10.78	0.1321 ± 0.0131	40.197 ± 0.406	142.0 ± 3.0
M25.1	∥ to S_T	rim	low	15.0	4.207E-03 ± 3.363E-04	6.08	0.0947 ± 0.0050	40.146 ± 0.583	149.6 ± 2.4
M25.2	∥ to S_T	core	high	14.7	2.855E-03 ± 3.659E-05	6.09	0.0948 ± 0.0046	38.970 ± 0.619	154.1 ± 2.6
M27.3	∟ to S_T	rim	low	8.1	7.680E-03 ± 5.433E-04	12.78	0.1481 ± 0.0134	38.211 ± 0.393	146.0 ± 3.2
Sample 43									
M30.3	∥ to S_T	rim	low	7.8	2.906E-04 ± 1.136E-04	1.31	0.0566 ± 0.0006	38.469 ± 0.396	164.0 ± 1.7
M31.3	Grt	rim	low	7.5	5.233E-04 ± 1.122E-04	1.43	0.0575 ± 0.0011	38.392 ± 0.515	164.1 ± 2.2
M31.4	Grt	core	high	13.0	1.226E-03 ± 2.077E-04	2.36	0.0650 ± 0.0013	36.820 ± 0.462	169.4 ± 2.1
M35.3	∟ to S_T	rim	low	11.6	1.026E-03 ± 1.219E-04	1.73	0.0599 ± 0.0007	38.493 ± 0.385	163.2 ± 1.6
M36.3	∥ to S_T	rim	low	8.1	3.207E-03 ± 2.923E-04	6.27	0.0962 ± 0.0032	38.852 ± 0.562	154.3 ± 2.3
M36.4	∥ to S_T	core	high	14.2	7.970E-03 ± 1.247E-03	12.95	0.1496 ± 0.0171	36.142 ± 0.781	154.0 ± 5.0
Sample 90									
M38.3	∥ to S_T	core	high	9.7	7.814E-04 ± 1.188E-04	1.52	0.0582 ± 0.0007	40.649 ± 0.418	154.9 ± 1.6
M38.4	∥ to S_T	rim	low	8.0	8.343E-04 ± 1.317E-04	1.62	0.0590 ± 0.0008	39.481 ± 0.650	159.3 ± 2.6
M41.2	∥ to S_T	N.A.	hom	9.8	1.205E-03 ± 1.362E-04	2.12	0.0630 ± 0.0007	40.458 ± 0.435	154.7 ± 1.7

[a] Spot: M20.2 = 2nd spot on monazite grain #20.

[b] Texture: location of monazite as inclusion in Grt, or as an elongate matrix grain (∥ to S_T = parallel to foliation, ∟ to S_T= at a high angle to foliation).

[c] Th: relative concentration from X-ray map at the spot of the analysis.

[d] f(206)^{207} refers to the fraction of total ^{206}Pb that is common Pb, calculated using the ^{207}Pb-method.

[e] Ages have been corrected for common Pb using the ^{207}Pb-method.

Note. Uncertainties reported at 1σ (absolute) and are calculated by numerical propagation of all known sources of error (Stern and Berman, 2000).

Table 3.4. SHRIMP U-Th-Pb analytical data for monazite corrected using the ^{204}Pb-method.

[a]Spot	[b]Texture	[c]f(206)^{204} (%)	^{208*}Pb/ ^{206*}Pb[d]	^{206*}Pb/^{238}U	^{207*}Pb/^{235}U	Corr. coeff.	^{207*}Pb/^{206*}Pb	Age (Ma) ^{207}Pb/^{235}U[e]	^{208}Pb/^{232}Th	^{206}Pb/^{238}U
Sample 32										
M20.1	ǁ to S_T	2.20	3.25	0.02527 ± 0.00029	0.1619 ± 0.0087	0.212	0.0465 ± 0.0024	152.3 ± 8.8	164.8 ± 2.1	160.9 ± 1.8
M20.2	ǁ to S_T	2.29	2.76	0.02402 ± 0.00028	0.1623 ± 0.0128	0.147	0.0490 ± 0.0038	152.7 ± 12.9	152.1 ± 1.7	153.0 ± 1.7
M21.1	ǁ to S_T	0.85	0.76	0.02385 ± 0.00026	0.1566 ± 0.0027	0.649	0.0476 ± 0.0006	147.7 ± 2.7	151.0 ± 1.6	152.0 ± 1.7
M21.2	ǁ to S_T	4.65	2.39	0.02370 ± 0.00035	0.1326 ± 0.0258	0.076	0.0406 ± 0.0079	126.4 ± 25.9	153.2 ± 2.1	151.0 ± 2.2
Sample 33										
M23.3	ǁ to S_T	4.86	2.75	0.02420 ± 0.00042	0.1651 ± 0.0350	0.083	0.0495 ± 0.0105	155.1 ± 34.9	154.7 ± 2.5	154.1 ± 2.7
M23.4	ǁ to S_T	3.40	4.79	0.02485 ± 0.00031	0.1725 ± 0.0157	0.138	0.0503 ± 0.0045	161.6 ± 15.8	160.4 ± 1.8	158.2 ± 2.0
M24.3	ǁ to S_T	8.60	4.82	0.02500 ± 0.00050	0.1044 ± 0.0394	0.053	0.0303 ± 0.0114	100.8 ± 39.3	158.6 ± 1.9	159.2 ± 3.1
M24.4	ǁ to S_T	12.20	1.92	0.02184 ± 0.00069	0.0998 ± 0.0856	0.037	0.0331 ± 0.0284	96.6 ± 83.4	152.6 ± 6.2	139.3 ± 4.3
M25.1	ǁ to S_T	7.77	4.81	0.02297 ± 0.00037	0.0995 ± 0.0246	0.065	0.0314 ± 0.0077	96.3 ± 24.7	148.1 ± 1.7	146.4 ± 2.3
M25.2	ǁ to S_T	5.27	4.59	0.02431 ± 0.00039	0.1776 ± 0.0165	0.171	0.0530 ± 0.0048	166.0 ± 16.6	152.7 ± 2.8	154.8 ± 2.4
M27.3	⊥ to S_T	14.20	2.56	0.02246 ± 0.00035	0.1016 ± 0.0565	0.028	0.0328 ± 0.0182	98.3 ± 55.8	143.8 ± 4.0	143.2 ± 2.2
Sample 43										
M30.3	ǁ to S_T	0.54	2.55	0.02586 ± 0.00027	0.1864 ± 0.0067	0.293	0.0523 ± 0.0018	173.6 ± 6.8	170.4 ± 1.9	164.6 ± 1.7
M31.3	Grt	0.97	2.45	0.02580 ± 0.00035	0.1771 ± 0.0074	0.324	0.0498 ± 0.0020	165.6 ± 7.5	168.7 ± 1.9	164.2 ± 2.2
M31.4	Grt	2.26	4.15	0.02655 ± 0.00035	0.1716 ± 0.0126	0.179	0.0469 ± 0.0034	160.8 ± 12.7	169.8 ± 2.3	168.9 ± 2.2
M35.3	⊥ to S_T	1.89	3.67	0.02549 ± 0.00026	0.1572 ± 0.0071	0.228	0.0447 ± 0.0020	148.3 ± 7.2	161.8 ± 1.9	162.2 ± 1.6
M36.3	ǁ to S_T	5.92	2.62	0.02421 ± 0.00038	0.1635 ± 0.0192	0.133	0.0490 ± 0.0057	153.8 ± 19.3	157.2 ± 1.9	154.2 ± 2.4
M36.4	ǁ to S_T	14.72	4.62	0.02360 ± 0.00082	0.0958 ± 0.0969	0.034	0.0295 ± 0.0298	92.9 ± 93.9	154.7 ± 2.5	150.3 ± 5.1
Sample 90										
M38.3	ǁ to S_T	1.44	3.08	0.02425 ± 0.00025	0.1562 ± 0.0066	0.249	0.0467 ± 0.0019	147.3 ± 6.7	155.1 ± 1.7	154.4 ± 1.6
M38.4	ǁ to S_T	1.54	2.52	0.02492 ± 0.00042	0.1605 ± 0.0078	0.345	0.0467 ± 0.0021	151.1 ± 7.8	158.0 ± 2.0	158.8 ± 2.6
M41.2	ǁ to S_T	2.23	3.11	0.02417 ± 0.00027	0.1506 ± 0.0075	0.222	0.0452 ± 0.0022	142.4 ± 7.6	154.9 ± 1.8	153.9 ± 1.7

a Spot: M20.2 = 2nd spot on monazite grain #20.
b Texture: location of monazite as inclusion in St, Ky, Crd, or as a matrix grain (ǁ = elongate monazite grain parallel to foliation).
c f(206)^{204} refers to the fraction of total ^{206}Pb that is common Pb, calculated using the ^{204}Pb-method.
d *Pb = Radiogenic Pb (corrected for common Pb using the ^{204}Pb-method).
e ^{207}Pb/^{235}U age is poorly constrained due to the low abundance of ^{207}Pb in young monazite.
Note. Uncertainties reported at 1σ (absolute) and are calculated by numerical propagation of all known sources of error (Stern and Berman, 2000).

3.8. Discussion

3.8.1. Absence of Older Permo-Triassic and Early Jurassic Metamorphism

The samples from the Finlayson Lake district record no evidence of the Permo-Triassic tectono-metamorphism that is so prominent in Yukon within the Yukon-Tanana terrane southwest of the Tintina fault (Berman et al., 2007; Beranek and Mortensen, 2011). It is possible that Permian monazite was present, but was later consumed during retrogression or via a dissolution-reprecipitation process to form new monazite in the Middle to Late Jurassic. Alternatively, monazite growth would depend upon the location within the thermal structure of the orogen. For instance, the Permian amphibolite facies metamorphism in west-central Yukon was coeval with, and is cospatial with, the arc that produced the middle to late Permian (263 – 253 Ma) Klondike assemblage (Berman et al., 2007; Nelson et al., 2006; Mortensen, 1992). Figure 3.2 shows the distribution of plutonic and volcanic rocks of the Permian Klondike assemblage and the inferred distribution of Permo-Triassic (c. 260-240 Ma; Berman et al., 2007) amphibolite facies metamorphism. As stated above, prior to offset along the Tintina fault in the Paleogene, and Cretaceous extension (Gabrielse et al., 2006), a belt of mid-Permian blueschist and eclogite facies rocks lay northeast of the Permian Klondike arc along the eastern margin of the Yukon-Tanana terrane (Erdmer et al., 1998; Creaser et al., 1997). Together, the coeval Klondike assemblage and belt of high P/T rocks reflects a middle to late Permian northeast-facing convergent margin (Nelson et al., 2006; Mortensen, 1992). The absence of a Permian metamorphic signature and the position of the Finlayson Lake district east of the Klondike arc-center and west of high P/T subduction complex eclogites suggest they occupied a position in the cool, brittle forearc region (Fig. 3.13A).

3.8.2. Revealing a younger, more protracted metamorphism

The identification of Middle Jurassic to Early Cretaceous (c. 169-142 Ma) ductile deformation and high-P, moderate-T (~7.5 kbar, 600°C) metamorphism within the Finlayson Lake district reveals a protracted and diachronous deformation and metamorphic history within the hinterland of the northern Cordilleran orogen. In the Early to Middle Triassic, detrital zircons with provenance ties to the Paleozoic arc

assemblages of the Yukon-Tanana terrane were deposited unconformably on the ancestral North American continental margin (Beranek and Mortensen, 2011), suggesting that the Yukon-Tanana terrane was on the North American continental margin and its detritus was deposited on it across the intervening Permo-Triassic suture zone. A 9 kbar and 600 °C metamorphic event is recorded within the Yukon-Tanana terrane west of the Finlayson Lake district between *c.* 260 and 239 Ma (Berman et al., 2007). This metamorphic event, and c. 260 and 253 Ma U-Pb crystallization ages of syn- and post-kinematic Permian intrusive rocks, respectively, is interpreted by Beranek and Mortensen (2011) to record the accretion of the Yukon-Tanana terrane onto the western ancestral margin of North America. In this same domain west of the Finlayson Lake district, Berman et al. (2007) documented an Early Jurassic (c. 195 Ma) metamorphic overprint characterized by a path of increasing pressure from 5.4 to 7.6 kbar (≈ 25 km depth). This Early Jurassic burial and metamorphism followed, or was partly contemporaneous with, the emplacement of Early Jurassic (c. 205 – 197 Ma; Tafti, 2005; Hood, 2012; Knight et al., 2013) granitic intrusions at moderate depths (14-23 km; McCausland et al., 2002; Tafti, 2005). Widespread Early Jurassic K/Ar and $^{40}Ar/^{39}Ar$ ages in this same domain west of the Finlayson Lake district are interpreted to record either cooling and exhumation associated with this contraction (Dusel-Bacon et al., 2002), or exhumation accommodated by a shift to extensional tectonics (Berman et al., 2007; Knight et al., 2013).

Prior to this study, there has been little evidence (Berman et al., 2007; Staples et al., 2013) for continued deep-seated tectono-metamorphism within the hinterland of the northern Cordilleran orogen following this Early Jurassic cooling event. Further south, in southwest Yukon and northern British Columbia, Middle Jurassic K/Ar and $^{40}Ar/^{39}Ar$ mica ages have been attributed to cooling and exhumation following the southwestward obduction of the Cache Creek terrane onto the Stikine terrane (Johnston et al., 1996; Mihalynuk et al., 2004). However, it is uncertain to what extent these events affected rocks in the Finlayson Lake district 350 to 500 kilometres along strike, and to the north, of the most northerly exposure of the Cache Creek terrane prior to movement along the Tintina fault (Nelson and Colpron, 2007).

Data from the Finlayson Lake district reveal renewed tectonic burial, ductile deformation and high-grade metamorphism in the northern Cordillera from Middle

Jurassic to Early Cretaceous. Therefore, while Yukon-Tanana rocks metamorphosed in the Permo-Triassic and again in the Early Jurassic occupied a high structural level from Early Jurassic onward, rocks to the northeast in the Finlayson Lake district occupied a lower structural level, being buried, heated and ductiley deformed at mid-crustal levels (~25 km depth) from the Middle Jurassic to earliest Cretaceous (c. 169 – 142 Ma). Metamorphism continued at an even deeper crustal level (~ 30 km depth, as recorded in the Australia Mountain domain), propagating downward into the parautochthonous North American crust in the Early to mid-Cretaceous (c. 146 – 118 Ma; Berman et al., 2007; Staples et al., 2013). This Early to mid-Cretaceous domain is exposed in a tectonic window juxtaposed against the Permo-Triassic/Early Jurassic metamorphic domain to the southwest across the Australia Creek normal fault and bounded on its northeast by the Tintina fault (Fig. 3.2; Staples et al., 2013). This domain is comparable to parautochthonous North American continental margin rocks (Lake George assemblage in Fig. 3.1) in east-central Alaska, which were exhumed from beneath the Yukon-Tanana terrane along mylonitic extensional faults in the mid-Cretaceous (Hansen, 1990; Hansen and Dusel-Bacon, 1998; Dusel-Bacon et al., 1995, 2002, 2006). Together, these data reveal a spatial and temporal pattern of structurally downward younging deformation and metamorphism.

Additionally, the apparent absence of Permo-Triassic and Early Jurassic metamorphism in the younger and deeper structural domains (Finlayson Lake district and Australia Mountain), suggests that deformation and metamorphism migrated progressively into cooler rocks. This suggests that the downward propagation of deformation and metamorphism corresponded with the foreland-directed growth of the orogenic wedge. As the orogenic wedge propagated toward the foreland, cooler rocks in front of the wedge were progressively buried and heated as they were underthrust beneath the warmer overriding wedge to the west.

Despite this apparent foreland-directed younging of deformation and metamorphism, the c. 146-118 Ma Australia Mountain metamorphic domain lies southwest (outboard) of the older (c. 169-142 Ma) Finlayson Lake metamorphic domain (Fig. 3.2). However, prior to accretion, the Australia Mountain domain is interpreted to have originally lain east of the Finlayson Lake domain (Yukon-Tanana terrane) based on the interpretation that it represents parautochthonous North American margin rocks. The

present exposure of the Australia Mountain domain west of the Finlayson Lake district is attributed to underthrusting down to the west beneath the Finlayson Lake district in Early Cretaceous, following burial and metamorphism of the Finlayson Lake district. K/Ar cooling ages (Hunt and Roddick, 1992) and retrograde monazite ages (Staples et al., 2013) reveal that both the Australia Mountain and Finlayson Lake metamorphic domains did not cool appreciably until they were exhumed along the mid-Cretaceous Australia Creek, Stewart River and North River faults (Fig. 3.2; Murphy, 2004; Staples et al., 2013). Focused exhumation along the Australia Creek and Stewart River faults relative to the North River fault can explain the exposure of the youngest and deepest crustal level found in the Australia Mountain domain (9 kbar metamorphism) west (outboard) of the Finlayson Lake district (7.5 kbar metamorphism). Comparable exhumation of parautochthonous rocks of the Lake George assemblage occurred <200 km to the east in east-central Alaska (Dusel-Bacon et al., 1995, 2002; Hansen and Dusel-Bacon, 1998).

The Middle Jurassic to Early Cretaceous metamorphic event recorded in the Finlayson Lake district in the northern Cordillera was contemporaneous with amphibolite facies metamorphic events recorded in the southern Cariboo and northern Monashee Mountains in the southeastern Canadian Cordillera (c. 135 Ma, Currie, 1988; c. 140 Ma, Digel et al., 1998; c. 163 Ma, Crowley et al., 2000; c. 148 Ma, Reid, 2003; c. 153 Ma, Gervais and Hynes, 2012). Furthermore, this pattern of structurally downward younging deformation and metamorphism described above is strikingly similar to, and in part contemporaneous with, that of the southeastern Canadian Cordillera. In the southeastern Canadian Cordillera, deformation and metamorphism progressed from Early Jurassic to Eocene (Evenchick et al., 2007, and references therein), with younger events recorded at progressively deeper crustal levels (Parrish, 1995; Simony and Carr, 2011). There, rocks presently in the upper structural levels were buried, heated and exhumed in the Jurassic (Murphy et al., 1995; Colpron et al., 1996; Crowley et al., 2000; Gibson et al., 2005, 2008), while structurally deeper levels continued to be buried and heated from Cretaceous to earliest Eocene (Carr, 1991; Parrish, 1995; Gibson et al., 1999, 2005, 2008; Crowley and Parrish, 1999; Crowley et al., 2000; Simony and Carr, 2011). This pattern has been attributed to progressive structural burial and underplating of cooler rocks to the east as deformation migrates toward the craton (Parrish, 1995; Brown, 2004; Simony and Carr, 2011).

We propose that a similar process was active from Middle Jurassic to mid-Cretaceous time in the northern Cordillera. The foreland-directed and downward migration of deformation and metamorphism is interpreted to have been driven by continued migration and underthrusting of the North American continent from the east, together with the accretion and underthrusting of the Insular terranes (Peninsular-Alexander-Wrangellia) beneath the western side of Yukon-Tanana terrane in the Middle to Late Jurassic (Fig. 3.13B; McClelland et al., 1992; van der Heyden, 1992, Saleeby, 2000; Gehrels, 2001; Trop and Ridgway, 2007). These results suggest that analogous orogenic processes may have been operating contemporaneously over 1000 kilometers along strike during the development of the Canadian Cordillera, and is a model that may have implications for unravelling the history of other orogenic belts around the world.

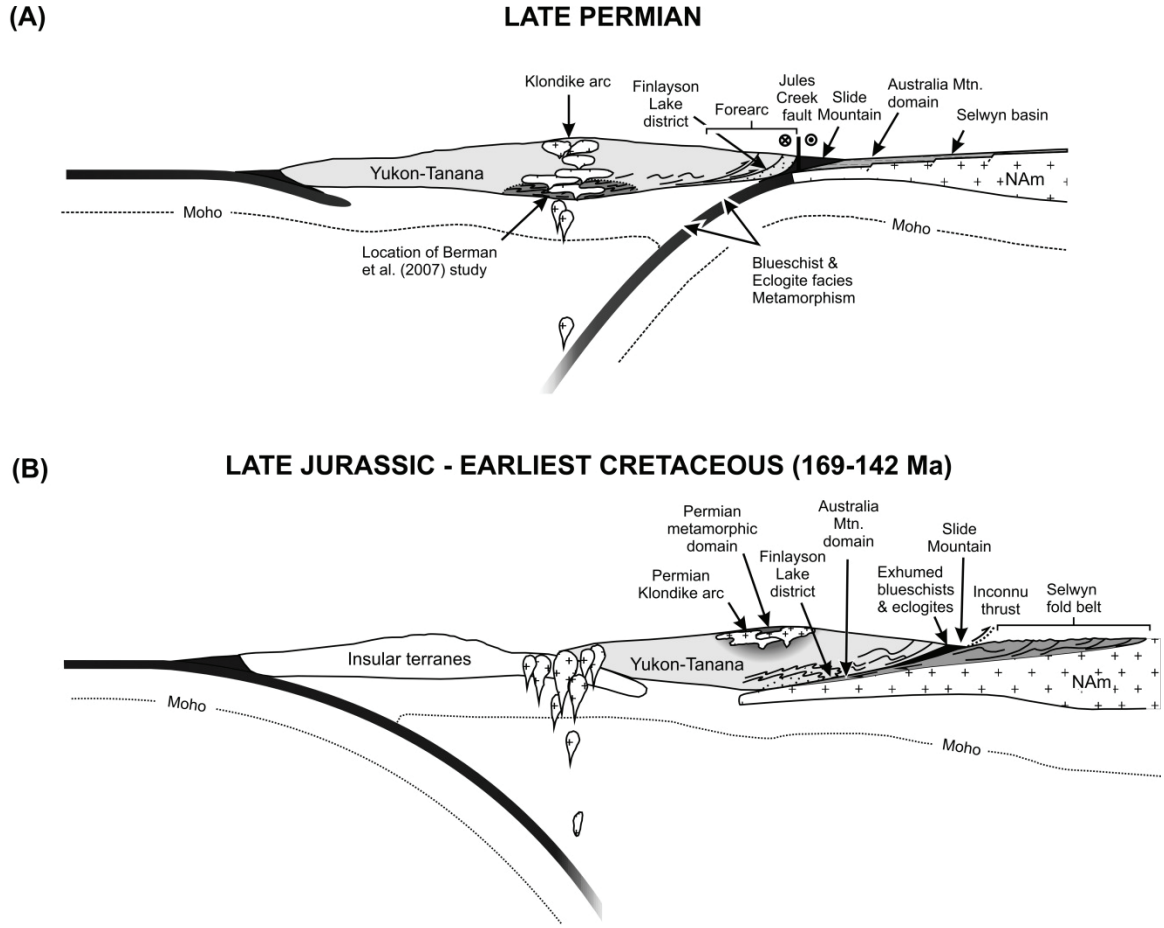

Figure 3.13. **Schematic crustal sections (not drawn to scale) of the northern Cordilleran margin showing the interpreted crustal position of the Finlayson Lake and other metamorphic domains before and during Mesozoic deformation and metamorphism of Yukon-Tanana terrane. (A) In Late Permian, the Finlayson Lake domain lied in the forearc region with respect to the Klondike domain. The Australia Mountain domain is inferred to have originated in distal extension of the ancestral North American margin prior to underthrusting beneath Yukon-Tanana terrane. This time frame post-dates extreme thinning of the Yukon-Tanana terrane in the latest Middle Permian (Johnston et al., 2007). (B) Middle Jurassic – Early Cretaceous (c. 169–142 Ma), prior to Paleogene offset along the Tintina fault and mid-Cretaceous extension within Yukon-Tanana terrane, and after the westward underthrusting of Yukon-Tanana terrane that produced the deformation and metamorphism recorded in the Finlayson Lake district, and initial shortening in the Selwyn fold belt. At that time, the Australia Mountain domain is inferred to have begun westward underthrusting beneath Yukon-Tanana terrane en-route to peak metamorphism of 9 kbar at c. 146-118 Ma (Staples et al., 2013).**

3.9. Conclusions

In situ SHRIMP monazite geochronology and mineral equilibria modelling reveal a previously unrecognized Middle Jurassic to earliest Cretaceous tectono-metamorphic event recorded in the Finlayson Lake district of eastern Yukon-Tanana terrane. The results of garnet isopleth thermobarometry applied to successive increments of single-stage, growth-zoned garnet record progressive growth from 550 °C and 6.1-6.6 kbar to 600 °C and 7.5 kbar. Monazite textures, chemical zoning and in situ U-Pb ages record a protracted episode of monazite growth from c. 169 to 142 Ma coeval with the development of transposition fabrics and the late stages of garnet growth. The absence of evidence for Permo-Triassic ductile deformation and metamorphism that is characteristic of Yukon-Tanana terrane in Yukon further to the west, and its position between the Permian arc axis to the west and the belt of Permian blueschists and eclogites to the east, suggests the Finlayson Lake district occupied the cold, brittle forearc region in the Permian. This eastern portion of the Yukon-Tanana terrane was not buried and heated sufficiently to grow metamorphic monazite until the Middle Jurassic to earliest Cretaceous, revealing a younger, more protracted and diachronous mid-crustal tectono-metamorphic history within the hinterland of the northern Cordillera than was previously recognized. These data, together with the identification of an Early Cretaceous tectono-metamorphic domain in adjacent and structurally deep (9 kbar) parautochthonous North American rocks to the west (Australia Mountain domain, Staples et al., 2013), reveal that deformation and metamorphism migrated toward the foreland and structurally downwards in the Middle Jurassic to Early Cretaceous. This pattern and timing is similar to and coeval with events documented in the southeastern Canadian Cordillera, which have been attributed to the progressive burial of cooler rocks to the east as deformation migrates toward the craton (Parrish, 1995; Brown, 2004; Gibson et al., 2008; Simony and Carr, 2011). Deformation and metamorphism is likewise considered to have migrated toward the craton and downwards in the Middle Jurassic to Early Cretaceous in the northern Cordillera as the orogen propagated toward the foreland above the westward underthrusting North American continent.

3.10. References

Ashworth, J.R., and Evirgen, M.M., 1985, Plagioclase relations in pelites, central Menderes Massif, Turkey. II. Perturbation of garnet-plagioclase geobarometers: Journal of Metamorphic Geology, v. 3, p. 219–229.

Bea, F., and Montero, P., 1999, Behavior of accessory phases and redistribution of Zr, REE, Y, Th, and U during metamorphism and partial melting of metapelites in the lower crust: an example from the Kinzigite Formation of Ivrea–Verbano, NW Italy: Geochimica et Cosmochimica Acta, v. 63, p. 1113– 1153.

Beranek, L.P., and Mortensen, J.K., 2011, The timing and provenance record of the Late Permian Klondike orogeny in northwestern Canada and arc-continent collision along western North America: Tectonics, v. 30, TC5017, doi:10.1029/2010TC002849.

Berman, R.G., 1991, Thermobarometry using multi-equilibrium calculations: A new technique, with petrological applications: Canadian Mineralogist, v. 29, p. 833–855.

Berman, R.G., 2007, winTWQ (version 2.3): A Microsoft Windows-compatible software package for performing internally-consistent thermobarometric calculations: Geological Survey of Canada Open File, 5462.

Berman, R.G., Ryan, J.J., Gordey, S.P., and Villeneuve, M., 2007, Permian to Cretaceous polymetamorphic evolution of the Stewart River region, Yukon-Tanana terrane, Yukon, Canada: P-T evolution linked with in-situ SHRIMP monazite geochronology: Journal of Metamorphic Geology, v. 25, p. 803–827.

Brown, R.L., 2004, Thrust belt accretion and hinterland underplating of orogenic wedges: an example from the Canadian Cordillera, *in* McClay, K.R. ed., Thrust Tectonics and Hydrocarbon Systems, American Association of Petroleum Geologists, Memoir 82, p. 51–64.

Brown, R.L., Carr, S.D., Johnson, B.J., Coleman, V.J., Cook, F.A., and Varsek, J.L., 1992, The Monashee décollement of the southern Canadian Cordillera: a crustal-scale shear zone linking the Rocky Mountain Foreland belt to lower crust beneath accreted terranes, *in* McClay, K.R., ed., Thrust Tectonics: London, Chapman & Hall, p. 357–364.

Carr, S.D., 1991, Three crustal zones in the Thor-Odin-Pinnacles area, southern Omineca belt, British Columbia: Canadian Journal of Earth Sciences, v. 28, p. 2003–2023.

Chernoff, C.B., and Carlson, W.D., 1997, Disequilibrium for Ca during growth of pelitic garnet: Journal of Metamorphic Geology, v. 15, p. 421–438.

Clift, P.D., Pavlis, T., Debari, S.M., Draut, A.E., Rioux, M., and Kalemen, P.B., 2005, Subduction erosion of the Jurassic Talkeetna-Bonanza arc and the Mesozoic accretionary tectonics of western North America: Geology, v. 33, p. 881–884.

Coggon, R., and Holland, T.J.B., 2002, Mixing properties of phengitic micas and revised garnet-phengite thermobarometers: Journal of Metamorphic Geology, v. 20, p. 683–696.

Colpron, M., and Nelson, J.L., 2009, A Palaeozoic northwest passage: incursion of Caledonian, Baltican and Siberian terranes into eastern Panthalassa, and the early evolution of the North American Cordillera, *in* Cawood, P.A., and Kröner, A., eds., Earth Accretionary Systems in Space and Time: The Geological Society of London Special Publications, v. 318, p. 273–307.

Colpron, M., Price, R.A., Archibald, D.A., and Carmichael, D.M., 1996, Middle Jurassic exhumation along the western flank of the Selkirk fan structure: Thermobarometric and thermochronometric constraints from the Illecillewaet synclinorium, southeastern British Columbia: Geological Society of America Bulletin, v. 108, p. 1372–1392.

Colpron, M., Nelson, J.L., and Murphy, D.C., 2006, A tectonostratigraphic framework for the pericratonic terranes of the northern Canadian Cordillera, *in* Colpron, M., and Nelson, J. L., eds., Paleozoic Evolution and Metallogeny of Pericratonic Terranes at the Ancient Pacific Margin of North America, Canadian and Alaskan Cordillera: Geological Association of Canada Special Paper 45, p. 1–23.

Colpron, M., Nelson, J.L., and Murphy, D.C., 2007, Northern Cordilleran terranes and their interactions through time: GSA Today, v. 17, p. 4–10.

Creaser, R.A., Heaman, L.M., and Erdmer, P., 1997, Timing of high-pressure metamorphism in the Yukon–Tanana terrane, Canadian Cordillera: Constraints from U–Pb zircon dating of eclogite from the Teslin tectonic zone: Canadian Journal of Earth Sciences, v. 34, p. 709–715.

Crowley, J.L., and Parrish, R.R., 1999, U–Pb isotopic constraints on diachronous metamorphism in the northern Monashee complex, southern Canadian Cordillera: Journal of Metamorphic Geology, v. 17, p. 483–502.

Crowley, J.L., Ghent, E.D., Carr, S.D., Simony, P.S., and Hamilton, M.A., 2000, Multiple thermotectonic events in a continuous metamorphic sequence, Mica Creek area, southeastern Canadian Cordillera: Geological Materials Research, v. 2, p. 1–45.

Currie, L.D., 1988, Geology of the Allan Creek area, Cariboo Mountains, British Columbia [M.Sc. thesis]: Calgary, University of Calgary, 152 p.

de Capitani, C., and Brown, T.H., 1987, The computation of chemical equilibrium in complex systems containing non-ideal solutions: Geochimica et Cosmochimica Acta, v. 51, p. 2639–2652.

de Capitani, C., and Petrakakis, K., 2010, The computation of equilibrium assemblage diagrams with Theriak/Domino software: American Mineralogist, v. 95, p. 1006–1016.

Digel, S.G., Ghent, E.D., Carr, S.D., and Simony, P.S., 1998, Early Cretaceous kyanite-sillimanite metamorphism and Paleocene sillimanite overprint near Mount Cheadle, southeastern British Columbia: Canadian Journal of Earth Sciences, v. 35, p. 1070–1087.

Droop, G.T.R., 1987, A general equation for estimating Fe^{3+} concentrations in ferromagnesian silicates and oxides using stoichiometric criteria: Mineralogical Magazine, v. 51, p. 431–437.

Dusel-Bacon, C., and Williams, I.S., 2009, Evidence for prolonged mid-Paleozoic plutonism and ages of crustal sources in east-central Alaska from SHRIMP U-Pb dating of syn-magmatic, inherited and detrital zircon: Canadian Journal of Earth Sciences, v. 46, p. 21–39.

Dusel-Bacon, C., Hansen, V.L. and Scala, J.A., 1995, High-pressure amphibolite facies dynamic metamorphism and the Mesozoic tectonic evolution of an ancient continental margin, east-central Alaska: Journal of Metamorphic Geology, v. 13, p. 9-24.

Dusel-Bacon, C., Lanphere, M.A., Sharp, W.D., Layer, P.W., and Hansen, V.L., 2002, Mesozoic thermal history and timing of structural events for the Yukon-Tanana Upland, east-central Alaska: $^{40}Ar/^{39}Ar$ data from metamorphic and plutonic rocks: Canadian Journal of Earth Sciences, v. 39, p. 1013–1051.

Dusel-Bacon, C., Hopkins, M.J., Mortensen, J.K., Dashevsky, S.S., Bressler, J.R. & Day, W.C., 2006, Paleozoic tectonic and metallogenic evolution of the pericratonic rocks of eastcentral Alaska and adjacent Yukon, *in* Colpron, M., and Nelson, J.L., eds., Paleozoic Evolution and Metallogeny of Pericratonic Terranes at the Ancient Pacific Margin of North America, Canadian and Alaskan Cordillera: Geological Association of Canada Special Paper 45, p. 75–105.

Eisbacher, G.H., 1976, Sedimentology of the Dezadeash flysch and its implications for strike-slip faulting along the Denali fault, Yukon Territory and Alaska: Canadian Journal of Earth Sciences, v. 13, p. 1495-1513.

Erdmer, P., Ghent, E. D., Archibald, D. A., and Stout, M. Z., 1998, Paleozoic and Mesozoic high-pressure metamorphism at the margin of ancestral North America in central Yukon: Geological Society of America Bulletin, v. 110, p. 615–629.

Evans, T.P., 2004, A method for calculating effective bulk composition modification due to crystal fractionation in garnetbearing schist: Implications for isopleth thermobarometry: Journal of Metamorphic Geology, v. 22, p. 547–557.

Evenchick, C.A., McMechan, M.E., McNicoll., V.J., Carr, S.D., 2007, A synthesis of the Jurassic-Cretaceous tectonic evolution of the central and southeastern Canadian Cordillera: Exploring links across the orogen, *in* Sears, J.W., Harms, T.A., and Evenchick, C.A. eds., Whence the Mountains? Inquiries into the Evolution of Orogenic Systems: A Volume in Honor of Raymond A. Price: Geological Society of America Special Paper 433, p. 117–145.

Florence, F.P., and Spear, F.S., 1993, Influences of reaction history and chemical diffusion on P-T calculations for staurolite schists from the Littleton Formation, northwestern New Hampshire: American Mineralogist, v. 78, p. 345–359.

Gabrielse, H., Murphy, D.C., and Mortensen, J.K., 2006, Cretaceous and Cenozoic dextral orogen-parallel displacements, magmatism and paleogeography, north-central Canadian Cordillera, *in* Haggart, J.W., Monger, J.W.H., and Enkin, R.J., eds., Paleogeography of the North American Cordillera: Evidence For and Against Large-Scale Displacements: Geological Association of Canada Special Paper 46, p. 255–276.

Gaidies, F., Abart, R. de Capitani, C., Schuster, R., Connelly, J.A.D., and Reusser, E., 2006, Characterization of polymetamorphism in the Austroalpine basement east of the Tauren Window using garnet isopleth thermobarometry: Journal of Metamorphic Geology, v. 24, p. 451–475.

Gehrels, G.E., 2001, Geology of the Chatham Sound region, southeast Alaska and coastal British Columbia: Canadian Journal of Earth Sciences, v. 38, p. 1579–1599.

Gehrels, G.E., 2002, Detrital zircon geochronology of the Taku terrane, southeast Alaska: Canadian Journal of Earth Sciences, v. 39, p. 921–931.

Gervais, F., and Hynes, A., 2012, Linking metamorphic textures to U-Pb monazite in-situ geochronology to determine the age and nature of aluminosilicate-forming reactions in the northern Monashee Mountains, British Columbia: Lithos, v. 160–161, p. 250–267.

Gibson, H.D., Brown, R.L., and Parrish, R.R., 1999, Deformation-induced inverted metamorphic field gradients: an example from the southeastern Canadian Cordillera: Journal of Structural Geology, v. 21, p. 751–767.

Gibson, H. D., Brown, R.L., and Carr, S.D., 2005, U-Th- Pb geochronologic constraints on the structural evolution of the Selkirk fan, northern Selkirk Mountains, southern Canadian Cordillera: Journal of Structural Geology, v. 27, p. 1899–1924.

Gibson, H.D., Brown, R.L., and Carr, S.D., 2008, Tectonic evolution of the Selkirk fan, southeastern Canadian Cordillera: A composite Middle Jurassic–Cretaceous orogenic structure: Tectonics, v. 27, TC6007, doi:10.1029/2007TC002160.

Gordey, S. P., and Ryan, J. J., 2005, Geology, Stewart River area (115N, 115-O and part of 115J), Yukon Territory: Geological Survey of Canada Open File 4970, scale 1:250 000, 1 sheet.

Gordey, S.P., McNicoll, V.J., and Mortensen, J.K., 1998, New U-Pb ages from the Teslin area, southern Yukon, and their bearing on terrane evolution in the northern Cordillera, *in* Radiogenic age and isotopic studies: Report 11, Geological Survey of Canada Current Research 1998-F, p. 129–148.

Hansen, V.L., 1990, Yukon-Tanana terrane: a partial acquittal: Geology, v. 18, p. 365–369.

Hansen, V.L., and Dusel-Bacon, C., 1998, Structural and Kinematic evolution of the Yukon-Tanana upland tectonites, east-central Alaska: a record of late Paleozoic to Mesozoic crustal assembly: Geological Society of America Bulletin, v. 110, p. 211–230.

Hansen, V.L., Heizler, M.T., and Harrison, T.M., 1991, Mesozoic thermal evolution of the Yukon-Tanana composite terrane; new evidence from $^{40}Ar/^{39}Ar$ data: Tectonics, v. 10, p. 51–76.

Hirsch, D.M., Prior, D.J., and Carlson, W.D., 2003, An overgrowth model to explain multiple, dispersed high-Mn regions in the cores of garnet porphyroblasts: American Mineralogist, v. 88, p. 131-141.

Holland, T.J.B., and Powell, R., 1998, An internally consistent thermodynamic data set for phases of petrological interest: Journal of Metamorphic Geology, v. 16, p. 309–343.

Holland, T., and Powell, R., 2003, Activity-composition relations for phases in petrological calculations; an asymmetric multicomponent formulation: Contributions to Mineralogy and Petrology, v. 145, p. 492–501.

Hollister, L.S., 1966, Garnet zoning: An interpretation based on Rayleigh fractionation Model: Science, v. 154, p. 1647–1651.

Hood, S.B., 2012, Mid-crustal Cu-Au mineralization during episodic pluton emplacement, hydrothermal fluid flow, and ductile deformation at the Minto deposit, YT, Canada [M.Sc. thesis]: Vancouver, University of British Columbia, 220 p.

Hults, C.P., Wilson, F.H., Donelick, R.A., and O'Sullivan, P.B., 2013, Two Flysch belts having distinctly different provenance suggest no stratigraphic link between Wrangellia composite terrane and the paleo-Alaskan margin: Lithosphere, v. 5, p. 575–594.

Hunt, P.A., and Roddick, J.C., 1987, A compilation of K-Ar ages, report 17, *in* Radiogenic age and isotopic studies: Report 1, Geological Survey of Canada Paper 87-2, p. 143–210.

Hunt, P.A., and Roddick, J.C., 1992, A compilation of K–Ar and ^{40}Ar–^{39}Ar ages, report 22, *in* Radiogenic age and isotopic studies: Report 6, Geological Survey of Canada Paper 92-2, p. 179–226.

Ireland, T.R., and Gibson, G.M., 1998, SHRIMP monazite and zircon geochronology of high-grade metamorphism in New Zealand: Journal of Metamorphic Geology, v. 16, p. 149–167.

Johnson, B.J., and Brown, R.L., 1996, Crustal structure and early Tertiary extensional tectonics of the Omineca belt at 51°N latitude, southern Canadian Cordillera: Canadian Journal of Earth Sciences, v. 33, p. 1596–1611.

Johnston, S.T., and Canil, D., 2007, Crustal architecture of SW Yukon, northern Cordillera: Implications for crustal growth in a convergent margin orogen: Tectonics, v. 26, doi:10.1029/2006TC001950

Johnston, S.T., Mortensen, J. K., and Erdmer, P., 1996, Igneous and metaigneous age constraints for the Aishihik metamorphic suite, southwest Yukon: Canadian Journal of Earth Sciences, v. 33, p. 1543–1555.

Johnston, S.T., Canil, D., and Heaman, L.H., 2007, Permian exhumation of the Buffalo Pitts orogenic massif, northern Cordillera, Yukon: Canadian Journal of Earth Sciences, v. 44, p. 275–286.

Kapp, P.A., and Gehrels, G.E., 1998, Detrital zircon constraints on the tectonic evolution of the Gravina belt, southeastern Alaska: Canadian Journal of Earth Sciences, v. 35, p. 1177–1180.

Knight, E., Schneider, D.A., and Ryan, J.J., 2013, Thermochronology of the Yukon-Tanana terrane, west-central Yukon: evidence for Jurassic extension and exhumation in the northern Canadian Cordillera: Journal of Geology, v. 121, p. 371–400.

Kohn, M.J., and Malloy, M.A., 2004, Formation of monazite via prograde reactions among common silicates: implications for age determinations: Geochimica et Cosmochimica Acta, v. 68, p. 101–113.

Kohn, M. J., and Spear, F., 2000, Retrograde net transfer reaction insurance for pressure-temperature estimates: Geology, v. 28, p. 1127–1130.

Kretz, R., 1983, Symbols for rock-forming minerals: American Mineralogist, v. 68, p. 277–279.

Lowey, G.W., 1998, A new estimate of the amount of displacement on the Denali fault system based on the occurrence of carbonate megaboulders in the Dezadeash Formation (Jura-Cretaceous), Yukon, and the Nutzotin Mountains sequence (Jura-Cretaceous), Alaska: Bulletin of Canadian Petroleum Geology, v. 46, p. 379-386.

Ludwig, K.R., 2008, Manual for Isoplot 3.7: A Geochronological Toolkit for Microsoft Excel, Berkeley Geochronology Center Special Publication No. 4, rev. August 26, 2008, 77 p.

Mahar, E.M., Baker, J.M., Powell, R, Holland, T.J.B, and Howell, N., 1997, The effect of Mn on mineral stability in metapelites: Journal of Metamorphic Geology, v. 15, p. 223–228.

Marmo, B.A., Clarke, G.L., and Powell, R., 2002, Fractionation of bulk rock composition due to porphyroblast growth; effects on eclogite facies mineral equilibria, Pam Peninsula, New Caledonia: Journal of Metamorphic Geology, v. 20, p. 151–165.

McCausland, P., Symons, D., Hart, C., and Blackburn, W., 2002, Paleomagnetism and geobarometry of the Granite Mountain batholith, Yukon: Minimal geotectonic motion of the Yukon-Tanana Terrane relative to North America: Yukon Exploration and Geology, p. 163–177.

McClelland, W.C., and Gehrels, G.E., 1990, The Duncan Canal shear zone: a right-lateral shear zone of Jurassic age along the inboard margin of the Alexander terrane: Geological Society of America Bulletin, v. 102, p. 1378–1392.

McClelland, W.C., Gehrels, G.E., and Saleeby, J.B., 1992, Upper Jurassic – Lower Cretaceous basinal strata along the Cordilleran margin: Implications for the accretionary history of the Alexander–Wrangellia–Peninsular Terrane: Tectonics, v. 11, p. 823–835.

Mihalynuk, M.G., Erdmer, P., Ghent, E.D., Cordey, F., Archibald, D.A., Friedman, R.M., and Johannson, G.G., 2004, Coherent French Range blueschist: subduction to exhumation in <2.5 m.y.?: Geological Society of America, v. 116, p. 910–922.

Monger, J.W.H., Price, R.A., and Tempelman-Kluit, D.J., 1982, Tectonic accretion and the origin of the two major metamorphic and plutonic welts in the Canadian Cordillera: Geology, v. 10, p. 70–75.

Monger, J.W.H., van der Heyden, P., Journeay, J.M., Evenchick, C.A., and Mahoney, J.B., 1994, Jurassic-Cretaceous basins along the Canadian Coast belt: Their bearing on pre-mid-Cretaceous sinistral displacements: Geology, v. 22, p. 175–178.

Mortensen, J.K., 1990, Geology and U-Pb geochronology of the Klondike District, west-central Yukon Territory: Canadian Journal of Earth Sciences, v. 27, p. 903–914.

Mortensen, J. K., 1992, Pre-mid-Mesozoic tectonic evolution of the Yukon-Tanana terrane, Yukon and Alaska: Tectonics, v. 11, p. 836–853.

Murphy, D.C., 1998, Stratigraphic framework for syngenetic mineral occurrences, Yukon-Tanana terrane south of Finlayson Lake: A progress report, *in* Yukon Exploration and Geology 1997, Exploration and Geological Services Division, Yukon, Indian and Northern Affairs Canada, p. 51-58.

Murphy, D.C., 2004, Devonian-Mississippian metavolcanic stratigraphy, massive sulphide potential and structural re-interpretation of Yukon-Tanana terrane south of the Finlayson Lake massive sulphide district, southeastern Yukon (105G/1, 105H/3,4,5), *in* Emond, D.S., and Lewis, L.L., eds., Yukon Exploration and Geology 2003, Yukon Geological Survey, p. 157–175.

Murphy, D.C., Colpron, M., Gordey, S.P., Roots, C.F., Abbott, J.G. and Lipovsky, P.S., 2001, Preliminary bedrock geological map of northern Finlayson Lake area (NTS 105G) Yukon Territory (1:100 000 scale). Exploration and Geological Services Division, Yukon Region, Indian and Northern Affairs Canada, Open File 2001-33.

Murphy, D.C., van der Heyden, P., Parrish, R.R., Klepacki, D.W., McMillan, W., Struik, L.C., and Gabites, J., 1995, New geochronological constraints on Jurassic deformation of the western edge of North America, southeastern Canadian Cordillera, *in* Miller, D.M., and Busby, C., eds., Jurassic Magmatism and Tectonics of the North American Cordillera: Geological Society of America Special Paper 299, p. 159–171.

Murphy, D.C., Mortensen, J.K., Piercey, S.J., Orchard, M.J., and Gehrels, G.E., 2006, Mid-Paleozoic to early Mesozoic tectonostratigraphic evolution of Yukon-Tanana and Slide Mountain terranes and affiliated overlap assemblages, Finlayson Lake massive sulphide district, southeastern Yukon, *in* Colpron, M., and Nelson, J.L., eds., Paleozoic Evolution and Metallogeny of Pericratonic Terranes at the Ancient Pacific Margin of North America, Canadian and Alaskan Cordillera: Geological Association of Canada Special Paper 45, p. 75–105.

Nelson, J.L., and Colpron, M., 2007, Tectonics and metallogeny of the Canadian and Alaskan Cordillera, 1.8 Ga to present, *in* Goodfellow, W.D., ed., Mineral Deposits of Canada: A Synthesis of Major Deposit Types, District Metallogeny, the Evolution of Geological Provinces, and Exploration Methods: Geological Association of Canada Special Publications 5, p. 755–791.

Nelson, J.L., Colpron, M., Piercey, S.J., Dusel-Bacon, C., Murphy, D.C., and Roots, C.F., 2006, Paleozoic tectonic and metallogenic evolution of the pericratonic terranes in Yukon, northern British Columbia and eastern Alaska., *in* Colpron, M., and Nelson, J.L., eds., Paleozoic Evolution and Metallogeny of Pericratonic Terranes at the Ancient Pacific Margin of North America, Canadian and Alaskan Cordillera: Geological Association of Canada Special Paper 45, p. 323–360.

Nelson, J.L., Colpron, M., and Israel, S., 2013, The Cordillera of British Columbia, Yukon and Alaska: Tectonics and Metallogeny, *in* Colpron, M., Bissig, T., Rusk, B.G., and Thompson, J.H.F., eds., Tectonics, Metallogeny, and Discovery: The North American Cordillera and Similar Accretionary Settings: Society of Economic Geologists, Special Publication 17, p. 53–109.

Parrish, R.R., 1995, Thermal evolution of the southeastern Canadian Cordillera: Canadian Journal of Earth Sciences, v. 32, p. 1618–1642.

Piercey, S.J., and Colpron, M., 2009, Composition and provenance of the Snowcap assemblage, basement to the Yukon-Tanana terrane, northern Cordillera: Implications for Cordilleran crustal growth: Geosphere, v. 5, p. 439–464.

Price, R.A., 1981, The Cordilleran foreland thrust and fold belt in the southern Canadian Rocky Mountains, *in* McClay, K.R., and Price, N.J., eds., Thrust and Nappe Tectonics: The Geological Society of London Special Publications, v. 9, p. 427–448.

Pyle, J.M., and Spear, F.S, 1999, Yttrium zoning in garnet: coupling of major and accessory phases during metamorphic reactions: Geological Materials Research, v. 1, p. 1–49.

Pyle, J.M, Spear, F.S., Cheney, J.T., and Layne, G., 2005, Monazite ages in the Chesham pond nappe, SW New Hampshire, U.S.A.: Implications for assembly of central New England thrust sheets: American Mineralogist, v. 90, p. 592–606.

Rayner, N., and Stern, R. A., 2002, Improved Sample Preparation Method for SHRIMP Analysis of Delicate Mineral Grains Exposed in Thin Sections, Geological Survey of Canada Current Research 2002-F10, p. 1–3.

Reid, L.F., 2003, Stratigraphy, structure, petrology, geochronology and geochemistry of the Hobson Lake area (Cariboo Mountains, British Columbia) in relation to the tectonic evolution of the southern Canadian Cordillera [Ph.D. thesis]: Calgary, University of Calgary, 221 p.

Saleeby, J.B., 2000, Geochronologic investigations along the Alexander–Taku terrane boundary, southern Revillagigedo Island to Cape Fox areas, southeast Alaska, *in* Stowell, H.H., and McClelland, W.C., eds., Tectonics of the Coast Mountains, southeast Alaska and coastal British Columbia: Geological Society of America Special Paper 343, p. 107–143.

Schärer, U., 1984, The effect of initial 230Th disequilibrium on young U–Pb ages: the Makalu case, Himalaya: Earth and Planetary Science Letters, v. 67, p. 191– 204.

Simony, P.S., and Carr, S.D., 2011, Cretaceous to Eocene evolution of the southeastern Canadian Cordillera: Continuity of Rocky Mountain thrust systems with zones of in-sequence mid-crustal flow: Journal of Structural Geology, v. 33, p. 1417–1434.

Spear, F.S., 1991, On the interpretation of peak metamorphic temperatures in light of garnet diffusion during cooling: Journal of Metamorphic Geology, v. 9, p. 379–388.

Spear, F.S., and Daniel, C.G., 2001, Diffusion control of garnet growth, Harpswell Neck, Maine, USA: Journal of Metamorphic Geology, v. 19, p. 179–195.

Spear, F.S., and Pyle, J.M., 2010, Theoretical modeling of monazite growth in a low-Ca metapelite: Chemical Geology, v. 273, p. 111–119.

Spear, F.S., Kohn, M.J., Florence, F.P., and Menard, T., 1990, A model for garnet and plagioclase growth in pelitic schists: Implications for thermobarometry and P-T path determinations: Journal of Metamorphic Geology, v. 8, p. 683–696.

Spear, F.S., Cheney, J.T., Pyle, J.M., Harrison, T.M., and Layne, G., 2008, Monazite geochronology in central New England: evidence for a fundamental terrane boundary: Journal of Metamorphic Geology, v. 26, p. 317–329.

Staples, R.D., Gibson, H.D., Berman, R.G., Ryan, J.J., and Colpron, M., 2013, A window into the Early to mid-Cretaceous infrastructure of the Yukon-Tanana terrane recorded in multi-stage garnet of west-central Yukon, Canada: Journal of Metamorphic Geology, v. 31, p. 729–753.

Stern, R. A., 1997, The GSC sensitive high resolution ion microprobe (SHRIMP): Analytical techniques of zircon U-Th-Pb age determinations and performance evaluation, in Radiogenic Age and Isotopic Studies: Report 10, Geological Survey of Canada, Current Research 1997-F, p. 1–31.

Stern, R. A., and Berman, R. G., 2000, Monazite U-Pb and Th-Pb geochronology by ion microprobe, with an application to in situ dating of an Archean metasedimentary rock: Chemical Geology, v. 172, p. 113–130.

Stern, R.A., and Sanborn, N., 1998, Monazite U–Pb and Th–Pb geochronology by high-resolution secondary ion mass spectrometry, *in* Radiogenic Age and Isotopic Studies: Report 11, Geological Survey of Canada Current Research 1998-F, p. 1–18.

Stevens, R.A., Mortensen, J.K., and Hunt, P.A., 1993, U–Pb and $^{40}Ar/^{39}Ar$ geochronology of plutonic rocks from the Teslin suture zone, Yukon Territory, *in* Radiogenic and isotope studies: Report 7, Geological Survey of Canada Paper 93-2, p. 83–90.

Stüwe, K., 1997, Effective bulk composition changes due to cooling: a model predicting complexities in retrograde reaction textures: Contributions to Mineralogy and Petrology, v. 129, p. 43–52.

Symmes, G.H., and Ferry, J.M., 1992, The effect of whole-rock MnO content on the stability of garnet in pelitic schists during metamorphism: Journal of Metamorphic Geology, v. 10, p. 221–237.

Tafti, R., 2005, Nature and origin of the Early Jurassic copper (-gold) deposits at Minto and Williams Creek, Carmack copper belt, western Yukon: Examples of deformed porphyry deposits [M.Sc. thesis]: Vancouver, University of British Columbia, 213 p.

Tinkham, D.K., and Ghent, E.D., 2005, Estimating P-T conditions of garnet growth with isochemical phase-diagram sections and the problem of effective bulk-composition: The Canadian Mineralogist, v. 43, p. 35–50.

Tinkham, D.K., Zuluaga, C.A., and Stowell, H.H., 2001, Metapelite phase equilibria modeling in MnNCKFMASH: the effect of variable Al_2O_3 and MgO/(MgO+FeO) on mineral stability: Geological Materials Research, v. 3, p. 1–42.

Todd, C., 1998, Limits on the precision of geobarometry at low grossular and anorthite content: American Mineralogist, v. 83, p. 1161–1167.

Trop, J.M., and Ridgway, K.D., 2007, Mesozoic and Cenozoic tectonic growth of southern Alaska: A sedimentary basin perspective, *in* Ridgway, J.M., Trop, J.M.G., Glen, and J.M., O'Neill, eds., Tectonic Growth of a Collisional Continental Margin: Crustal Evolution of Southern Alaska: Geological Society of America Special Paper 43, p. 55–94.

van der Heyden, P., 1992, A Middle Jurassic to Early Tertiary Andean–Sierran arc model for the Coast Belt of British Columbia: Tectonics, v. 11, p. 82–97.

Vance, D., and Mahar, E., 1998, Pressure–temperature paths from P–T pseudosections and zoned garnets; potential, limitations and examples from the Zanskar Himalaya, NW India: Contributions to Mineralogy and Petrology, v. 132, p. 225–245.

White, R.W., Powell, R., Holland, T.J.B., and Worley, B.A., 2000, The effect of TiO2 and Fe2O3 on metapelitic assemblages at greenschist and amphibolite facies conditions: mineral equilibria calculations in the system K_2O–FeO–MgO–Al_2O_3–SiO_2–H_2O–TiO_2–Fe_2O_3: Journal of Metamorphic Geology, v. 18, p. 497–511.

White, R.W., Powell, R., and Holland, T.J.B., 2007, Progress relating to calculations of partial melting equilibria for metapelites: Journal of Metamorphic Geology, v. 25, p. 511–527.

Zeh, A., 2006, Calculation of garnet fractionation in metamorphic rocks, with application to a flat-top, Y-rich garnet population from the Ruhla crystalline complex, central Germany: Journal of Petrology, v. 47, p. 2335–2356.

Chapter 4.

A model for diachronous ductile deformation, metamorphism and exhumation in the metamorphic hinterland of the northern Canadian Cordillera

4.1. Abstract

Structural transposition fabrics and the associated amphibolite facies metamorphism that is nearly ubiquitous in the hinterland of the northern Canadian Cordillera did not develop during a single tectono-metamorphic event. Rather, ductile deformation and amphibolite facies metamorphism developed diachronously, with events recorded in the Late Permian-Early Triassic, Early Jurassic, Middle to Late Jurassic and Early to mid-Cetaceous. Rocks deformed and metamorphosed in the Permo-Triassic and Early Jurassic were exhumed in the Early Jurassic, while rocks within the hinterland immediately to the northeast (toward the foreland) of this tectono-metamorphic domain were progressively buried and heated from Middle Jurassic to mid-Cretaceous. We suggest that from Early Jurassic to mid-Cretaceous, the allochthonous Yukon-Tanana terrane had been further obducted onto the North American continental margin, and together with the underlying parautochthonous continental margin formed an orogenic wedge that episodically propagated toward the foreland. Cooler rocks in front of the wedge were progressively buried and metamorphosed to amphibolite facies conditions from the Jurassic to Early-Cretaceous as they were underthrust into a distributed, amphibolite facies shear zone near the base of the overriding orogenic wedge. Rocks that were previously incorporated into this zone were displaced within the wedge and ultimately exhumed through the combined effects of renewed underplating at depth and compensating extensional denudation above in order to maintain a critically tapered wedge. By mid-Cretaceous, the dynamics of the orogen had changed resulting

in southeastward-directed, orogen-parallel extension and collapse of the orogen. Rocks that occupied the mid-crustal shear zone in the Middle Jurassic to Early Cretaceous were exhumed in the mid-Cretaceous along southeast-directed extensional faults, from beneath a supracrustal 'lid' that had previously been metamorphosed and ductiley deformed at amphibolite facies in the Permo-Triassic and Early Jurassic.

4.2. Introduction

Deformation and metamorphism is commonly diachronous across orogens, with multiple overprinting events. Williams (1985) illustrated the difficulty of correlating such events throughout an orogen only on the basis of structural overprinting, style, pattern of orientation and relationship of fabrics to metamorphic minerals and assemblages. However, understanding how deformation and metamorphism vary temporally throughout the orogen is critical to our understanding of the tectonic processes operating in orogenic belts.

Recent advances in phase equilibria modelling and in situ geochronological techniques present an opportunity to link the timing of accessory mineral growth (e.g. monazite) not only to specific porphyroblasts and associated P-T conditions (e.g. Foster et al., 2002, 2004; Gibson et al., 2004), but also specific deformation fabrics (e.g. Williams and Jercinovic, 2002; Berman et al., 2005, 2012). The application of these techniques makes it possible to definitively correlate or differentiate metamorphic and deformational fabrics within an area or across an orogen. For example, application of these techniques has facilitated identification of multiple metamorphic events in terrains that have been intensely reworked (e.g. Cutts et al., 2010; Berman et al., 2010, 2012). Furthermore, this approach has revealed domains with contrasting P-T-t-D histories that were previously considered a single tectono-metamorphic unit (Crowley et al., 2000; Berman et al., 2007; Horvath et al., 2010).

This chapter describes the diachronous pattern of deformation and metamorphism within the metamorphic hinterland of the northern Cordilleran orogen by reviewing previously published structural, thermobarometric, in situ U-Pb SHRIMP, K-Ar and $^{40}Ar/^{39}Ar$ data. From this analysis, it is concluded that the transposition fabrics and

the associated amphibolite facies metamorphism that is nearly ubiquitous throughout the hinterland did not develop during a single tectono-metamorphic event. Rather, ductile deformation and amphibolite facies metamorphism developed diachronously, younging both structurally downwards and northeastward toward the foreland. The transitory nature of deformation and metamorphism imply that these processes operate in different places at different times. Therefore, even though we describe a similar transposition foliation, denoted S_T, accompanied by amphibolite facies metamorphism with similar calculated P-T conditions throughout the hinterland, the diachronous nature of these processes strongly suggests they may not be correlative across the orogen.

It is suggested that this diachronous pattern may be explained by the foreland-directed growth of a critically tapered orogenic wedge. In this model, rocks in front of the wedge are episodically underthrust downward into a distributed, amphibolite facies, transposition-forming shear zone at 25 to 30 kilometres depth near the base of the overriding wedge. Rocks previously underthrust, buried and metamorphosed are progressively exhumed to higher structural levels within the wedge, as the upper crust enters a state of extension in order to maintain a critically tapered wedge. This model is akin to a similar model originally proposed by Platt (1986) and later adapted by Brown (2004) to explain a similar diachronous pattern of structurally downward younging ductile deformation in the southeastern Canadian Cordillera.

The documentation of structurally downward and northeastward (toward the foreland) younging of deformation and metamorphism is argued to be the result of continued orogen-perpendicular compression. However, data presented here suggest that by mid-Cretaceous the dynamics of the orogen had changed, resulting in southeastward-directed, orogen-parallel extension and orogenic collapse.

4.3. The Northern Cordilleran Orogen

The North American Cordilleran orogen formed as a result of the successive accretion of allochthonous terranes to the western Laurentian margin (Coney et al., 1980). The core of the northern Cordilleran orogen in British Columbia, Yukon and eastern Alaska consists of an interrelated set of magmatic arcs (Quesnel and Stikine

terranes), arcs built on continental fragments (Yukon-Tanana terrane), and an ocean basin (Slide Mountain terrane), collectively referred to as the peri-Laurentian terranes that accreted to the western Laurentian margin in Permo-Triassic time (Fig. 4.1) (Colpron et al., 2007). These rocks enclose the Cache Creek terrane – an accretionary complex consisting in part of carbonate bodies that cap seamounts or oceanic plateaus and which contain fauna that suggest portions of the Cache Creek terrane lay far to the west of the North American continent during the Permian to Middle Triassic (Orchard et al., 2001; Nelson et al., 2013).

Crustal fragments and magmatic arcs of the Insular terranes (Peninsular, Alexander and Wrangellia terranes) subsequently accreted to the outboard margin of the Yukon-Tanana and Stikine terranes starting in the Middle Jurassic (McClelland et al., 1992; van der Hayden, 1992, Saleeby, 2000; Gehrels, 2001). In the southern Canadian Cordillera, the accretion of these two composite terranes and associated crustal thickening resulted in two major metamorphic belts separated by a zone of low-grade, weakly deformed rocks of the Quesnel, Cache Creek and Stikine terranes (Monger et al., 1982). By contrast, in the northern Cordillera in west-central Yukon and east-central Alaska, amphibolite facies metamorphism is laterally continuous across the Yukon-Tanana terrane west of North American margin sedimentary rocks all the way to the Denali fault. The subsequent collision of the Insular terranes against Yukon-Tanana terrane, may have resulted in complex overprinting and reworking of earlier deformation and metamorphism within the growing northern Cordilleran hinterland.

Herein, we focus on the tectono-metamorphic history of the north-central and northeastern portions of Yukon-Tanana terrane and the structurally underlying parautochthonous continental margin rocks (outlined in Fig. 4.2), which record both the early accretionary history of the peri-Laurentian terranes with western Laurentia, as well as events coeval with the subsequent accretion of the Insular terranes. The northeast portion of the Yukon-Tanana terrane (Finlayson Lake district) is interpreted to have been offset approximately 490 kilometres to the southeast through a combined 430 kilometres of dextral strike-slip displacement along the Tintina fault in the Paleogene, and approximately 60 kilometres of extension in the Cretaceous (Roddick, 1967; Dover, 1994; Gabrielse et al., 2006). Figures 4.2, 4.3 and 4.4 show the restored position of this

offset block of the Yukon-Tanana terrane (Finlayson Lake district) relative to its counterpart to the west.

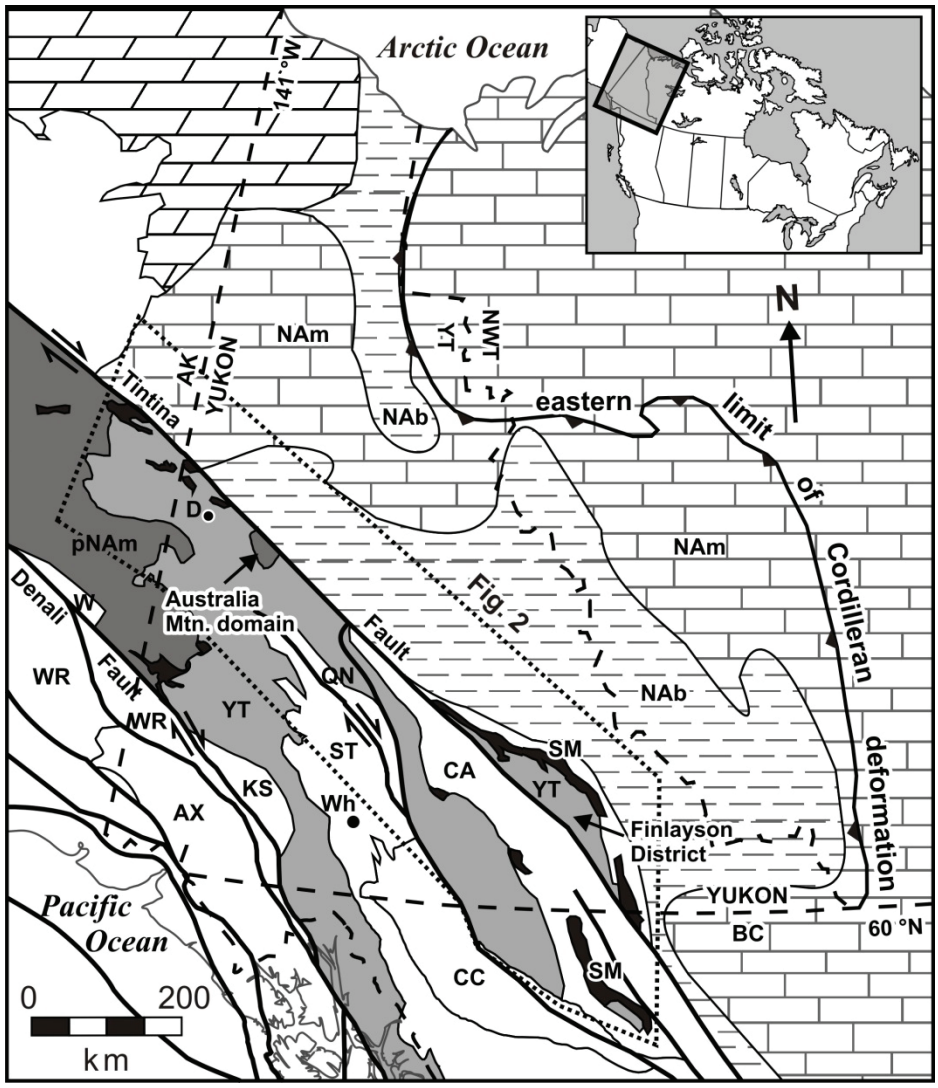

Figure 4.1. **Simplified terrane map of the northern Canadian Cordillera (modified from Colpron et al., 2006) showing location of Figure 4.2. Note, much of Yukon-Tanana terrane southwest of the Tintina fault is at amphibolite facies (cf., Read et al., 1991). D, Dawson; Wh, Whitehorse. Lithotectonic terrane abbreviations: AX, Alexander; CA, Cassiar; CC, Cache Creek; KS, Kluane Schist; NAb, North American basinal strata; NAm, North American platformal strata; pNAm, parautochthonous North American continental margin; SM, Slide Mountain; ST, Stikinia; YT, Yukon-Tanana; W, Windy; WR, Wrangellia.**

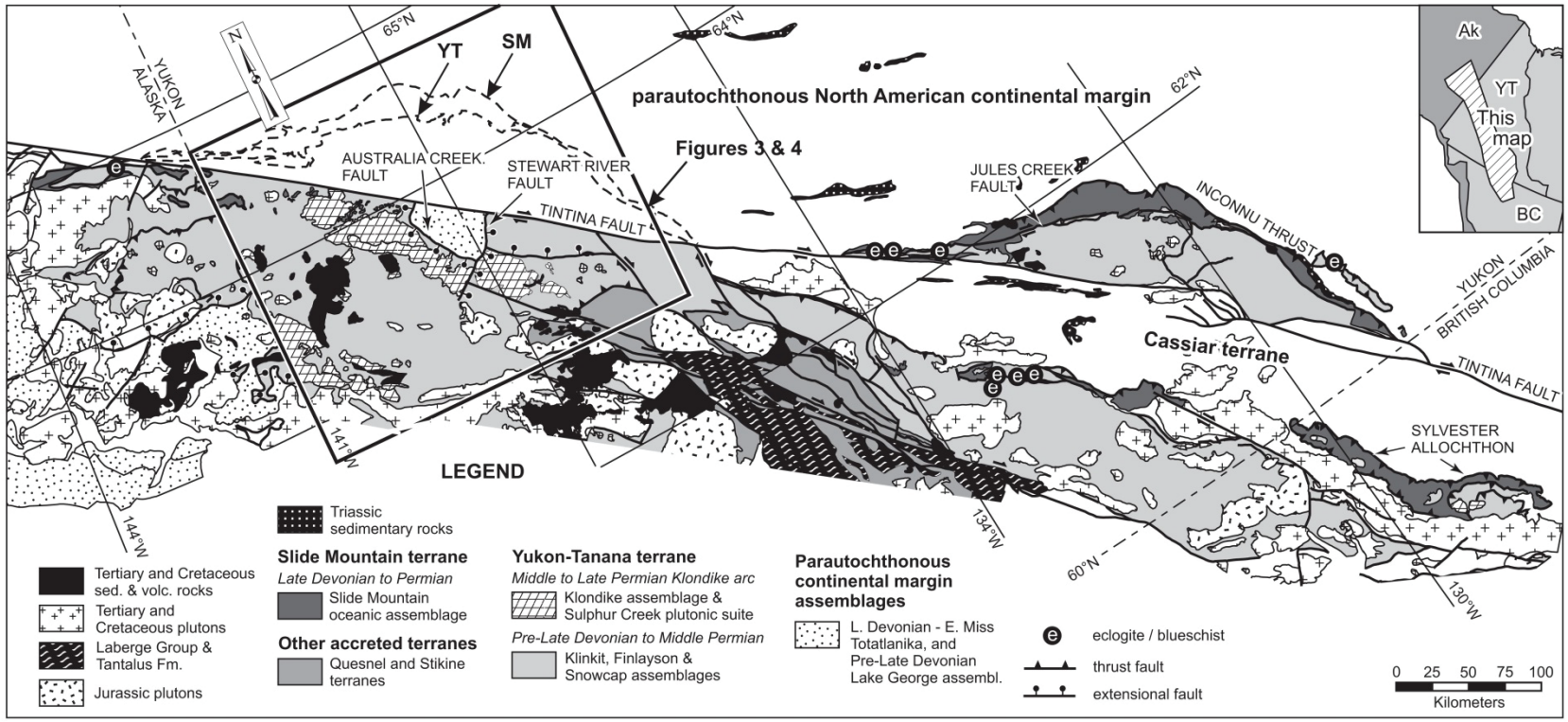
YUKON
ALASKA
65°N
64°N
62°N
60°N
141°W
144°W
134°W
130°W
YT
SM
parautochthonous North American continental margin
Figures 3 & 4
AUSTRALIA CREEK FAULT
STEWART RIVER FAULT
TINTINA FAULT
JULES CREEK FAULT
INCONNU THRUST
YUKON
BRITISH COLUMBIA
Cassiar terrane
TINTINA FAULT
SYLVESTER ALLOCHTHON
Ak
YT
This map
BC
LEGEND
Tertiary and Cretaceous sed. & volc. rocks
Tertiary and Cretaceous plutons
Laberge Group & Tantalus Fm.
Jurassic plutons
Triassic sedimentary rocks
Slide Mountain terrane
Late Devonian to Permian
Slide Mountain oceanic assemblage
Other accreted terranes
Quesnel and Stikine terranes
Yukon-Tanana terrane
Middle to Late Permian Klondike arc
Klondike assemblage & Sulphur Creek plutonic suite
Pre-Late Devonian to Middle Permian
Klinkit, Finlayson & Snowcap assemblages
Parautochthonous continental margin assemblages
L. Devonian - E. Miss Totatlanika, and Pre-Late Devonian Lake George assembl.
eclogite / blueschist
thrust fault
extensional fault
0 25 50 75 100
Kilometers

Figure 4.2. Tectonic assemblage map of Yukon-Tanana and adjacent terranes of the northern Cordillera in east-central Alaska, central Yukon and northern British Columbia. The location of Figures 4.3 and 4.4 is outlined by a thick black square. Dashed outlines labelled SM and YT show the original position of the Slide Mountain and Yukon-Tanana terranes now located within the Finlayson Lake district, prior to offset along the Tintina fault (Gabrielse et al., 2006). Figure modified from Colpron et al. (2006).

4.4. Regional Geology

4.4.1. Terrane Nomenclature

The Yukon-Tanana terrane consists of a pre-Late Devonian metasedimentary basement (Snowcap assemblage) with lithological, geochemical and isotopic compositions that suggest it represents a rifted portion of the western Laurentian continental margin (Piercey and Colpron, 2009; Colpron and Nelson, 2009). The Snowcap assemblage is overlain by three unconformity bounded Upper Devonian to Permian volcanic arc sequences (Finlayson, Klinkit, Klondike assemblages) that are coeval with oceanic chert, argillite and mafic volcanic rocks of the Slide Mountain terrane (Colpron et al., 2006). The Slide Mountain terrane represents the preserved remnants of a Late Devonian to Permian back-arc ocean basin that opened between the continental margin and the Devonian-Permian arcs within the Yukon-Tanana terrane (Nelson et al., 2006).

Ductiley deformed, amphibolite facies rocks in east-central Alaska, previously mapped as allochthonous rocks of the Yukon-Tanana terrane, have recently been re-interpreted as parautochthonous North American continental margin rocks (Lake George and Tatatlanika assemblages in Fig. 4.2) exhumed from beneath the Yukon-Tanana terrane along mylonitic extensional faults in the mid-Cretaceous (Hansen and Dusel-Bacon, 1998; Dusel-Bacon et al., 2002, 2006). A parautochthonous North American origin for these rocks in east-central Alaska is based on Archean and Proterozoic U-Pb zircon inheritance and detrital ages, stratigraphic similarity with rocks in the Selwyn Basin, their structural position, and a lack of late Paleozoic arc assemblages characteristic of the Yukon-Tanana terrane (Dusel-Bacon et al., 2006; Nelson et al., 2006; Dusel-Bacon and Williams, 2009). Similar characteristics, including the

exhumation of moderate to high-pressure amphibolite facies rocks from beneath the Yukon-Tanana terrane along mid-Cretaceous extensional shear zones, leads us to interpret a small domain (Australia Mountain domain, Figs. 4.3 and 4.4; Staples et al., 2013) in west-central Yukon to also represent parautochthonous North American rocks. Collectively, these allochthonous and parautochthonous rocks of the Yukon-Tanana terrane and North American continental margin, respectively, record a protracted and diachronous history of ductile deformation and amphibolite facies metamorphism associated with terrane accretion and subsequent crustal thickening (Dusel-Bacon et al., 1995; Berman et al., 2007; Beranek and Mortensen, 2011; Staples et al., 2013; this study, Chapter 3).

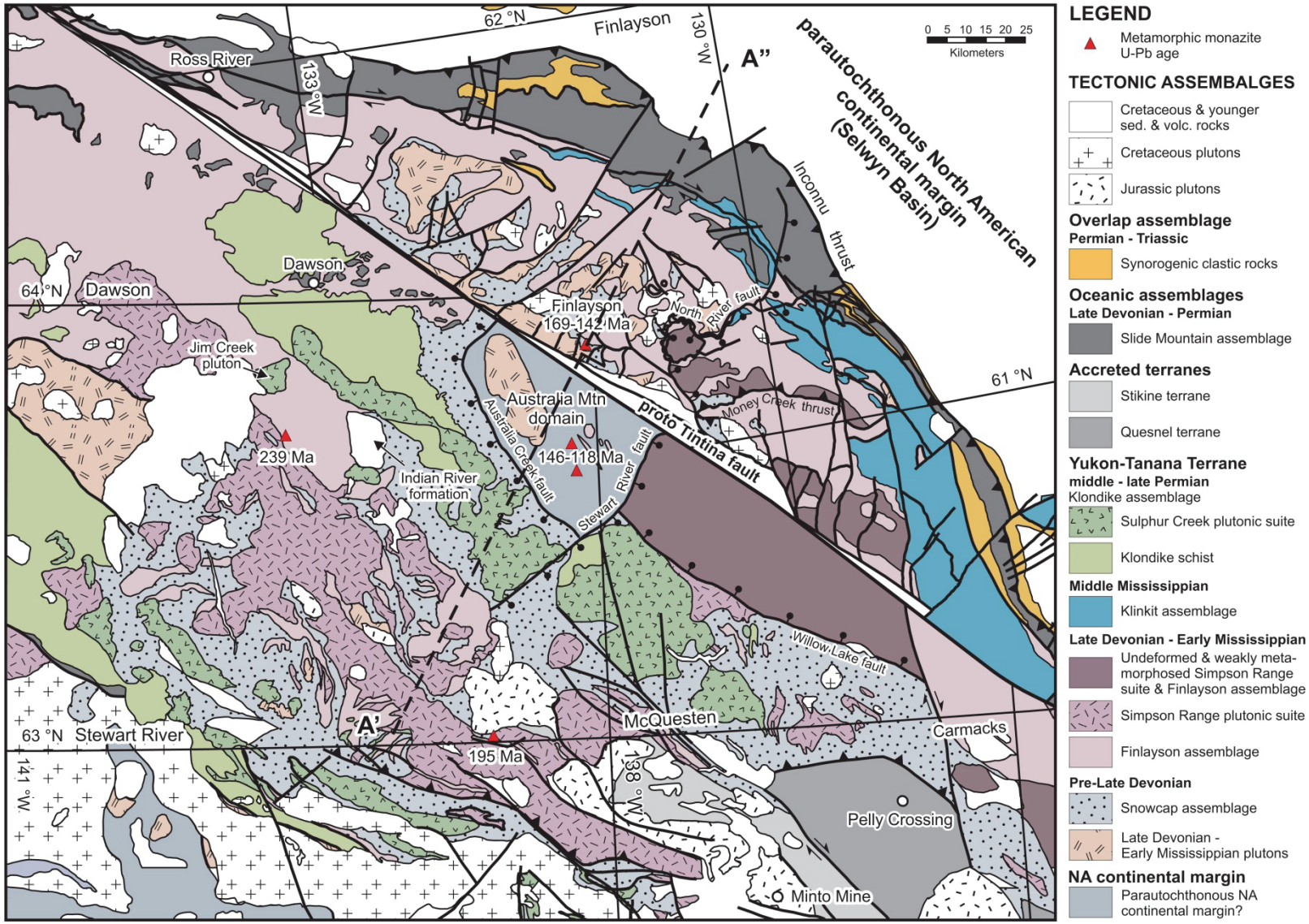
62 °N
Finlayson
130 °W
A"
Ross River
133 °W
parautochthonous North American continental margin (Selwyn Basin)
0 5 10 15 20 25
Kilometers
Inconnu thrust
Dawson
64 °N
Dawson
Finlayson 169-142 Ma
North River fault
Jim Creek pluton
61 °N
Australia Mtn domain
Money Creek thrust
proto Tintina fault
239 Ma
146-118 Ma
Australia Creek fault
Stewart River fault
Indian River formation
Willow Lake fault
A'
McQuesten
Carmacks
63 °N
Stewart River
195 Ma
141 °W
138 °W
Pelly Crossing
Minto Mine
LEGEND
Metamorphic monazite U-Pb age
TECTONIC ASSEMBALGES
Cretaceous & younger sed. & volc. rocks
Cretaceous plutons
Jurassic plutons
Overlap assemblage
Permian - Triassic
Synorogenic clastic rocks
Oceanic assemblages
Late Devonian - Permian
Slide Mountain assemblage
Accreted terranes
Stikine terrane
Quesnel terrane
Yukon-Tanana Terrane
middle - late Permian
Klondike assemblage
Sulphur Creek plutonic suite
Klondike schist
Middle Mississippian
Klinkit assemblage
Late Devonian - Early Mississippian
Undeformed & weakly meta-morphosed Simpson Range suite & Finlayson assemblage
Simpson Range plutonic suite
Finlayson assemblage
Pre-Late Devonian
Snowcap assemblage
Late Devonian - Early Mississippian plutons
NA continental margin
Parautochthonous NA continental margin?

Figure 4.3. Tectonic assemblage map of the northern Yukon-Tanana terrane and underlying parauthochthonous North American rocks prior to post-Late Cretaceous offset along the Tintina fault. U-Pb ages are from Berman et al. (2007); Staples et al. (2013); Ryan and Villeneuve (unpublished data); Chapter 3. See Fig. 4.2 for reference location in west-central Yukon. Labels A' and A" locate the end points of line of section for the cross-section in Figure 4.5.

4.5. Spatial and Temporal Record of Diachronous Amphibolite Facies Metamorphism and Ductile Deformation

Highly deformed and transposed amphibolite facies rocks of the pericratonic Yukon-Tanana terrane and the structurally underlying parautochthonous North American continental margin are exposed across a wide area (at least 100,000 km^2) within the metamorphic core of the northern Cordilleran orogen in west-central Yukon and east-central Alaska. These amphibolite facies rocks share a similar style and pattern of deformation characterized by the transposition of lithologic contacts and primary compositional layering into a regional ductile foliation (S_T) with at least one generation of intrafolial isoclinal folds (Foster et al., 1985, 1994; Colpron, 1999, 2005; de Keijzer et al., 1999; Gallagher, 1999; Gordey and Ryan, 2005; Berman et al., 2007; Staples et al., 2013; Chapter 3). Petrology and phase equilibria modeling (Dusel-Bacon et al., 1995; Berman et al., 2007; Staples et al., 2013; Chapter 3) indicate these rocks were ductiley deformed and metamorphosed under nearly identical conditions at 7.5 – 9 kbar and 600 – 680 °C. However, monazite growth associated with this deformation and metamorphism was strongly diachronous across the orogen, with events recorded in the Late Permian – Early Triassic, Early Jurassic, Middle to Late Jurassic and Early to mid-Cetaceous (Berman et al., 2007; Staples et al., 2013; Chapter 3). Each of these tectono-metamorphic events is recorded in distinct domains, and typically lack evidence of the older or younger events recorded in the other domains (Fig. 4.4). Both the Permo-Triassic and Early Jurassic metamorphic events are recorded in Yukon-Tanana terrane rocks within the Stewart River map area southwest of the Tintina fault. Rocks deformed and metamorphosed in the Permo-Triassic and Early Jurassic were exhumed in the Early Jurassic (Dusel-Bacon et al., 2002; Berman et al., 2007). By contrast, rocks farther to the east were progressively buried and heated from Middle Jurassic to Early

Cretaceous in the Finlayson Lake district (Chapter 3), here on referred to as the Finlayson domain, and the Early Cretaceous in the Australia Mountain domain (Staples et al., 2013) (Fig. 4.4). Figure 4.5 shows a cross-sectional view that cuts through each of these three tectono-metamorphic domains. A fourth domain of weakly deformed and essentially unmetamorphosed rocks with Mississippian cooling ages are juxtaposed to the southeast in the hanging wall of mid-Cretaceous normal faults (Fig. 4.4).

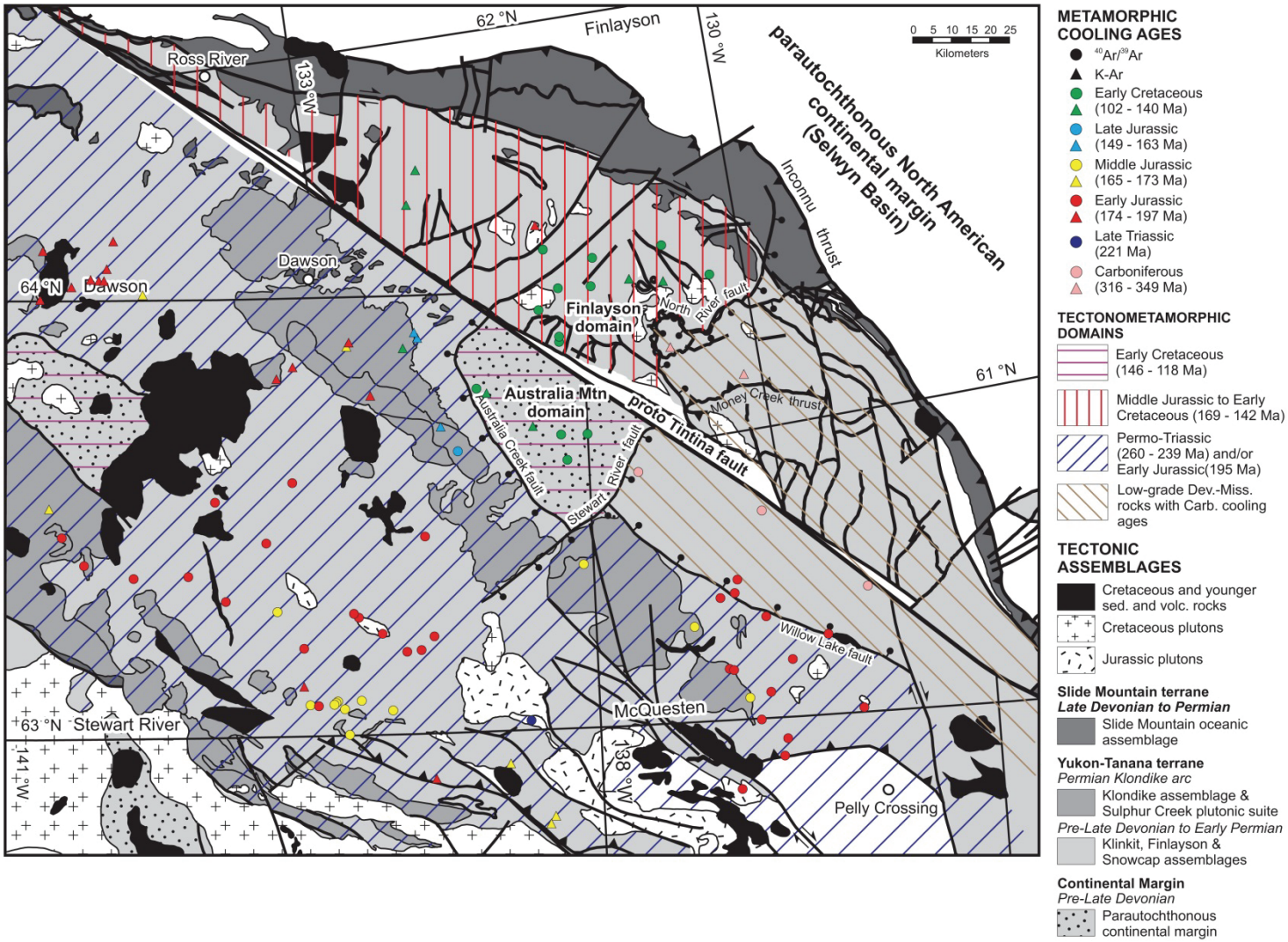

LEGEND

Thrust fault .....

Normal fault .....

METAMORPHIC COOLING AGES

- $^{40}Ar/^{39}Ar$
- K-Ar
- Early Cretaceous (102 - 140 Ma)
- Late Jurassic (149 - 163 Ma)
- Middle Jurassic (165 - 173 Ma)
- Early Jurassic (174 - 197 Ma)
- Late Triassic (221 Ma)
- Carboniferous (316 - 349 Ma)

TECTONOMETAMORPHIC DOMAINS

- Early Cretaceous (146 - 118 Ma)
- Middle Jurassic to Early Cretaceous (169 - 142 Ma)
- Permo-Triassic (260 - 239 Ma) and/or Early Jurassic(195 Ma)
- Low-grade Dev.-Miss. rocks with Carb. cooling ages

TECTONIC ASSEMBLAGES

- Cretaceous and younger sed. and volc. rocks
- Cretaceous plutons
- Jurassic plutons

Slide Mountain terrane
Late Devonian to Permian
- Slide Mountain oceanic assemblage

Yukon-Tanana terrane
Permian Klondike arc
- Klondike assemblage & Sulphur Creek plutonic suite

Pre-Late Devonian to Early Permian
- Klinkit, Finlayson & Snowcap assemblages

Continental Margin
Pre-Late Devonian
- Parautochthonous continental margin

Figure 4.4. **Simplified tectonic assemblage map of the northern Yukon-Tanana terrane, with the offset portion of Yukon-Tanana on the northeast side of the Tintina fault (Finlayson Lake district) restored to its pre-Paleogene position. This map shows the inferred distribution of the Permo-Triassic/Early Jurassic, Middle Jurassic – Early Cretaceous, and Early Cretaceous tectonometamorphic domains prior to post-Late Cretaceous offset along the Tintina fault. Superimposed are $^{40}Ar/^{39}Ar$ and K-Ar metamorphic cooling ages. K-Ar ages are from Wanless et al. (1967; 1978); Stevens et al. (1982); Debicki (1985); Hunt and Roddick (1987; 1991; 1992; 1993); Breitsprecher and Mortensen (2004). $^{40}Ar/^{39}Ar$ ages are from Breitsprecher and Mortensen (2004); Knight et al. (2013); Murphy and Villeneuve (unpublished data); this study, Appendix C; Ryan and Villeneuve (unpublished data).**

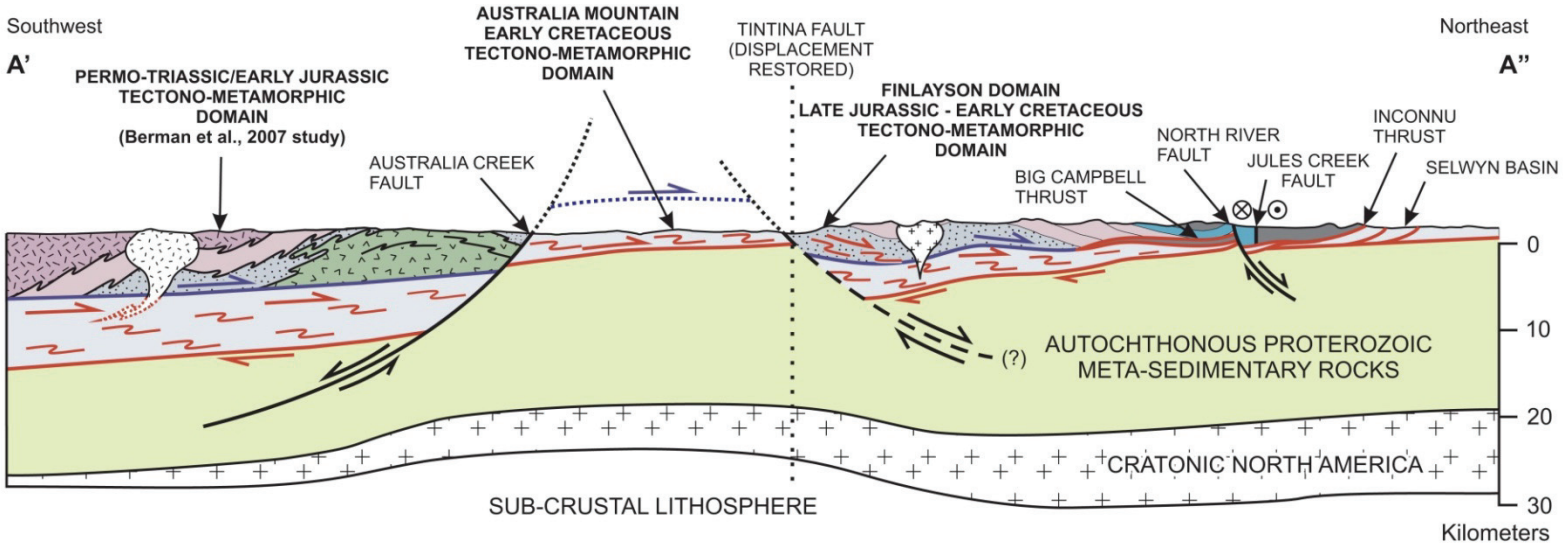

LEGEND

INTRUSIVE ROCKS

MID-CRETACEOUS

Cassiar plutonic suite

JURASSIC

Walhalla Creek pluton

YUKON-TANANA TERRANE

MIDDLE TO LATE PERMIAN

Sulphur Creek Plutonic Suite

MIDDLE MISSISSIPPIAN

Klinkit assemblage

LATE DEVONIAN - EARLY MISSISSIPPIAN

Simpson Range plutonic suite

Finlayson assemblage

PRE-LATE DEVONIAN

Snowcap assemblage

SLIDE MOUNTAIN

LATE DEVONIAN TO EARLY PERMIAN

Fortin Creek group & Campbell Range formation

PARAUTOCHTHONOUS NORTH AMERICA

Selwyn Basin (?)

AUTOCHTHONOUS NORTH AMERICA

Proterozoic metasedimentary rocks

Crystalline North American basement

MID-CRETACEOUS EXTENSIONAL FAULT

EARLY CRETACEOUS SHEAR ZONE

JURASSIC THRUST

Figure 4.5. Cross-section from points A' to A" on Figure 4.3. Crosss-section through all three of the temporally distinct tectono-metamorphic domains: Permo-Triassic/Early Jurassic domain (Berman et al., 2007); Early Cretaceous domain (Australia Mountain domain; Staples et al., 2013); Middle Jurassic – Early Cretaceous domain (Finlayson domain; Chapter 3). This cross-section also illustrates the downward migration of the Early Cretaceous shear zone (in red) relative to the Jurassic shear zone (in blue). The dashed normal fault coinciding with the proto-Tintina fault, is inferred as one possible explanation for the 5 kilometres of structural relief between the Australia Mountain (9 kbar metamorphism) and Finlayson (7.5 kbar metamorphism) domains. No vertical exaggeration.

4.5.1. Permo-Triassic and Early Jurassic Tectono-Metamorphic Domain – North-Cental Yukon-Tanana Terrane, West-Central Yukon

Permo-Triassic

Timing estimates for the development of a regional transposition foliation (S_T) and associated amphibolite facies metamorphism in the north-central portion of Yukon-Tanana terrane in west-central Yukon range from Late Permian (c. 260 – 253 Ma; Beranek and Mortensen, 2011; Berman et al., 2007) to Middle Triassic (c. 239 Ma; Berman et al., 2007). In the Klondike district, Beranek and Mortensen (2011) obtained a c. 259 Ma age from a "strongly foliated" quartz monzonite sill. They interpret that this sill was affected by the same ductile deformation that produced the regional foliation (S_T) at lower amphibolite facies within the host Devono-Mississippian Finlayson assemblage of Yukon-Tanana terrane. If this interpretation is correct, then the c. 259 Ma age from the deformed sill provides a maximum age for the development of the regional ductile deformation. However, if the regional foliation in the country rock (Finlayson assemblage) is not the same as that in the sill c. 259 Ma sill, it may be possible that the regional foliation is older (e.g. Devono-Mississippian). In the same area, the little-deformed Jim Creek pluton (Fig. 4.3) and associated dikes cut transposed Nasina assemblage rocks and yield an age of c. 253 Ma (Beranek and Mortensen, 2011), suggesting that distributed, penetrative deformation had ceased by this time. However, only approximately 10 kilometres to the south (Fig. 4.3), Berman et al. (2007) dated c. 239 Ma monazite included in garnet rims grown in pressure shadows that parallel the transposition foliation. These monazite are linked to an ~9 kbar and 600 °C metamorphic

event responsible for the garnet overgrowths (Berman et al., 2007), indicating that ductile deformation at amphibolite facies conditions continued until the Middle Triassic, somewhat younger than the presently known duration of plutonism between c. 260 and 253 Ma.

Permo-Triassic metamorphism (c. 260 - 240 Ma; Berman et al., 2007) in the north-central portion of the Yukon-Tanana terrane is spatially and temporally associated with a belt of Permian (c. 265-253 Ma) arc magmatism (Klondike assemblage; Mortensen, 1990; Gordey and Ryan, 2005; Ruks et al., 2006). Figure 4.4 shows the distribution of plutonic and volcanic rocks of the Permian Klondike arc and the inferred distribution of Permo-Triassic (c. 260-240 Ma; Berman et al., 2007) amphibolite facies metamorphism. The middle to late Permian Klondike assemblage and a discontinuous belt of early to middle Permian (c. 273-260 Ma) blueschist and eclogite to the northeast locally occurring along the eastern side of the Yukon-Tanana terrane (Figs. 4.2 and 4.3; Creaser et al., 1997; Erdmer et al., 1998) are interpreted to record a Permian northeast-facing magmatic arc and accretionary wedge, respectively (Mortensen, 1992; Nelson et al., 2006).

By Middle Triassic, siliciclastic strata that contain detrital zircon sourced from the Paleozoic arc assemblages of Yukon-Tanana terrane were deposited on the ancestral North American continental margin (Beranek et al., 2010; Beranek and Mortensen, 2011). This depositional relationship implies that the Slide Mountain ocean had closed by the Early Triassic and the Yukon-Tanana terrane had been accreted and uplifted, forming a highland that shed detritus into the depocentre of the western Laurentian margin at this time (Fig. 4.6). Beranek and Mortensen (2011) suggest that the Late Permian tectono-metamorphism is therefore the result of the accretion of the Yukon-Tanana terrane onto the western Laurentian margin. The presence of c. 239 Ma monazite linked to 600 °C and ~9 kbar metamorphism and ductile deformation (Berman et al., 2007) suggests this event continued into the Middle Triassic.

Map relationships in the northern Carmacks suggest that Late Triassic volcanic rocks (Stikine terrane, Fig. 4.3) unconformably overlie basement rocks of the Yukon-Tanana terrane (Ryan et al., 2010), thus indicating that this portion of the Yukon-Tanana

terrane was exhumed by Late Triassic. However, possibility of a structural contact cannot be ruled out because of poor exposure.

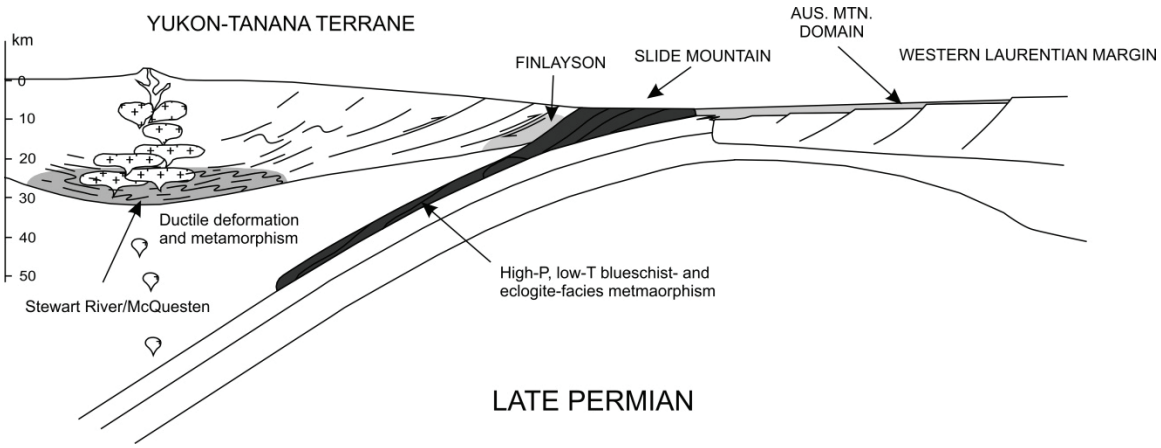

Figure 4.6. Schematic crustal section showing the onset of accretion of Yukon-Tanana terrane to the thinned western edge of western Laurentia (260-252 Ma; Beranek and Mortensen, 2011) coeval with the late stages of arc magmatism within Yukon-Tanana terrane (263-253 Ma; Mortensen, 1990). Postulated Late Permian positions of the Australia Mountain and Finlayson domains are also shown.

Early Jurassic

Late Triassic-Early Jurassic granitic plutons intrude into the Yukon-Tanana, Quesnel and Stikine terranes. Similar to the present day geometry of Yukon-Tanana terrane, these intrusions are exposed in a hairpin shape outlining the northern limit of the Quesnel and Stikine terranes (Fig. 4.2). Al-in-hornblende geobarometric estimates (4-7 kbar; McCausland et al., 2002; Tafti, 2005) and U-Pb zircon ages (Tafti, 2005; Hood, 2012; Knight et al., 2013) indicate emplacement at moderate depths (13-23 km assuming 1 kbar ≈ 3.3 km) between 205 and 197 Ma. This may have been prior to, and possibly synchronous with, c. 195 Ma regional metamorphism, which culminated at 600 °C and ~7.6 kbar (Berman et al., 2007), equivalent to a depth of approximately 25 kilometres. Early to Middle Jurassic (c. 197-171 Ma) K-Ar and $^{40}Ar/^{39}Ar$ mica cooling ages throughout this region of Yukon-Tanana terrane (Fig. 4.4; Hunt and Roddick, 1991, 1992; Breitsprecher and Mortensen, 2004; Knight et al., 2013; Ryan and Villeneuve, unpub. data) overlap with U-Pb metamorphic monazite ages and pluton crystallization ages, suggesting that exhumation was synchronous with, or occurred very rapidly after, plutonism and metamorphism. An Y-rich monazite interpreted to have grown during

retrogression, which yielded a crystallization age of c. 187 Ma (Berman et al., 2007), as well as c.185 Ma plutons that contain miarolitic cavities indicative of emplacement at shallow crustal levels (Johnston et al., 1996), are consistent with rapid exhumation, and indicate that plutonism was synchronous with exhumation. The preservation of Early Jurassic K/Ar and $^{40}Ar/^{39}Ar$ mica cooling ages within the Permo-Triassic and Early Jurassic metamorphic domain reveals that this domain was unaffected by younger Middle Jurassic and Early Cretaceous metamorphic events recorded in structurally lower levels now presently exposed to the northeast (Fig. 4.4; Finlayson and Australia Mountain domains, respectively).

Based on the presence of randomly oriented Early Jurassic kyanite crystals and Early Jurassic intrusions that cross cut the regional penetrative transposition foliation, Berman et al. (2007) suggest that the Jurassic metamorphic event was not accompanied by distributed, penetrative fabric formation. However, Early Jurassic intrusions are in places variably deformed and locally strongly foliated (Hood, 2012), which is indicative of partitioning of Early Jurassic deformation. This is most evident within syn-kinematic Early Jurassic intrusions observed in drill core and the open pit wall at the Minto mine (location shown in Fig. 4.3; Hood, 2012). There, Hood (2012) has observed shallowly-dipping, ductile shear zones ranging in scale from millimetres to metres that grade outwards into undeformed, massive granitoids.

The partitioning of Early Jurassic deformation into localized shear zones may explain the less deformed nature of the Late Triassic volcanic rocks in northern Carmacks map sheet (Stikine terrane in Fig. 4.3), relative to rocks metamorphosed and deformed in the Permo-Triassic. Late Triassic volcanic rocks in the northern Carmacks map sheet are metamorphosed to greenschist facies and have a weakly to moderately developed cleavage (Colpron and Ryan, 2010; Ryan et al., 2010). These Late Triassic volcanic rocks are intruded and bound to the southwest by Early Jurassic granitoids with magmatic epidote, and interpreted to be the northwest extension of the Minto pluton (Colpron and Ryan, 2010; Ryan et al. 2010), which was emplaced at moderate depths of 13-23 km (Tafti, 2005). Furthermore, <40 kilometres to the northwest are kyanite-bearing basement rocks of Yukon-Tanana, which were metamorphosed at a depth of approximately 25 kilometres in the Early Jurassic (Berman et al., 2007). These relationships suggest the Triassic volcanic rocks were likewise buried to significant

depths in the Early Jurassic; however they lack the penetrative foliation observed in rocks metamorphosed in the Permo-Triassic. Deformation of the Triassic volcanic rocks is restricted to rafts within the margin of the Early Jurassic pluton suggesting that Early Jurassic strain was partitioned around the volcanic rocks into the 'wet' Jurassic intrusion. The partitioning of strain around these volcanic rocks may have inhibited metamorphic recrystallization, which may explain the apparent lower metamorphic grade (greenschist vs amphibolite) in the surrounding Yukon-Tanana terrane rocks.

4.5.2. Middle Jurassic to Early Cretaceous Tectono-Metamorphic Domain – Northeastern Yukon-Tanana Terrane, Finlayson Domain

After restoration of the Tintina fault, the offset portion of the Yukon-Tanana terrane in the Finlayson Lake district restores to the northeast of the Permo-Triassic and Early Jurassic domain in western Yukon (Figs. 4.2, 4.3 and 4.4). The Finlayson Lake district is bisected by the North River fault, a regional-scale mid-Cretaceous normal fault that cuts across Yukon-Tanana terrane in a roughly northeast-southwest trend (Figs. 4.3 and 4.4; Murphy, 2004). Rocks in the footwall record mid-Cretaceous $^{40}Ar/^{39}Ar$ and K-Ar cooling ages (Fig. 4.4; Wanless et al., 1967; Hunt and Roddick, 1992; Murphy et al., 2001), are intruded by mid-Cretaceous granite plutons (Murphy et al., 2001), and have been ductiley deformed at amphibolite facies prior to the emplacement of the granites (Murphy, 2004; Chapter 3). Staples et al. (this study, Chapter 3) showed that rocks in the footwall of the North River fault experienced a protracted episode of monazite growth from c. 169 to 142 Ma coeval with the development of ductile transposition fabrics and garnet growth from ~ 550 °C and 6.5 kbar to 600 °C and 7.5 kbar. Sub-greenschist to greenschist facies rocks in the hanging wall to the southeast comprise the upper thrust sheets of imbricated Yukon-Tanana terrane that lack Cretaceous granites and contain Mississippian and Pennsylvanian K-Ar cooling ages (Fig. 4.4; Stevens et al., 1982; Hunt and Roddick, 1987).

There is no record of Permo-Triassic tectono-metamorphism in the Finlayson domain. It is possible that evidence of this event, for example recorded by the growth of a metamorphic thermochronometer such as monazite, may have been destroyed by the low-temperature dissolution of such minerals (e.g. Williams et al., 2011). Alternatively, it

is more likely that monazite growth was a function of location within the thermal structure of the terrane in the Permo-Triassic. The Permo-Triassic amphibolite facies metamorphism in west-central Yukon was temporally conicident with, and spatially associated with, the middle to late Permian (265 – 253 Ma) Klondike arc (Fig. 4.4; Berman et al., 2007; Nelson et al., 2006; Mortensen, 1992). The absence of a Permian metamorphic signature and the position of Yukon-Tanana terrane assemblages in the Finlayson domain northeast of the Klondike arc-center and west of high P/T subduction complex eclogites suggest it occupied a position in the cooler, stronger forearc region of a middle to late Permian northeast-facing convergent margin (Fig. 4.6; Ch. 3).

4.5.3. Early Cretaceous Tectono-Metamorphic Domain – Australia Mountain Domain

Building on the work of Berman et al. (2007), Staples et al. (2013) identified an Early Cretaceous (c. 146 - 118 Ma) syn- to post-S_T amphibolite facies (9 kbar and 650 °C) metamorphic domain at Australia Mountain, immediately east of the Permo-Triassic tectono-metamorphic domain (Fig. 4.4). Slightly younger (c. 112 Ma) texturally and chemically distinct monazite within resorbed portions of garnet from Australia Mountain record the onset of near isothermal decompression in the mid-Cretaceous following the peak of metamorphism. There is no record of Permo-Triassic or Early Jurassic metamorphism and deformation in the Australia Mountain domain. However, syn-kinematic garnet cores from Australia Mountain, with the incipient stages of garnet growth recorded at ~ 600 °C and 8 kbar, remain undated. Potential metamorphic events responsible for this garnet growth include the Permo-Triassic, Early Jurassic, Middle to Late Jurassic, and Early Cretaceous events, all of which are recorded regionally. If the Australia Mountain domain is in fact parautochthonous (Chapter 2 and 3), it would have lain east of the Permian subduction zone on the impinging western Laurentian margin. In this case, the absence of a Permian metamorphic signature in the Australia Mountain domain suggests it had lain well inboard (cratonward) of the orogenic front in the Permian.

The abrupt juxtaposition of this domain against rocks with Early to Late Jurassic cooling to the west and south (Fig. 4.4; Hunt and Roddick, 1992; Knight et al., 2013), and Paleozoic and Early and Middle Jurassic cooling ages to the southeast (Fig. 4.4;

Knight et al., 2013), suggests the Australia Mountain domain is bound by two crustal-scale mid-Cretaceous normal faults (Figs. 4.3 and 4.4); the Australia Creek and Stewart River faults, respectively (Staples et al., 2013). The position of these two faults are constrained by an abrupt change in mica cooling ages, the presence of distinct discontinuities in aeromagnetic data, and differences in lithologies. Poor exposure in the area has prevented the direct observation of faults bounding this Early Cretaceous tectono-metamorphic domain.

After restoration of the Tintina fault, the trace of the North River fault restores along trend of the mid-Cretaceous Stewart River fault west of the Tintina fault (Figs. 4.3 and 4.4). Both the North River and Stewart River faults juxtaposes rocks ductiley deformed and metamorphosed in the Early Cretaceous against rocks to the southeast that are generally undeformed and weakly metamorphosed rocks with Mississippian cooling ages (Figs. 4.3 and 4.4; Murphy et al., 2001; Murphy, 2004; Staples et al., 2013; Colpron and Ryan, 2010; Knight et al., 2013). Therefore, prior to Paleogene offset along the Tintina fault, the Stewart River and North River faults likely formed a continuous normal fault. Both the Permo-Triassic and Early Jurassic metamorphic domain to the west and the Devono-Mississippian rocks to the south were presumably the suprastructural 'lid' from beneath which the Jura-Cretaceous metamorphic domains were exhumed along the mid-Cretaceous Australia Creek and Stewart River-North River faults, respectively.

4.6. Explanation of Diachronous Deformational and Thermochronologic Data in Terms of Critically Tapered Wedge Theory

Despite the diachronous timing, each of the Permo-Triassic, Early Jurassic, Middle to Late Jurassic and Early to mid-Cretaceous events occurred under approximately the same set of physical conditions (600 – 680 °C and 7.5 – 9 kbar, or 25 - 30 km depth; Berman et al., 2007; Staples et al., 2013; Chapter 3). Any tectonic model which attempts to address this pattern must also take into account K-Ar and $^{40}Ar/^{39}Ar$ metamorphic cooling ages within the Permo-Triassic metamorphic domain, which indicate this domain was rapidly exhumed to upper crustal levels in the Early Jurassic

(Hunt and Roddick, 1991, 1992; Breitsprecher and Mortensen, 2004; Knight et al., 2013; Ryan and Villeneuve, unpub. data) prior to the development of transposition fabrics and metamorphism to the northeast in both the Finlayson domain and the structurally deeper Australia Mountain domain. This requires that rocks which previously occupied the middle crust were exhumed by erosion and/or tectonic denudation prior to, or coeval with, the progressive ductile underthrusting and burial of rocks to the northeast, nearer to the foreland. We propose these data and observations can be reconciled by the episodic westward ductile underthrusting of new, cool material beneath an orogenic wedge at critical taper propagating toward the foreland.

4.6.1. Description of Model

The original concept of critical wedge theory was developed to model the mechanics of accretionary complexes of fold-and-thrust belts in a manner analogous to a wedge of sand in front of a moving bulldozer (Davis et al., 1983; Dahlen, 1984). Critical wedge theory was later extended to account for ductile deformation at deeper levels (Williams et al., 1994; Willet, 1999) and has since been recognized to approximate the form of orogenic belts at a larger scale (Platt, 1986; Jamieson and Beaumont, 1988; Willet et al., 1993). Critical wedge theory proposes that an orogenic wedge will deform internally until it reaches a 'critical' taper, after which if no material is added or removed from the wedge, the wedge then slides stably without any internal deformation. If material is accreted to the toe or underplated beneath the advancing wedge, it will again deform internally in order maintain its critical taper (Davis et al., 1983; Platt, 1986). The addition of material at the base of a wedge during underthrusting will cause the wedge to thicken and its taper to become supercritical. The predicted result is that even during continued convergence and burial, the upper crust may enter a state of extension, coeval with contraction at depth, in order to regain a stable taper (Platt, 1986). Platt (1986) recognized that such coeval underthrusting of material beneath the wedge and compensating extension above provides a mechanism for exhuming high-pressure metamorphic rocks to upper crustal levels in the rear of the wedge. In this model, rocks continuously, or episodically, pass through a cycle of burial, heating and subsequent exhumation as they are underthrust into the basal shear zone and then displaced upwards and ultimately exhumed, through the combined effects of underplating from

below and compensating extensional denudation at the surface to maintain a critical taper (cf. Platt, 1986).

Brown (2004) adopted the model of Platt (1986) to explain how mid-crustal levels in the hinterland of the southern Canadian Cordillera could also be exhumed by a similar process, however one that involved ductile underthrusting as opposed to discrete, brittle thrust faulting. A pattern of downward younging ductile deformation and metamorphism in the hinterland of the southern Canadian Cordillera was interpreted by Parrish (1995) to be consistent with a thrust belt setting, in which rocks are progressively overridden as the wedge migrates toward the foreland. Brown (2004) and Williams and Jiang (2005) refined this model, noting that deformation at the mid- to deep-crustal level is characterized primarily by penetrative flow, not by stacking of discrete thrust sheets and partitioned strain. Brown (2004) suggested that the localized shear zone that underlies the base of the wedge in foreland thrust-and-fold belt becomes a distributed ductile shear zone toward the rear of the wedge (Fig. 4.7).

Williams and Jiang (2005) suggest that penetratively deformed, high-grade metamorphic rocks characterized by a shallowly dipping transposition fabric (or enveloping surface) with abundant intrafolial folds, and a non-coaxial deformation history represent crustal-scale (kilometres thick) shear zones. In contrast to localized zones of deformation – detachment surfaces with no coupling – thick shear zones are zones of displacement gradients and therefore allow some kinematic and mechanical coupling with the overlying crust (Tikoff et al., 2002). This is supported by the observation in some orogens where the axial surfaces of upright folds in the upper crust are overturned and become part of the transposition foliation at lower crustal levels (e.g. Murphy, 1987). This style of penetrative flow within a kilometres-thick section of transposed rock can therefore transport weak mid-crustal levels toward the foreland above a strong underlying crust (e.g. basement rocks), while also passively carrying the upper crustal levels (c.f. Williams et al., 2006).

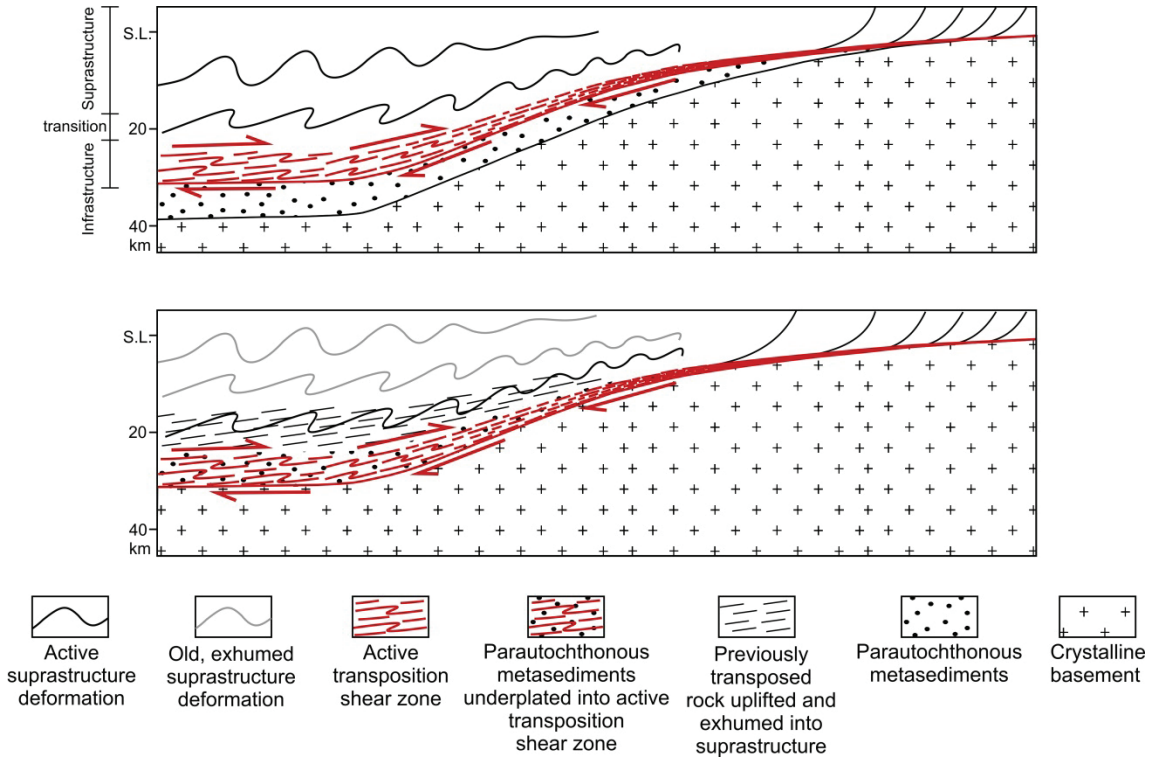

Figure 4.7. Schematic diagram illustrating: 1) how the localized shear zone that underlies the base of the wedge in foreland thrust-and-fold belt becomes a distributed (km's thick) ductile shear zone toward the rear of the wedge; and 2) how the underplating of new rocks into the shear zone causes rocks that were previously ductiley deformed (transposed) and metamorphosed in this high-grade shear zone (infrastructure) to be uplifted and exhumed into the overlying suprastructure where they are overprinted at low metamorphic grade by upright, brittle structures. (See text for further explanation; diagram modified after Brown, 2004).

4.6.2. Description of a Distributed, Kilometre-Thick, Ductile Shear Zone in the Northern Cordillera

Deformational fabrics, and the metamorphic grade at which they formed, are strikingly similar across Yukon-Tanana terrane and the structurally underlying parautochthonous rocks. They are characterized by a shallowly-dipping, penetrative, composite transposition foliation (S_T) that is coplanar with the limbs of tight to isoclinal folds (Foster et al., 1985, 1994; Colpron, 1999, 2005; de Keijzer et al., 1999; Gallagher, 1999; Gordey and Ryan, 2005; Berman et al., 2007; Staples et al., 2013; Chapter 3). Relict primary compositional layering, contacts (veins and dykes), a pre-existing foliation, and rare rootless isoclinal folds can be traced around these fold closures indicating the

folds are at least F_2 structures. However, it is possible that the pre-existing isoclinal folds and the associated axial-planar foliation may have been refolded in a self-similar style during a single, progressive deformation event. There has been very limited detailed structural and kinematic analysis within the hinterland of the northern Cordillera; however, a few studies have observed that the mineral lineation, where present, is parallel to the fold axes of the youngest tight to isoclinal syn-transposition folds (F_T; Colpron, 1999; de Keijzer et al., 1999; Dusel-Bacon et al., 2002; Gordey and Ryan, 2005; Berman et al., 2007). Parallelism of the mineral lineation with syn-transposition fold axes suggests intense progressive non-coaxial deformation wherein the fold axes have progressively rotated into approximate parallelism with the extension direction (shear direction; Escher and Watterson, 1974; Williams and Zwart, 1977).

The amphibolite facies metamorphism, shallowly-dipping transposition foliation, and non-coaxial deformation history described here for much of the lowest exposed structural and stratigraphic levels of Yukon-Tanana terrane and the structurally underlying parautochthonous rocks is consistent with a crustal-scale (kilometres thick) shear zone as described by Williams and Jiang (2005). Rocks are envisaged as being underthrust and underplated along a discrete brittle thrust fault toward the toe of the wedge, transitioning into a diffuse, kilometres-thick, ductile shear zone at greater depths toward the back of the wedge (Figs. 4.7 and 4.8). However, monazite geochronology on these rocks (Berman et al., 2007; Staples et al., 2013, Chapter 3) demonstrates that the development of this distributed, ductile shear zone was not synchronous throughout the terrane. Rather the deformation and associated amphibolite facies metamorphism youngs both downwards and toward the foreland, similar to that described by Brown (2004) in the southeastern Canadian Cordillera.

The development of transposition fabrics at amphibolite facies occurred diachronously within the Yukon-Tanana terrane in the Permo-Triassic, Early Jurassic, Middle to Late Jurassic and Early to mid-Cretaceous (Berman et al., 2007; Beranek and Mortensen, 2011; Staples et al., 2013, this study). However, each event occurred at approximately the same crustal level (7.5 – 9 kbar, or 25 - 30 km depth: Berman et al., 2007; Staples et al., 2013, this study), and resulted in a widespread tectonic pile of schist and gneiss with similar appearance. This requires that rocks which previously occupied the distributed ductile shear zone in the middle crust were subsequently

exhumed by erosion and/or tectonic denudation prior to, or coeval with, the progressive ductile underthrusting and burial of subsequent rocks to mid-crustal levels (Fig. 4.7).

The repeated cycling of rocks down into the distributed shear zone and then upwards into the overlying crust implies that rocks that occupy the upper crust at any time, may contain older, relict structures that are identical to the deformational and metamorphic fabrics forming at the same time in the mid-crustal, distributed shear zone. However, there is a panel of weakly deformed and essentially unmetamorphosed rocks with Carboniferous cooling ages in this part of the orogen (Figs. 4.3 and 4.4), indicating that this panel has occupied a high crustal level since the Carboniferous, and thus not all upper-crustal rocks were buried into the mid-crustal shear zone.

In addition to the shallowly dipping, high-grade, penetrative fabrics that develop within the ductile shear zone at depth, upright, brittle structures overprint the earlier ductile fabrics at lower metamorphic grade as they are progressively exhumed to upper crustal levels. We apply the term 'infrastructure' in a similar sense to that suggested by De Sitter and Zwart (1960) and Culshaw *et al*. (2006) when describing mid- to lower-crustal levels in an orogen characterized by high-grade, shallowly dipping, ductiley deformed and transposed rocks. Conversely, the overlying 'suprastructure' would be characterized by upright, brittle structures and low-metamorphic grade (Fig. 4.7). In the northern Cordillera, this rheological contrast between upper and lower crustal levels is time specific. We make this distinction because, as explained above, rocks formerly situated in the lower crust, the infrastructure, were progressively exhumed in the Jurassic and incorporated into the suprastructure above the Middle Jurassic to Early Cretaceous infrastructure (Fig. 4.7).

4.6.3. Early Jurassic Wedge

Abundant evidence of Early Jurassic contraction, imbrication and metamorphism within Yukon-Tanana and Slide Mountain terranes (Hansen and Dusel-Bacon, 1998; Dusel-Bacon et al., 2002; Berman et al., 2007; Murphy et al., 2006), suggests that by this time these terranes had been obducted and thrust onto the continental margin forming an orogenic wedge above the westward migrating and underthrusting North American continent (Figs. 4.8A and 4.9A; Nelson et al., 2006). As the orogenic wedge

propagated at critical taper toward the craton, cooler rocks were progressively buried and heated as they were underthrust beneath the burgeoning wedge. The underplating of new material at the base of the wedge resulted in thickening the wedge beyond its critical taper, causing the rear of the wedge to extend internally, coeval with contraction at depth, in order to maintain critical taper (e.g. Platt, 1986). Therefore, the underthrusting of new material into the basal shear zone in the Early Jurassic caused rocks that were previously ductiley deformed and metamorphosed at depth within the infrastructure to be displaced upward into the overlying suprastructure of the wedge and ultimately exhumed. This is recorded from the abundance of Early Jurassic K-Ar and $^{40}Ar/^{39}Ar$ cooling ages within Yukon-Tanana terrane rocks (Hunt and Roddick, 1991, 1992; Breitsprecher and Mortensen, 2004; Knight et al., 2013; Ryan and Villeneuve, unpub. data) that experienced ductile transposition and metamorphism in Permo-Triassic and Early Jurassic (Berman et al., 2007). Early Jurassic extensional exhumation was accommodated in part by the Willow Lake normal fault (Fig. 4.4), which bounds a portion of the Permo-Triassic metamorphic domain (Colpron and Ryan, 2010; Knight et al., 2013).

Uplift and exhumation in the upper levels of the wedge, contemporaneous with contraction and burial at depth is also indirectly recorded by sedimentation in the Whitehorse trough (Early to Middle Jurassic Laberge Group; Fig. 4.2). Clast types and provenance studies of the Laberge Group show a temporal transition from volcanic clasts to sedimentary clasts to granitic clasts, which record the erosion of the Lewes River arc (Stikine terrane), progressing to shelf uplift, and then uplift and erosion of the arc's plutonic roots, respectively, during the Early Jurassic (Dickie and Hein, 1995; Hart et al., 1995; Hart, 1997). Further evidence for syn-contractional exhumation is provided by geological relationships that suggest Early Jurassic exhumation was accommodated along both contractional (Dusel-Bacon et al., 2002) and extensional structures (Knight et al., 2013).

The underthrusting of cooler rocks that gradually made their way toward the back of the wedge in the Early Jurassic would have provided a new source of fertile material from which fluids may be derived via dehydration reactions upon heating of these newly buried rocks. Migration of this fluid upwards into overlying rocks, which were previously metamorphosed and dehydrated in the Permian, but were subsequently displaced

upwards and exhumed in the Early Jurassic, may have provided the catalyst for renewed metamorphic reactions and Early Jurassic monazite growth in that overlying, partially exhumed panel (Permo-Triassic infrastructure in Fig. 4.8A). The introduction of reaction catalyzing fluids contemporaneous with exhumation would explain the overlap of Early Jurassic U-Pb metamorphic monazite and regional $^{40}Ar/^{39}Ar$ cooling ages (Berman et al., 2007). Additionally, strain may have been localized within zones of enhanced fluid flow, which may explain the absence of a ubiquitous penetrative ductile fabric, but rather the more discrete, localized deformation associated with metamorphism in the Early Jurassic. Alternatively, deformation may have been localized where fluids evolved from the Early Jurassic intrusions.

Alternatively, given the large range of K/Ar $^{40}Ar/^{39}Ar$ mica cooling ages (c. 197-177 Ma; Hunt and Roddick, 1991, 1992; Breitsprecher and Mortensen, 2004; Knight et al., 2013; Ryan and Villeneuve, unpub. Data), within what is presently considered a coherent structural panel, exhumation may have therefore post-dated Early Jurassic (c. 195 Ma; Berman et al., 2007) metamorphism by 10-20 Myr. In fact, Berman et al. (2007) obtained the c. 195 Ma metamorphic age from monazite included within garnet and kyanite, linking it to ~7.6 kbar (≈ 25 km depth), and thus mid-crustal levels. However, even if there was a delay between underthrusting at depth and compensating extensional denudation above, the underthrusting of fertile, hydrous material may have still provided the reaction catalyzing fluid for Early Jurassic metamorphic reactions within these mid-crustal levels that had previously been dehydrated in the Permo-Triassic.

4.6.4. Middle Jurassic to Early Cretaceous Wedge

Widespread Early Jurassic cooling ages across the northern Yukon-Tanana terrane reveal that Yukon-Tanana terrane rocks metamorphosed in the Permo-Triassic and again in the Early Jurassic remained at a high structural level from Early Jurassic onward. By contrast, the highly transposed nature, as well as P-T data and U-Pb monazite geochronology (Staples et al., 2013, Chapter 3), indicate that rocks in the Finlayson and Australia Mountain domains to the northeast were being buried, heated and incorporated into a distributed, ductile shear zone at 25-30 km depth in the Middle Jurassic to Early Cretaceous (Fig. 4.8B). Accretion and underthrusting of the Insular terranes beneath the western side of the Yukon-Tanana terrane in the Middle Jurassic

(McClelland et al., 1992; van der Hayden, 1992; Saleeby, 2000; Gehrels, 2001) may have provided the necessary rigid backstop to drive the orogenic wedge toward the foreland during the continued westerly migration and underthrusting of the North American continent (Fig. 3.13). However, the dynamics outboard (to the west) of this portion of the Yukon-Tanana terrane in the Middle Jurassic to Early Cretaceous is unclear. Estimates for the timing of accretion of the Insular terranes varies from Middle Jurassic (e.g. Gehrels, 2001) to Late Cretaceous (Hults et al., 2013) along the length of the orogen. The along-strike paleogeographic setting of the Yukon-Tanana terrane relative to the Insular terranes is uncertain due to post-Early Cretaceous dextral displacement along the Tintina and Denali faults (Gabrielse et al., 2006; Dodds, 1995), as well as Late Jurassic to Early Cretaceous sinistral motion of the Insular terranes (Monger et al., 1994). Furthermore, sedimentation in the Late Jurassic–Early Cretaceous Gravina basin between the Alexander and Yukon-Tanana terranes has been interpreted to record back-arc extension and pulling away of the arc in the Insular terranes (Monger et al., 1994; Gehrels et al., 2009). This would appear to be inconsistent with simultaneous contraction and the foreland-directed (northeastward) migration of the orogen further inboard within Yukon-Tanana terrane.

The post-Early Jurassic record of metamorphism is restricted to rocks exposed to the northeast (toward the foreland) of the Permo-Triassic/Early Jurassic metamorphic domain (Fig. 4.4). The apparent absence of Permo-Triassic and Early Jurassic metamorphism in these younger domains to the northeast suggests that deformation and metamorphism migrated into cooler rocks toward the foreland. Furthermore, data from the Finlayson and Australia Mountain domains, which reveal a pattern of structurally downward younging deformation and metamorphism (169-142 Ma at ~25 km depth; 145-118 Ma at ~30 km depth; Staples et al., 2013; Chapter 3), is interpreted to correspond with the progressive underthrusting of new material as the orogenic wedge propagates toward the foreland.

Despite an apparent foreland-directed younging of deformation and metamorphism, as recorded from the absence of older Permo-Triassic and Early Jurassic metamorphism in the younger domains to the northeast toward the foreland, the c. 146-118 Ma Australia Mountain domain lies southwest (outboard) of the older (c. 169-142 Ma) Finlayson domain (Fig. 4.4). However, prior to accretion, the Australia Mountain

domain is interpreted to have originated east of the Finlayson domain (Yukon-Tanana terrane) based on the interpretation that it represents parautochthonous North American margin (Fig. 4.6). The present exposure of the Australia Mountain domain west of the Finlayson domain is attributed to underthrusting down to the west beneath the Finlayson domain in the Early Cretaceous (Fig. 4.8B), following burial and metamorphism of the Finlayson domain.

If the Australia Mountain domain is parautochthonous North American margin that originally lain east of the Slide Mountain Ocean prior to the accretion of the Yukon-Tanana terrane (Fig. 4.6), then this ductile underthrusting and underplating of the Australia Moutnain domain beneath Yukon-Tanana terrane (Fig. 4.8A and B), likely also incorporated and transposed lenses of intervening Slide Mountain rocks into the overlying wedge together with the Australia Mountain domain. This model would suggest that the highly altered lenses of ultramafic rock at Australia Mountain, which are concordant with the foliation, may be slivers of Slide Mountain terrane.

Possible Origin of Late Jurassic Gold-Bearing Metamorphic Fluids

Underplating, heating and devolatilization of cool, fertile (hydrous) material in the Finlayson and Australia Mountain domains in the Middle to Late Jurassic and Early Cretaceous may have provided a source of fluids for Late Jurassic 'orogenic' gold-bearing veins (Bailey, 2013) within the structurally overlying, colder and previously dehydrated rocks of the Klondike-White Gold district (located within the Permo-Triassic/Early Jurassic metamorphic domain; Figs. 3 and 8B). Gold-bearing quartz veins at the Golden Saddle deposit of the White Gold area were emplaced along brittle structures (Bailey, 2013) within rocks previously metamorphosed in the Permo-Triassic and Early Jurassic (Berman et al., 2007). The age of gold mineralization is constrained by $^{187}Re/^{187}Os$ model ages of 163–155 Ma from molybdenite interpreted to be paragenetically related to the gold (Bailey, 2013). These ages are contemporaneous with amphibolite facies metamorphism, devolatilization and ductile deformation (c. 169-142 Ma) at deeper crustal levels in the Finlayson domain (Chapter 3), and thus provide a possible metamorphic fluid-source for the gold-bearing veins. However, data from this study does does not provide any insight as to the gold source. Late Jurassic K-Ar and $^{40}Ar/^{39}Ar$ cooling ages within the Klondike and White Gold area are anomalous relative to

more widespread Early Jurassic cooling ages in the surrounding regions, and may also be the result of the Ar system resetting during localized circulation of these metamorphic fluids.

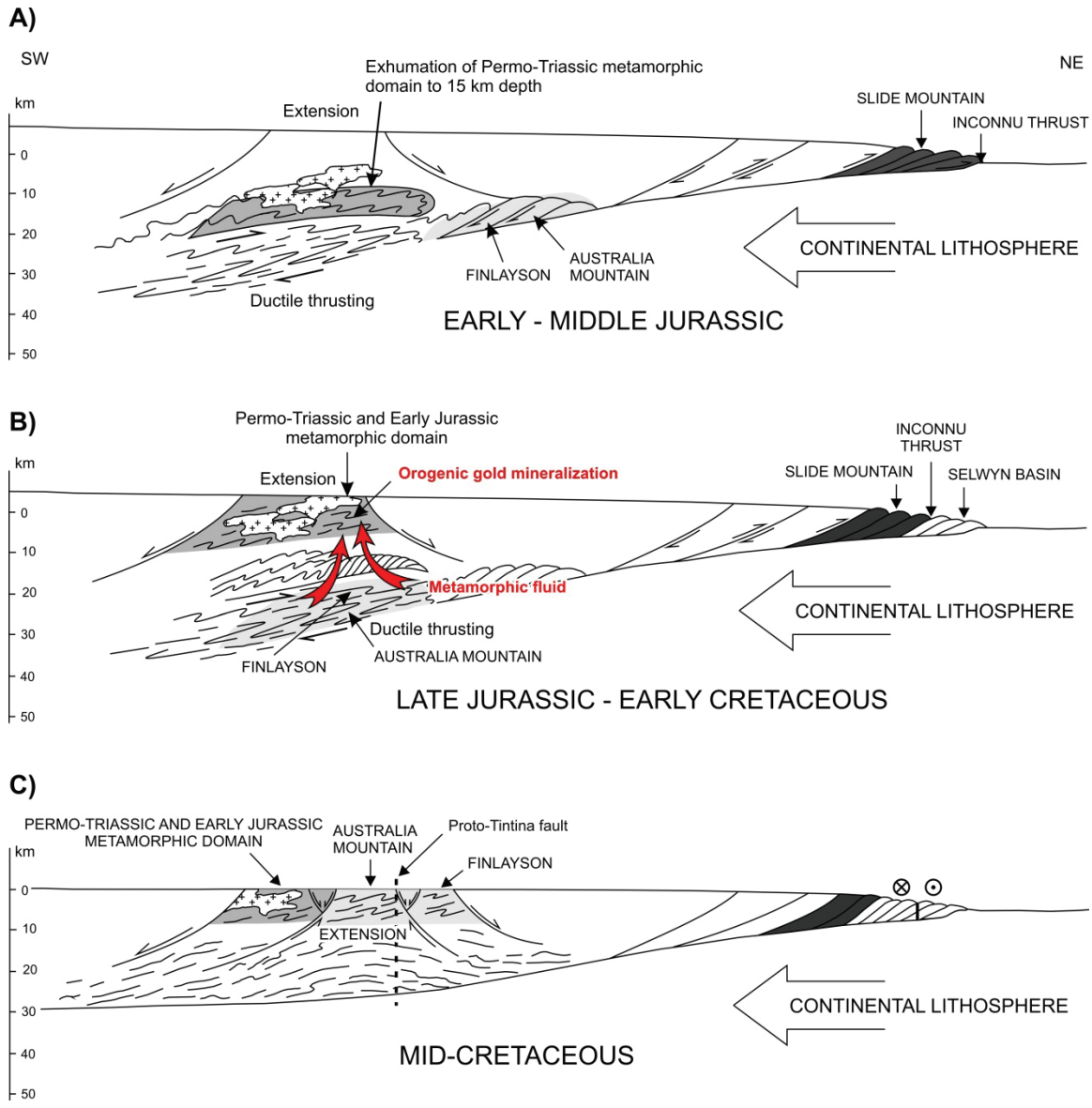
A)
SW
NE
km
Exhumation of Permo-Triassic metamorphic domain to 15 km depth
Extension
SLIDE MOUNTAIN
INCONNU THRUST
0
10
20
30
40
50
FINLAYSON
AUSTRALIA MOUNTAIN
CONTINENTAL LITHOSPHERE
Ductile thrusting
EARLY - MIDDLE JURASSIC
B)
Permo-Triassic and Early Jurassic metamorphic domain
INCONNU THRUST
km
Extension
Orogenic gold mineralization
SLIDE MOUNTAIN
SELWYN BASIN
Metamorphic fluid
CONTINENTAL LITHOSPHERE
Ductile thrusting
AUSTRALIA MOUNTAIN
FINLAYSON
LATE JURASSIC - EARLY CRETACEOUS
C)
PERMO-TRIASSIC AND EARLY JURASSIC METAMORPHIC DOMAIN
AUSTRALIA MOUNTAIN
Proto-Tintina fault
km
FINLAYSON
EXTENSION
CONTINENTAL LITHOSPHERE
MID-CRETACEOUS

Figure 4.8. **Schematic evolutionary model of the northern Canadian Cordilleran orogenic wedge. (A) Early – Middle Jurassic: The exhumation of rocks previously buried and metamorphosed in the Permian is driven by combined underplating at depth and compensating extensional denudation above in order to maintain a critical taper as the North American crust is underthrust to the west. The Finlayson and Australia Mountain domains may have been underthrust and incorporated into the wedge at this time, but are still within the cool toe of the wedge. (B) Late Jurassic – Early Cretaceous: Continued underthrusting of the North American crust causes the Finlayson and Australia Mountain domains to be buried and ductiley underthrust to ~25-30 km's depth toward the rear of the wedge, causing rocks which previously occupied this shear zone to be displaced upwards due to compensating extension above. The Australia Mountain domain, which was closer to the foreland, or craton, relative to the Finlayson domain in the Permian, was ductiley underthrust and metamorphosed after the Finlayson domain in the Early Cretaceous, and thus lies structurally beneath the Finlayson domain at this time. Following this, in the mid-Cretaceous, the Australia Mountain domain had been underthrust beneath the Finlayson domain. (C) Post mid-Cretaceous: The Finlayson and Australia Mountain domains are exhumed in the mid-Cretaceous along the Australia Creek and Stewart River - North River faults following a change in kinematics. Orogen-scale shortening was accommodated by horizontal, orogen-parallel extension along the Stewart River – North River faults, and comparable faults in east-central Alaska, in the mid-Creteous, as opposed to the previous vertical extension (crustal thickening) that was occurring during the Jurassic and Early Cretaceous.**

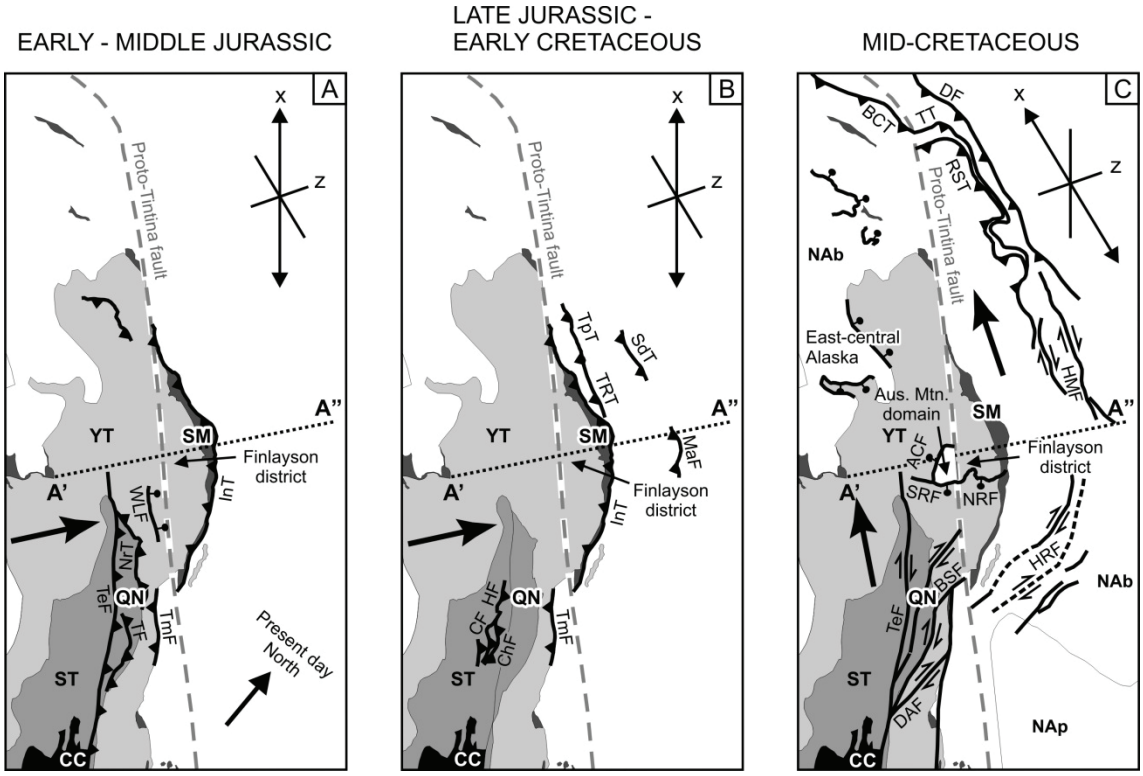
EARLY - MIDDLE JURASSIC
LATE JURASSIC -
EARLY CRETACEOUS
MID-CRETACEOUS
A
B
C
x
z
Proto-Tintina fault
YT
SM
ST
CC
QN
A'
A"
Finlayson
district
InT
WLF
LNT
TeF
TF
TmF
Present day
North
TpT
SdT
TRT
MaF
CF
HF
ChF
BCT
TT
DF
RST
NAb
East-central
Alaska
Aus. Mtn.
domain
HMF
ACF
SRF
NRF
HRF
BSF
DAF
NAp

Figure 4.9. Generalized geological maps illustrating the orientation and kinematics of active structures at the time of each corresponding wedge section in Figure 4.8. Strain axes show the directions of the minimum (x) and maximum (z) shortening directions within metamorphic hinterland (Yukon-Tanana terrane). Large black arrows illustrate the direction of transport of the Intermontane terranes. The southwest-northeast trending dotted line from A' to A" is the approximate location of the schematic wedges in Fig. 4.8. (A) Early – Middle Jurassic: characterized by northeast- and southwest-vergent thrust faults, reflecting a dynamic of orogen-perpendicular compression and vertical extension (crustal thickening). (B) Late Jurassic – Early Cretaceous: Northeast- and southwest-vergent thrusts related to continued orogen perpendicular compression and vertical extension. (C) Mid-Cretaceous: This time was characterized by a change in the orogen's dynamic from veterical extension (crustal thickening) to horizontal, orogen-parallel extension as interpreted for the Stewart River and North River faults and comparable faults in east-central Alaska (Hansen and Dusel-Bacon, 1998; Dusel-Bacon et al., 2002). Fault abbreviations: ACF = Australia Creek fault; BCT = Beaver Creek thrust; BSF = Big Salmon fault; CF = Coghlan fault; ChF = Chain fault; DAF = D'Abbadie fault; DF = Dawson fault; HF = Hoochekoo fault; HMF = Hess-MacMillan fault system; HRF = Hyland River fault system; InT = Inconnu thrust; MaF = March fault; NRF = North River fault; NrT = Needlerock thrust; RST = Robert Service thrust; SdT = Sheldon thrust; SRF = Stewart River fault; TaF = Tadru fault; TeF = Teslin fault; TF = Towhata fault; TmF = Tummel fault; TT = Tombstone thrust; TpT = Twopete thrust; TRT = Tay River Thrust; WLF = Willow Lake fault. City abbreviations: D = Dawson; Fb = Fairbanks; RR = Ross River; Wh = Whitehorse; WL = Watson Lake. Terrane abbreviations: CC = Cache Creek; QN = Quesnellia; ST = Stikine; YT = Yukon-Tanana; Nab = North America basinal; Nap = North America platform.

4.6.5. Mid-Cretaceous – A Changing Geodynamic

Thin-skinned, northeast-vergent regional-scale folds and extensive, shallow-dipping thrust faults in the Selwyn basin immediately to the northeast of Yukon-Tanana terrane and the Finlayson domain (Fig. 4.9B) are bracketed between Early and mid-Cretaceous (Gordey, 2013), coeval with thick-skinned deformation in the Finlayson and Australia Mountain domains. The northeastward, foreland-directed, migration of ductile deformation and amphibolite facies metamorphism into the Finlayson and Australia Mountain domains in the Late Jurassic to Early Cretaceous coeval with northeast-vergent folding and thrust-faulting immediately to the northeast within the foreland, records orogen-perpendicular (northeast-directed) contraction and thickening across the

northern Cordilleran orogen until the mid-Cretaceous. The peak metamorphic pressures of 7.5 and 9 kbar from rocks presently exposed at the surface in the Finlayson and Australia Mountain domains (Staples et al., 2013; Chapter 3), respectively, correspond to approximately 25-30 km depth. Considering the moho is currently located at approximately 35 kilometres depth in the northern Cordillera (Cook and Erdmer, 2005), this suggests the crust was approximately 60-65 kilometres thick prior to mid-Cretaceous exhumation. Gibson et al. (2008) determined a similar crustal thickeness in the southeastern Canadian Cordillera, and on the basis of local Airy isostasy suggest this would produce a high standing topography at least 5 km above sea level.

The Albian (113-100 Ma) Indian River formation (Lowey and Hills, 1988), located approximately 35 km west of the Australia Mountain domain in the hanging wall of the Australia Creek fault (Fig. 4.3), was deposited roughly coeval with extensional exhumation of the Australia Mountain domain. In addition to the synchronicity between deposition of the Indian River formation and exhumation of the Australia Mountain domain, as well as its location in the hanging wall of the Australia Creek fault, the Indian River formation contains metamorphic detritus (quartz with undulatory extinction, and lesser amounts of muscovite, feldspar and foliated lithic fragments) (Lowey and Hills, 1988), which altogether suggests it represents a syn-extensional detachment basin to the Australia Creek fault. The presence of the dinoflagellate *Muderongia asymmetrica* within the Indian River formation is interpreted by Lowey (1984) to indicate deposition in a marine influenced environment, requiring that this portion of the hinterland of the northern Cordillera had been reduced to sea-level by 110-100 Ma. Reduction of the metamorphic hinterland of the Cordillera to sea-level by 110-100 Ma indicates that the orogenic wedge had collapsed by this time, and that extensional denudation along the Australia Creek and Stewart River/North River faults was extremely rapid. This is corroborated by 116-104 Ma K-Ar mica cooling ages from the Australia Mountain domain (Appendix C; Hunt and Roddick, 1992), which are consistent with rapid extensional exhumation following peak metamorphism at c. 118 Ma at approximately 30 km depth.

The northwest-southeast trending Australia Creek fault is cut by the southwest-northeast trending Stewart River – North River fault (Figs. 4.3 and 4.4); therefore, exhumation of the Australia Mountain domain likely began along the Australia Creek fault. Tilting of the footwall during exhumation along the Australia Creek fault may

explain the exposure of the deepest crustal level in the Australia Mountain domain closest to the fault, and a slightly higher crustal level in the Finlayson domain to the northeast further from the fault. Alternatively, an un-named, roughly northeast-dipping normal fault, hidden within the Tintina trench (Fig. 5), may have accommodated enough displacement to account for the 5 kilometres of structural relief between these two domains. Furthermore, if this hidden fault is shallowly dipping, the Finlayson domain would restore directly above the Australia Mountain domain. A normal fault of this orientation would explain how the youngest metamorphic domain is exposed west (outboard) of the Finlayson district, contrary to the overall pattern of northeastward younging of deformation and metamorphism toward the foreland. The orogen-parallel orientation of the Australia Creek fault suggests extension along this fault was directed perpendicular to the orogen, and was therefore still being driven by the same orogen-perpendicular wedge dynamics that had operated throughout the Jurassic.

Subsequent mid-Cretaceous extension along the Stewart River and North River faults is interpreted to document northwest-southeast orogen-parallel extension (Fig. 4.9C). Similar southeast-directed extension is documented less than 200 kilometres to the west in east-central Alaska, where parautochthonous North American continental margin rocks (Lake George assemblage in Fig. 4.2) have been exhumed from beneath Yukon-Tanana terrane along mylonitic extensional faults in the mid-Cretaceous. The timing of this extensional exhumation in east-central Alaska, as constrained by c. 135-110 Ma $^{40}Ar/^{39}Ar$ cooling ages (Hansen and Dusel-Bacon, 1998; Dusel-Bacon et al., 2002), is approximately coeval with extension in west-central Yukon. At approximately this time, the trajectory of the North American plate changed from west-northwest to west-southwest at about 110 Ma, based on Phanerozoic apparent polar wander paths (Elston et al., 2002; Nelson et al., 2013). This resulted in a change from sinistral-oblique to near orthogonal convergence between the North American and Farallon plates (Engebretson et al, 1985), and presumably an ensuing increase in the orogen-perpendicular component of horizontal stress. Extension along the Stewart River and North River faults, and comparable mid-Cretacoeus faults in east-central Alaska (Hansen and Dusel-Bacon, 1998; Dusel-Bacon et al., 2002), suggest that this orogen-perpendicular compression was being accommodated by orogen-parallel extension, as

opposed to the previous vertical extension (crustal thickening) that had operated throughout the Jurassic and Early Cretaceous.

This shift from vertical-extension (crustal thickening), to orogen-parallel extension in the orogens interior, contemporaneously with compression in the peripheral fold-and-thrust belts, has also been documented in the Tibetan plateau of the Himalyan orogen (England and Houseman, 1989), the Alps (Ratschbacher et al., 1991), and the Anatolian region of Turkey (Dewey et al., 1986). Furthermore, three-dimensional thermomechanical modelling by Seyferth and Henk (2004) similarly predict that orogen-parallel extension is intimately related to continental collision and occurs contemporaneously with orogen-perpendicular convergence. Similar to the modelling of Seyferth and Henk (2004) the zone of orogen-parallel extension, within the centre (metamorphic hinterland) of the northern Cordilleran orogen, is bound by a zone of strike-slip faults that separate it from orogen-perpendicular shortening in the fold-and-thrust-belts (Fig. 4.9C).

The mechanisms responsible for this kinematic reorganization within the orogen are not necessarily identical for each of the aforementioned orogens. However, several mechanisms, which have previously been ascribed to one or more of these other orogens, may also apply to the northern Cordillera. Vertical thickening in the central and southern Canadian Cordillera coeval with extension and vertical thinning of previously thickened crust in the northern Cordillera (e.g. Australia Creek fault, Staples et al., 2013; Miller and Hudson, 1991) may have created an orogen-parallel crustal thickness gradient, causing rocks to extend and flow outward toward the northwest (e.g. England and McKenzie, 1982; Ratschbacher et al., 1991). Additionally, both the impingement of the foreland-propagating orogenic wedge against a crustal ramp inherited from Late Proterozoic or Paleozoic rifting, and/or the development of a rigid buttress following folding and thrusting in the foreland (e.g., Ratschbacher et al., 1991), may have created a new stress regime such that is was easier to accommodate continued convergence by extending at least a portion of the orogen laterally parallel to the length of the orogen.

4.7. Conclusions

Transposition fabrics and the associated amphibolite facies metamorphism that is nearly ubiquitous throughout the northern Yukon-Tanana terrane and the underlying parautochthonous North American rocks did not develop during a single tectono-metamorphic event. Rather, ductile deformation and amphibolite facies metamorphism developed diachronously, with events recorded in the Late Permian-Early Triassic, Early Jurassic, Middle to Late Jurassic and Early to mid-Cetaceous. Rocks deformed and metamorphosed in the Permo-Triassic and Early Jurassic were exhumed in the Early Jurassic, while rocks to the northeast (toward the foreland) within Yukon were progressively buried and heated from Middle Jurassic to mid-Cretaceous, with deformation and metamorphism younging at progressively deeper crustal levels. These data reveal that deformation and metamorphism migrated toward the foreland and structurally downwards in the Middle Jurassic to Early Cretaceous.

These data and observations are reconciled in terms of critically tapered wedge theory in which cooler rocks in front of the wedge were episodically underthrust, buried and metamorphosed from the Jurassic to mid-Cretaceous beneath an orogenic wedge propagating toward the foreland at critical taper. Rocks that were previously metamorphosed and ductiley deformed in the Permo-Triassic were displaced upward and exhumed through the combined effects of renewed underplating at depth and compensating extensional denudation above in order to maintain a critical taper. Following on the work of Brown (2004) to explain similar patterns in the hinterland of the orogen in the southeastern Canadian Cordillera, we interpret that the localized shear zone that underlies the base of the wedge in foreland thrust-and-fold belt became a distributed (km thick) ductile shear zone (transposition zone) toward the rear of the wedge (hinterland). This zone was a transient feature beneath the propagating wedge as new material was underthrust and incorporated into the distributed shear zone in the Jurassic to mid-Cretaceous causing rocks which previously occupied this zone to be displaced upward into the overlying wedge and ultimately exhumed.

Rocks which occupied the mid-crustal shear zone in the Middle Jurassic to Early Cretaceous (Finlayson and Australia Mountain domains) were first exhumed in the mid-Cretaceous along the Australia Creek fault from beneath a supracrustal ‘lid’ that had

previously been metamorphosed and ductiley deformed (transposed) at amphibolite facies in the Permo-Triassic and Early Jurassic. Continued mid-Cretaceous extension along the Stewart River and North River faults, and comparable faults in east-central Alaska (Hansen and Dusel-Bacon, 1998; Dusel-Bacon et al., 2002), record a shift in the orogens dynamics with extension now directed laterally, parallel to the length of the orogen. The development of an internal zone of orogen-parallel extension, bounded by strike-slip faults, and coeval with continued orogen-perpendicular shortening in the foreland, suggests that continued orogen-perpendicular convergence in the mid-Cretaceous was being accommodated by horizontal extension in the center of the orogen, as opposed to the earlier vertical extension (crustal thickening) documented for the Jurassic and Early Cretaceous. Dinoflagellae within a syn-extensional detachment basin (Indian River formation) to the Australia Creek fault, requires that the orogenic wedge had collapsed and was reduced to sea-level by c. 110-100 Ma, and that extensional denudation along the Australia Creek, Stewart River and North River faults was extremely rapid.

4.8. References

Angen, J., 2013, Structural and geochronological investigation of the southern Alexander terrane in the vicinity of Porcher Island, northwestern British Columbia: Unpublished M.Sc. thesis, Ontario, Canada, University of Waterloo, 121 p.

Aleinikoff, J.N., Dusel-Bacon, C., Foster, H.L., and Futs, K., 1981, Proterozoic zircon from augen gneiss, Yukon-Tanana Upland, east-central Alaska: Geology, v. 9, p. 469–473.

Bailey, L.A., 2013, Late Jurassic fault-hosted gold mineralization of the Golden Saddle deposit, White Gold district, Yukon Territory: Unpublished M.Sc. thesis, Vancouver, Canada, The University of British Columbia, 170 p.

Beranek, L.P., and Mortensen, J.K., 2011, The timing and provenance record of the Late Permian Klondike orogeny in northwestern Canada and arc-continent collision along western North America: Tectonics, v. 30, TC5017, doi:10.1029/2010TC002849.

Beranek, L.P., Mortensen, J K., Orchard, M.J., and Ullrich, T., 2010, Provenance of North American Triassic strata from west-central and southeastern Yukon: Correlations with coeval strata in the Western Canada Sedimentary Basin and Canadian Arctic Islands: Canadian Journal of Earth Sciences, v. 47, 53–73.

Berman, R., Sanborn-Barrie, M., Stern, R., and Carson, C., 2005, Tectonometamorphism at c. 2.35 and 1.85 Ga in the Rae domain, western Churchill Province, Nunavut, Canada: insights from structural, metamorphic and in situ geochronological analysis of the southwestern Committee Bay belt: Canadian Mineralogist, v. 43, p. 409–442.

Berman, R.G., Ryan, J.J., Gordey, S.P., and Villeneuve, M., 2007, Permian to Cretaceous polymetamorphic evolution of the Stewart River region, Yukon-Tanana terrane, Yukon, Canada: P-T evolution linked with in-situ SHRIMP monazite geochronology: Journal of Metamorphic Geology, v. 25, p. 803–827.

Berman, R.G., Sanborn-Barrie, M., Rayner, N., Carson, C., Sandeman, H.A., and Skulski, T., 2010, Petrological and in situ SHRIMP geochronological constraints on the tectonometamorphic evolution of the Committee Bay belt, Rae Province, Nunavut: Precambrian Research, v. 181, p. 1–20.

Berman, R.G., Rayner, N., Sanborn-Barrie, M., and Whalen, J., 2012, The tectonometamorphic evolution of Southampton Island, Nunavut: Insight from petrologic modeling and in situ SHRIMP geochronology of multiple episodes of monazite growth: Precambrian Research v. 232, p. 140–166.

Breitsprecher, K., and Mortensen, J.K., 2004, YukonAge 2004: A database of isotopic age determinations for rock units from Yukon Territory, Canada: Yukon Geological Survey, http://www.geology.gov.yk.ca/databases_gis.html.

Brown, R.L., 2004, Thrust belt accretion and hinterland underplating of orogenic wedges: an example from the Canadian Cordillera, *in* McClay, K.R. ed., Thrust Tectonics and Hydrocarbon Systems, American Association of Petroleum Geologists, Memoir 82, p. 51–64.

Coney, P.J., Jones, D.L., and Monger, J.W.H., 1980, Cordilleran suspect terranes: Nature, v. 288, p. 329–333.

Colpron, M., 1999, Glenlyon Project: Preliminary stratigraphy and structure of Yukon-Tanana terrane, Little Kalzas Lake area, central Yukon (105L/13), *in* Roots, C.F., and Emond, D.S., eds., Yukon Exploration and Geology 1998: Exploration and Geological Services Division, Yukon Region, Indian and Northern Affairs Canada, p. 63-72.

Colpron, M., 2005. Preliminary investigation of the bedrock geology of the Livingstone Creek area (NTS 105E/8), south-central Yukon, *in* Emond, D.S., Lewis, L.L., and Bradshaw, G.D., eds., Yukon Exploration and Geology 2004: Yukon Geological Survey, p. 95-107.

Colpron, M., and Nelson, J.L., 2009, A Palaeozoic northwest passage: incursion of Caledonian, Baltican and Siberian terranes into eastern Panthalassa, and the early evolution of the North American Cordillera, *in* Cawood, P.A., and Kröner, A., eds., Earth Accretionary Systems in Space and Time: The Geological Society of London Special Publications, v. 318, p. 273–307.

Colpron, M., and Ryan, J.J., 2010, Bedrock geology of southwest McQuesten (NTS 115P) and part of northern Carmacks (NTS 115I) map area, *in* MacFarlane, K.E., Weston, L.H. & Blackburn, L.R., eds., Yukon Exploration and Geology, Yukon Geological Survey, p. 159–184.

Colpron, M., Nelson, J.L., and Murphy, D.C., 2006, A tectonostratigraphic framework for the pericratonic terranes of the northern Canadian Cordillera, *in* Colpron, M., and Nelson, J. L., eds., Paleozoic Evolution and Metallogeny of Pericratonic Terranes at the Ancient Pacific Margin of North America, Canadian and Alaskan Cordillera: Geological Association of Canada Special Paper 45, p. 1–23.

Colpron, M., Nelson, J.L., and Murphy, D.C., 2007, Northern Cordilleran terranes and their interactions through time: GSA Today, v. 17, p. 4–10.

Cook, F.A., and Erdmer, P., 2005, An 1800 km cross section of the lithosphere through the northwestern North American plate: lessons from 4.0 billion years of Earth's History: Canadian Journal of Earth Sciences, v. 42, p. 1295–1311.

Crowley, J.L., Ghent, E.D., Carr, S.D., Simony, P.S., and Hamilton, M.A., 2000, Multiple thermotectonic events in a continuous metamorphic sequence, Mica Creek area, southeastern Canadian Cordillera: Geological Materials Research, v. 2, p. 1–45.

Creaser, R.A., Heaman, L.M., and Erdmer, P., 1997, Timing of high-pressure metamorphism in the Yukon–Tanana terrane, Canadian Cordillera: Constraints from U–Pb zircon dating of eclogite from the Teslin tectonic zone: Canadian Journal of Earth Sciences, v. 34, p. 709–715.

Culshaw, N.G., Beaumont, C., and Jamieson, R.A., 2006, The orogenic superstructure-infrastructure concept: Revisited, quantified, and revived: Geology, v. 34, p. 733–736.

Cutts, K.A., Kinny, P.D., Strachan, R.A., Hand, M., Kelsey, D.E., Emery, M., Friend, C.R.L., and Leslie, A.G., 2010, Three metamorphic events recorded in a single garnet: Integrated phase modelling, in situ LA-ICPMS and SIMS geochronology from the Moine Supergroup, NW Scotland: Journal of Metamorphic Geology, v. 28, p. 249–267.

Dahlen, F.A., 1984, Noncohesive critical Coulomb wedges: An exact solution: Journal of Geophysical Research, v. 89, p. 10125–10133.

Davis, D., Suppe, J., and Dahlen, F.A., 1983, Mechanics of fold-and-thrust belts and accretionary wedges: Journal of Geophysical Research, v. 88, p. 1153–1172.

Day, W.C., Aleinikoff, J.N., Roberts, P., Smith, M., Gamble, B.M., Henning, M.W., Gough, L.P., and Morath, L.C., 2003, Geologic map of the Big Delta B-2 Quadrangle, east-central Alaska: U.S. Geological Survey Geologic Investigations Series Map 2788, 1 sheet, scale 1:63,360.

de Keijzer, M., Williams, P.F., and Brown, R.L., 1999, Kilometre-scale folding in the Teslin zone, northern Canadian Cordillera, and its tectonic implications for the accretion of the Yukon–Tanana terrane to North America: Canadian Journal of Earth Sciences, v. 36, p. 479–494.

De Sitter, L.U., and Zwart, H.J., 1960, Tectonic development in supra- and infra-structures of a mountain chain: 21st International Geological Congress, Copenhagen, v. 18, p. 249–256.

Dewey, J.F., Hempton, M.R., Kidd, W.S.F., Saroglu, F., and Sengör, A.M.C., 1986, Shortening of continental lithosphere: the neotectonics of eastern Anatolia – a young collision zone, *in* Coward, M.P. and Ries, A.C., eds., Collision tectonics, Geological Society of London – Special Publications, v. 19, p. 3–36.

Dickie, J.R., and Hein, F.J., 1995, Conglomeratic fan deltas and submarine fans of the Jurassic Laberge Group, Whitehorse trough, Yukon Territory, Canada: fore-arc sedimentation and unroofing of a volcanic island-arc complex: Sedimentary Geology, v. 98, p. 263–292.

Dodds, C.J., 1995, Denali fault system, *in* Gabrielse, H., and Yorath, C.J., eds., Structural Styles, Chapter 17, Geology of the Cordilleran orogen in Canada: Geological Survey of Canada, Geology of Canada, no. 4, p. 656–657.

Dover, J.H., 1994, Geology of part of east-central Alaska, *in* Plafker, G. and Berg, H.C., eds., The Geology of Alaska: Geological Society of America, The Geology of North America, v. G-1, p. 153–204.

Dusel-Bacon, C., and Williams, I.S., 2009, Evidence for prolonged mid-Paleozoic plutonism and ages of crustal sources in east-central Alaska from SHRIMP U-Pb dating of syn-magmatic, inherited and detrital zircon: Canadian Journal of Earth Sciences, v. 46, p. 21–39.

Dusel-Bacon, C., Hansen, V.L., and Scala, J.A., 1995, High-pressure amphibolite facies dynamic metamorphism and the Mesozoic tectonic evolution of an ancient continental margin, east-central Alaska: Journal of Metamorphic Geology, v. 13, p. 9–24.

Dusel-Bacon, C., Lanphere, M.A., Sharp, W.D., Layer, P.W., and Hansen, V.L., 2002, Mesozoic thermal history and timing of structural events for the Yukon-Tanana Upland, east-central Alaska: $^{40}Ar/^{39}Ar$ data from metamorphic and plutonic rocks: Canadian Journal of Earth Sciences, v. 39, p. 1013–1051.

Dusel-Bacon, C., Hopkins, M.J., Mortensen, J.K., Dashevsky, S.S., Bressler, J.R. & Day, W.C., 2006, Paleozoic tectonic and metallogenic evolution of the pericratonic rocks of eastcentral Alaska and adjacent Yukon, *in* Colpron, M., and Nelson, J.L., eds., Paleozoic Evolution and Metallogeny of Pericratonic Terranes at the Ancient Pacific Margin of North America, Canadian and Alaskan Cordillera: Geological Association of Canada Special Paper 45, p. 75–105.

Engebretson, D.C., Cox, A., and Gordon, R.C., 1985, Relative motions between oceanic and continental plates in the Pacific basin: Geological Society of America Special Paper 206, 59 p.

England, P., and McKenzie, D., 1982, A thin viscous sheet model for continental deformation: Geophysical Journal of the Royal Astronomical Society, v. 141, p. 295–321.

England, P., and Houseman, G., 1989, Extension during continental convergence, with application to the Tibetan Plateau: Journal of Geophysical Research, v. 94, p. 17561–17579.

Erdmer, P., 1985, An examination of the cataclastic fabrics and structures of parts of the Nisutlin, Anvil and Simpson allochthons, central Yukon: test of the arc–continent collision model: Journal of Structural Geology, v. 7, p. 57–72.

Erdmer, P., Ghent, E. D., Archibald, D. A., and Stout, M. Z., 1998, Paleozoic and Mesozoic high-pressure metamorphism at the margin of ancestral North America in central Yukon: Geological Society of America Bulletin, v. 110, p. 615–629.

Fallas, K.M., Erdmer, P., Archibald, D.A., Heaman, L.M., and Creaser, R.A., 1998, The St. Cyr klippe, south-central Yukon: an outlier of the Teslin tectonic zone?, *in* Cook, F., and Erdmer, P., compilers, Slave-Northern Cordillera Lithospheric Evolution (SNORCLE) and Cordilleran Tectonics Workshop: Lithoprobe Report no. 64, p. 131–138.

Foster, G., Gibson, H.D., Parrish, R.R., Horstwood, M., Fraser, J., and Tindle, A., 2002, Textural, chemical and isotopic insights into the nature and behaviour of metamorphic monazite: Chemical Geology, v. 191, p. 183–207.

Foster, G., Parrish, R.R., Horstwood, M.S.A., Chenery, S., Pyle, J., and Gibson, H.D., 2004, The generation of prograde P–T–t points and paths; a textural, compositional, and chronological study of metamorphic monazite: Earth Planetary Science Letters, v. 228, p. 125–142.

Foster, H.L., Cushing, G.W., and Keith, T.E.C., 1985, Early Mesozoic tectonic history of the boundary area, east-central Alaska: Geophysical Research Letters, v. 12, p. 553–556.

Foster, H.L., Keith, T.E.C., and Menzie, W.D., 1994, Geology of the Yukon-Tanana area of east-central Alaska, *in* Plafker, G. and Berg, H.C., eds., The Geology of Alaska: Geological Society of America, The Geology of North America, v. G-1, p. 205-240.

Gabrielse, H., Murphy, D.C., and Mortensen, J.K., 2006, Cretaceous and Cenozoic dextral orogen-parallel displacements, magmatism and paleogeography, north-central Canadian Cordillera, *in* Haggart, J.W., Monger, J.W.H., and Enkin, R.J., eds., Paleogeography of the North American Cordillera: Evidence For and Against Large-Scale Displacements: Geological Association of Canada Special Paper 46, p. 255–276.

Gallagher, C.C., 1999, Regional-scale transposition and late large-scale folding in the Teslin zone, Pelly Mountains, Yukon [M.Sc. thesis]: Ottawa, Carleton University, 181 p.

Gehrels, G.E., 2001, Geology of the Chatham Sound region, southeast Alaska and coastal British Columbia: Canadian Journal of Earth Sciences, v. 38, p. 1579–1599.

Gehrels, G.E., Rusmore, M., Woodsworth, G., Crawford, M., Andronicos, C., Hollister, L., Patchett, J., Ducea, M., Butler, R., Klepeis, K., Davidson, C., Friedman, R., Haggart, J., Mahoney, B., Crawford, W., Pearson, D., and Girardi, J., 2009, U-Th-Pb geochronology of the Coast Mountains batholith in north coastal British Columbia: Constraints on age and tectonic evolution: Geological Society of America Bulletin, v. 121, p. 1341–1361.

Gibson, H. D., Carr, S. D., Brown, R. L., and Hamilton, M. A., 2004, Correlations between chemical and age domains in monazite, and metamorphic reactions involving major politic phases: an integration of ID-TIMS and SHRIMP geochronology with Y–Th–U X-ray mapping: Chemical Geology, v. 211, p. 237–260.

Gordey, S.P., 2013, Geology, Selwyn Basin (Sheldon Lake and Tay River), Yukon; Geological Survey of Canada, Map 2149A, 2 map sheets, scale 1:250 000 and 1 sheet of cross-sections, scale 1:100 000.

Gordey, S.P., and Ryan, J.J., 2005, Geology, Stewart River area (115N, 115-O and part of 115J), Yukon Territory: Geological Survey of Canada Open File 4970, scale 1:250 000, 1 sheet.

Hansen, V.L., 1989, Structural and kinematic evolution of the Teslin suture zone, Yukon: record of an ancient transpressional margin: Journal of Structural Geology, v. 11, p. 717–733.

Hansen, V.L., and Dusel-Bacon, C., 1998, Structural and Kinematic evolution of the Yukon-Tanana upland tectonites, east-central Alaska: a record of late Paleozoic to Mesozoic crustal assembly: Geological Society of America Bulletin, v. 110, p. 211–230.

Hart, C.J.R., 1997, A transect across northern Stikinia: Geology of the northern Whitehorse map area, southern Yukon Territory (105D/13-16): Yukon Geological Survey, Bulletin 8, 112 p.

Hart, C.J.R., Dickie, J.R., Ghosh, D.K., and Armstrong, R.L., 1995, Provenance constraints for Whitehorse Trough conglomerate: U-Pb zircon dates and initial Sr ratios of granitic clasts in Jurassic Laberge Group, Yukon Territory: Geological Society of America, Special Paper 299, p. 47–63.

Hood, S.B., 2012, Mid-crustal Cu-Au mineralization during episodic pluton emplacement, hydrothermal fluid flow, and ductile deformation at the Minto deposit, YT, Canada [M.Sc. thesis]: Vancouver, University of British Columbia, 220 p.

Horváth, P., Balen, D., Finger, F., Tomljenović, B., and Krenn, E., 2010, Contrasting P–T–t paths from the basement of the Tisia Unit (Slavonian Mts., NE Croatia): Application of quantitative phase diagrams and monazite age dating: Lithos, v. 117, p. 269–282.

Hults, C.P., Wilson, F.H., Donelick, R.A., and O'Sullivan, P.B., 2013, Two Flysch belts having distinctly different provenance suggest no stratigraphic link between Wrangellia composite terrane and the paleo-Alaskan margin: Lithosphere, v. 5, p. 575–594.

Hunt, P.A., and Roddick, J.C., 1987, A compilation of K-Ar ages, report 17, *in* Radiogenic age and isotopic studies: Report 1, Geological Survey of Canada Paper 87-2, p. 143–210.

Hunt, P.A., and Roddick, J.C., 1991, A compilation of K–Ar and ^{40}Ar–^{39}Ar ages, report 20, *in* Radiogenic age and isotopic studies: Report 4, Geological Survey of Canada Paper 90-2, p. 113–143.

Hunt, P.A., and Roddick, J.C., 1992, A compilation of K–Ar and ^{40}Ar–^{39}Ar ages, report 21, *in* Radiogenic age and isotopic studies: Report 5, Geological Survey of Canada Paper 91-2, p. 207–261.

Hunt, P.A., and Roddick, J.C., 1993, A compilation of K–Ar and ^{40}Ar–^{39}Ar ages, report 23, *in* Radiogenic age and isotopic studies: Report 7, Geological Survey of Canada Paper 93-2, p. 127–154.

Jamieson, R.A., and Beaumont, C., 1988, Orogeny and metamorphism: A model for deformation and pressure-temperature-time paths with applications to the central and southern Appalachians: Tectonics, v. 7, p. 417–445.

Johnston, S. T., Mortensen, J. K., and Erdmer, P., 1996, Igneous and metaigneous age constraints for the Aishihik metamorphic suite, southwest Yukon: Canadian Journal of Earth Sciences, v. 33, p. 1543–1555.

Knight, E., Schneider, D.A., and Ryan, J.J., 2013, Thermochronology of the Yukon-Tanana terrane, west-central Yukon: evidence for Jurassic extension and exhumation in the northern Canadian Cordillera: Journal of Geology, v. 121, p. 371–400.

Long, D.G.F., Lowey, G., and Sweet, A.R., 2001, Age and setting of dinosaur trackways, Ross River area, Yukon Territory (105F/15), *in* Emond, D.S., and Weston, L.H., eds., Exploration and Geological Services Division, Yukon, Indian and Northern Affairs Canada, p. 181-198.

Lowey, G.W., and Hills, L.V., 1988, Lithofacies, petrography, and environments of deposition, Tantalus Formation (Lower Cretaceous) Indian River area, west-central Yukon: Bulletin of Canadian Petroleum Geology, v. 36, p. 296–310.

McCausland, P., Symons, D., Hart, C., and Blackburn, W., 2002, Paleomagnetism and geobarometry of the Granite Mountain batholith, Yukon: Minimal geotectonic motion of the Yukon-Tanana Terrane relative to North America, *in* Emond, D.S., Weston, L.H., and Lewis, L.L., eds., Yukon Exploration and Geology, Yukon Geological Survey, p. 163–177.

McClelland, W.C., Gehrels, G.E., and Saleeby, J.B., 1992, Upper Jurassic – Lower Cretaceous basinal strata along the Cordilleran margin: Implications for the accretionary history of the Alexander–Wrangellia–Peninsular Terrane: Tectonics, v. 11, p. 823–835.

Mihalynuk, M.G., Nelson, J.L., and Diakow, L.J., 1994, Cache Creek terrane: oroclinal paradox within the Canadian Cordillera: Tectonics, v. 13, p. 575-5–595.

Miller, E.L., and Hudson, T.L., 1991, Mid-Cretaceous extensional fragmentation of a Jurassic-Early Cretaceous compressional orogen, Alaska: Tectonics, v. 10, p. 781-796.

Monger, J.W.H., and Price, R.A., 2002, The Canadian Cordillera: Geology and tectonic evolution: Canadian Society of Exploration Geophysicists Recorder, February 2002, p. 17–36.

Monger, J.W.H., Price, R.A., and Tempelman-Kluit, D.J., 1982, Tectonic accretion and the origin of the two major metamorphic and tectonic welts in the Canadian Cordillera: Geology, v. 10, p. 70–75.

Monger, J.W.H., van der Heyden, P., Journeay, J.M., Evenchick, C.A., and Mahoney, J.B., 1994, Jurassic-Cretaceous basins along the Canadian Coast belt: Their bearing on pre-mid-Cretaceous sinistral displacements: Geology, v. 22, p. 175–178.

Mortensen, J.K., 1990, Geology and U-Pb geochronology of the Klondike District, west-central Yukon Territory: Canadian Journal of Earth Sciences, v. 27, p. 903–914.

Mortensen, J. K., 1992, Pre-mid-Mesozoic tectonic evolution of the Yukon-Tanana terrane, Yukon and Alaska: Tectonics, v. 11, p. 836–853.

Murphy, D.C., 1987, Suprastructure/infrastructure transition, east-central Cariboo Mountains, British Columbia: geometry, kinematics and tectonic implications: Journal of Structural Geology, v. 9, p. 13–29.

Murphy, D.C., 2004, Devonian-Mississippian metavolcanic stratigraphy, massive sulphide potential and structural re-interpretation of Yukon-Tanana terrane south of the Finlayson Lake massive sulphide district, southeastern Yukon (105G/1, 105H/3,4,5), *in* Emond, D.S., and Lewis, L.L., eds., Yukon Exploration and Geology 2003, Yukon Geological Survey, p. 157–175.

Murphy, D.C., Colpron, M., Gordey, S.P., Roots, C.F., Abbott, J.G. and Lipovsky, P.S., 2001, Preliminary bedrock geological map of northern Finlayson Lake area (NTS 105G) Yukon Territory (1:100 000 scale). Exploration and Geological Services Division, Yukon Region, Indian and Northern Affairs Canada, Open File 2001-33.

Murphy, D.C., Mortensen, J.K., Piercey, S.J., Orchard, M.J., and Gehrels, G.E., 2006, Mid-Paleozoic to early Mesozoic tectonostratigraphic evolution of Yukon-Tanana and Slide Moutnain terranes and affiliated overlap assemblages, Finlayson Lake massive sulphide district, southeastern Yukon, *in* Colpron, M., and Nelson, J.L., eds., Paleozoic Evolution and Metallogeny of Pericratonic Terranes at the Ancient Pacific Margin of North America, Canadian and Alaskan Cordillera: Geological Association of Canada Special Paper 45, p. 75–105.

Nelson, J.L., Colpron, M., Piercey, S.J., Dusel-Bacon, C., Murphy, D.C., and Roots, C.F., 2006, Paleozoic tectonic and metallogenic evolution of the pericratonic terranes in Yukon, northern British Columbia and eastern Alaska., *in* Colpron, M., and Nelson, J.L., eds., Paleozoic Evolution and Metallogeny of Pericratonic Terranes at the Ancient Pacific Margin of North America, Canadian and Alaskan Cordillera: Geological Association of Canada Special Paper 45, p. 323–360.

Nelson, J.L., Colpron, M., and Israel, S., 2013, The Cordillera of British Columbia, Yukon and Alaska: Tectonics and Metallogeny, *in* Colpron, M., Bissig, T., Rusk, B.G., and Thompson, J.H.F., eds., Tectonics, Metallogeny, and Discovery: The North American Cordillera and Similar Accretionary Settings: Society of Economic Geologists, Special Publication 17, p. 53–109.

Parrish, R.R., 1995, Thermal evolution of the southeastern Canadian Cordillera: Canadian Journal of Earth Sciences, v. 32, p. 1618–1642.

Piercey, S.J., and Colpron, M., 2009, Composition and provenance of the Snowcap assemblage, basement to the Yukon-Tanana terrane, northern Cordillera: Implications for Cordilleran crustal growth: Geosphere, v. 5, p. 439–464.

Platt, J.P., 1986, Dynamics of orogenic wedges and the uplift of high-pressure metamorphic rocks: Geological Society of America Bulletin, v. 97, p. 1037–1053.

Ratschbacher, L., Frisch, W., and Linzer, H., 1991, Lateral extrusion in the eastern Alps, Part 2: structural analysis: Tectonics, v. 10, p. 257–271.

Read, P.B., Woodsworth, G.J., Greenwood, H.J., Ghent, E.D., and Evenchick, C.A.,1991, Metamorphic Map of the Canadian Cordillera: Geological Survey of Canada, Map 1714A, scale 1:2 000 000.

Roddick, J.A., 1967, Tintina Trench: Journal of Geology, v. 75, p. 23–32.

Ruks, T.W., Piercey, S.J., Ryan, J.J., Villeneuve, M.E., and Creaser, R.A., 2006, Mid- to Late Paleozoic K-feldspar augen granitoids of the Yukon-Tanana terrane, Yukon: Implications for crustal growth and tectonic evolution of the northern Cordillera: Geological Society of America Bulletin, v. 118, p. 1212–1231.

Ryan, J.J., Colpron, M. & Hayward, N., 2010, Geology, southwestern McQuesten and parts of northern Carmacks, Yukon: Geological Survey of Canada, Canadian Geoscience Map 7, (preliminary version), scale 1:125 000.

Saleeby, J.B., 2000, Geochronologic investigations along the Alexander–Taku terrane boundary, southern Revillagigedo Island to Cape Fox areas, southeast Alaska, *in* Stowell, H.H., and McClelland, W.C., eds., Tectonics of the Coast Mountains, southeast Alaska and coastal British Columbia: Geological Society of America Special Paper 343, p. 107–143.

Seyferth, M., and Henk, A., 2004, Syn-convergent exhumation and lateral extrusion in continental collision zones—insights from three-dimensional numerical models: Tectonophysics, v. 382, p. 1–29.

Staples, R.D., Gibson, H.D., Berman, R.G., Ryan, J.J., and Colpron, M., 2013, A window into the Early to mid-Cretaceous infrastructure of the Yukon-Tanana terrane recorded in multi-stage garnet of west-central Yukon, Canada: Journal of Metamorphic Geology, v. 31, p. 729–753.

Stevens, R.D., Delabio, R.N., and Lachance, G.R., 1982, Age determinations and geological studies, K-Ar isotopic ages, report 15: Geological Survey of Canada Paper 81-2.

Tafti, R., 2005, Nature and origin of the Early Jurassic copper (-gold) deposits at Minto and Williams Creek, Carmack copper belt, western Yukon: Examples of deformed porphyry deposits [M.Sc. thesis]: Vancouver, University of British Columbia, 213 p.

Tempelman-Kluit, D.J., 1979, Transported cataclasite, ophiolite and granodiorite in Yukon: evidence of arc–continent collision: Geological Survey of Canada Paper 79-14, p. 1–27.

van der Heyden, P., 1992, A Middle Jurassic to Early Tertiary Andean–Sierran arc model for the Coast Belt of British Columbia: Tectonics, v. 11, p. 82–97.

Wanless, R.K., Stevens, R.D., Lachance, G.R., and Edmonds, C.M., 1967, Age determinations and geological studies, K-Ar isotopic ages: Report 7, Geological Survey of Canada Paper 66-17.

Willet, S.D., 1999, Rheological dependence of extension in wedge models of convergent orogens: Tectonophysics, v. 305, p. 419–435.

Willet, S., Beaumont, C., and Fullsack, P., 1993, Mechanical model for the tectonics of doubly vergent compressional orogens: Geology, v. 21, p. 371–374.

Williams, C.A., Connors, C., Dahlen, F.A., Price, E.J., and Suppe, J., 1994, Effect of the brittle-ductile transition on the topography of compressive mountain belts on Earth and Venus: Journal of Geophysical Research, v. 99, p. 19,947–19,974.

Williams, M.L., and Jercinovic, M.J., 2002, Microprobe monazite geochronology: putting absolute time into microstructural analysis: Journal of Structural Geology, v. 24, p. 1013–1028.

Williams, M.L., Jercinovic, M.J., Harlov, D.E., Budzyń, B., and Hetherington, C.J., 2011, Resetting monazite ages during fluid-related alteration: Chemical Geology, v. 283, p. 218–225.

Williams, P.F., 1985, Multiply deformed terrains-problems of correlation: Journal of Structural Geology, v. 7, p. 269–280.

Williams, P.F., and Jiang, D., 2005, An investigation of lower crustal deformation: Evidence for channel flow and its implications for tectonics and structural studies: Journal of Structural Geology, v. 27, p. 1486–1504.

Williams, P.F., Jiang, D., and Lin, S., 2006, Interpretation of deformation fabrics of infrastructure zone rocks in the context of channel flow and other tectonic models, *in* Law, R.D., Searle, M.P., and Godin, L., eds., Channel Flow, Ductile Extrusion and Exhumation in Continental Collision Zones: Geological Society, London, Special Publications 268, p. 221–235.

Chapter 5.

Conclusions

The lowest structural and stratigraphic levels of the Yukon-Tanana terrane (Snowcap assemblage; Colpron et al., 2006) and the structurally underlying parauthochthonous North American margin rocks were metamorphosed to amphibolite facies conditions. These rocks share a similar style of deformation characterized by the ductile transposition of lithologic contacts and primary compositional layering into a regional foliation (S_T) with at least one generation of intrafolial isoclinal folds (Foster et al., 1994; Hansen and Dusel-Bacon, 1998; Dusel-Bacon et al., 2002; 2006; Gordey and Ryan, 2005; Berman et al., 2007). This thesis adds to the work done by Berman et al. (2007), in the Stewart River map area of north central Yukon-Tanana terrane, by expanding the application of equilibrium assemblage modeling and *in situ* U-Th-Pb SHRIMP dating of monazite to place quantitative constraints on the conditions and timing of deformation, metamorphism and subsequent decompression in similar, adjacent rocks to the northeast.

Data presented in Chapter 2, together with the data of Berman et al. (2007), elucidate a high-pressure Cretaceous tectono-metamorphic domain (Australia Mountain domain) that is distinct from an adjacent domain of Yukon-Tanana terrane rocks to the west and south that were affected by Permo-Triassic and Early Jurassic events, and exhumed to upper crustal levels in the Early Jurassic (Berman et al., 2007). Petrology, phase equilibria modeling and *in situ* SHRIMP monazite geochronology record the waning development of transposition foliation at near-thermal peak P-T conditions of ~ 650-680 °C and 9 kbar (≈ 30 km depth) in the Early Cretaceous (c. 146-118 Ma). Slightly younger (c. 112 Ma), texturally and chemically distinct monazite within resorbed portions of garnet from Australia Mountain record the onset of near isothermal decompression in the mid-Cretaceous following the peak of metamorphism. Therefore, contrary to much of the Yukon-Tanana terrane to the west and south, which was deformed and

metamorphosed in the Permo-Triassic and exhumed to upper crustal levels in the Jurassic, the Australia Mountain domain occupied a deep crustal level (~25–30 km) in the Early to mid-Cretaceous. Poor exposure in the area prevents field recognition of faults bounding this Early Cretaceous tectono-metamorphic domain. However, the abrupt juxtaposition of this domain against rocks with Early to Middle Jurassic cooling to the west and south (Hunt and Roddick, 1992; Knight et al., 2013) and Paleozoic and Mesozoic cooling ages to the southeast (Knight et al., 2013), suggests the Australia Mountain domain is bound by crustal-scale mid-Cretaceous normal faults (Australia Creek and Stewart River normal faults, respectively). This area therefore represents a tectonic window into Early to mid-Cretaceous infrastructure of the Yukon-Tanana terrane, potentially comparable to parautochthonous North American continental margin rocks beneath the Yukon-Tanana terrane in east-central Alaska, and may be akin to, but older than, extensional core complexes identified throughout the North American Cordillera.

In situ SHRIMP monazite geochronology and garnet isopleth thermobarometry, presented in Chapter 3 reveal a previously unrecognized Middle Jurassic to earliest Cretaceous (c. 169-142 Ma) mid-crustal metamorphic event coeval with the development of transposition fabrics in the eastern portion of the Yukon-Tanana terrane (Finlayson Lake district, southeast Yukon; referred to as the Finlayson domain) that culminated at conditions of approximately 600 °C and 7.5 kbar. The rocks which record this event are located in the footwall of the North River fault (Murphy, 2004). The North River fault is a regional-scale mid-Cretaceous normal fault that cuts across Yukon-Tanana terrane in the Finlayson Lake district in a roughly northeast-southwest trend (Murphy, 2004). Rocks in the footwall record mid-Cretaceous $^{40}Ar/^{39}Ar$ and K-Ar cooling ages (Wanless et al., 1967; Hunt and Roddick, 1992; Murphy and Villeneuve, unpub. data), are intruded by mid-Cretaceous granite plutons, and were ductiley deformed at amphibolite facies prior to the emplacement of the granites. Low grade rocks in the hanging wall to the southeast comprise the upper thrust sheets of Yukon-Tanana terrane; these lack Cretaceous granites and contain Mississippian and Pennsylvanian K-Ar cooling ages (Stevens et al., 1982; Hunt and Roddick, 1987). Restoration of approximately 430 kilometres of dextral strike-slip displacement along the Tintina fault in the Paleogene, and approximately 60 kilometres of extension in the Cretaceous

(Gabrielse et al., 2006), places the trace of the North River fault approximately adjacent to the trace of the mid-Cretaceous Stewart River fault southwest of the Tintina fault. The Stewart River fault likewise juxtaposes rocks ductiley deformed and metamorphosed in the Early Cretaceous against generally undeformed and weakly metamorphosed rocks to the southeast with Mississippian cooling ages (Colpron and Ryan, 2010; Knight et al., 2013). Therefore, prior to Paleogene offset along the Tintina fault, the Stewart River and North River faults possibly formed a continuous normal fault. Both the Permo-Triassic and Early Jurassic metamorphic domain to the west and the Devono-Mississippian rocks to the south were presumably located within the superstructural 'lid' fabove Jura-Cretaceous metamorphic domains that were exhumed along the Australia Creek and Stewart River/North River faults, respectively, in the mid-Cretaceous.

The data presented in chapters 2 and 3 reveal that the ductile deformation (transposition) fabrics, which formed under nearly identical metamorphic conditions at 7.5 – 9 kbar and 600 – 680 °C), did not develop during a single tectono-metamorphic event. Rather, deformation and metamorphism developed diachronously. across the northern portion of Yukon-Tanana terrane and underlying parautochthonous North American margin rocks in west-central Yukon, with events recorded in the Late Permian-Early Triassic, Early Jurassic, Middle to Late Jurassic and Early to mid-Cetaceous. Rocks deformed and metamorphosed within Yukon-Tanana terrane in the Permo-Triassic and Early Jurassic were exhumed in the Early Jurassic, while Yukon-Tanana terrane rocks to the northeast in the Finlayson domain were buried, heated and ductiley deformed at mid-crustal levels (~25 km depth) from the Middle Jurassic to earliest Cretaceous (c. 169 – 142 Ma). Metamorphism continued to migrate to an even deeper crustal level (~ 30 km depth, as recorded in the Australia Mountain domain), propagating downward into the parautochthonous North American crust in the Early to mid-Cretaceous (c. 146 – 118 Ma). Additionally, the apparent absence of Permo-Triassic and Early Jurassic metamorphism in the younger and lower structural domains (Australia Mountain and Finlayson domains), suggests that deformation and metamorphism migrated into cooler rocks to the northeast toward the foreland that had yet to be incorporated into the burgeoning orogenic wedge. Together, these data reveal a spatial and temporal pattern of structurally downward younging deformation and metamorphism that corresponds with the foreland-directed growth of the orogenic wedge. In this model,

rocks in front of the wedge are episodically underthrust downward into a distributed, amphibolite facies transposition shear zone at 25 to 30 kilometres depth near the base of the overriding wedge. Rocks previously underthrust, buried and metamorphosed are progressively exhumed to higher structural levels within the wedge, as the upper crust enters a state of extension in order to maintain a critically tapered wedge. This model is akin to a model originally proposed by Platt (1986) and later adapted by Brown (2004) to explain a similar, and partly coeval, diachronous pattern of structurally downward younging ductile deformation in the southeastern Canadian Cordillera.

Despite an apparent foreland-directed younging of deformation and metamorphism, as recorded from the absence of older Permo-Triassic and Early Jurassic metamorphism in the younger domains to the northeast (toward the foreland), the c. 146-118 Ma Australia Mountain metamorphic domain lies southwest (outboard) of the older (c. 169-142 Ma) Finlayson metamorphic domain. However, prior to accretion, the Australia Mountain domain is interpreted to have originally lied east of the Finlayson domain (Yukon-Tanana terrane) based on the interpretation that it represents parautochthonous North American margin. The present exposure of the Australia Mountain domain west of the Finlayson Lake district is attributed to underthrusting down to the west beneath the Finlayson Lake district in the Early Cretaceous, following burial and metamorphism of the Finlayson Lake district.

The Middle Jurassic to Early Cretaceous and Early Cretaceous metamorphic events recorded in the Finlayson Australia Mountain domains, respectively, in the northern Cordillera was contemporaneous with amphibolite facies metamorphic events recorded in the southern Cariboo and northern Monashee and Selkirk Mountains in the southeastern Canadian Cordillera (c. 135 Ma, Currie, 1988; c. 140 Ma, Digel et al., 1998; c. 163 Ma, Crowley et al., 2000; c. 148, Ma Reid, 2003; c. 144, Gibson et al., 2004; c. 153 Ma, Gervais and Hynes, 2012). Furthermore, the pattern of structurally downward younging deformation and metamorphism in the northern Cordillera described above is strikingly similar to, and in part contemporaneous, with the southeastern Canadian Cordillera. In the southeastern Canadian Cordillera, deformation and metamorphism progressed from Early Jurassic to Eocene (Evenchick et al., 2007, and references therein), with younger events recorded at progressively deeper crustal levels (Parrish, 1995). There, rocks presently in the upper structural levels were buried, heated and

exhumed in the Jurassic (Murphy et al., 1995; Colpron et al., 1996; Crowley et al., 2000; Gibson et al., 2005, 2008), while structurally deeper levels continued to be buried and heated from Cretaceous to earliest Eocene (Carr, 1991; Parrish, 1995; Gibson et al., 1999, 2005, 2008; Crowley and Parrish, 1999; Crowley et al., 2000). This pattern has been attributed to progressive structural burial and underplating of cooler rocks to the east as deformation migrates toward the craton (Parrish, 1995; Brown, 2004).

It seems a similar process was active from Middle Jurassic to mid-Cretaceous time in the northern Cordillera. The foreland-directed and downward migration of deformation and metamorphism is interpreted to have been driven by continued migration and underthrusting of the North American continent from the east, together with the accretion and underthrusting of the Insular terranes (Peninsular-Alexander-Wrangellia) beneath the western side of Yukon-Tanana terrane in the Middle to Late Jurassic (Fig. 13B; McClelland et al., 1992; van der Heyden, 1992, Saleeby, 2000; Gehrels, 2001; Trop and Ridgway, 2007). These results suggest that analogous orogenic processes may have been operating contemporaneously over 1000 kilometres along strike during the development of the Canadian Cordillera, and is a model that may have implications for unravelling the history of other orogenic belts around the world.

5.1. Summary of Tectonic Model

The lower structural and stratigraphic levels of the Yukon-Tanana terrane and the structurally underlying parautochthonous North American margin are penetratively deformed, amphibolite facies rocks characterized by a shallowly dipping transposition fabric with abundant intrafolial folds, and a non-coaxial deformation history. These rocks are interpreted to represent a crustal-scale (kilometres thick) shear zone as described by Williams and Jiang (2005). Although, as monazite geochronology on these rocks reveals (Berman et al., 2007; Chapters 2 & 3), the development of this amphibolite facies transposition fabric was not necessarily synchronous throughout the terrane, but rather appears to be a transient feature that youngs both structurally downwards and toward the foreland, similar to that described by Brown (2004) in the SE Canadian Cordillera.

Despite the diachronous timing, each of the Permo-Triassic, Early Jurassic, Middle to Late Jurassic and Early Cretaceous events occurred under approximately the same set of physical conditions (600 – 680 °C and 7.5 – 9 kbar = 25 - 30 km depth: Berman et al., 2007; Chapters 2 & 3). This requires that rocks which previously occupied the transposition zone in the middle crust were subsequently exhumed by erosion and/or tectonic denudation prior to, or coeval with, the progressive ductile underthrusting, burial and incorporation of new rocks into the transposition zone. It is proposed in this thesis that from Early Jurassic to mid-Cretaceous, the allochthonous Yukon-Tanana terrane was obducted onto the North American continental margin, and together with the underlying parautochthonous continental margin, formed an orogenic wedge that episodically propagated toward the foreland (Chapter 4). Cooler rocks in front of the wedge were progressively buried and metamorphosed from the Jurassic to mid-Cretaceous as they were underthrust into a distributed, amphibolite facies transposition shear zone beneath the overriding orogenic wedge.

Rocks that were previously buried and metamorphosed at approximately 30 km depth in the Permo-Triassic were displaced upward into the overlying wedge and ultimately exhumed in the Early Jurassic through the combined effects of renewed underplating at depth and compensating extensional denudation above in order to maintain a critically tapered wedge (cf. Platt, 1986; Chapter 4). The underthrusting of cooler rocks toward the rear of the wedge in the Early Jurassic would provide a new source of fertile material from which fluids may be derived upon heating which would drive dehydration reactions. Migration of this fluid upwards may have provided the catalyst for renewed metamorphic reactions and Early Jurassic monazite growth in the overlying rocks that were previously metamorphosed and dehydrated in the Permian, and subsequently exhumed to upper structural levels in the Early Jurassic. The introduction of reaction catalyzing fluids contemporaneous with exhumation would explain the overlap of Early Jurassic U-Pb metamorphic monazite and $^{40}Ar/^{39}Ar$ cooling ages (Berman et al., 2007). Additionally, the presence of fluids and a slightly higher position within the crust may explain the absence of associated penetrative ductile strain, and the more discrete, localized deformation associated with metamorphism in the Early Jurassic within the Permo-Triassic and Early Jurassic metamorphic domain.

This procress continued into the Late Jurassic – Early Cretaceous. The highly transposed nature, P-T data and U-Pb monazite geochronology of rocks in the Finlayson and Australia Mountain domains to the northeast (toward the foreland) of the Permo-Triassic and Early Jurassic metamorphic domain indicate they were eventually buried into a high-grade transposition shear zone at 25-30 km's depth in the Middle Jurassic to Early Cretaceous. In order to maintain a stable taper during Middle Jurassic to Early Cretaceous underthrusting and thickening, the upper crust likely entered a state of extension coeval with contraction at depth.

Underplating, heating and devolatilization of cool, fertile (hydrous) material in the Finlayson and Australia Mountain domains in the Middle to Late Jurassic and Early Cretaceous may have provided a source of fluids for Late Jurassic 'orogenic' gold-bearing veins (Bailey, 2013) within the structurally overlying, colder and previously dehydrated rocks of the Klondike-White Gold district (located within the Permo-Triassic/Early Jurassic metamorphic domain). This is supported by the 163 – 155 Ma age of gold mineralization (Bailey, 2013), which is contemporaneous with amphibolite facies metamorphism, devolatilization and ductile deformation (c. 169-142 Ma) at deeper crustal levels in the Finlayson domain (Chapter 3).

Rocks which occupied the mid-crustal shear zone in the Middle Jurassic to Early Cretaceous (Finlayson and Australia Mountain domains) were exhumed in the mid-Cretaceous along the Australia Creek fault from beneath a supracrustal 'lid' that had previously been metamorphosed and ductiley deformed (transposed) at amphibolite facies in the Permo-Triassic and Early Jurassic. Southeast-northwest directed extension along the Stewart River and North River faults, as well as comparable faults in east-central Alaska, indicate that the dynamics within the orogen had changed immediately following some initial period of exhumation along the Australia Creek, which they cut at a high angle. The Stewart River and North River faults exhumed the Early Cretaceous metamorphic domain from beneath low-grade rocks with Carboniferous cooling ages, indicating that they've occupied a high crustal level since the Carboniferous. Horizontal, orogen-parallel directed extension along these faults, during ongoing orthogonal plate convergence between the North American and Farallon plates in the mid-Cretaceous (Engebretson et al., 1985), suggests that shortening in this portion of the orogen was being accommodated by horizontal extension at this time, as opposed to vertical

extension (crustal thickening) that occurred throughout the Jurassic and Early Cretaceous. Dinoflagellae within a syn-extensional detachment basin (Indian River formation) to the Australia Creek fault requires that the orogenic wedge had collapsed and was reduced to sea-level by c. 110-100 Ma, and that extensional denudation along the Australia Creek, Stewart River and North River faults was extremely rapid.

5.2. References

Bailey, L.A., 2013, Late Jurassic fault-hosted gold mineralization of the Golden Saddle deposit, White Gold district, Yukon Territory: Unpublished M.Sc. thesis, Vancouver, Canada, The University of British Columbia, 170 p.

Berman, R.G., Ryan, J.J., Gordey, S.P., and Villeneuve, M., 2007, Permian to Cretaceous polymetamorphic evolution of the Stewart River region, Yukon-Tanana terrane, Yukon, Canada: P-T evolution linked with in-situ SHRIMP monazite geochronology: Journal of Metamorphic Geology, v. 25, p. 803–827.

Brown, R.L., 2004, Thrust belt accretion and hinterland underplating of orogenic wedges: an example from the Canadian Cordillera, *in* McClay, K.R. ed., Thrust Tectonics and Hydrocarbon Systems, American Association of Petroleum Geologists, Memoir 82, p. 51–64.

Colpron, M., and Ryan, J.J., 2010, Bedrock geology of southwest McQuesten (NTS 115P) and part of northern Carmacks (NTS 115I) map area, *in* MacFarlane, K.E., Weston, L.H. & Blackburn, L.R., eds., Yukon Exploration and Geology, Yukon Geological Survey, p. 159–184.

Colpron, M., Nelson, J.L., and Murphy, D.C., 2006, A tectonostratigraphic framework for the pericratonic terranes of the northern Canadian Cordillera, *in* Colpron, M., and Nelson, J. L., eds., Paleozoic Evolution and Metallogeny of Pericratonic Terranes at the Ancient Pacific Margin of North America, Canadian and Alaskan Cordillera: Geological Association of Canada Special Paper 45, p. 1–23.

Dusel-Bacon, C., Hansen, V.L., and Scala, J.A., 1995, High-pressure amphibolite facies dynamic metamorphism and the Mesozoic tectonic evolution of an ancient continental margin, east-central Alaska: Journal of Metamorphic Geology, v. 13, p. 9–24.

Dusel-Bacon, C., Lanphere, M.A., Sharp, W.D., Layer, P.W., and Hansen, V.L., 2002, Mesozoic thermal history and timing of structural events for the Yukon-Tanana Upland, east-central Alaska: $^{40}Ar/^{39}Ar$ data from metamorphic and plutonic rocks: Canadian Journal of Earth Sciences, v. 39, p. 1013–1051.

Dusel-Bacon, C., Hopkins, M.J., Mortensen, J.K., Dashevsky, S.S., Bressler, J.R. & Day, W.C., 2006, Paleozoic tectonic and metallogenic evolution of the pericratonic rocks of eastcentral Alaska and adjacent Yukon, *in* Colpron, M., and Nelson, J.L., eds., Paleozoic Evolution and Metallogeny of Pericratonic Terranes at the Ancient Pacific Margin of North America, Canadian and Alaskan Cordillera: Geological Association of Canada Special Paper 45, p. 75–105.

Elston, D.P., Enkin, R.J., Baker, J., and Kisilevsky, D.K., 2002, Tightening the Belt: paleomagnetic stratigraphic constraints on deposition, correlation and deformation of the middle Proterozoic (ca. 1.4 Ga) Belt-Purcell Supergroup, United States and Canada: Geological Society of America Bulletin, v. 114, p. 619–638.

Foster, H.L., Keith, T.E.C., and Menzie, W.D., 1994, Geology of the Yukon-Tanana area of east-central Alaska, *in* Plafker, G. and Berg, H.C., eds., The Geology of Alaska: Geological Society of America, The Geology of North America, v. G-1, p. 205-240.

Gabrielse, H., Murphy, D.C., and Mortensen, J.K., 2006, Cretaceous and Cenozoic dextral orogen-parallel displacements, magmatism and paleogeography, north-central Canadian Cordillera, *in* Haggart, J.W., Monger, J.W.H., and Enkin, R.J., eds., Paleogeography of the North American Cordillera: Evidence For and Against Large-Scale Displacements: Geological Association of Canada Special Paper 46, p. 255–276.

Gibson, H. D., Carr, S. D., Brown, R. L. & Hamilton, M. A., 2004. Correlations between chemical and age domains in monazite, and metamorphic reactions involving major politic phases: an integration of ID-TIMS and SHRIMP geochronology with Y–Th–U X-ray mapping. Chemical Geology, **211,** 237–260.

Gordey, S. P., and Ryan, J. J., 2005, Geology, Stewart River area (115N, 115-O and part of 115J), Yukon Territory: Geological Survey of Canada Open File 4970, scale 1:250 000, 1 sheet.

Hansen, V.L., and Dusel-Bacon, C., 1998, Structural and Kinematic evolution of the Yukon-Tanana upland tectonites, east-central Alaska: a record of late Paleozoic to Mesozoic crustal assembly: Geological Society of America Bulletin, v. 110, p. 211–230.

Hunt, P.A., and Roddick, J.C., 1987, A compilation of K-Ar ages, report 17, *in* Radiogenic age and isotopic studies: Report 1, Geological Survey of Canada Paper 87-2, p. 143–210.

Hunt, P.A., and Roddick, J.C., 1992, A compilation of K–Ar and ^{40}Ar–^{39}Ar ages, report 21, *in* Radiogenic age and isotopic studies: Report 5, Geological Survey of Canada Paper 91-2, p. 207–261.

Knight, E., Schneider, D.A., and Ryan, J.J., 2013, Thermochronology of the Yukon-Tanana terrane, west-central Yukon: evidence for Jurassic extension and exhumation in the northern Canadian Cordillera: Journal of Geology, v. 121, p. 371–400.

Murphy, D.C., 2004, Devonian-Mississippian metavolcanic stratigraphy, massive sulphide potential and structural re-interpretation of Yukon-Tanana terrane south of the Finlayson Lake massive sulphide district, southeastern Yukon (105G/1, 105H/3,4,5), *in* Emond, D.S., and Lewis, L.L., eds., Yukon Exploration and Geology 2003, Yukon Geological Survey, p. 157–175.

Platt, J.P., 1986, Dynamics of orogenic wedges and the uplift of high-pressure metamorphic rocks: Geological Society of America Bulletin, v. 97, p. 1037–1053.

Staples, R.D., Gibson, H.D., Berman, R.G., Ryan, J.J., and Colpron, M., 2013, A window into the Early to mid-Cretaceous infrastructure of the Yukon-Tanana terrane recorded in multi-stage garnet of west-central Yukon, Canada: Journal of Metamorphic Geology, v. 31, p. 729–753.

Stevens, R.D., Delabio, R.N., and Lachance, G.R., 1982, Age determinations and geological studies, K-Ar isotopic ages, report 15: Geological Survey of Canada Paper 81-2.

Wanless, R.K., Stevens, R.D., Lachance, G.R., and Edmonds, C.M., 1967, Age determinations and geological studies, K-Ar isotopic ages: Report 7, Geological Survey of Canada Paper 66-17.

Williams, P.F., and Jiang, D., 2005, An investigation of lower crustal deformation: Evidence for channel flow and its implications for tectonics and structural studies: Journal of Structural Geology, v. 27, p. 1486–1504.

Appendix A.

Sample field locations and summary of P-T-t data

Table A1. Summary table of P-T-t data and corresponding sample locations

Sample no.	Field no.	UTM (NAD 83) Easting	UTM (NAD 83) Northing	[a]Main assemblage	Peak thermobarometry [b]P (kbar)	Peak thermobarometry T (°C)	Peak thermobarometry Eq.[c]	Event	[d]Age (Ma)	Interpretation
Chapter 2		zone 7								
1	09RS190A1	642809	7056955	St-Grt-Bt-Pl-Qtz	8.8	650	1,3	M2	[e]120 ± 3	Prograde M2, syn- to post-S_T
					8	650	pd	M2	[e]112 ± 6	M2 decompression
2	09RS172B1	641621	7063232	Ky-St-Crd-Grt-Bt Qtz-Pl	8.9	650	1,2,3	M2	[e]118 ± 2	Prograde M2, syn- to post-S_T
3	09RS171A1	641101	7063420	Ms-Bt-Grt-Pl-Qtz	9 - 10	680	1,3,4	M2	–	Prograde M2, syn- to post-S_T
4	09RS188A2	642122	7057171	Sil-Grt-Crd-St-Ky-Bt-Pl-Qtz	–	–	–	-	[e]117 ± 1	Prograde M2, syn- to post-S_T
Chapter 3		zone 9								
32	11RS032	401388	6794817	Grt-Bt-Ms-Pl-Qtz-Ilm	-	-	-		[f]152-161	Prograde (near-peak), syn-S_T
33	11RS033A1	401205	6794906	Grt-Bt-St-Ms-Pl-Qtz-Ilm	7.3	595	Grt. Isopl.		[f]142-163	Prograde (near-peak), syn-S_T
43	11RS043A1	400468	6793654	Grt-Bt-St-Ms-Pl-Qtz-Ilm	7.5	600	Grt. Isopl.		[f]154-169	Prograde (near-peak), syn-S_T
90	11RS090	401384	6794518	Grt-Bt-St-Ms-Pl-Qtz-Ilm	-	-	-		[f]155-159	Prograde (near-peak), syn-S_T

[a] Minerals listed from least to most abundant.
[b] Estimated uncertainties are ± 1 kbar and 50 °C (Berman, 1991).
[c] Equilibria used to derive listed *P-T* values (pd = phase diagram constraints; Grt. Isopl. = garnet isopleth thermobarometry).
[d] All ages are ^{207}Pb-corrected $^{206}Pb/^{238}U$ ages determined by *in situ* SHRIMP analysis of monazite.
[e] Age represents weighted mean ages (2 sigma errors) of texturally and chemically similar monazite grains discussed in text.
[f] Ages represent range of individual monazite spot ages (1 sigma errors) for each sample.

Appendix B.

McQuesten in situ SHRIMP U-Th-Pb monazite data

Sample Location and Description

Two monazite grains (M138 and M32) from sample RS-09-003A were analyzed in situ for U-Th-Pb dating with the SHRIMP. Sample RS-09-003A was collected west of Tintina fault in the McQuesten map area of west-central Yukon (Fig. B1; UTM NAD 83: zone 8, 387660E 7011676N), and is considered part of the Snowcap assemblage of the Yukon-Tanana terrane (Ryan et al., 2010). The Snowcap assemblage is the pre-Late Devonian metasedimentary basement of Yukon-Tanana terrane, with lithological, geochemical and isotopic compositions that suggest it represents a distal portion of the continental margin that was rifted off western Laurentia in mid-Palaeozoic time (Nelson et al., 2006; Colpron and Nelson, 2009; Piercey and Colpron, 2009). The Snowcap assemblage formed the nucleus into, and upon, which three unconformity-bounded Upper Devonian to Permian volcanic arc sequences (Finlayson, Klinkit, Klondike assemblages) were intruded and deposited (Colpron et al., 2006; Nelson et al., 2006).

Sample RS-09-003A is a Grt-Ms-Bt schist with a well-developed transposition foliation (S_T) defined by aligned biotite and ribbon quartz (Fig. B2a and B2b), and intrafolial rootless, isoclinal folds. A post-transposition deformation event has folded the transposition foliation, with the folds accompanied by the growth of muscovite parallel to the axial plane (S_{T+1}) of these post-transposition folds (Fig. B2a and B2b). The timing of garnet growth relative to the transposition foliation is unclear, as there appears to have been a significant amount of static recrystallization of matrix biotite around garnet.

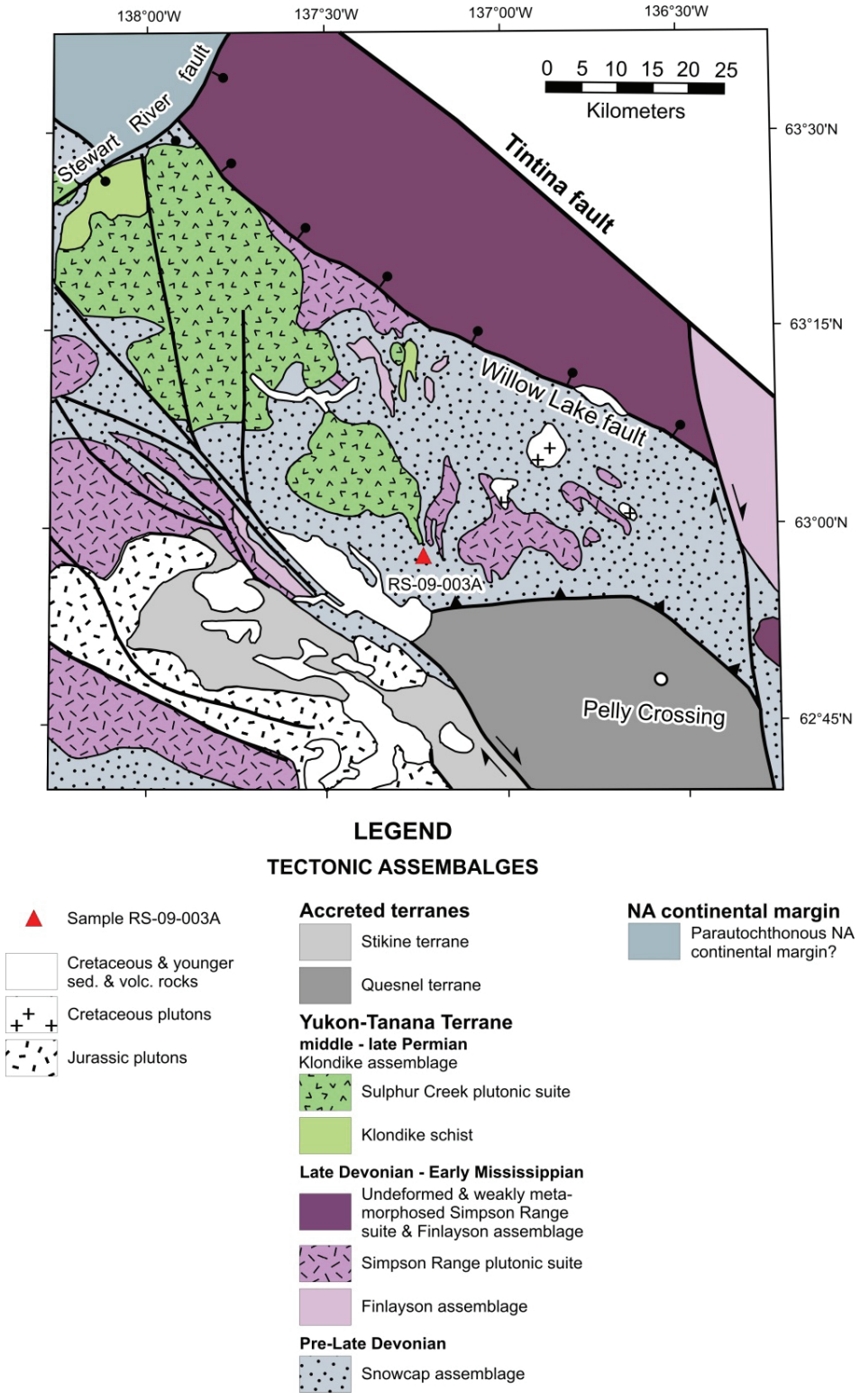

Figure B1. Tectonic assemblage map of the McQuesten area, showing the location of sample RS-09-003A. (modified from Ryan et al., 2010, and Colpron et al., 2006)

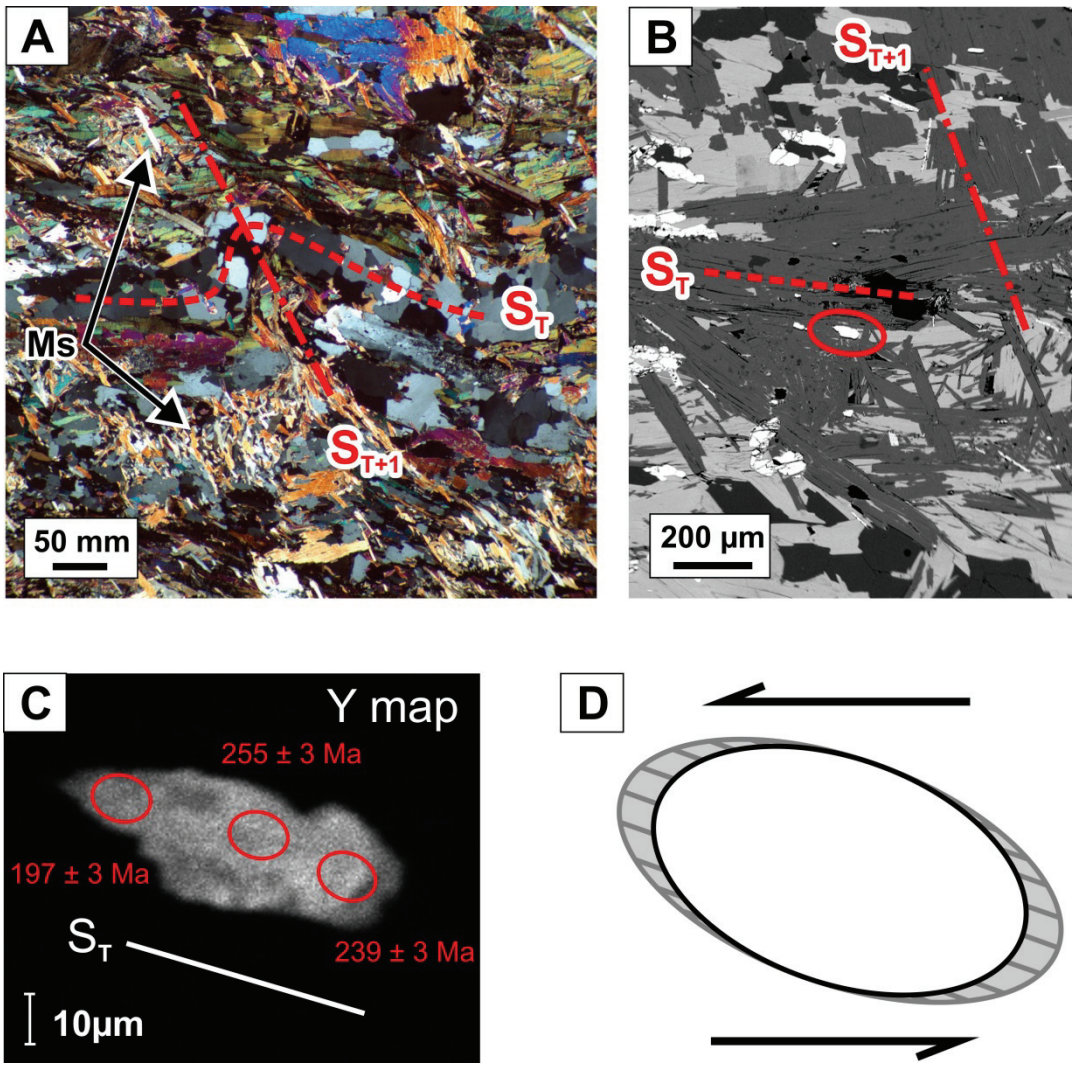

Figure B2. **Images of sample sample RS-09-003A and monazite M32 (A) Photomicrograph showing the transposition foliation (S_T) folded by a post-transposition fold, with muscovite aligned parallel to the axial plane (S_{T+1}) of this post-transposition fold. (B) Back-scattered electron image of monazite M32, which is elongate and aligned parallel to the transposition foliation. (C) Y-map of monazite M32, showing a Y-rich core and two Y-poor zones on opposite long ends of the elongated monazite grain aligned parallel to S_T. Ellipses show the location of the SHRIMP spots. (D) Schematic illustration of mineral growth within the extensional quadrants developed during shearing.**

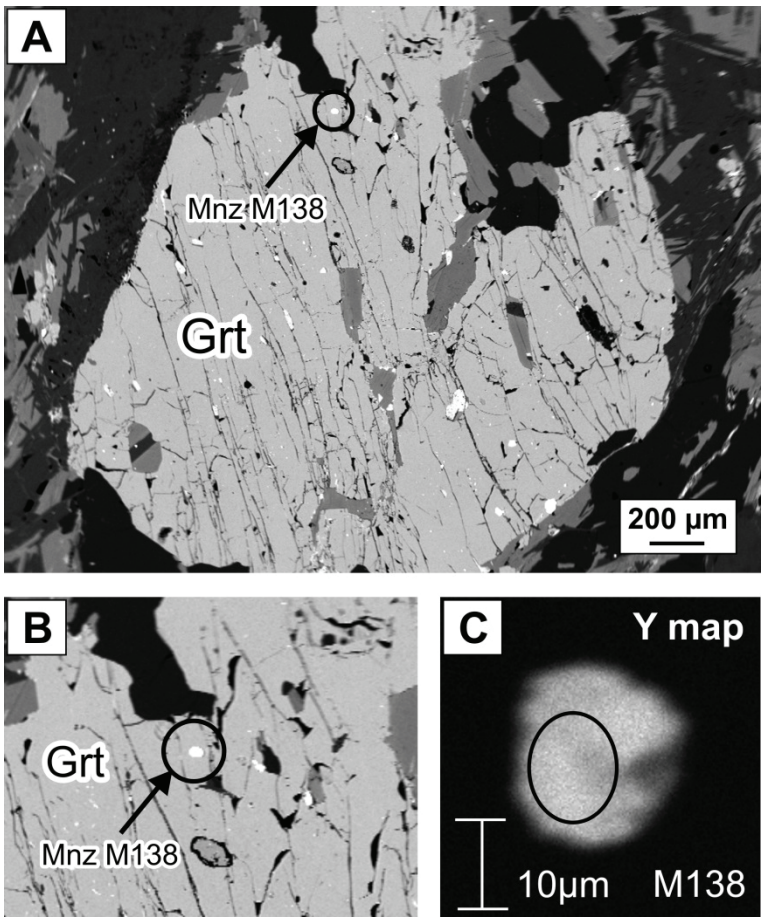

Figure B3. **Images of monazite M138 from sample RS-09-003A. (A) and (B) Back-scattered electron (BSE) images monazite M138 included within garnet. (C) Y-map of monazite M138. Ellipse shows the location of the SHRIMP spot.**

U-Pb Geochronologic methods

Prior to U-Th-Pb analysis, petrographic and back scattered electron (BSE) images of the in situ monazite grains were obtained to provide insight into their petrological context and internal zoning, identify cracks and mineral inclusions, and guide analytical spot placement (Figs B2c and B3c). In order to better characterize chemical zonation and potential age domains within individual monazite grains, chemical X-ray maps of Y, U, Th and Ca in strategically selected monazite grains were produced using a Cameca SX50 electron microprobe at the University of Massachusetts operating at a high current (240-260 nA), with small step sizes (0.25-0.62 μm) and rastering of the electron beam.

In situ U-Th-Pb analyses using the SHRIMP II at the Geological Survey of Canada in Ottawa were performed on monazite cored from polished thin sections and mounted in epoxy together with pre-polished monazite standards according to the methods of Rayner and Stern (2002). Targeted areas of monazite were analyzed using a mass-filtered O_2^- primary beam focused with a Kohler aperture to a spot measuring 9 x 12 μm. The methods employed follow the SHRIMP analytical protocols described in detail by Stern (1997), Stern and Sanborn (1998) and Stern and Berman (2000). Tera-Wasserburg and concordia plots, data regression and weighted mean calculations were made using the program ISOPLOT (Ludwig, 2008). Errors assigned to SHRIMP U–Th–Pb ages were determined using numerical propagation of all known sources of error as outlined by Stern (1997), Stern and Sanborn (1998), and Stern and Berman (2000). Uncertainties for individual analyses (ratios, ages and error ellipses) shown in Figures B2c, B3c and B4, Tables B1 and B2 and in the text are presented at the 1σ level.

The analyses were corrected for common Pb based on the ^{207}Pb (Table B1) and ^{204}Pb (Table B2) methods following the procedures of Stern and Berman (2000) and Ireland and Gibson (1998), respectively. The two correction methods yield ages indistinguishable within error. However, considering the potential for overcorrection using the ^{204}Pb method due to errors arising from low ^{204}Pb counts, background interference and a 204 isobar (different ionic species having the same nominal mass), the $^{206}Pb/^{238}U$ chronometer corrected using the ^{207}Pb method is thought to provide the most meaningful

ages for this study. Accordingly, all ages are based on the $^{206}Pb/^{238}U$ chronometer corrected using the ^{207}Pb method.

Results and Interpretations

A plot of the monazite SHRIMP data for sample RS-09-003A on a conventional (Wetherill) U-Pb concordia diagram reveals a very slight reverse discordance exhibited by some monazite analyses (Fig. B4). Excess ^{206}Pb due to incorporation of ^{230}Th into monazite at the time of crystallization will lead to an overestimation of $^{206}Pb/^{238}U$ ages and reverse discordance paralleling the $^{206}Pb/^{238}U$ axis on conventional U-Pb concordia diagrams (Schärer, 1984). Although the $^{208}Pb/^{232}Th$ chronometer is considered ideal for monazite since it is not known to be affected by isotopic disequilibrium, namely unsupported ^{206}Pb (due to an excess intermediate isotope (^{230}Th) in the ^{238}U-^{206}Pb chain; Schärer, 1984), we chose not to use it because one of the three monazite standards routinely yielded a high Th-Pb age. The problem may arise from an indeterminate matrix effect, which creates an unquantifiable uncertainty in the Th-Pb ages for the monazite. Fortunately, the $^{206}Pb/^{238}U$ ages do not appear to be affected by significant excess ^{206}Pb because they are mostly younger than $^{208}Pb/^{232}Th$ (Table B2). Furthermore, the excess ^{206}Pb correction of Schärer (1984) reveals that even monazite that grew from a metamorphic fluid with extremely low Th/U (0.3 - 0.6), and hence a large amount of Th fractionation (f = 21-29), should produce an excess in age no greater than 2.1 – 2.9 Ma, which is less than analytical error. Thus, despite any minor excess of ^{206}Pb, we are confident the $^{206}Pb/^{238}U$ ages provide reasonably accurate constraints within the resolution required for this study to differentiate the metamorphic and deformation events.

Monazite M138 occurs as an inclusion within garnet (Fig. B3a), and does not appear to be intersected by any microfractures within garnet (Fig. B3b). An yttrium (Y) chemical map of M138 reveals a fairly homogenous Y content through the grain. It's uncertain whether the slight decrease in Y (darker shade of grey) at the grains edge represents a separate chemical zone, or if this is simply a grain edge effect during mapping. The SHRIMP spot analysis is shown in Figure B3c, with the spot lying entirely within the Y-rich core. This spot yielded an age of 263.6 ± 3.4 Ma.

Monazite M32 is an elongate matrix grain aligned parallel to the transposition foliation (Fig. B2b). The Y-map of M32 shows a Y-rich core (light grey) and Y-poor (dark grey) zones at opposite ends of the grain in the direction parallel to the elongated direction of the grain, which also parallels the transposition foliation (Fig. B2c). Three SHRIMP spot analyses were obtained from grain M32 (Fig. B2d). Spot M32.1 from within the Y-rich core yielded an age of 254.7 ± 2.6. Spot M32.3 analyzed one of the two Y-poor zones at opposite ends of the elongated grain, and yielded an age of 196.8 ± 3.4 (Fig. B2d). Several studies have demonstrated a link between distinct age domains and zones of relative Y depletion or enrichment (Foster et al., 2002; Gibson et al., 2004), and spots M32.1 and M32.3 are consistent with this. Spot M32.2 partly overlapped the Y-rich core and the Y-poor zone at the other end of the grain (Fig. B2d), and yielded an age intermediate to M32.1 and M32.3 of 238.6 ± 2.9, which is likely due to an analysis that overlapped the two Y-zones. The presence of Y-poor zones, with a distinct age, on either end of the long axis of monazite M32 aligned parallel to S_T, suggests that these Y-poor zones are overgrowths that preferentially crystallized in the extensional quadrants associated with development of the transposition foliation (Fig. B2d). This would suggest that the transposition foliation developed, or was at least reactivated in the Early Jurassic (c. 196 Ma). Alternatively, monazite growth in the Early Jurassic may have grown in a static environment and been pinned by adajcent biotite grains leading to growth in only a single direction.

Previous work by Berman et al. (2007) within the adjacent 1:250 000 scale map sheet to the west (Stewart River map sheet) suggest that the penetrative ductile deformation and transposition with the Snowcap assemblage developed in the late Permian – Early Triassic (c. 260-239 Ma) accompanied by amphibolite facies metamorphism at ~600 ºC. Additional work by Beranek and Mortensen (2011) bracketed the timing of penetrative ductile deformation between c. 260 and 253 Ma in lower amphibolite facies rocks in the northern Stewart River map area near the Jim Creek pluton. The ages presented here are consistent with a late Permian (c. 264-255 Ma) metamorphic event. Berman et al., (2007) also documented an Early Jurassic (c. 195 Ma) metamorphic event with peak conditions of approximately 600 ºC and 7.8 kbar. Berman et al. (2007) suggested that Early Jurassic metamorphism occurred in a static environment, and that growth of Early Jurassic garnet rims in “D2” (transposition)

pressure shadows reflects local fabric reactivation during heterogeneously distributed strain.

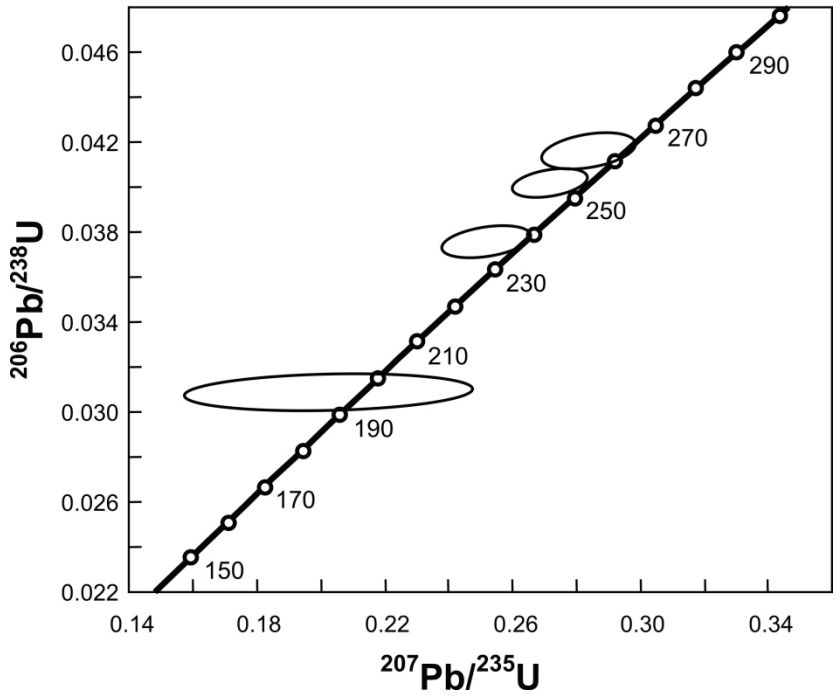

Figure B4. U-Pb concordia plot of of analyses from monazite grains M138 and M32 of sample RS-09-003A. Error ellipses represent 1σ level of uncertainty.

Table B1. SHRIMP U-Th-Pb analytical data for monazite corrected using the ^{207}Pb-method.

Spot[a]	Texture[b]	Grain location	Y[c]	Th/U	$^{204}Pb/^{206}Pb$	$^{d}f(206)^{207}$ (%)	Total $^{207}Pb/^{206}Pb$	Total $^{238}U/^{206}Pb$	Age (Ma)[e] $^{206}Pb/^{238}U$
Sample RS-09-003A									
M138.1	Incl. in Grt	core	hom.	14.6	7.193E-04 ± 6.763E-05	1.73	0.0600 ± 0.0011	23.709 ± 0.308	263.6 ± 3.4
M32.1	ll to S_T	core	high	12.7	7.357E-04 ± 7.985E-05	1.71	0.0598 ± 0.0005	24.549 ± 0.258	254.7 ± 2.6
M32.2	ll to S_T	core/rim	high/low	8.2	2.881E-03 ± 3.160E-04	5.47	0.0900 ± 0.0046	30.652 ± 0.506	196.8 ± 3.4
M32.3	ll to S_T	rim	low	11.2	1.424E-03 ± 1.038E-04	1.71	0.0695 ± 0.0006	25.904 ± 0.321	238.6 ± 2.9

[a] Spot: M32.2 = 2nd spot on monazite grain #32.
[b] Texture: location of monazite as inclusion in Grt, or as an elongate matrix grain (ll to S_T = parallel to foliation).
[c] Y: relative concentration from X-ray map at the spot of the analysis (hom. = homogenous Y)
[d] $f(206)^{207}$ refers to the fraction of total ^{206}Pb that is common Pb, calculated using the ^{207}Pb-method.
[e] Ages have been corrected for common Pb using the ^{207}Pb-method.
Note. Uncertainties reported at 1σ (absolute) and are calculated by numerical propagation of all known sources of error (Stern and Berman, 2000).

Table B2. SHRIMP U-Th-Pb analytical data for monazite corrected using the 204Pb-method

[a]Spot	[b]Texture	[c]f(206)^{204} (%)	^{208*}Pb/ ^{206*}Pb[d]	^{206*}Pb/^{238}U	^{207*}Pb/^{235}U	Corr. coeff.	^{207*}Pb/^{206*}Pb	Age (Ma)[e] ^{207}Pb/^{235}U[f]	^{208}Pb/^{232}Th	^{206}Pb/^{238}U
Sample RS-09-003A										
M138.1	Incl. in Grt	1.32	4.6364 ± 0.0207	0.04162 ± 0.00054	0.2835 ± 0.0095	0.389	0.0494 ± 0.0015	253.4 ± 9.6	266.1 ± 2.8	263.9 ± 3.4
M32.1	ll to S_T	1.35	4.2147 ± 0.0207	0.04019 ± 0.00043	0.2716 ± 0.0077	0.373	0.0490 ± 0.0013	244.0 ± 7.8	267.8 ± 3.1	254.0 ± 2.6
M32.2	ll to S_T	5.30	2.5095 ± 0.0181	0.03089 ± 0.00054	0.2023 ± 0.0297	0.120	0.0475 ± 0.0069	187.1 ± 29.7	190.1 ± 2.1	196.1 ± 3.4
M32.3	ll to S_T	2.61	3.6770 ± 0.0201	0.03760 ± 0.00047	0.2517 ± 0.0092	0.342	0.0485 ± 0.0017	227.9 ± 9.3	248.0 ± 2.9	237.9 ± 2.9

[a] Spot: M32.2 = 2nd spot on monazite grain #20.

[b] Texture: location of monazite as inclusion in Grt, or as an elongate matrix grain (ll to S_T = parallel to foliation).

[c] f(206)^{204} refers to the fraction of total ^{206}Pb that is common Pb, calculated using the ^{204}Pb-method.

[d] *Pb = Radiogenic Pb (corrected for common Pb using the ^{204}Pb-method).

[e] Ages have been corrected for common Pb using the ^{204}Pb-method.

[f] ^{207}Pb/^{235}U age is poorly constrained due to the low abundance of ^{207}Pb in young monazite.

References

Beranek, L.P., and Mortensen, J.K., 2011, The timing and provenance record of the Late Permian Klondike orogeny in northwestern Canada and arc-continent collision along western North America: Tectonics, v. 30, TC5017, doi:10.1029/2010TC002849.

Berman, R.G., Ryan, J.J., Gordey, S.P., and Villeneuve, M., 2007, Permian to Cretaceous polymetamorphic evolution of the Stewart River region, Yukon-Tanana terrane, Yukon, Canada: P-T evolution linked with in-situ SHRIMP monazite geochronology: Journal of Metamorphic Geology, v. 25, p. 803–827.

Colpron, M., Nelson, J.L. & Murphy, D.C., 2006. A tectonostratigraphic framework for the pericratonic terranes of the northern Canadian Cordillera. In: Paleozoic Evolution and Metallogeny of Pericratonic Terranes at the Ancient Pacific Margin of North America, Canadian and Alaskan Cordillera, Special Paper 45 (eds Colpron, M. & Nelson, J. L.), pp. 1–23. Geological Association of Canada.

Colpron, M., and Nelson, J.L., 2009, A Palaeozoic northwest passage: incursion of Caledonian, Baltican and Siberian terranes into eastern Panthalassa, and the early evolution of the North American Cordillera, *in* Cawood, P.A., and Kröner, A., eds., Earth Accretionary Systems in Space and Time: The Geological Society of London Special Publications, v. 318, p. 273–307.

Foster, G., Gibson, H.D., Parrish, R.R., Horstwood, M., Fraser, J., and Tindle, A., 2002, Textural, chemical and isotopic insights into the nature and behaviour of metamorphic monazite: Chemical Geology, v. 191, p. 183–207.

Gibson, H. D., Carr, S. D., Brown, R. L., and Hamilton, M. A., 2004, Correlations between chemical and age domains in monazite, and metamorphic reactions involving major politic phases: an integration of ID-TIMS and SHRIMP geochronology with Y–Th–U X-ray mapping: Chemical Geology, v. 211, p. 237–260.

Ireland, T.R. & Gibson, G.M., 1998. SHRIMP monazite and zircon geochronology of high-grade metamorphism in New Zealand. Journal of Metamorphic Geology, v. 16, p. 149–167.

Ludwig, K.R., 2008. Manual for Isoplot 3.7: A Geochronological Toolkit for Microsoft Excel. Special Publication No. 4. rev. August 26, 2008, Berkeley Geochronology Center, pp. 77.

Nelson, J.L., Colpron, M., Piercey, S.J., Dusel-Bacon, C., Murphy, D.C., and Roots, C.F., 2006, Paleozoic tectonic and metallogenic evolution of the pericratonic terranes in Yukon, northern British Columbia and eastern Alaska., *in* Colpron, M., and Nelson, J.L., eds., Paleozoic Evolution and Metallogeny of Pericratonic Terranes at the Ancient Pacific Margin of North America, Canadian and Alaskan Cordillera: Geological Association of Canada Special Paper 45, p. 323–360.

Piercey, S.J., and Colpron, M., 2009, Composition and provenance of the Snowcap assemblage, basement to the Yukon-Tanana terrane, northern Cordillera: Implications for Cordilleran crustal growth: Geosphere, v. 5, p. 439–464.

Rayner, N. & Stern, R. A., 2002. Improved Sample Preparation Method for SHRIMP Analysis of Delicate Mineral Grains Exposed in Thin Sections. Geological Survey of Canada, Current Research 2002-F10, 1–3.

Ryan, J.J., Colpron, M. & Hayward, N., 2010. Geology, southwestern McQuesten and parts of northern Carmacks, Yukon; Geological Survey of Canada, Canadian Geoscience Map 7, (preliminary version), scale 1:125 000.

Schärer, U., 1984. The effect of initial 230Th disequilibrium on young U–Pb ages: the Makalu case, Himalaya: Earth and Planetary Science Letters, v. 67, p. 191– 204.

Stern, R. A., 1997. The GSC sensitive high resolution ion microphobe (SHRIMP): analytical techniques of zircon U-Th-Pb age determinations and performance evaluation. Radiogenic Age and Isotopic Studies: Report 10. Geological Survey of Canada, Current Research 1997-F, 1–31.

Stern, R. A. & Berman, R. G., 2000. Monazite U-Pb and Th-Pb geochronology by ion microprobe, with an application to in situ dating of an Archean metasedimentary rock: Chemical Geology, v. 172, p. 113–130.

Stern, R.A. & Sanborn, N., 1998. Monazite U–Pb and Th–Pb geochronology by high-resolution secondary ion mass spectrometry. Radiogenic Age and Isotopic Studies: Report 11. Geological Survey of Canada, Current Research 1998-F. 1–18.

Appendix C.

$^{40}Ar/^{39}Ar$ data

Methodology

The samples were crushed in a ring mill, washed in distilled water and ethanol, and sieved when dry to -40+60mesh. Appropriate mineral grains were picked out of the bulk fraction. Mineral separates were wrapped in aluminum foil and stacked in an irradiation capsule with similar-aged samples and neutron flux monitors (Fish Canyon Tuff sanidine (FCs), 28.03 Ma (Renne et al., 1998).

The samples were irradiated on July 10-16, 2012 at the McMaster Nuclear Reactor in Hamilton, Ontario, for 180 MWH in the medium flux site 8B. Analyses (n=33) of 11 neutron flux monitor positions produced errors of <0.5% in the J value.

The sample was analyzed during August and September 2012 at the Noble Gas Laboratory, Pacific Centre for Isotopic and Geochemical Research (PCIGR), University of British Columbia, Vancouver, BC, Canada. The mineral separates were step-heated at incrementally higher powers in the defocused beam of a 10W CO_2 laser (New Wave Research MIR10) until fused. The gas evolved from each step was analyzed by a VG5400 mass spectrometer equipped with an ion-counting electron multiplier. All measurements were corrected for total system blank, mass spectrometer sensitivity, mass discrimination, radioactive decay during and subsequent to irradiation, as well as interfering Ar from atmospheric contamination and the irradiation of Ca, Cl and K (Isotope production ratios: $(^{40}Ar/^{39}Ar)_K$=0.0302±0.00006, $(^{37}Ar/^{39}Ar)_{Ca}$=1416.4±0.5, $(^{36}Ar/^{39}Ar)_{Ca}$=0.3952±0.0004, Ca/K=1.83±0.01($^{37}Ar_{Ca}/^{39}Ar_K$).).

Results

Sample locations are shown in Figure C2. Preliminary results as provided by Janet Gabites from the PCIGR at UBC are presented in Tables C1 and C2, Figure C2, and are displayed on release spectra and isochron plots (Fig. C3). Initial data entry and calculations were carried out using the software ArArCalc (Koppers, 2002). The plateau and correlation ages were calculated using Isoplot ver.3.09 (Ludwig, 2003). Data error

box heights and error ellipses in release spectra and isochron plots, respectively, of Figure C3 and quoted ages are at the 2-sigma (95% confidence) level and are propagated from all sources except mass spectrometer sensitivity and age of the flux monitor. The best statistically-justified plateau and plateau age were picked based on the following criteria:

1. Three or more contiguous steps comprising more than 60% of the ^{39}Ar;
2. Probability of fit of the weighted mean age greater than 5%;
3. Slope of the error-weighted line through the plateau ages equals zero at 5% confidence;
4. Ages of the two outermost steps on a plateau are not significantly different from the weighted-mean plateau age (at 1.8σ, six or more steps only);
5. Outermost two steps on either side of a plateau must not have nonzero slopes with the same sign (at 1.8σ, nine or more steps only)

Table C1. **$^{40}Ar/^{39}Ar$ summary table (interpreted age, location, rock type, etc.)**

Sample #	(Geoid 83) UTM zone	Northing	Easting	Mineral	Age (Ma)	Age Method	Rock Type	1:250 000 Map Sheet
09RS189A1	7	7057000	642922	Biotite	112.9 ± 2.5	inverse isochron	meta-psammite	Stewart River
09RS189A1	7	7057000	642922	Muscovite	104.0 ± 3.3	inverse isochron	meta-psammite	Stewart River
00RAY225A	7	7074275	619423	Biotite	105.0 ± 3.7	inverse isochron	meta-psammite	Stewart River
00RAY225A	7	7074275	619423	Muscovite	115.9 ± 2.9	inverse isochron	meta-psammite	Stewart River
03RAYP001B1	7	7063288	641315	Biotite	108.3 ± 0.8	pseudo-plateau	meta-semipelite	Stewart River
03RAYP001B1	7	7063288	641315	Muscovite	114.2 ± 2.5	pseudo-plateau	meta-semipelite	Stewart River
09RS179A	7	7063183	647766	Hornblende	107.7 ± 1.8	pseudo-plateau	amphibolite	Stewart River
00GGA073A	7	7059683	614848	Biotite	150.8 ± 2.2	pseudo-plateau	orthogneiss	Stewart River
03GAR42A	7	7037801	606716	Biotite	190.3 ± 1.9	pseudo-plateau	meta-semipelite	Stewart River
10RS020	8	6747238	576285	Muscovite	190.9 ± 9.9	inverse isochron	meta-psammite	Teslin
10RS026	8	6747448	578166	Muscovite	196.5 ± 4.9	normal isochron	meta-semipelite	Teslin
10RS073A	9	6678295	365941	Muscovite	185.4	integrated age	meta-semipelite	Wolf Lake
10RS088B1	9	6678536	365407	Muscovite	-	-	meta-semipelite	Wolf Lake
10RS041B3	9	6548208	425023	Hornblende	126.5 ± 4.3	inverse isochron	amphibolite	Jennings River
10RS049A2	9	6550131	425666	Biotite	114.4 ± 1.0	pseudo-plateau	meta-semipelite	Jennings River
10RS057B1	9	6548493	425518	Muscovite	118.3 ± 1.1	pseudo-plateau	meta-psammite	Jennings River

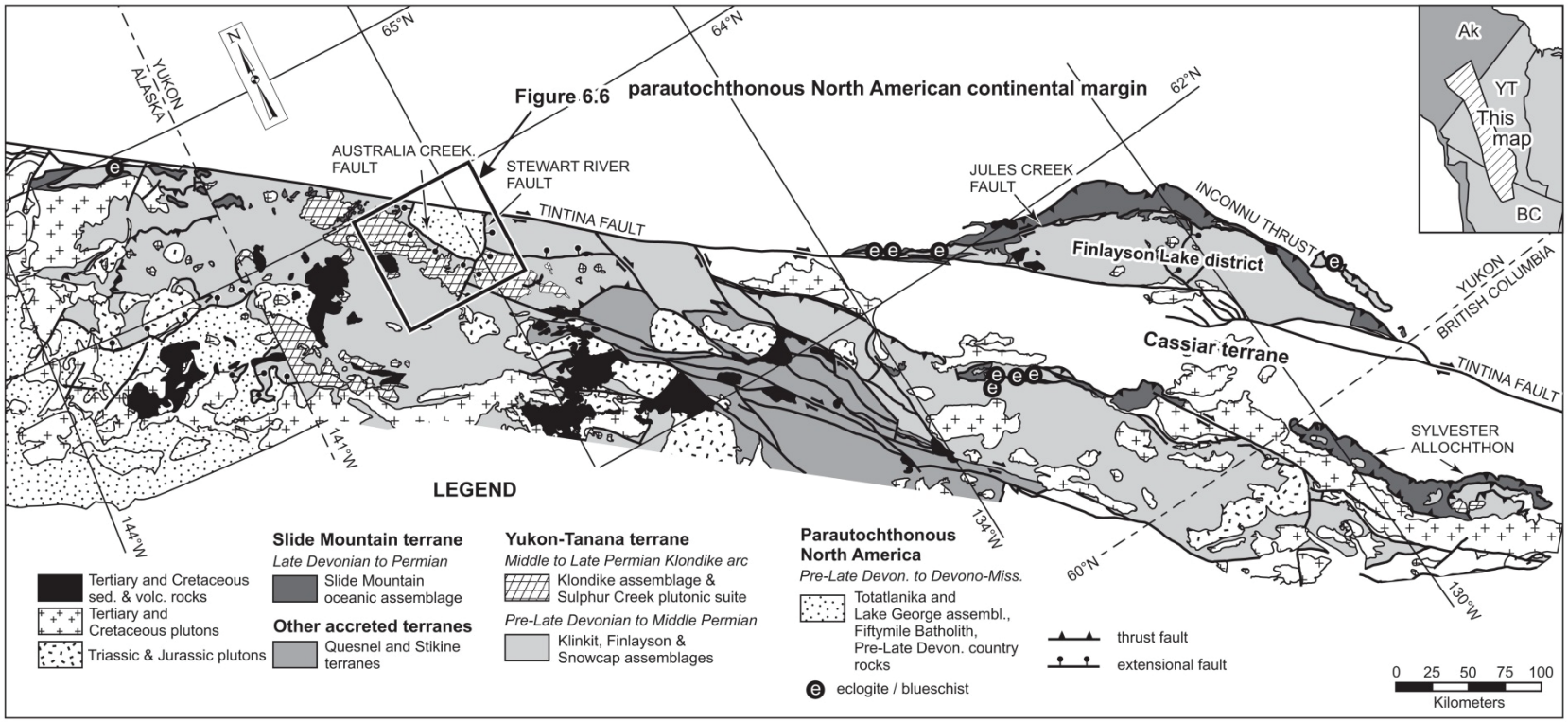
Figure 6.6 parautochthonous North American continental margin
YUKON
ALASKA
65°N
64°N
62°N
60°N
141°W
144°W
134°W
130°W
AUSTRALIA CREEK FAULT
STEWART RIVER FAULT
TINTINA FAULT
JULES CREEK FAULT
INCONNU THRUST
Finlayson Lake district
Cassiar terrane
SYLVESTER ALLOCHTHON
YUKON
BRITISH COLUMBIA
Ak
YT
This map
BC
LEGEND
Tertiary and Cretaceous sed. & volc. rocks
Tertiary and Cretaceous plutons
Triassic & Jurassic plutons
Slide Mountain terrane
Late Devonian to Permian
Slide Mountain oceanic assemblage
Other accreted terranes
Quesnel and Stikine terranes
Yukon-Tanana terrane
Middle to Late Permian Klondike arc
Klondike assemblage & Sulphur Creek plutonic suite
Pre-Late Devonian to Middle Permian
Klinkit, Finlayson & Snowcap assemblages
Parautochthonous North America
Pre-Late Devon. to Devono-Miss.
Totatlanika and Lake George assembl., Fiftymile Batholith, Pre-Late Devon. country rocks
eclogite / blueschist
thrust fault
extensional fault
0 25 50 75 100
Kilometers

Figure C1. **Index map showing the location of Figure C2 outlined by a thick black square. Tectonic assemblage map of Yukon-Tanana and adjacent terranes of the northern Cordillera in east-central Alaska, central Yukon and northern British Columbia. Figure modified from Colpron et al. (2006).**

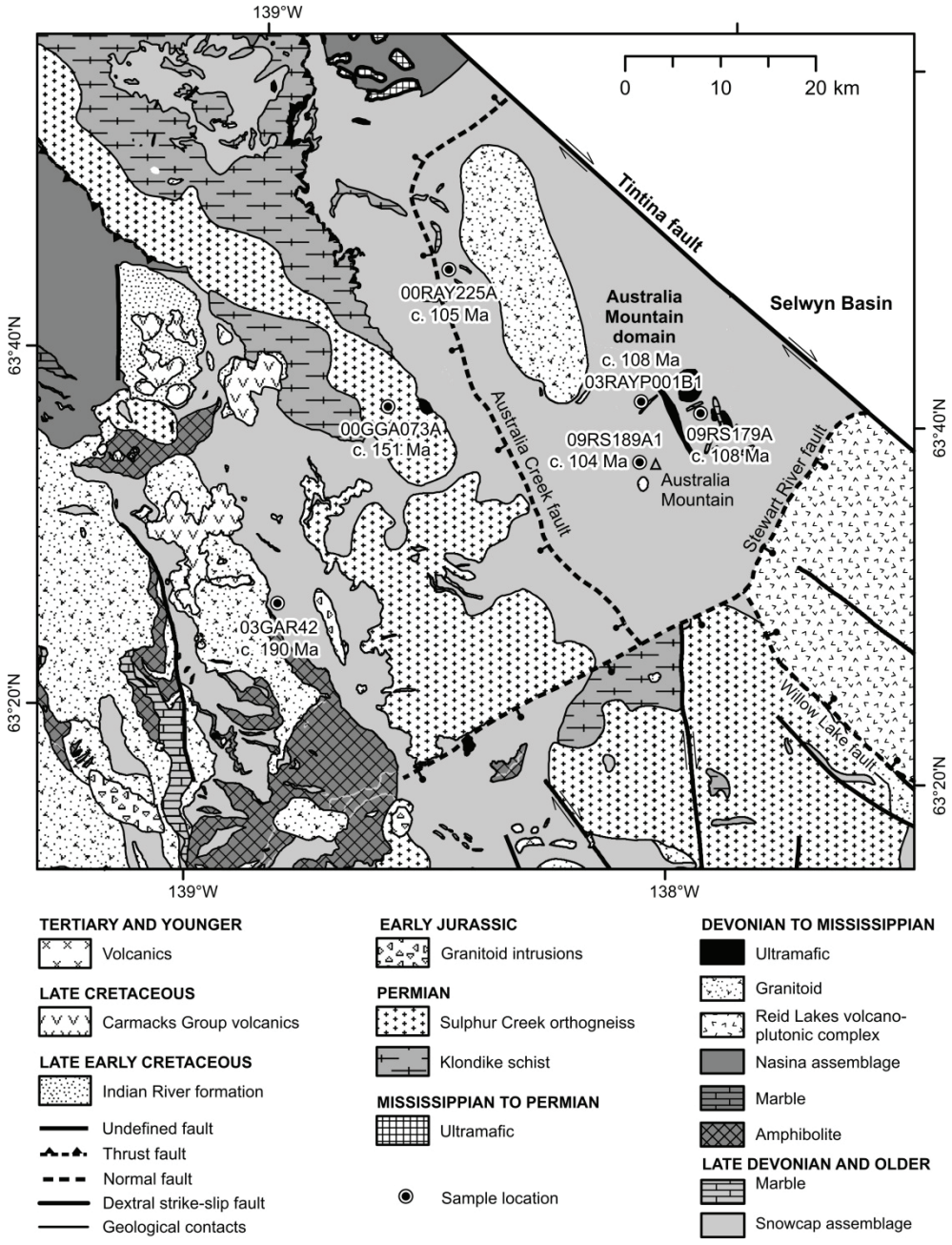

Figure C2. Simplified geological map of part of the Stewart River and McQuesten map areas showing the location of $^{40}Ar/^{39}Ar$ samples. Geology modified from Gordey & Ryan, 2005; Ryan et al., 2010.

Figure C3. Ar release spectra and isochron plots

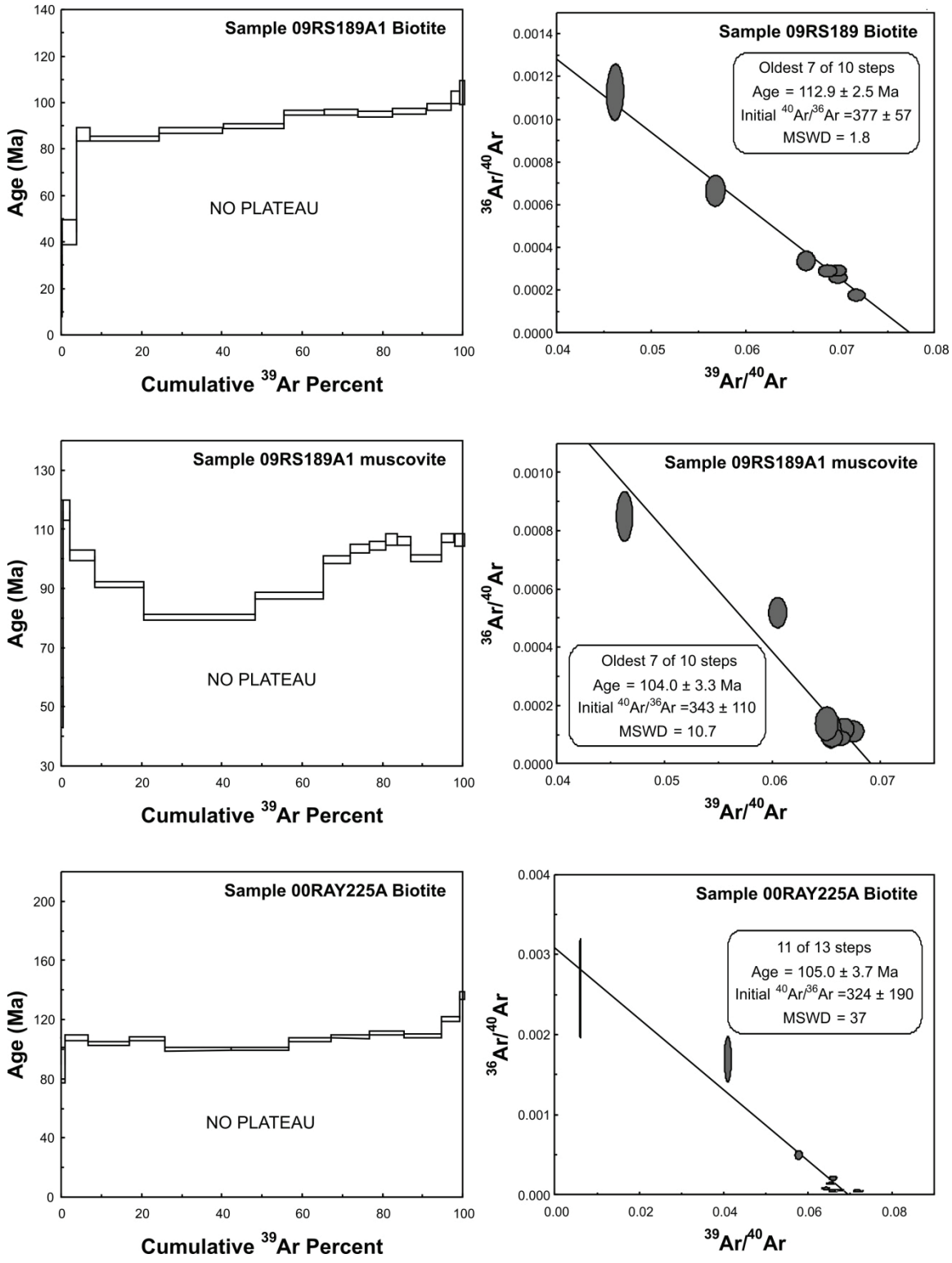

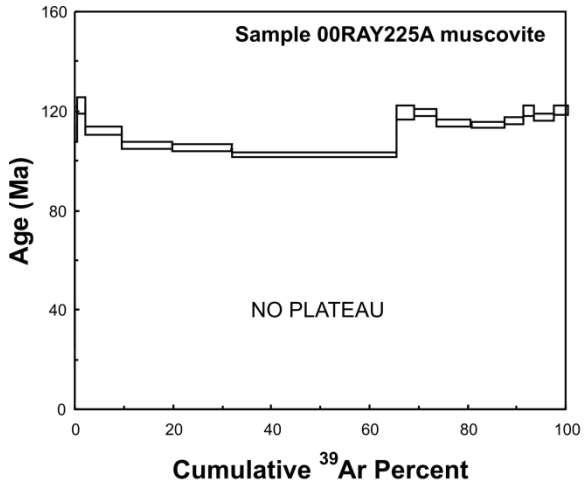
Sample 00RAY225A muscovite
NO PLATEAU
Age (Ma)
Cumulative ^{39}Ar Percent

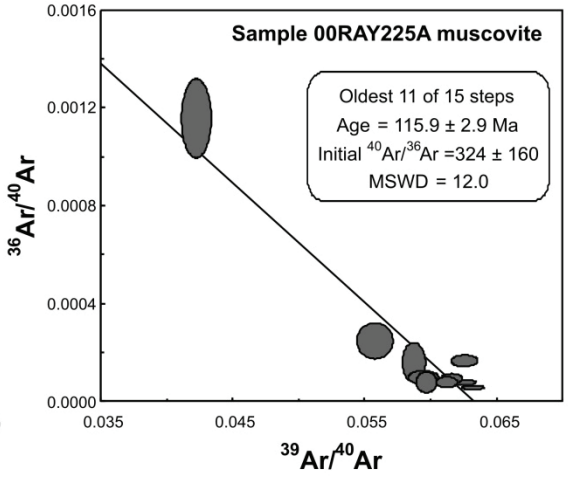
Sample 00RAY225A muscovite
Oldest 11 of 15 steps
Age = 115.9 ± 2.9 Ma
Initial ^{40}Ar/^{36}Ar =324 ± 160
MSWD = 12.0
^{36}Ar/^{40}Ar
^{39}Ar/^{40}Ar

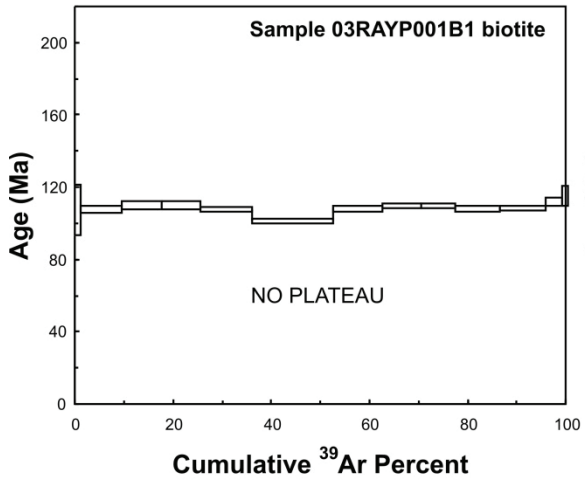
Sample 03RAYP001B1 biotite
NO PLATEAU
Age (Ma)
Cumulative ^{39}Ar Percent

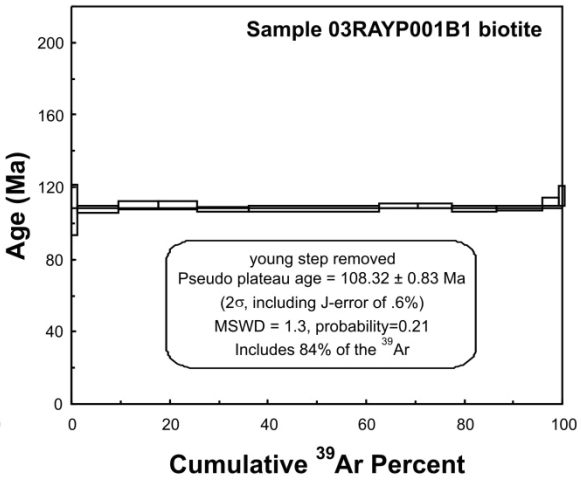
Sample 03RAYP001B1 biotite
young step removed
Pseudo plateau age = 108.32 ± 0.83 Ma
(2σ, including J-error of .6%)
MSWD = 1.3, probability=0.21
Includes 84% of the ^{39}Ar
Age (Ma)
Cumulative ^{39}Ar Percent

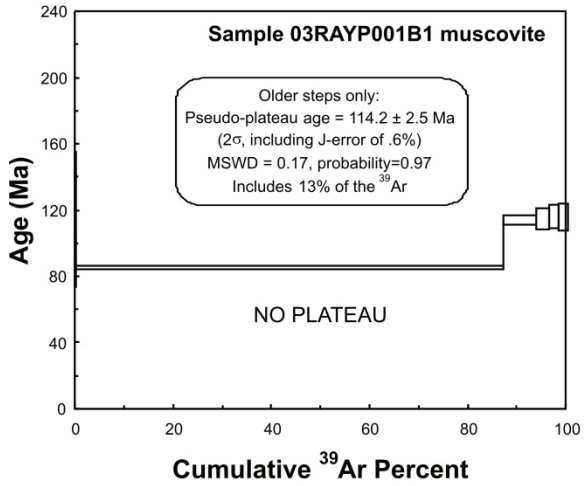
Sample 03RAYP001B1 muscovite
Older steps only:
Pseudo-plateau age = 114.2 ± 2.5 Ma
(2σ, including J-error of .6%)
MSWD = 0.17, probability=0.97
Includes 13% of the ^{39}Ar
NO PLATEAU
Age (Ma)
Cumulative ^{39}Ar Percent

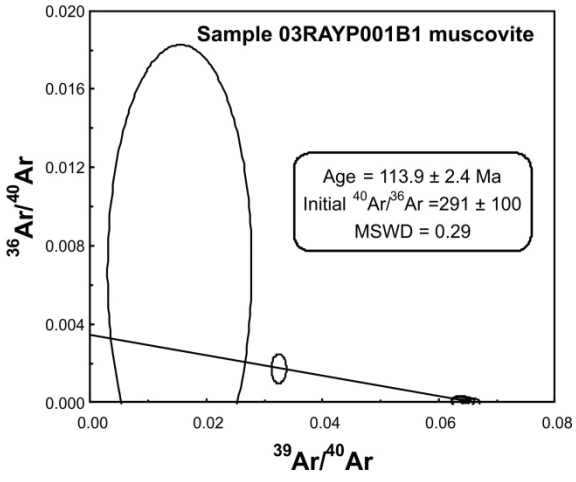
Sample 03RAYP001B1 muscovite
Age = 113.9 ± 2.4 Ma
Initial ^{40}Ar/^{36}Ar =291 ± 100
MSWD = 0.29
^{36}Ar/^{40}Ar
^{39}Ar/^{40}Ar

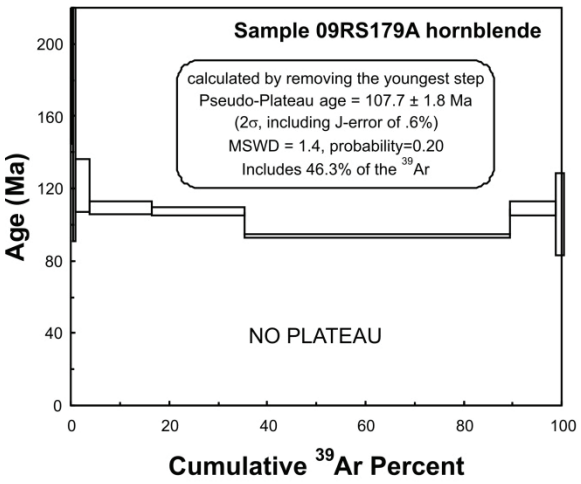
Sample 09RS179A hornblende
calculated by removing the youngest step
Pseudo-Plateau age = 107.7 ± 1.8 Ma
(2σ, including J-error of .6%)
MSWD = 1.4, probability=0.20
Includes 46.3% of the 39Ar
NO PLATEAU
Age (Ma)
Cumulative 39Ar Percent

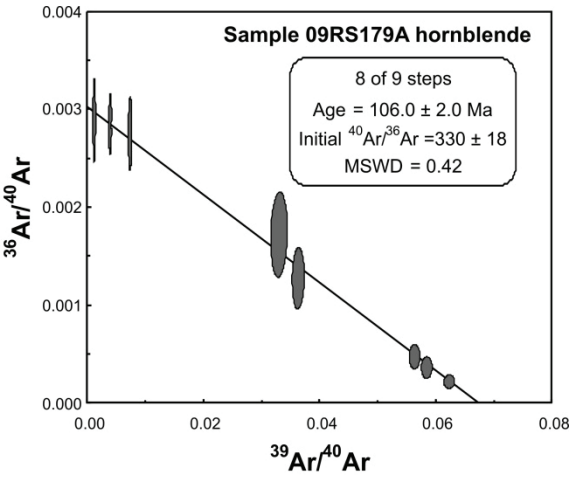
Sample 09RS179A hornblende
8 of 9 steps
Age = 106.0 ± 2.0 Ma
Initial 40Ar/36Ar =330 ± 18
MSWD = 0.42
36Ar/40Ar
39Ar/40Ar

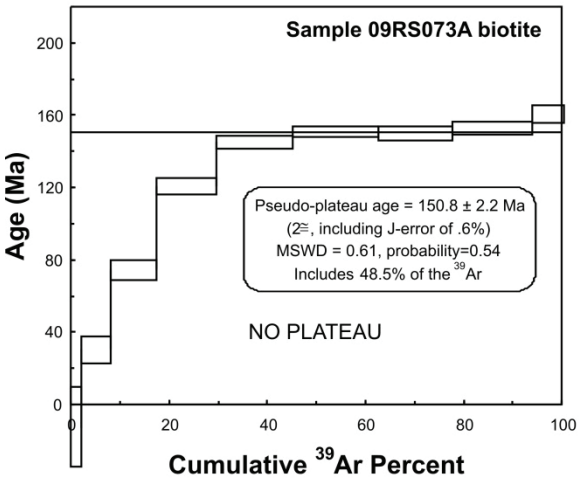
Sample 09RS073A biotite
Pseudo-plateau age = 150.8 ± 2.2 Ma
(2≅, including J-error of .6%)
MSWD = 0.61, probability=0.54
Includes 48.5% of the 39Ar
NO PLATEAU
Age (Ma)
Cumulative 39Ar Percent

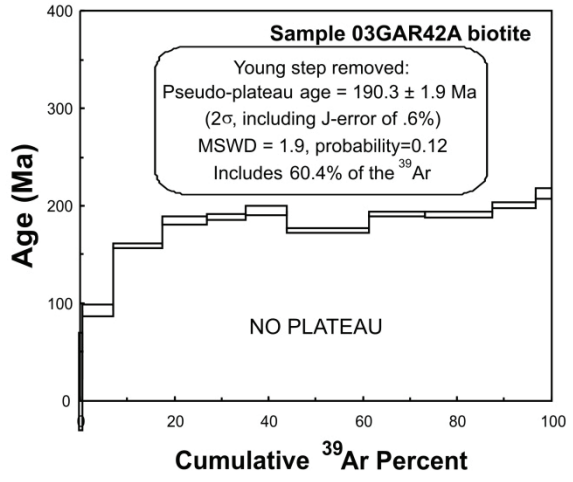
Sample 03GAR42A biotite
Young step removed:
Pseudo-plateau age = 190.3 ± 1.9 Ma
(2σ, including J-error of .6%)
MSWD = 1.9, probability=0.12
Includes 60.4% of the 39Ar
NO PLATEAU
Age (Ma)
Cumulative 39Ar Percent

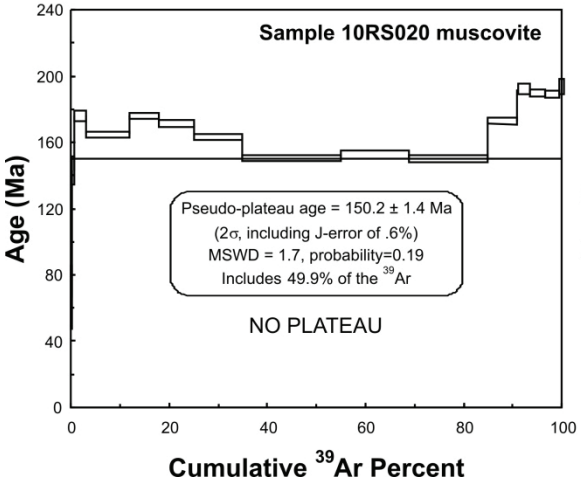
Sample 10RS020 muscovite
Pseudo-plateau age = 150.2 ± 1.4 Ma
(2σ, including J-error of .6%)
MSWD = 1.7, probability=0.19
Includes 49.9% of the 39Ar
NO PLATEAU
Age (Ma)
Cumulative 39Ar Percent

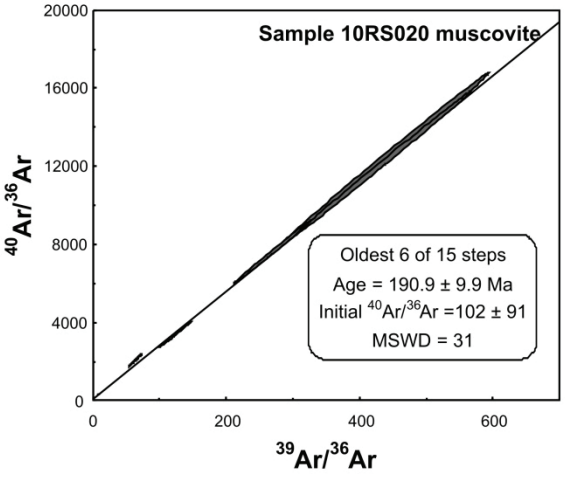
Sample 10RS020 muscovite
Oldest 6 of 15 steps
Age = 190.9 ± 9.9 Ma
Initial 40Ar/36Ar =102 ± 91
MSWD = 31
40Ar/36Ar
39Ar/36Ar

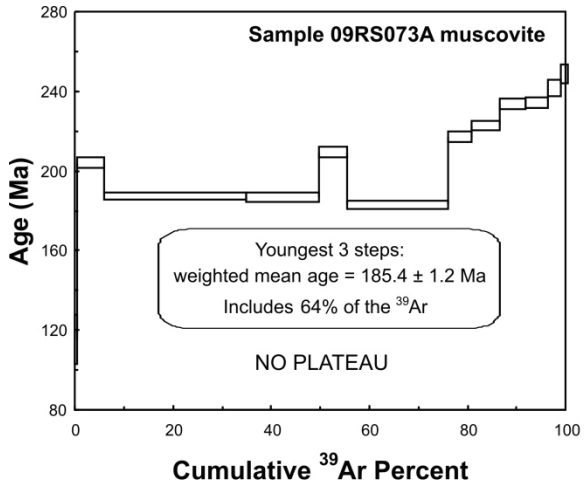
Sample 09RS073A muscovite
Age (Ma)
Youngest 3 steps:
weighted mean age = 185.4 ± 1.2 Ma
Includes 64% of the 39Ar
NO PLATEAU
Cumulative 39Ar Percent

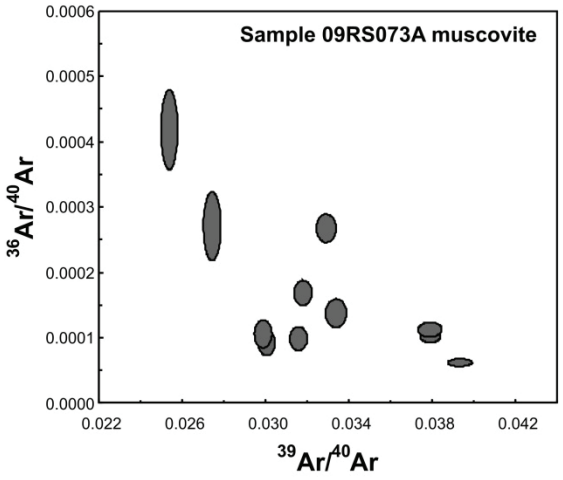
Sample 09RS073A muscovite
36Ar/40Ar
39Ar/40Ar

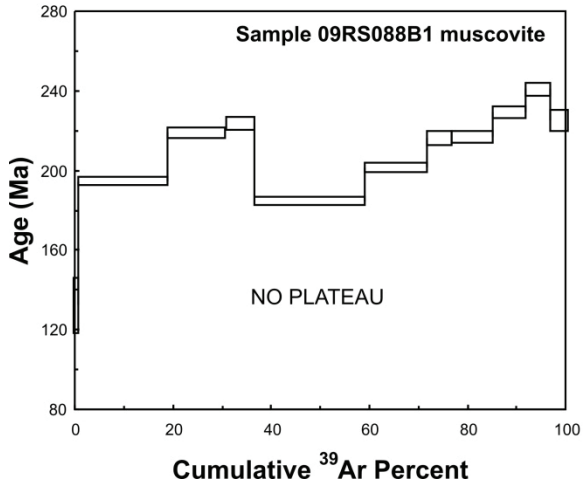
Sample 09RS088B1 muscovite
Age (Ma)
NO PLATEAU
Cumulative 39Ar Percent

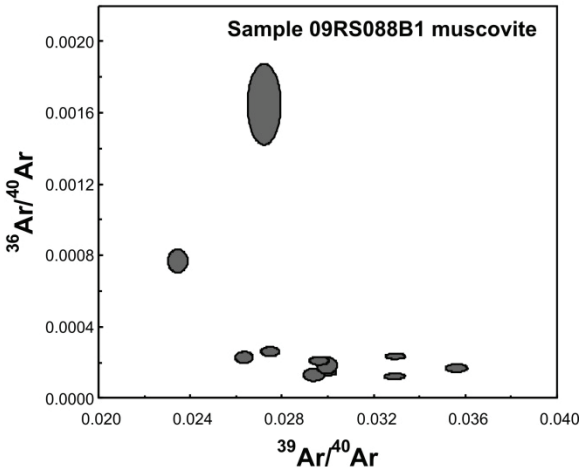
Sample 09RS088B1 muscovite
36Ar/40Ar
39Ar/40Ar

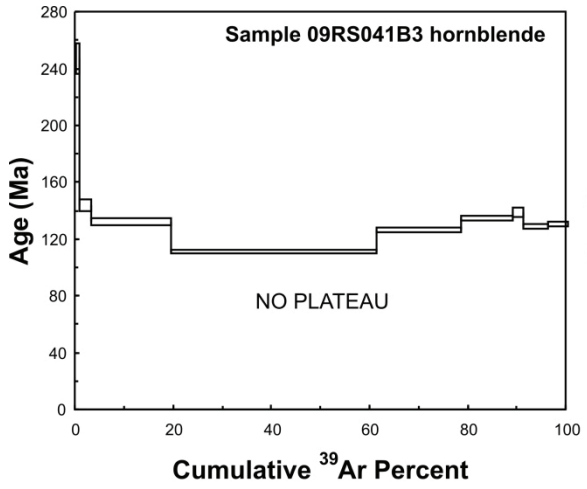
Sample 09RS041B3 hornblende
Age (Ma)
NO PLATEAU
Cumulative 39Ar Percent

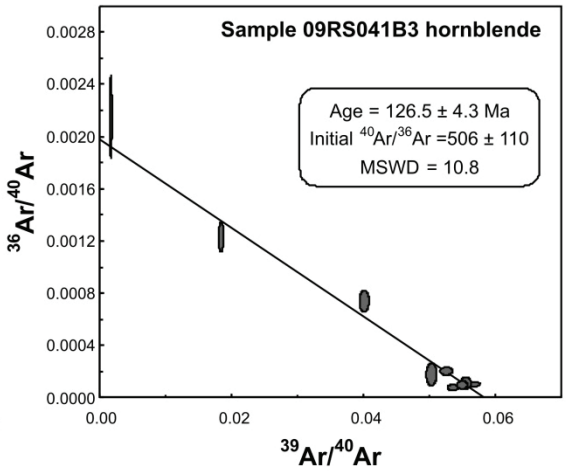
Sample 09RS041B3 hornblende
Age = 126.5 ± 4.3 Ma
Initial 40Ar/36Ar =506 ± 110
MSWD = 10.8
36Ar/40Ar
39Ar/40Ar

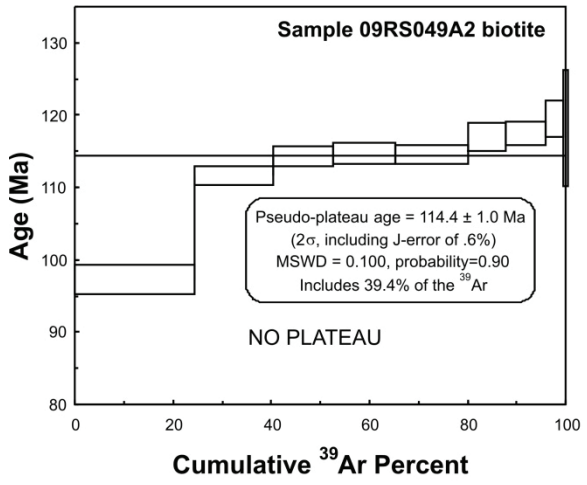
Sample 09RS049A2 biotite
Pseudo-plateau age = 114.4 ± 1.0 Ma
(2σ, including J-error of .6%)
MSWD = 0.100, probability=0.90
Includes 39.4% of the 39Ar
NO PLATEAU
Age (Ma)
Cumulative 39Ar Percent

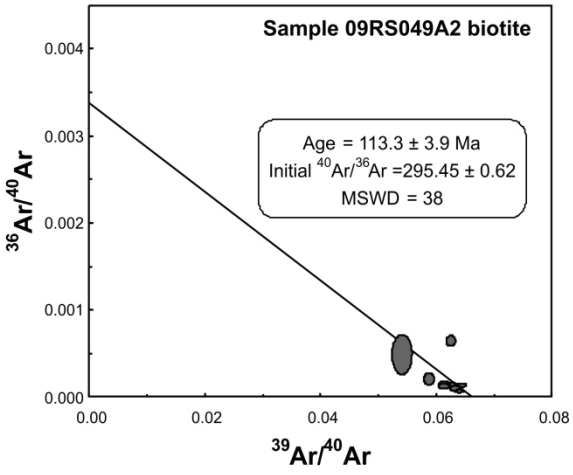
Sample 09RS049A2 biotite
Age = 113.3 ± 3.9 Ma
Initial 40Ar/36Ar =295.45 ± 0.62
MSWD = 38
36Ar/40Ar
39Ar/40Ar

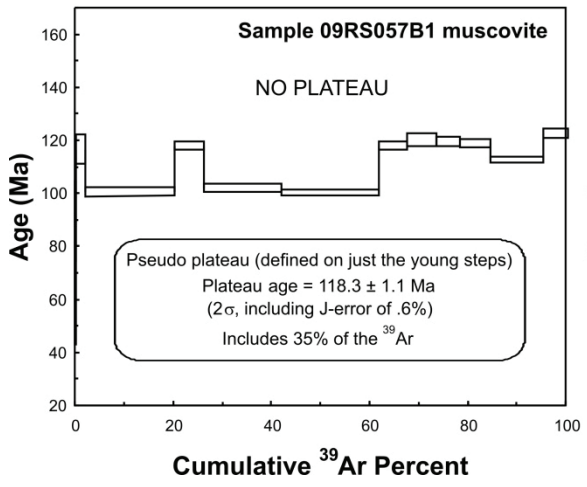
Sample 09RS057B1 muscovite
NO PLATEAU
Pseudo plateau (defined on just the young steps)
Plateau age = 118.3 ± 1.1 Ma
(2σ, including J-error of .6%)
Includes 35% of the 39Ar
Age (Ma)
Cumulative 39Ar Percent

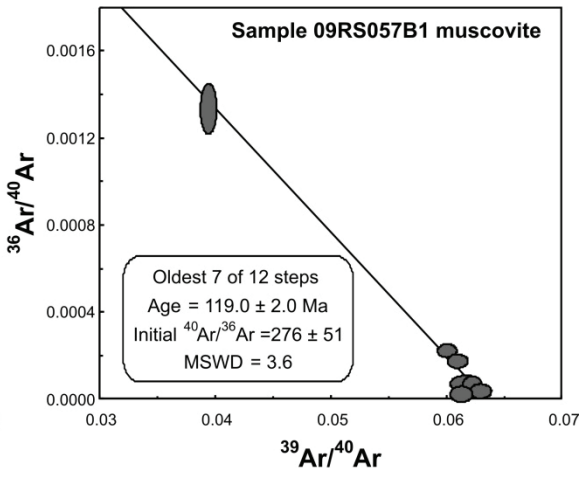
Sample 09RS057B1 muscovite
Oldest 7 of 12 steps
Age = 119.0 ± 2.0 Ma
Initial 40Ar/36Ar =276 ± 51
MSWD = 3.6
36Ar/40Ar
39Ar/40Ar

Table C2. $^{40}Ar/^{39}Ar$ analyses

Laser Power(%)	$^{40}Ar/^{39}Ar$	1σ	$^{37}Ar/^{39}Ar$	1σ	$^{36}Ar/^{39}Ar$	1σ	Ca/K	$\%^{40}Ar$ atm	$f\ ^{39}Ar$	$^{40}Ar^*/^{39}ArK$	Age	2σ
Sample **09RS189A1 biotite** (J = 0.0040994 ± 0.0000205)												
2.30 W	12.078	0.122	0.004	0.016	0.031	0.003	0.007	76.29	0.32	2.863	21.10	± 13.24
2.60 W	22.736	0.139	0.001	0.001	0.057	0.001	0.002	73.60	3.58	6.002	43.95	± 5.37
2.80 W	16.770	0.091	0.002	0.002	0.017	0.001	0.004	29.32	3.37	11.852	85.79	± 2.85
3.00 W	13.408	0.072	0.006	0.001	0.006	0.000	0.012	13.40	16.99	11.612	84.09	± 1.10
3.20 W	13.029	0.072	0.003	0.001	0.003	0.000	0.006	7.07	15.97	12.108	87.60	± 1.05
3.40 W	13.059	0.074	0.003	0.001	0.002	0.000	0.005	5.21	15.09	12.378	89.51	± 1.21
3.60 W	13.979	0.072	0.003	0.001	0.003	0.000	0.006	5.57	9.99	13.200	95.30	± 1.16
3.80 W	14.367	0.079	0.002	0.001	0.004	0.000	0.003	7.98	8.27	13.220	95.44	± 1.22
4.10 W	14.384	0.079	0.000	0.001	0.004	0.000	0.000	8.91	8.68	13.103	94.61	± 1.20
4.50 W	14.594	0.085	0.001	0.001	0.004	0.000	0.002	8.87	8.40	13.300	96.00	± 1.30
5.00 W	15.098	0.088	0.004	0.002	0.005	0.000	0.007	10.24	6.15	13.552	97.77	± 1.62
5.50 W	17.629	0.131	0.001	0.005	0.012	0.001	0.002	19.86	2.02	14.128	101.81	± 2.62
6.00 W	21.667	0.173	0.001	0.009	0.024	0.001	0.001	33.37	1.16	14.437	103.98	± 5.07

Laser Power(%)	$^{40}Ar/^{39}Ar$	1σ	$^{37}Ar/^{39}Ar$	1σ	$^{36}Ar/^{39}Ar$	1σ	Ca/K	$\%^{40}Ar$ atm	$f\ ^{39}Ar$	$^{40}Ar^*/^{39}ArK$	Age	2σ
Sample **09RS189A1 muscovite** (J = 0.0040994 ± 0.0000205)												
2.30 W	18.743	0.177	-0.044	0.019	0.040	0.002	-0.081	63.73	0.50	6.797	49.70	± 7.01
2.60 W	21.624	0.141	0.006	0.003	0.018	0.001	0.011	25.21	1.71	16.172	116.08	± 3.40
2.80 W	16.571	0.092	0.001	0.001	0.009	0.000	0.002	15.55	6.18	13.995	100.88	± 1.82
3.00 W	13.994	0.077	0.005	0.001	0.005	0.000	0.009	9.96	12.07	12.601	91.08	± 1.13
3.20 W	11.596	0.064	0.004	0.000	0.002	0.000	0.007	4.57	27.60	11.066	80.23	± 0.93
3.30 W	12.693	0.072	0.004	0.001	0.002	0.000	0.008	4.79	17.06	12.085	87.44	± 1.04
3.40 W	14.621	0.085	0.003	0.001	0.003	0.000	0.006	5.68	6.51	13.791	99.45	± 1.30
3.60 W	14.858	0.087	0.004	0.001	0.002	0.000	0.008	3.58	4.92	14.325	103.19	± 1.47
3.80 W	15.051	0.087	0.004	0.002	0.002	0.000	0.007	3.82	4.06	14.477	104.25	± 1.48
4.10 W	15.319	0.088	0.001	0.002	0.002	0.000	0.001	3.65	2.84	14.760	106.23	± 1.91
4.70 W	15.134	0.091	0.001	0.002	0.001	0.000	0.001	2.89	3.33	14.697	105.79	± 1.39
5.70 W	14.129	0.076	0.001	0.001	0.001	0.000	0.002	1.93	7.58	13.856	99.90	± 1.11
6.70 W	15.302	0.093	0.003	0.002	0.001	0.000	0.005	2.96	3.20	14.848	106.85	± 1.52
7.50 W	15.413	0.102	0.005	0.004	0.002	0.000	0.008	4.35	2.43	14.743	106.11	± 2.03

Laser Power(%)	$^{40}Ar/^{39}Ar$	1σ	$^{37}Ar/^{39}Ar$	1σ	$^{36}Ar/^{39}Ar$	1σ	Ca/K	$\%^{40}Ar$ atm	$f\ ^{39}Ar$	$^{40}Ar^*/^{39}ArK$	Age	2σ
Sample **00RAY225A biotite** (J = 0.0041647 ± 0.0000208)												
2.30	158.127	2.070	0.001	0.076	0.408	0.040	0.002	76.31	0.07	37.456	262.13	± 154.56
2.70	24.331	0.198	0.049	0.005	0.041	0.003	0.089	50.29	0.87	12.096	88.88	± 11.77
3.10	17.311	0.099	0.058	0.002	0.009	0.000	0.106	15.23	5.81	14.676	107.28	± 2.06
3.40	15.179	0.084	0.030	0.002	0.003	0.000	0.054	6.76	10.25	14.154	103.57	± 1.32
3.60	15.331	0.087	0.011	0.001	0.002	0.000	0.021	4.82	8.68	14.593	106.69	± 1.23
3.90	13.893	0.077	0.015	0.001	0.001	0.000	0.027	1.95	16.43	13.623	99.79	± 1.10
4.20	13.961	0.075	0.012	0.001	0.001	0.000	0.022	2.12	14.36	13.665	100.09	± 1.08
4.50	14.856	0.083	0.020	0.001	0.001	0.000	0.037	2.35	10.44	14.507	106.08	± 1.18
4.80	15.126	0.083	0.013	0.001	0.001	0.000	0.024	2.16	9.60	14.800	108.16	± 1.20
5.20	15.585	0.087	0.010	0.001	0.001	0.000	0.019	2.96	8.42	15.125	110.46	± 1.27
5.80	15.210	0.082	0.017	0.001	0.001	0.000	0.032	2.17	9.38	14.881	108.73	± 1.18
6.50	16.940	0.095	0.035	0.001	0.001	0.000	0.065	2.76	4.52	16.472	119.98	± 1.44
7.50	19.899	0.130	0.037	0.004	0.004	0.000	0.067	5.99	1.17	18.706	135.66	± 2.41

Laser Power(%)	$^{40}Ar/^{39}Ar$	1σ	$^{37}Ar/^{39}Ar$	1σ	$^{36}Ar/^{39}Ar$	1σ	Ca/K	$\%^{40}Ar$ atm	$f\ ^{39}Ar$	$^{40}Ar^*/^{39}ArK$	Age	2σ
Sample **00RAY225A muscovite** (J = 0.0041987 ± 0.0000210)												
2.30	58.408	1.021	0.132	0.037	0.187	0.006	0.241	94.46	0.13	3.235	24.40	± 21.26
2.60	23.660	0.258	0.083	0.009	0.027	0.002	0.151	34.30	0.52	15.546	114.34	± 6.94
2.90	17.948	0.179	0.122	0.008	0.005	0.001	0.224	7.59	1.56	16.587	121.75	± 3.26
3.10	16.011	0.104	0.058	0.002	0.003	0.000	0.107	5.24	7.39	15.172	111.68	± 1.58
3.30	15.147	0.105	0.019	0.001	0.003	0.000	0.035	5.20	10.29	14.360	105.87	± 1.50
3.50	15.390	0.091	0.013	0.000	0.004	0.000	0.024	7.53	12.02	14.232	104.95	± 1.31
3.70	14.106	0.072	0.014	0.000	0.001	0.000	0.026	2.15	33.42	13.803	101.88	± 1.02
3.80	17.049	0.104	0.039	0.003	0.003	0.001	0.072	5.03	3.57	16.193	118.95	± 2.73
4.10	16.707	0.099	0.043	0.002	0.002	0.000	0.079	3.08	4.50	16.193	118.94	± 1.41
4.50	16.019	0.094	0.080	0.002	0.001	0.000	0.146	2.62	7.00	15.600	114.72	± 1.33
5.00	15.848	0.090	0.064	0.002	0.001	0.000	0.117	2.01	6.79	15.530	114.23	± 1.28
5.50	16.260	0.086	0.046	0.002	0.002	0.000	0.085	3.09	3.84	15.758	115.85	± 1.32
6.00	16.842	0.132	0.036	0.003	0.002	0.000	0.065	3.21	2.30	16.303	119.73	± 1.99
6.80	16.361	0.088	0.035	0.005	0.001	0.000	0.063	2.67	3.88	15.924	117.03	± 1.36
7.50	16.776	0.092	0.020	0.002	0.001	0.000	0.036	2.63	2.79	16.336	119.96	± 1.75

Laser Power(%)	$^{40}Ar/^{39}Ar$	1σ	$^{37}Ar/^{39}Ar$	1σ	$^{36}Ar/^{39}Ar$	1σ	Ca/K	$\%^{40}Ar$ atm	$f\ ^{39}Ar$	$^{40}Ar^*/^{39}ArK$	Age	2σ
Sample **03RAYP001B1 Biotite** (J = 0.0042850 ± 0.0000214)												
2.30	28.071	2.182	0.021	0.077	0.070	0.023	0.039	73.85	0.15	7.342	56.01	± 105.44
2.60	24.169	0.323	0.005	0.010	0.034	0.003	0.009	41.23	1.14	14.205	106.85	± 13.77
2.90	15.274	0.094	0.003	0.001	0.003	0.000	0.006	6.51	8.39	14.279	107.39	± 2.15
3.10	15.017	0.094	0.003	0.002	0.001	0.000	0.006	2.90	7.94	14.582	109.60	± 2.21
3.30	15.038	0.126	0.002	0.002	0.001	0.000	0.004	3.07	7.88	14.576	109.56	± 2.24
3.50	14.530	0.086	0.005	0.001	0.001	0.000	0.010	1.87	10.57	14.257	107.23	± 1.36
3.70	13.639	0.075	0.011	0.001	0.001	0.000	0.021	1.72	16.17	13.403	100.99	± 1.12
3.90	14.624	0.089	0.002	0.001	0.001	0.000	0.004	2.09	10.26	14.318	107.68	± 1.36
4.10	14.959	0.090	0.005	0.001	0.001	0.000	0.009	2.66	7.71	14.562	109.45	± 1.44
4.50	14.981	0.089	0.002	0.002	0.001	0.000	0.005	2.85	7.00	14.554	109.40	± 1.45
5.00	14.682	0.083	0.005	0.001	0.001	0.000	0.009	2.36	9.15	14.336	107.81	± 1.34
5.50	14.638	0.079	0.006	0.001	0.001	0.000	0.010	1.79	9.25	14.376	108.10	± 1.24
6.00	15.241	0.127	0.007	0.002	0.001	0.000	0.013	2.57	3.29	14.850	111.55	± 2.42
6.50	15.823	0.223	0.012	0.010	0.002	0.001	0.022	3.23	1.13	15.312	114.92	± 5.39

Laser Power(%)	$^{40}Ar/^{39}Ar$	1σ	$^{37}Ar/^{39}Ar$	1σ	$^{36}Ar/^{39}Ar$	1σ	Ca/K	$\%^{40}Ar$ atm	$f\ ^{39}Ar$	$^{40}Ar^*/^{39}ArK$	Age	2σ
Sample **03RAYP001B1 muscovite** (J = 0.0042850 ± 0.0000214)												
2.00	64.902	21.360	2.223	1.145	0.442	0.335	4.079	201.11	0.01	65.726	-598.15	± 1990.00
2.50	30.844	0.499	0.001	0.013	0.053	0.009	0.002	50.83	0.44	15.165	113.85	± 40.55
3.00	12.175	0.067	0.000	0.000	0.003	0.000	0.001	7.63	86.57	11.246	85.11	± 1.03
3.20	15.522	0.105	0.000	0.001	0.001	0.001	0.001	2.42	6.63	15.147	113.72	± 2.92
3.40	15.282	0.150	0.001	0.003	0.000	0.001	0.001	0.37	2.62	15.225	114.29	± 6.06
3.80	15.619	0.205	0.003	0.003	0.001	0.002	0.006	1.47	1.85	15.389	115.48	± 7.23
4.50	15.713	0.160	0.000	0.004	0.001	0.002	0.000	1.96	1.88	15.405	115.59	± 7.94

Laser Power(%)	$^{40}Ar/^{39}Ar$	1σ	$^{37}Ar/^{39}Ar$	1σ	$^{36}Ar/^{39}Ar$	1σ	Ca/K	$\%^{40}Ar$ atm	$f\ ^{39}Ar$	$^{40}Ar^*/^{39}ArK$	Age	2σ
Sample **09RS179A hornblende** (J = 0.0040708 ± 0.0000204)												
2.30	686.352	46.423	3.226	0.336	1.987	0.176	5.922	85.53	0.08	99.523	615.07	± 377.75
2.80	239.222	5.108	4.676	0.170	0.683	0.033	8.593	84.16	0.37	38.007	260.14	± 115.78
3.30	130.719	2.180	10.446	0.360	0.363	0.021	19.274	81.46	0.62	24.415	171.35	± 80.78
3.70	27.376	0.318	4.699	0.192	0.036	0.003	8.635	37.96	2.74	17.041	121.28	± 14.69
4.20	17.096	0.117	4.114	0.135	0.008	0.001	7.556	11.19	12.81	15.227	108.75	± 3.52
4.50	16.020	0.095	3.944	0.086	0.005	0.000	7.244	7.04	18.77	14.934	106.72	± 2.22
5.00	13.676	0.075	4.171	0.074	0.003	0.000	7.662	4.89	53.74	13.046	93.57	± 1.19
5.40	17.707	0.125	4.187	0.129	0.010	0.001	7.691	14.46	9.37	15.192	108.51	± 3.96
6.00	30.124	0.557	4.259	0.180	0.053	0.005	7.824	51.15	1.50	14.761	105.52	± 22.70

Laser Power(%)	$^{40}Ar/^{39}Ar$	1σ	$^{37}Ar/^{39}Ar$	1σ	$^{36}Ar/^{39}Ar$	1σ	Ca/K	$\%^{40}Ar$ atm	$f\ ^{39}Ar$	$^{40}Ar^*/^{39}ArK$	Age	2σ
Sample **00GGA073A biotite** (J = 0.0043265 ± 0.0000216)												
2.30	57.752	0.471	0.053	0.004	0.201	0.005	0.097	102.88	2.21	1.662	-13.05	± 22.37
2.60	23.494	0.190	0.026	0.002	0.066	0.002	0.048	83.59	5.90	3.854	29.91	± 7.45
2.90	25.432	0.175	0.023	0.002	0.053	0.001	0.041	61.91	9.39	9.687	74.25	± 5.58
3.20	27.336	0.157	0.015	0.002	0.039	0.001	0.028	41.78	12.11	15.916	120.43	± 4.42
3.50	27.065	0.168	0.012	0.002	0.026	0.001	0.022	28.84	15.51	19.258	144.72	± 3.75
3.80	26.767	0.160	0.017	0.001	0.023	0.001	0.031	25.07	17.35	20.057	150.48	± 2.93
4.20	27.594	0.187	0.036	0.001	0.026	0.001	0.066	27.87	14.95	19.902	149.37	± 4.14
4.80	27.744	0.163	0.085	0.002	0.025	0.001	0.156	26.77	16.15	20.316	152.34	± 3.71
5.50	29.692	0.249	0.080	0.002	0.028	0.001	0.146	27.93	6.42	21.398	160.11	± 4.88

Laser Power(%)	$^{40}Ar/^{39}Ar$	1σ	$^{37}Ar/^{39}Ar$	1σ	$^{36}Ar/^{39}Ar$	1σ	Ca/K	$\%^{40}Ar$ atm	$f\ ^{39}Ar$	$^{40}Ar^*/^{39}ArK$	Age	2σ
Sample **03GAR42A biotite** (J = 0.0043120 ± 0.0000216)												
2.40	71.680	0.722	0.006	0.016	0.233	0.011	0.010	96.19	0.55	2.730	21.16	± 48.52
2.80	23.526	0.144	0.011	0.002	0.038	0.001	0.020	48.19	6.64	12.188	92.63	± 5.51
3.00	25.451	0.150	0.005	0.001	0.014	0.000	0.009	16.72	10.34	21.196	158.15	± 2.49
3.20	27.296	0.205	0.004	0.001	0.008	0.001	0.007	8.77	9.26	24.901	184.43	± 3.96
3.40	27.631	0.172	0.004	0.001	0.007	0.000	0.007	8.02	8.47	25.415	188.05	± 2.65
3.60	28.113	0.210	0.001	0.001	0.006	0.001	0.003	6.52	8.43	26.279	194.11	± 4.79
3.90	25.459	0.145	0.002	0.001	0.007	0.000	0.004	7.80	17.65	23.473	174.35	± 2.06
4.20	27.207	0.170	0.004	0.001	0.005	0.000	0.006	5.04	11.82	25.834	190.99	± 2.62
4.60	26.806	0.163	0.005	0.001	0.003	0.000	0.008	3.83	14.04	25.778	190.60	± 2.77
5.10	27.999	0.177	0.013	0.002	0.003	0.000	0.024	3.14	9.30	27.121	200.00	± 2.70
5.80	29.655	0.278	0.008	0.002	0.003	0.001	0.015	3.01	3.49	28.763	211.43	± 5.35

Laser Power(%)	$^{40}Ar/^{39}Ar$	1σ	$^{37}Ar/^{39}Ar$	1σ	$^{36}Ar/^{39}Ar$	1σ	Ca/K	$\%^{40}Ar$ atm	$f\ ^{39}Ar$	$^{40}Ar^*/^{39}ArK$	Age	2σ
Sample **10RS020 muscovite** (J = 0.0040470 ± 0.0000202)												
2.30	36.410	0.393	0.046	0.031	0.092	0.005	0.085	74.70	0.34	9.211	66.18	± 18.88
2.50	25.181	0.218	0.010	0.022	0.017	0.002	0.018	19.55	0.42	20.258	142.49	± 8.32
2.80	27.575	0.153	0.019	0.005	0.008	0.001	0.035	8.69	2.52	25.178	175.47	± 3.06
3.10	24.508	0.132	0.012	0.001	0.003	0.000	0.022	4.24	8.57	23.469	164.08	± 1.97
3.30	26.201	0.139	0.015	0.002	0.003	0.000	0.028	3.99	6.00	25.156	175.32	± 1.93
3.50	25.191	0.146	0.026	0.002	0.002	0.000	0.047	2.75	7.13	24.499	170.95	± 1.98
3.70	23.937	0.130	0.034	0.003	0.002	0.000	0.063	2.73	9.73	23.284	162.84	± 1.84
4.20	21.881	0.116	0.111	0.002	0.002	0.000	0.203	2.36	20.08	21.367	149.97	± 1.54
4.50	22.354	0.134	0.028	0.001	0.002	0.000	0.051	3.07	13.85	21.669	152.01	± 2.30
4.80	21.726	0.124	0.020	0.001	0.001	0.000	0.036	2.09	15.93	21.273	149.34	± 1.98
5.00	25.559	0.136	0.025	0.002	0.003	0.000	0.046	3.42	6.09	24.686	172.19	± 1.85
5.30	28.313	0.228	0.034	0.005	0.002	0.000	0.062	2.48	2.39	27.610	191.55	± 3.19
5.60	27.955	0.154	0.019	0.008	0.002	0.000	0.035	2.54	3.16	27.246	189.15	± 2.27
6.50	28.267	0.154	0.043	0.005	0.004	0.000	0.080	3.97	3.00	27.145	188.48	± 2.32
7.50	32.300	0.218	0.201	0.014	0.015	0.001	0.368	13.92	0.80	27.809	192.85	± 4.39

Laser Power(%)	$^{40}Ar/^{39}Ar$	1σ	$^{37}Ar/^{39}Ar$	1σ	$^{36}Ar/^{39}Ar$	1σ	Ca/K	$\%^{40}Ar$ atm	$f\ ^{39}Ar$	$^{40}Ar^*/^{39}ArK$	Age	2σ
Sample **10RS026 muscovite** (J = 0.0043300 ± 0.0000217)												
2.30	38.452	0.876	-0.054	0.019	0.067	0.015	-0.099	51.60	0.37	18.612	140.16	± 65.12
2.60	28.895	0.231	0.003	0.004	0.012	0.002	0.006	12.19	2.19	25.372	188.49	± 9.02
2.90	25.750	0.153	0.000	0.001	0.004	0.000	0.001	4.47	20.79	24.598	183.02	± 2.40
3.20	23.294	0.131	0.000	0.000	0.000	0.000	0.000	0.74	45.20	23.122	172.54	± 1.91
3.40	26.767	0.167	0.000	0.000	0.001	0.000	0.001	1.27	18.46	26.426	195.91	± 2.50
3.60	28.409	0.224	0.002	0.002	0.002	0.001	0.003	2.70	3.72	27.642	204.43	± 6.32
4.60	28.126	0.392	0.000	0.002	0.001	0.001	0.001	1.52	4.85	27.697	204.82	± 6.15
6.00	28.813	0.245	0.005	0.003	0.004	0.001	0.009	4.23	4.44	27.596	204.11	± 6.10

Laser Power(%)	$^{40}Ar/^{39}Ar$	1σ	$^{37}Ar/^{39}Ar$	1σ	$^{36}Ar/^{39}Ar$	1σ	Ca/K	$\%^{40}Ar$ atm	$f\ ^{39}Ar$	$^{40}Ar^*/^{39}ArK$	Age	2σ
Sample **10RS073A muscovite** (J = 0.0042619 ± 0.0000213)												
2.30	25.967	0.297	0.002	0.015	0.036	0.003	0.003	40.60	0.52	15.424	115.13	± 12.22
2.60	30.386	0.178	0.002	0.002	0.008	0.000	0.004	8.02	5.65	27.949	203.51	± 2.51
2.80	26.407	0.140	0.005	0.000	0.003	0.000	0.008	3.17	28.62	25.569	187.04	± 1.93
2.90	26.424	0.162	0.012	0.001	0.003	0.000	0.021	3.48	14.86	25.506	186.60	± 2.25
3.00	29.979	0.181	0.015	0.004	0.004	0.000	0.028	4.20	5.54	28.720	208.81	± 2.64
3.20	25.457	0.155	0.013	0.001	0.002	0.000	0.023	2.00	20.57	24.948	182.72	± 2.14
3.30	31.458	0.173	0.024	0.003	0.005	0.000	0.045	5.11	4.82	29.850	216.55	± 2.46
3.50	31.659	0.171	0.001	0.001	0.003	0.000	0.002	3.06	5.70	30.692	222.30	± 2.44
3.80	33.263	0.182	0.002	0.002	0.003	0.000	0.004	2.86	5.21	32.313	233.31	± 2.62
4.20	33.463	0.192	0.005	0.002	0.004	0.000	0.008	3.25	4.56	32.375	233.73	± 2.78
4.90	36.421	0.223	-0.005	0.003	0.010	0.001	-0.009	8.10	2.65	33.470	241.13	± 4.18
5.80	39.385	0.255	0.015	0.010	0.016	0.001	0.028	12.44	1.30	34.484	247.96	± 4.92

Laser Power(%)	$^{40}Ar/^{39}Ar$	1σ	$^{37}Ar/^{39}Ar$	1σ	$^{36}Ar/^{39}Ar$	1σ	Ca/K	$\%^{40}Ar$ atm	$f\ ^{39}Ar$	$^{40}Ar^*/^{39}ArK$	Age	2σ
Sample **10RS088B1 muscovite** (J = 0.0040292 ± 0.0000201)												
2.30	36.737	0.402	0.066	0.010	0.061	0.003	0.121	48.76	0.75	18.823	132.20	± 13.92
2.60	30.365	0.162	0.010	0.001	0.007	0.000	0.019	7.25	18.22	28.165	194.38	± 2.11
2.70	33.387	0.187	0.004	0.002	0.005	0.000	0.007	4.54	11.70	31.869	218.46	± 2.46
2.80	34.025	0.222	0.006	0.003	0.005	0.000	0.012	4.20	5.83	32.595	223.14	± 3.32
3.00	28.112	0.156	0.004	0.001	0.005	0.000	0.008	5.32	22.26	26.617	184.23	± 2.17
3.20	30.399	0.170	0.009	0.001	0.004	0.000	0.016	3.94	12.67	29.201	201.14	± 2.27
3.40	33.392	0.198	0.006	0.003	0.006	0.001	0.010	5.73	5.08	31.481	215.95	± 3.45
3.70	33.765	0.203	0.006	0.003	0.007	0.000	0.011	6.49	8.29	31.573	216.55	± 2.75
4.10	36.377	0.211	0.004	0.003	0.010	0.000	0.007	7.99	6.77	33.472	228.77	± 2.92
4.70	37.945	0.219	0.003	0.004	0.009	0.001	0.006	7.02	4.93	35.283	240.36	± 3.23
5.50	42.619	0.315	0.024	0.007	0.033	0.001	0.045	22.91	3.50	32.856	224.82	± 5.33

Laser Power(%)	$^{40}Ar/^{39}Ar$	1σ	$^{37}Ar/^{39}Ar$	1σ	$^{36}Ar/^{39}Ar$	1σ	Ca/K	$\%^{40}Ar$ atm	$f\ ^{39}Ar$	$^{40}Ar^*/^{39}ArK$	Age	2σ
Sample **10RS041B3 hornblende** (J = 0.0042315 ± 0.0000212)												
2.30	557.230	16.651	3.089	0.231	1.200	0.081	5.669	63.59	0.10	203.352	1122.67	± 184.63
2.60	178.604	2.388	1.897	0.122	0.207	0.018	3.479	34.11	0.14	117.839	731.57	± 55.56
3.00	54.217	0.457	0.516	0.025	0.067	0.003	0.946	36.51	0.83	34.432	245.96	± 10.69
3.40	24.956	0.193	0.562	0.026	0.019	0.001	1.029	22.15	2.28	19.435	142.92	± 4.14
3.80	19.023	0.140	4.512	0.101	0.005	0.000	8.289	6.44	16.30	17.855	131.71	± 2.16
4.00	15.394	0.098	4.402	0.076	0.003	0.000	8.088	3.45	41.62	14.909	110.63	± 1.43
4.10	17.625	0.109	4.185	0.174	0.003	0.000	7.688	3.48	17.22	17.061	126.05	± 1.62
4.30	18.690	0.114	4.229	0.080	0.003	0.000	7.768	2.78	10.48	18.225	134.34	± 1.73
4.60	19.890	0.135	3.361	0.060	0.005	0.001	6.170	5.69	2.04	18.803	138.44	± 3.44
5.60	18.039	0.101	1.998	0.034	0.003	0.000	3.664	3.75	4.91	17.386	128.37	± 1.98
6.50	18.242	0.110	2.054	0.044	0.003	0.000	3.767	3.35	4.08	17.656	130.29	± 1.80

Laser Power(%)	$^{40}Ar/^{39}Ar$	1σ	$^{37}Ar/^{39}Ar$	1σ	$^{36}Ar/^{39}Ar$	1σ	Ca/K	$\%^{40}Ar$ atm	$f\ ^{39}Ar$	$^{40}Ar^*/^{39}ArK$	Age	2σ
Sample **10RS049A2 biotite** (J = 0.0042884 ± 0.0000214)												
3.00	16.017	0.089	0.003	0.001	0.011	0.000	0.005	19.62	24.31	12.875	97.19	± 2.06
3.20	15.550	0.080	0.009	0.001	0.002	0.000	0.016	4.64	16.09	14.829	111.49	± 1.28
3.40	15.945	0.083	0.002	0.001	0.002	0.000	0.003	4.69	11.87	15.197	114.17	± 1.33
3.60	15.838	0.087	0.004	0.001	0.002	0.000	0.007	3.66	12.71	15.258	114.61	± 1.49
3.80	15.640	0.085	0.003	0.001	0.001	0.000	0.005	2.66	14.81	15.225	114.37	± 1.30
4.00	16.320	0.107	0.007	0.001	0.002	0.000	0.013	4.66	7.68	15.560	116.81	± 1.98
4.40	16.340	0.101	0.003	0.001	0.002	0.000	0.005	4.32	8.06	15.634	117.35	± 1.67
5.00	17.050	0.103	0.005	0.005	0.004	0.000	0.010	6.66	3.60	15.915	119.39	± 2.44
6.00	18.505	0.237	0.016	0.014	0.009	0.002	0.029	14.98	0.88	15.732	118.06	± 7.94

Laser Power(%)	$^{40}Ar/^{39}Ar$	1σ	$^{37}Ar/^{39}Ar$	1σ	$^{36}Ar/^{39}Ar$	1σ	Ca/K	$\%^{40}Ar$ atm	$f\ ^{39}Ar$	$^{40}Ar^*/^{39}ArK$	Age	2σ
Sample **10RS057B1 muscovite** (J = 0.0043239 ± 0.0000216)												
2.30	53.814	0.664	0.000	0.010	0.150	0.007	0.000	82.15	0.31	9.605	73.58	± 30.56
2.60	25.368	0.184	0.001	0.001	0.034	0.001	0.002	39.51	1.80	15.345	116.17	± 5.42
2.80	15.602	0.093	0.000	0.000	0.008	0.000	0.000	15.33	18.07	13.210	100.45	± 1.72
2.90	16.681	0.093	0.001	0.000	0.004	0.000	0.001	6.87	6.08	15.535	117.56	± 1.57
3.10	15.533	0.087	0.001	0.000	0.007	0.000	0.001	13.86	15.76	13.381	101.71	± 1.45
3.30	14.364	0.080	0.001	0.000	0.004	0.000	0.001	8.47	19.64	13.147	99.98	± 1.22
3.50	16.430	0.096	0.002	0.001	0.003	0.000	0.003	5.47	5.71	15.531	117.53	± 1.63
3.80	16.242	0.144	0.000	0.001	0.001	0.000	0.000	2.45	5.91	15.844	119.83	± 2.32
4.20	16.097	0.091	0.000	0.001	0.001	0.000	0.000	2.08	4.81	15.762	119.22	± 1.86
4.80	15.917	0.097	0.000	0.000	0.001	0.000	0.000	1.44	6.24	15.688	118.68	± 1.68
5.50	15.050	0.081	0.000	0.000	0.001	0.000	0.000	1.45	10.87	14.832	112.40	± 1.24
6.50	16.347	0.104	0.001	0.001	0.000	0.000	0.002	1.01	4.79	16.182	122.30	± 1.85

References

Koppers, Anthony, A.P., 2002, ArArCALC – software for $^{40}Ar/^{39}Ar$ age calculations: Computers and Geosciences, v. 28, p. 605–619.

Ludwig, K.R., 2003, Isoplot 3.09 A Geochronological toolkit for Microsoft Excel. Berkeley Geochronology Center, Special Publication No. 4.

Renne, P.R., Swisher, C.C., Deino, A.L., Karner, D.B., Owens, T.L., and DePaulo, D.J., 1998, Intercalibration of standards, absolute ages and uncertainties in $^{40}Ar/^{39}Ar$ dating: Chemical Geology, v. 145, p. 117–152.